8-1-1989

Performance Characteristics of Switched Reluctance Motor Drive

M. Moallem
Purdue University

C. M. Ong
Purdue University

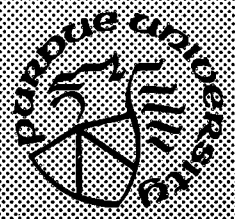

Performance Characteristics of Switched Reluctance Motor Drive

M. Moallem
C. M. Ong

TR-EE 89-52
August, 1989

School of Electrical Engineering
Purdue University
West Lafayette, Indiana 47907

TABLE OF CONTENTS

page

APPENDICES

LIST OF TABLES

Table Page

Appendix Table

LIST OF FIGURES

Figure Page

Figure Page

Figure Page

Appendix Figure

LIST OF PRINCIPAL SYMBOLS

$\underline{A}$ ..... Magnetic vector potential(MVP)
$\overline{A}$ ..... Vector containing node potentials
B ..... Magnetic flux density
C_ω ..... Coefficient of the speed voltage, $\frac{\partial \lambda}{\partial \theta}$
H ..... Magnetic field intensity
i ..... Phase current
J_s ..... Current density
J ..... Jacobian matrix
L ..... Inductance
N ..... Number of winding turns
$\overline{N}$ ..... Vector containing turn contribution of each node
N_r ..... Number of rotor poles
N_s ..... Number of stator poles
n ..... Total number of nodes in the mesh
n_e ..... Total number of elements in the mesh
P ..... Power
q ..... Number of phases
R ..... Winding resistance per phase
T ..... Torque
V_{DC} ..... DC Supply voltage
V_s ..... Source voltage
V_{ph} ..... Phase terminal voltage
w ..... Energy density
W ..... Energy
W' ..... Coenergy
X ..... Reactance
Z ..... Effective stack length
β_r ..... Rotor pole arc
β_s ..... Stator pole arc
Δ_e ..... Area of the e^{th} element
θ_{on} ..... Ignition angle
θ_c ..... Conduction angle
θ_{off} ..... Commutation angle
θ_{ext} ..... Extinction angle

θ_{cy} .....Period of phase inductance variation
λ .....Flux linkage
μ .....Permeability
ν.....Reluctivity
τ.....Surface stress
ϕ .....Magnetic flux
ω.....Angular speed

ABSTRACT

In this report, methods and computational techniques for predicting the static and steady state characteristics of a switched reluctance motor drive are developed and the predicted characteristics are compared with experimental results. Because of high local saturation and narrow airgap in the SR motor, accurate calculation of the static characteristics of the torque, flux linkage, inductances, and speed emf from its FE field solution is not straightforward. For the purpose of this study, a two-dimensional finite element model is developed to handle the nonlinear magnetic field inside the machine. Based on a thorough study of the potential sources of errors in the field solution and in the computational methods used in postprocessing, new guidelines are developed regarding the shape and uniformity of the mesh in the airgap and the preservation of these qualities of the mesh as the rotor is rotated. When the proposed guidelines on the mesh configuration and its rotation were used, significant improvement in the accuracy of the field distribution and in the accuracy of the predicted torque/angle characteristics as compared to the experimentally measured torque was observed. Furthermore, all three methods of torque calculation, namely global virtual work, local virtual work, and Maxwell-stress tensor methods are converging to the same results and the torque/angle characteristics are smooth. Improvement in the prediction of such static characteristics is also essential to a realistic prediction of the steady state behavior. In the study of steady state performance of the SRM drive, the converter is approximated by a controlled, square wave pulse generator. In the integration process, the coefficients of the governing differential equation, being dependent on the phase current and rotor angle, are updated using surface interpolation method on the static characteristics. The predicted steady state characteristics compare favorably with the experimental results over a wide range of torque/speed variation.

CHAPTER 1
INTRODUCTION

The Switched Reluctance Motor (SRM) is a variable reluctance stepping motor that is designed to convert energy efficiently. The motor is double salient, and it is essential to machine operation that the number of rotor and stator poles be different. Torque is produced by the tendency of the rotor poles to align with the poles of the excited stator phase, and is independent of the direction of phase current, giving rise to the possibility of unipolar current in which only one main switching device is required per phase.

The SRM is of very simple structure: its rotor is brushless and has no winding of any kind. The motor is singly excited from stator windings, which are concentric coils wound in series on diagonally opposite stator poles. Both rotor and stator are made of laminated iron.

A typical example of an SRM cross-section is shown in Fig. 1.1. Also shown in this figure is the phase winding and switching circuit of one phase. The current in stator phases must be switched on and off in accordance with the rotor position. For example, for motoring action, a stator phase must be excited when a pair of opposite rotor poles is approaching its poles , and must be turned off before rotor and stator poles actually come into alignment. Continuous rotation of the rotor is obtained by sequential excitation of stator phases ; the rotor steps around in a direction opposite to that of stator phase excitation around the airgap. For the machine shown in Fig. 1.1, a counterclockwise rotation requires a stator excitation sequence of 1-2-3-4-1. The rotor position is sensed by optical devices placed on the stator. When interrupted by a disk rotating with the rotor and having the shape of rotor poles, the sensors generate the switching reference signals. For efficient and smooth energy conversion, the ignition and conduction angles of the stator phase current then must be varied as functions of rotor speed and load torque. To enhance the energy conversion efficiency, SR motors are usually designed to work under highly saturated condition.

In this chapter, first the fundamental principles in SRM design and their relation to its performance are briefly reviewed. Different switching circuit

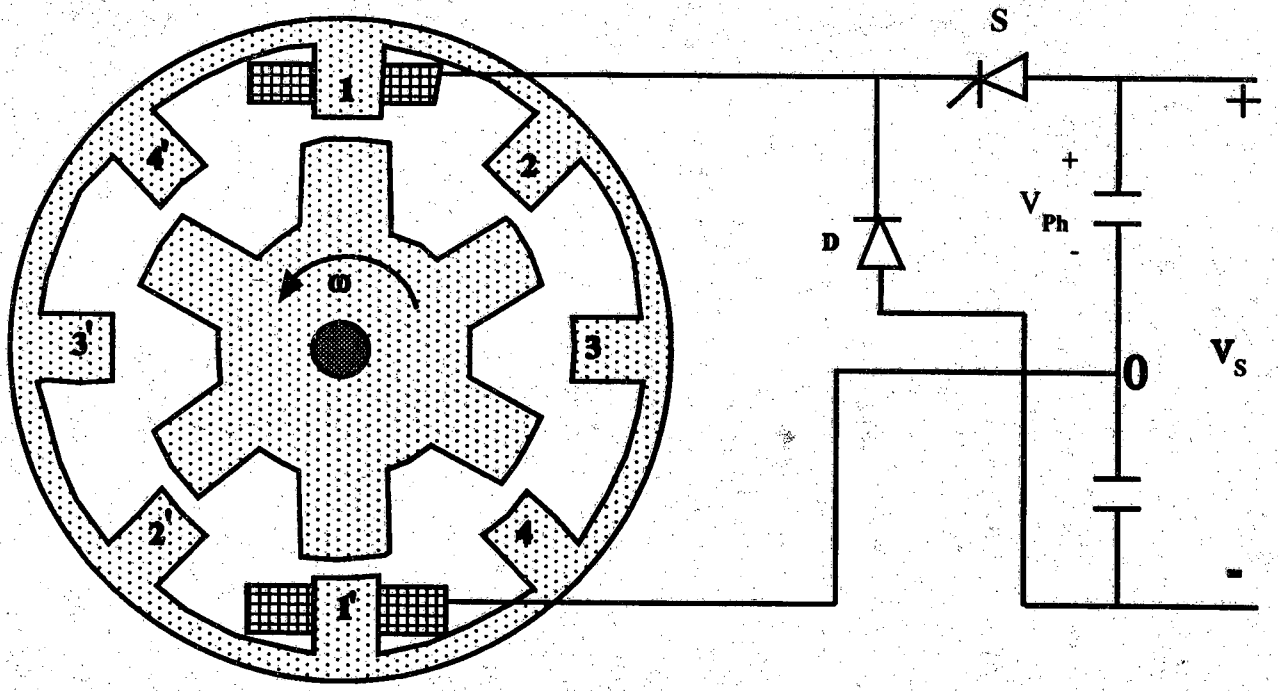

Figure 1.1. Schematic Cross-Section of SR Motor

configurations that can be used in an SRM drive are discussed next. The simple structure of SRM can be deceiving, because its analysis is indeed complicated. The difficulties in predicting the performance characteristics of SRM drive and the objective of this study are explained in detail next in the chapter. This will be followed by a review of technical papers on SRM drive. Finally, an overview of the report is presented.

1.1. Fundamentals of Design and Operation

Torque in an SR motor is developed by the tendency of the rotor to adopt a position of minimum reluctance or maximum phase inductance, and in doing so converting some of the field energy to mechanical energy. The instantaneous torque developed is time-varying; its magnitude and average depend on the profile of the excitation current waveform and its timing relative to the rotor position. For smooth and efficient performance at some particular speed and load condition the current must be initiated and commutated at certain rotor angles in relation to the rise and fall of the stator inductance.

Fig. 1.2 shows the hypothetical inductance waveform of an SR motor. In each revolution the inductance of each stator phase undergoes a cyclic variation; the number of cycles of inductance variation per revolution is the same as the number of rotor poles, N_r. A current pulse is applied to each phase during each cycle of inductance. Thus, the number of current pulses per revolution is qN_r, which is the same as the number of steps per revolution. The shape and peak of current pulse at any speed depend on its relative timing with respect to inductance waveform. The inductance profile, in turn, depends on such parameters as: the number of poles on rotor and stator, stator and rotor pole pitches, the ratio of pole arcs, the airgap separation in aligned and unaligned positions, the number of winding turns, and the magnetic characteristic of the iron used.

The following are some of the basic design considerations which have profound effects on the performance of an SR motor. The mutual inductances should be kept as small as possible in order to minimize their negative effect on torque production. Since electromagnetic torque produced is directly proportional to the derivative of phase inductance with respect to rotor position, $\frac{\partial L}{\partial \theta}$, the slope should be maximized by increasing maximum inductance at the aligned position and decreasing minimum inductance at the unaligned position. In order to increase the average positive torque and

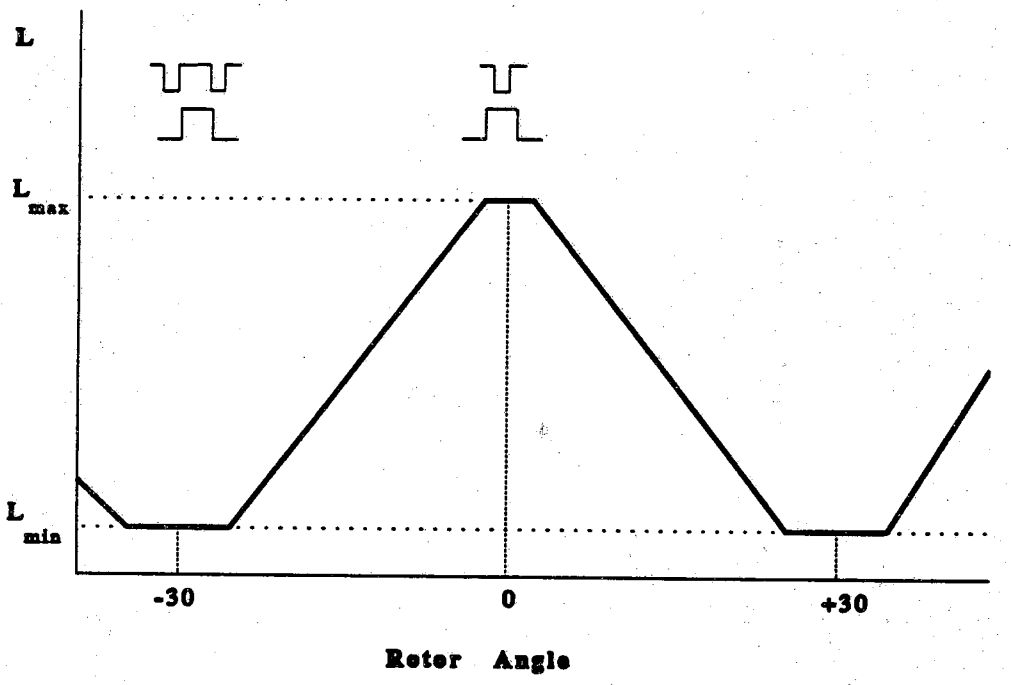

Figure 1.2. Stator phase inductance variation

decrease the negative torque production and copper losses, fast increase and also decrease of current at ignition and commutation angles are desirable. To achieve maximum $\frac{di}{dt}$ at the two ends of the positive torque region ($\frac{\partial L}{\partial \theta}>0$) inductance waveform is designed to have two flat regions which are usually called "dead zones" of torque production ($\frac{\partial L}{\partial \theta}=0$). To allow for flat top inductance waveform, the rotor and stator pole arcs are made to be not equal. and to provide more winding space, stator pole arc is usually smaller than rotor pole arc. Other factors in determining the number of poles, pole ratio, pole pitches, and pole arc ratio are: starting and reversibility capabilities, maximum switching frequency, low rotor inertia for quick mechanical response, and finally allowance for sufficient winding space. The consideration given to a combination of these factors has resulted in several practical stator/rotor pole ratios, such as 8/6, 6/4, and 10/4.

The large airgap separation in the unaligned position decreases the minimum inductance and mutual inductances and is the main reason for adoption of a double salient structure. On the other hand, a very small airgap at the aligned position provides a larger maximum inductance. More importantly, a small airgap with the same level of excitation produces a higher saturation level which is essential in efficient power conversion. The effect of saturation on the energy conversion efficiency is illustrated in Fig. 1.3. In this figure, i_0 is the smallest current in which the core saturates at the aligned position. If the motor is designed to operate under saturated conditions, at excitation current $i_1>i_0$, the converted energy is W_m and unconverted field energy which returns to source is W_f. With the same ignition and conduction angles and excitation current, the linear magnetic circuit results in additional converted energy of ΔW_m and unconverted field energy of ΔW_f. However, to obtain a higher flux linkage in linear case,λ_2, a larger source voltage is required, since

$$\lambda=\frac{V_s \theta_c}{\omega} \tag{1.1}$$

where speed ω, and conduction angle θ_c, are assumed to be the same in both cases. Thus, the linear magnetic circuit has slightly higher energy conversion capability, but the source voltage and unconverted energy are much higher than in a saturated circuit. In the saturated case, additional energy ΔW_m can be obtained by increasing the current from i_1 to i_2 without an increase in the unconverted energy. Higher unconverted field energy results in higher copper

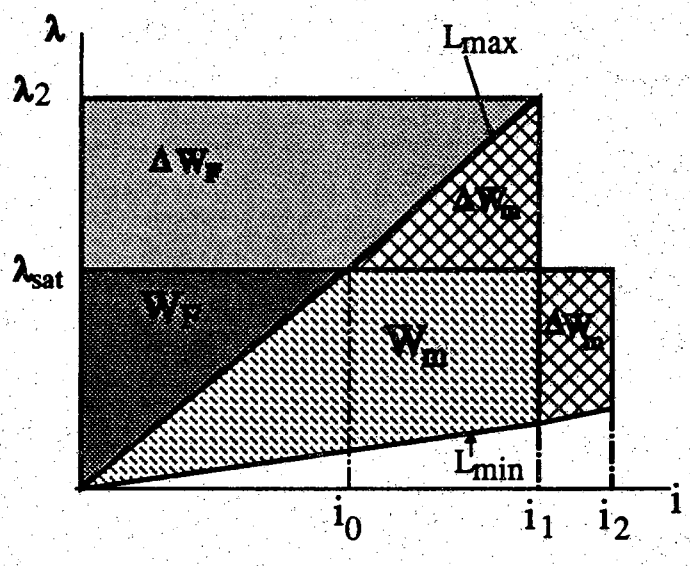

Figure 1.3. Effect of saturation

losses which reduces the overall efficiency. As a result, by operating the motor under a high saturated condition, the efficiency of the energy conversion process as defined by the ratio of converted energy W_m, to input apparent energy will increase significantly. Also a lower volt-ampere rating is required for switching devices and the overall efficiency is higher because of smaller copper losses.

In order to maximize the efficiency of the energy conversion process, the highest saturation level is desirable. At the same time, to decrease the motor size for the same power requirement, the torque producing capability can be increased by increasing the ratio of $\frac{L_{max}}{L_{min}}$ in the unsaturated condition. These conditions are met, to some extent, by keeping the airgap as small as manufacturing tolerance allows, and using very high permeability silicon steel lamination in the stator and rotor structure.

By appropriate timing of current pulse with respect to inductance waveform, SRM can operate as a motor or generator. In the region where $\frac{\partial L}{\partial \theta} > 0$, positive or motoring torque is produced (see Fig. 1.4); in the region where $\frac{\partial L}{\partial \theta} = 0$, no torque is produced (dead zone); and in the region where $\frac{\partial L}{\partial \theta} < 0$, negative or generating torque is produced. It is clear that excitation in the $\frac{\partial L}{\partial \theta} = 0$ region is just transitional in that it does not contribute to any torque production, but it does contribute to stator copper losses.

1.2. Switching Circuit

In a switched reluctance motor the production of torque in any direction of rotation is independent of the direction of the phase current, and depends only on the excitation sequence of the stator phases. This means that the phase current can be unipolar, which will then permit the use of only one switching device per phase, reducing the number of switches per phase required by half in comparison to other drives.

Many different power circuits have been designed for SRM drives [15]. Figure 1.5 shows three common power circuits that have been designed for an SRM drive. These circuits have the following common features: the phase winding is in series with its switching device, protecting the device against shoot-through; the phases can operate independently, which permits, operation at reduced power level even if one of the phases is lost.

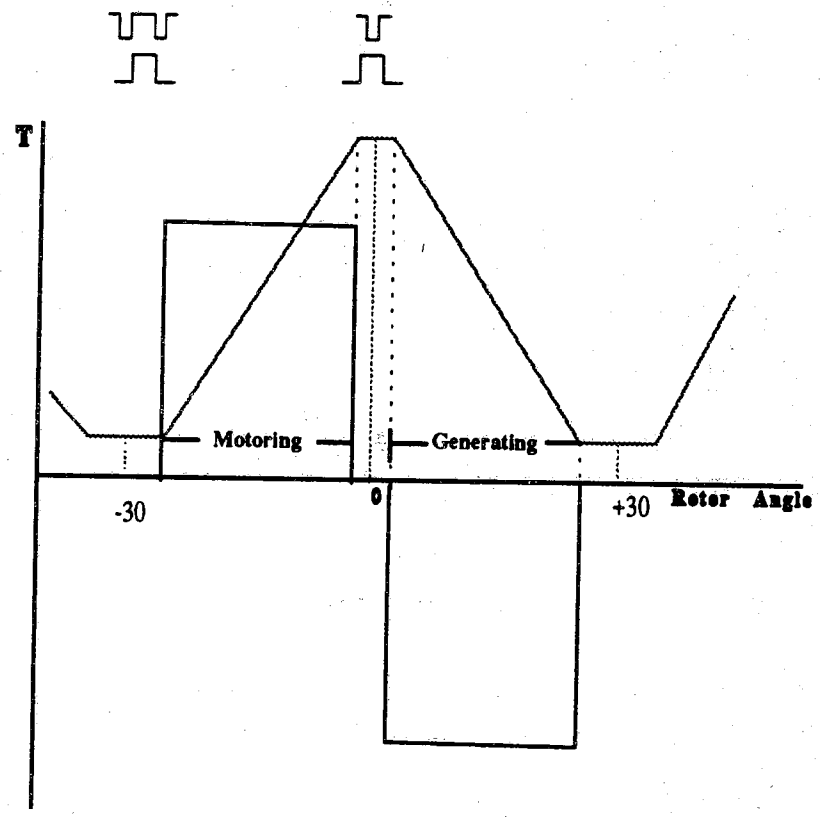

Figure 1.4. Ideal torque profile with constant current and linear inductance

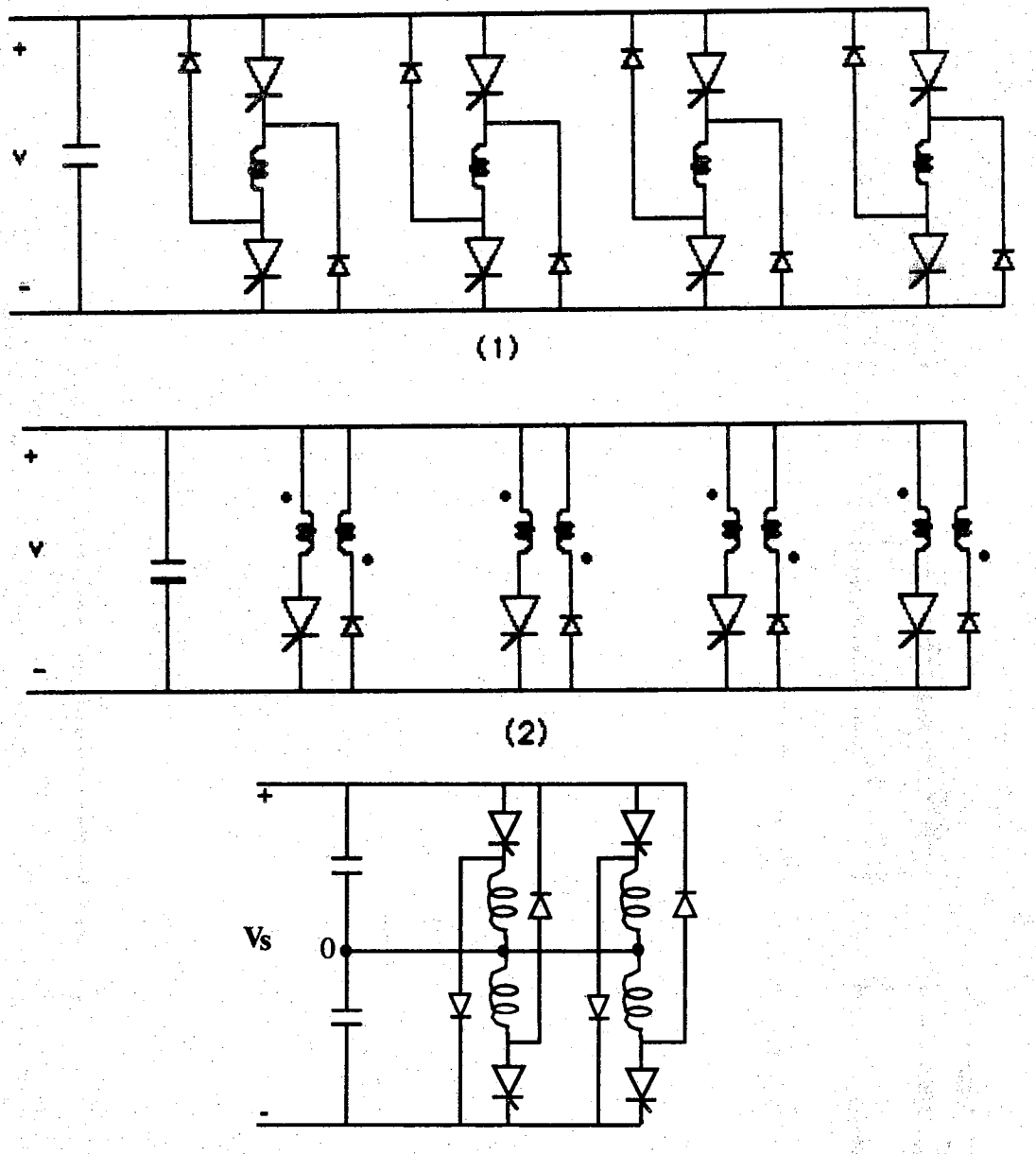

Figure 1.5. Common switching circuits for SRM drive

In drive circuit 1.5(1), which has two switches per phase, both switches are turned on and off together. The diodes provide the path for energy return after the main switches are turned off. An SRM with bifilar wound stator winding requires a simpler drive circuit as shown in Fig. 1.5(2); in exchange bifilar windings have poor space factor and double the number of terminal connections. Drive circuit 1.5(3) also has the advantage of one main switching device per phase, but requires a split source to provide a path for the return energy.

1.3. Motivation and Objective

Although the first application of a switched reluctance motor dates back to the 19^{th} century, the history of its development has not been a continuous one. It is only in the past 10 years or so that the development of the modern SRM took off with great fervor. In this short period of time, through the work of many in this field, the inherent advantages and potentials of the SRM drive were investigated. Yet, there is still a lot that can be done in the design and control of the drive. The outward simplicity of the motor's construction is deceiving; the modeling complexity of the field inside the motor still takes the modeling capability of many workers, as can be seen from publications on the subject.

The study of the SRM drive is indeed complicated by the large number of parameters involved. The static characteristics of an SR motor such as the static torque, flux linkages, and inductances are functions of both rotor position and current. In continuous operation, the profiles of the current and the torque are affected by switching angles that places the current pulse relative to the stator phase inductance waveform or rotor position. The average torque, of course, is a complicated function of not only iron geometry and current level (saturation), but also the timing and shape of the current pulse, the shape of which, in turn, is affected by the timing relative to the rotor position and the speed. The main hurdles in any study aimed at prediction of SRM drive performance are those from the close inter-relationship between switching strategies and motor parameters on one hand and the numerical difficulties in obtaining an accurate prediction of even the static characteristics of the machine on the other.

Today's technical literature on the SRM drive contains reports of analysis and performance evaluation based on experimental results, and on a linear or simplified nonlinear model of the magnetic field. To our knowledge, there is no available report of a numerical model for predicting the performance

characteristics of an SRM drive over the full range of torque/speed characteristics.

Analyses that are based on linear or simplified nonlinear models provide good starting points to the qualitative study of machine operation, to the preliminary design of the motor, and to the estimation of converter rating. However, the study of the effects of new designs or the improvements from new control strategies on the drive performance requires a realistic model of the drive system. Such a realistic model should be able to predict drive performance over a wide range of torque/speed characteristics with sufficient accuracy. To establish such a model, a thorough knowledge of machine parameters, static characteristics, control strategies, and switching circuit limitations (current and frequency) is necessary. Obviously an understanding of the relationships between the machine, control, and converter operation is a prerequisite in devising a realistic model.

The main objective of this study is to establish a mathematical model, along with the required computational techniques, for predicting the performance characteristics of an SRM drive. As shown in Fig. 1.6, the mathematical model of an SRM drive is divided into three major blocks: motor, control, and converter. The mathematical model of the motor itself consists of three components: magnetic field, windings, and mechanical system. The inter-relations among the blocks are shown by arrows. In this study, the nonlinear magnetic field of the machine will be handled by a two-dimensional finite element model. The stator phase windings are represented by phase voltage equations, and the converter approximated by a controlled, square wave, voltage pulse generator where the number and duration of voltage pulses depend on speed and loading. The transients within the converter circuit will be neglected as these will vary with the circuit topology. If required, detail modeling of a given converter can be handled using the C_n matrix method given in [63].

Accurate prediction of the parameters and the static characteristics of an SR motor using FE method is not a straightforward procedure because the field distribution in the SR motor is highly nonuniform, and contains pockets of very high field gradient in the narrow airgap region of overlapped poles. Most FE studies of an SR motor [30-33] are concerned with the determination of the gross behavior of its static characteristics; few deal with the accuracy problems in postprocessing of FE field solution for prediction of static characteristics [88]. This is especially evident in the noticeable discrepancies between predicted and measured static torque/angle characteristics. A major

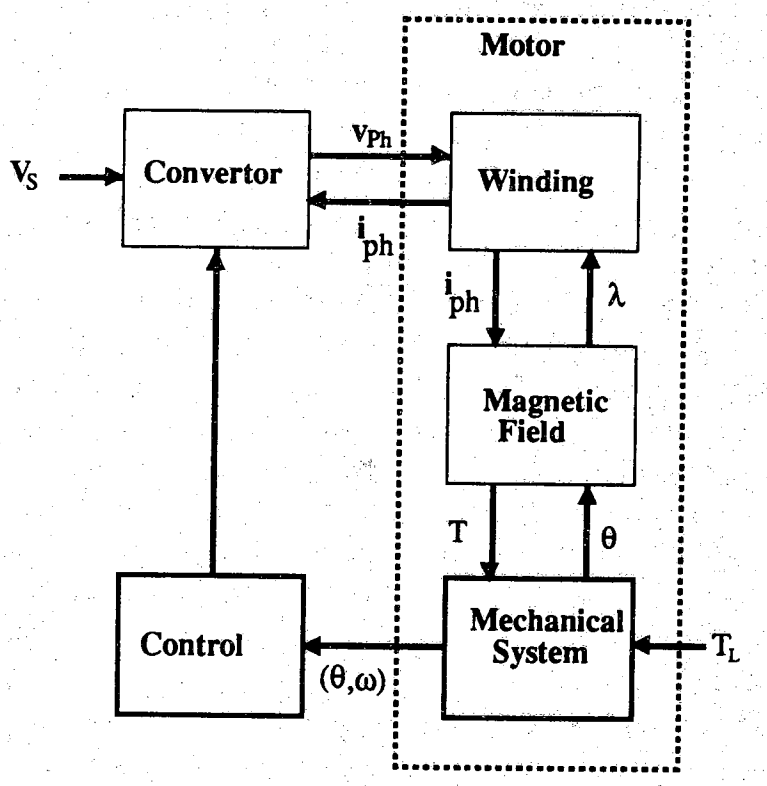

Figure 1.6. Components of SRM drive

part of this study is devoted to the analysis of the field patterns and torque distribution in a SR motor, and experimentation with the different methods to improve the accuracy in the torque calculation. The study reveals that most of the field energy is concentrated in the narrow airgap region between overlapped poles of the rotor and stator where local saturation occurs and the fringing flux lines curve sharply. Unfortunately, inadequate modeling of the field in this region will adversely affect the accuracy of results in the postprocessing stage regardless of the method used. In [88], it was suggested that the accuracy in torque prediction can be improved by increasing the number of elements in the critical region.

In FE literature, increasing the mesh resolution is an accepted remedy for overcoming the accuracy problem. For a SRM that has a narrow airgap, increasing the mesh resolution in the airgap could be meaningful only if the resolution in radial and θ directions is kept about the same and similar increases in resolution of neighboring layers of the mesh are made, in which case the order of the mathematical model will escalate, thus increasing the computational storage and time substantially. Furthermore, if such an increase in resolution is not carried out judiciously, the result is no better than in the case when more layers are added in the narrow airgap with no corresponding increase in the mesh resolution circumferentially in which the resulting elongated elements with large aspect ratio yield poor accuracy of the field solution.

In this study, a new method based on uniform distribution of nodes in the airgap is devised which results in finite elements that have low aspect ratio and significantly improve the accuracy of both the overall field solution and the postprocessing results, especially those that require taking the derivatives of the field solution as in the case of torque calculation. Using this method, the static torque calculated using this method shows very good agreement with the measured result.

Having the capability to accurately predict the static torque/angle characteristics and other machine parameters enables us to proceed to prediction of performance characteristics of the SRM drive.

1.4. Literature Review

The principle behind the torque production in an SR motor is a basic principle in electromagnetic theory. Early designers of electromechanical devices long recognized that the electromagnetic force on movable iron parts tends to orientate them in such a way as to achieve minimum reluctance to the magnetic flux path , or into a position of minimum field energy. In the course of the movement, some of the field energy will be converted to mechanical energy.

The concept of variable reluctance led to the development of a wide variety of devices such as linear solenoids and relays. By the 1920s the analysis of variable reluctance was extended to the synchronous motors [1], leading to the design of unexcited synchronous motors several years later [2,3].

The first switched reluctance motor used mechanical switches and it was employed by the British Navy during World War II to perform remote positioning of the guns on the ship. Because of the unavailability of fast switching devices like today's electronic switches, and because of the advent of closed-loop position servo mechanism using DC motors, the early VRM drives were not competitive and they faded into the background. But with the availability of inexpensive and fast electronic power switches (power transistors and thyrestors) and high performance digital controllers to manage the switching strategies, by the late 1960's the idea of a high-power variable reluctance motor was revived by several researchers in universities, notably Lawrenson [4-7], Unnewehr and Koch [8], Wagner [9-10], and Lang [11]. They examined various aspects of the VR motor, such as new designs for better performance, torque production process in doubly-salient structure, and new drive circuit configurations.

It was not until 1980 that Lawrenson [13] laid the foundation for a practical design of the switched reluctance motor drive with comparable performance to that of an an induction motor drive. In [13], they examined the fundamental design considerations of an SR motor, such as the number of stator and rotor poles, the pole pitches, suitable configurations and rating of the drive circuit. They also presented informative data measured from their machine, such as flux-current, inductance-angle, and torque-angle curves.

There were also notable contributions from other researchers. Davis and Ray in [14] examined different inverter drive circuits and component ratings for an SR motor; Miller et al. [15-17] examined microprocessor control strategies for an SR motor and the drive circuit ratings; and Harris in [18]

discussed the effects of using multiple teeth on the pole surface.

In all these papers, the analyses were based on a linear or an idealized nonlinear model of magnetic circuit. Furthermore, only the static characteristics of the SR motor were examined. Most of the papers [19-24] published between 1980-1985 on the SR drive dealt with refinements and/or special applications.

Idealized approximation of the magnetic saturation for a machine in which the saturation level is high, at best, can be used for qualitative analysis of drive performance, estimation of design parameters, and switching circuit ratings. With a numerical approach, the nonlinear magnetic field in an electrical machine can be handled by finite element method. The application of the FE method for solving magnetostatic field problems was first reported by Sylvester [45]. Ever since, there have been numerous reports on the application of finite element method for field analysis of a wide variety of electric machines [50-55].

Lindsay, Lowther, and Krishnan in [30] used a two- dimensional finite element model to determine the flux patterns of a 4/6 pole, SR motor at different rotor positions. From the FE field solution, they predicted the variation of the stator winding inductance with respect to rotor position. Later, in [32], they extended their work to predict the inductances of an SR motor with multiple teeth per pole. Dawson et al. in [33] used the FE field solution to predict the static torque characteristics of an SR motor. They used the coenergy method for the torque calculation, but the computed result shows discrepancies with test results. In a recent paper [88], the same authors reported improvement in their computational results of the torque by introducing more elements in the region where the field gradient is high. Also, they compared the computed results for two methods of torque calculation: namely, Maxwell stress tensor method and global virtual work method. Nevertheless, the calculated torque/angle characteristics in these studies still do not compare well with the experimental results.

On the subject of dynamic modeling, cases of current waveform at speeds near nominal speed have been reported in the literature, but without details of what methods have been used. To our knowledge, there is no published method that can be used satisfactorily to predict accurately the performance characteristics of an SRM drive.

The potential advantages of the SRM drive attracted the attention of many researchers in recent years. Reports of recent studies range from

statistical modeling of the phase current based on measured data [34,35], new design refinements to increase the energy conversion ability of motor by introducing a higher level of saturation [38], sensitivity analysis of pole arcs for more efficient performance [37], iron loss estimation [40], to refinements in switching strategies for higher energy conversion [41,42].

1.5. Report Overview

In this report, a mathematical model and simulation techniques required for prediction of steady state characteristics of an SRM drive system are developed. The content of the work is organized as follows: In Chapter 2, a review of the finite element method to solve for the magnetic field is presented. The formulation and basic concepts of FE method are briefly discussed. The discretization (mesh or grid generation) of a motor cross-section is explained next. The discretization errors are discussed and the methods of computer implementation is presented. An efficient technique for updating the mesh after each rotor movement is given next. Then the modeling of nonlinear magnetization curve for computer simulation is described. Finally, the solution techniques and different convergence criteria are explained and the results of FE field solution for an SR motor are presented.

Chapter 3 deals with the problems affecting the accuracy of torque calculation using the FE field solution. It begins with a review of the common methods of torque calculation and their formulation. This is followed by a discussion of the problems affecting the accuracy of FE-based torque calculation in general, and the additional problems related to the special geometry of the SR motor. Based on the examination of the problems affecting the accuracy of torque calculation, it is later shown that a rearrangement in mesh can significantly improve the accuracy of the field solution and of the torque calculation. The method is new and computationally is more efficient than previous methods reported in the literature. As a verification of the new technique, the static torque/angle characteristics of SR motor computed using the global virtual work, Maxwell-stress tensor, and local virtual work methods are presented, and compared with measured results.

In Chapter 4, the postprocessing techniques used to calculate the energy, the flux linkages, the stator phase inductance, and the winding emf are presented.

Chapter 5 describes the modeling techniques used to determine the steady state performance of the SRM drive. To explain the underlying philosophy of

the switching strategy used, an analysis based on a simplified magnetic model of the SRM is given at the beginning. Control strategies and their relation to machine parameters are discussed next. The techniques for simulating the different modes of operation, low speed and high speed, of an SRM drive are given. Simulated results of the instantaneous current, flux, and torque, and computed average torque and power are all presented. Also, experimental results of the current and flux linkage characteristics at different speeds and loading are presented.

Finally, Chapter 6 presents a summary of the contributions and findings of this work, and suggestions for future research.

CHAPTER 2
FINITE ELEMENT SOLUTION OF ELECTROMAGNETIC FIELD

The distribution of the electromagnetic field in electrical machines may be determined by solving Maxwell's field equations with the given boundary conditions. Since closed form solutions to Maxwell's equations are very difficult or impossible to obtain for such a device having complicated geometrics and nonlinear materials, numerical solution of the Maxwell's equations becomes a necessity. The method of finite element (FE), an excellent numerical method for structures with complicated geometries and material nonlinearities, is used here to obtain an approximate solution to the two-dimensional field distribution in the SRM cross-section. The solution technique accounts for the material nonlinearity and the rotor movement.

Due to high local saturation and nonuniform field distribution in the SRM, even with the FE method, special care has to be taken in modeling the field in the critical regions. In this chapter, a review of the finite element formulation for solving two-dimensional electromagnetic field problems is presented. The assembly of the equations and implementation of the FE program are discussed next. Because the size, shape, and uniformity of elements has profound effect on the accuracy of the final solution, the choice of proper mesh is important, and because the SRM has high local saturation, the representation of material nonlinearity (magnetization curve) is important too. As the iterative solution of large numbers of nonlinear equations requires a lot of computer time and memory, efficient sparsity-oriented algorithms have to be used. The field solution from the FE method has to be further processed to obtain important machine parameters and terminal variables, such as inductances, flux linkages, torque, and induced electromotive forces (emfs).

2.1. Finite Element Formulation

The field distribution inside the machine is governed by Maxwell's electromagnetic field equations:

$$\nabla \times \vec{E} = \frac{\partial \vec{B}}{\partial t} \tag{2.1}$$

$$\nabla \times \vec{H} = \vec{J}_s \tag{2.2}$$

$$\nabla \cdot \vec{D} = 0 \tag{2.3}$$

$$\nabla \cdot \vec{B} = 0 \tag{2.4}$$

where $\vec{E}$ and $\vec{H}$ are the electric and magnetic field intensities, respectively, $\vec{D}$ and $\vec{B}$ the corresponding field densities, and $\vec{J}_s$ is the source current density. The displacement current and electric charge terms have been excluded from these equations, because the machine can be considered as a low frequency device with neglible electrostatic flux.

For two dimensional field distribution problems with current input, it is convenient to express these equations in terms of the magnetic vector potential. As with any other solenoidal field ($\nabla \cdot B = 0$), a vector potential can be defined as

$$\vec{B} = \nabla \times \vec{A} \tag{2.5}$$

where A is magnetic vector potential (MVP). This definition does not determine $\vec{A}$ uniquely; like any other potential, MVP should be specified with respect to some reference. Ignoring the end condition, the winding currents are assumed to flow only in the axial direction (z-direction) of the machine, hence only the axial (or z) component of the vector potential $\vec{A}$ exists. Consequently, the vector equations reduce to single partial differential equations of the axial component of vector potential.

The relation between the field density $\vec{B}$ and the field intensity $\vec{H}$ is the constitutive relation

$$\vec{H} = \nu \vec{B} \tag{2.6}$$

which describes the material characteristic of the medium in term of the reluctivity ν ($\nu = \frac{1}{\mu}$), where μ is the permeability of the medium. Using (2.6) to substitute for $\vec{H}$ in (2.2) and (2.5) for $\vec{B}$, the resulting partial differential equation for $\vec{A}$ is

$$\nabla\times(\nu\nabla\times\vec{A}) = \vec{J}_s \tag{2.7}$$

When the excitation current is assumed to flow only in the axial direction (z-direction) of machine, $\vec{A}$ will only have A_z component too, which then (2.7) reduces to

$$\nabla \times (\nu\nabla\times A_z\vec{a}_z) = J_s\vec{a}_z \tag{2.8}$$

Performing the curl operations in (2.8) yields

$$\frac{\partial}{\partial x}\left(\nu\,\frac{\partial A_z}{\partial x}\right) + \frac{\partial}{\partial y}\left(\nu\,\frac{\partial A_z}{\partial y}\right) = -J_s \tag{2.9}$$

Equation (2.9) is the nonhomogeneous, nonlinear diffusion equation which should be solved along with the appropriate boundary conditions to obtain the vector potential distribution over the entire cross-section of machine.

The spatial PDE of (2.9) takes different forms, depending on the material property, ν, and presence of J_s. The SRM like other electromechanical devices has iron for directing the flux lines, air for relative motion between rotor and the stator, and current carrying conductors to provide the field and to convey the power. Figure 2.1 shows different sub-regions of the SRM cross-section. In the current carrying region (region 1), linear Poisson's PDE holds, since the permeability of copper is nearly unity.

$$\nu_o\,\nabla^2 A_z = -J_s \tag{2.10}$$

In region 2, the iron has nonlinear magnetic characteristics and its reluctivity ,ν, is space-dependent. However, with no current source in the iron region, (2.8) reduces to a nonlinear pseudo Laplaces equation of the form

$$\nabla\times(\nu\nabla\times A_z) = 0 \tag{2.11}$$

The normal reluctivity, ν, is assumed to be single-valued for the iron region; it is the reciprocal of the normal permeability, μ, that is defined as

$$\mu = |\vec{B}|\,/\,|\vec{H}| \tag{2.12}$$

Equation (2.11) is a nonlinear equation because ν is a function of the field density $\vec{B}$, or

$$\nu = \nu(\vec{B}) \tag{2.13}$$

In the air region, the reluctivity of air is independent of $\vec{B}$ and the resulting PDE is a linear, homogeneous Laplace equation of the form

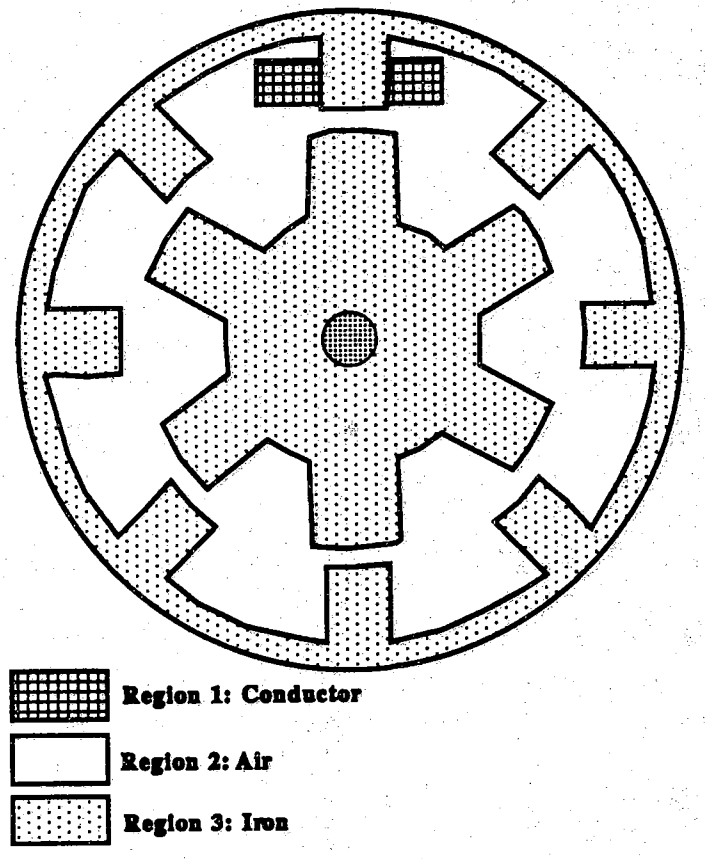

Figure 2.1. Sub-regions in SRM cross-section

$$\nu_o \nabla^2 A_z = 0 \tag{2.14}$$

Specifying the boundary conditions for the field distribution uniquely determines the field solution for the partial differential equation (2.9). The boundary conditions specifying the relations between field components at the material interfaces are derivable from Maxwell's equations; for magnetostatic field problem these boundary conditions are

$$n \times \left(\vec{H}_1 - \vec{H}_2\right) = \vec{J}_s \tag{2.15}$$

$$n \cdot \left(\vec{B}_1 - \vec{B}_2\right) = 0 \tag{2.16}$$

The first condition of (2.15) states that there is a discontinuity in the tangential component of the field intensity $\vec{H}$ at the interface between two media separated by a current carrying surface. However, if both media are current-free, the tangential component should be continuous ($H_{t1} = H_{t2}$). The second condition of (2.16) expresses the continuity of the normal component of flux density at the interface of two neighboring regions ($B_{n1} = B_{n2}$).

2.1.1 Variational Formulation

The variational formulation seeks an approximate solution for the differential equation of (2.9) in the form of a linear combination of independent basis functions each of which satisfies the stated boundary conditions. For a two-dimensional field problem with only z-th component of vector potential, A at each point (x,y) can be approximated as

$$A(x,y) \simeq \sum_{i=1}^{N} c_i L_i(x,y) \tag{2.17}$$

where $L_i(x,y)$'s are N linearly independent functions. The error or residual resulting from using such an approximation in (2.9) can be expressed as

$$E(x,y,c_i) = \frac{\partial}{\partial x}\left(\nu \frac{\partial A}{\partial x}\right) + \frac{\partial}{\partial y}\left(\nu \frac{\partial A}{\partial y}\right) + J_s \tag{2.18}$$

In the weighted-residual method, the coefficients are determined in such a way that the partial differential equation is satisfied with minimal error. For this purpose, a set of N independent weighting functions, ψ_i's, is chosen so that

$$\int_R \psi_i(x,y)\, E(x,y,c_i)\, dxdy = 0 \quad \text{for } i = 1, 2, \cdots, N \tag{2.19}$$

Therefore, each of the weighting functions ψ_i is orthogonal to the residual E. The set of N parameters c_i can be determined from (2.19). For obvious reasons, this method is called the weighted-residual solution of the PD equation.

If the set of weighting functions, ψ_i's, is chosen to be the same as the basis functions, L_i's, the method is called the Galerkin method, that is

$$\int_R L_i(x,y)\left[\frac{\partial}{\partial x}\left(\nu \frac{\partial A}{\partial x}\right) + \frac{\partial}{\partial y}\left(\nu \frac{\partial A}{\partial y}\right) + J_s\right] dxdy = 0 \tag{2.20}$$

Integrating the first two terms by part, we obtain

$$\int_R L_i(x,y) \frac{\partial}{\partial x}\left(\nu \frac{\partial A}{\partial x}\right) dxdy = \oint_S L_i(x,y)\, \nu \frac{\partial A}{\partial x}\, dy - \int_R \nu \frac{\partial L_i}{\partial x} \frac{\partial A}{\partial x}\, dxdy \tag{2.21}$$

$$\int_R L_i(x,y) \frac{\partial}{\partial y}\left(\nu \frac{\partial A}{\partial y}\right) dxdy = \oint_S L_i(x,y)\, \nu \frac{\partial A}{\partial y}\, dx - \int_R \nu \frac{\partial L_i}{\partial y} \frac{\partial A}{\partial y}\, dxdy \tag{2.22}$$

Since on the boundary of the region either homogeneous Dirichlet or Neumann condition holds($A=0$ or $\frac{\partial A}{\partial n}=0$), the combination of line integrals on the right hand side of (2.21) and (2.22) is always zero; consequently (2.20) reduces to

$$\int_R \left[\nu \frac{\partial L_i}{\partial x} \frac{\partial A}{\partial x} + \nu \frac{\partial L_i}{\partial y} \frac{\partial A}{\partial y} - L_i J_s\right] dxdy = 0 \tag{2.23}$$

Equation (2.23) indicates that the basis functions $L_i(x,y)$ must belong to a set of once differentiable functions or C^1; the lowest order being a set of continuous, piecewise, linear basis functions. However, with the choice of linear basis function, continuity of only one of the field components can be guaranteed at the interfaces.

It can be shown that the Galerkin method formulation given in (2.22) is equivalent to that of minimizing the error in the field energy. The difference between the field energy and the input energy is given as

$$F = \int_{\Omega} \left[\int_{o}^{B} \nu B dB - J_s A \right] dv \tag{2.24}$$

where Ω is the volume of whole region. For simplicity, let's consider the linear case of (2.24) in which the energy per unit volume can be written as

$$\Delta W_F = \int_{o}^{B} \nu B dB = \tfrac{1}{2} \nu B^2 \tag{2.25}$$

The component of flux density can be obtained by performing the curl operation in (2.5), that is

$$B_x = \frac{\partial A}{\partial y} \quad , \quad B_y = -\frac{\partial A}{\partial x} \tag{2.26}$$

Representing A by the expression of (2.17), the partial derivatives can be expressed as

$$\frac{\partial A}{\partial x} \simeq \sum_{i=1}^{N} c_i \frac{\partial L_i}{\partial x} \tag{2.27}$$

$$\frac{\partial A}{\partial y} \simeq \sum_{i-1}^{N} c_i \frac{\partial L_i}{\partial y} \tag{2.28}$$

Since the square of the flux density may be written as

$$B^2 = \left(\frac{\partial A}{\partial x} \right)^2 + \left(\frac{\partial A}{\partial y} \right)^2 \tag{2.29}$$

(2.25) can be written as

$$\Delta W_F = \tfrac{1}{2} \nu \left[\left(\sum_{i=1}^{N} c_i L_{ix} \right)^2 + \left(\sum_{i=1}^{N} c_i L_{iy} \right)^2 \right] \tag{2.30}$$

where L_{ix} and L_{iy} are the partial derivatives of shape function ,L_i, with respect to x and to y, respectively. Substituting (2.30) for the field energy, and (2.17) for A in (2.24), yields

$$F(c_1, c_2, \cdots, c_n) = \int_{\Omega} \left\{ \tfrac{1}{2} \nu \left[\left(\sum c_i L_{ix} \right)^2 + \left(\sum c_i L_{iy} \right)^2 \right] - J_s \sum c_i L_i \right\} dv \tag{2.31}$$

The minimizing function of the functional F is the solution of the Euler-

Lagrange equation which is the same as the partial differential equation in (2.9). But a direct minimization of F with respect to coefficients ,c_i's, yields

$$\frac{\partial F}{\partial c_i} = \int_{\Omega} \left[\nu L_i \sum c_i L_{ix} + \nu L_i \sum c_i L_{iy} - J_s L_i \right] dv = 0 \qquad (2.32)$$

which, in the two-dimensional region R, is the same as the Galerkin variational form given in (2.22).

2.1.2 Derivation of Element Matrices

The finite element method used in this study is based on first order triangular elements. The two-dimensional region R is divided into triangular subregions as shown in Fig. 2.2, where an effort is made to ensure that material interfaces and other physical boundaries coincide with the edges of the triangles. In each triangle, the vector potential A is assumed to be a linear polynomial in x and y.

$$A(x,y) = \alpha_1 + \alpha_2 x + \alpha_3 y \qquad (2.33)$$

In the two-dimensional problems only the z-th component of the vector potential exists at each node, so each node has one degree of freedom; the total degree of freedom for a triangular element is three. This is consistent with the 3 unknown parameters in (2.33).

Vector potential, A, at any interior point of the triangle can be expressed as a linear combination of the values of A at its vertices.

$$A(x,y) = \sum_{i \in \Omega} A_i L_i(x,y) \qquad (2.34)$$

The index i is the sum over Ω , the set of nodes {l, m, n} of the triangle, and the basis, L_i, have the property

$$L_i (x_j, y_j) = \delta_{ij} \qquad (2.35)$$

where δ_{ij} is the Kronecker delta

$$\delta_{ij} = \begin{cases} 1 & \text{if } i=j \\ 0 & \text{if } i \neq j \end{cases}$$

and

$$\sum_{i \in \Omega} L_i = 1 \qquad (2.36)$$

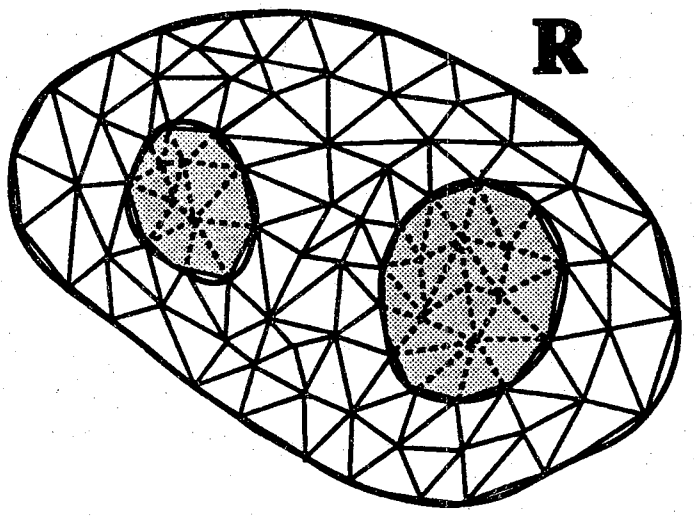

Figure 2.2. Subdivision of region R by triangular elements

In order to facilitate the analysis, the so-called area co-ordinates (see Appendix A) will be used. As shown in Appendix A, the value of A at some interior point (x,y) of the triangle, expressed in terms of the area coordinates, is

$$A(x,y) = \frac{1}{D}\left[p_l A_l + p_m A_m + p_n A_n\right] + \frac{x}{D}\left[q_l A_l + q_m A_m + q_n A_n\right] \tag{2.37}$$

$$+ \frac{y}{D}\left[r_l A_l + r_m A_m + r_n A_n\right]$$

where D is twice the area of element, Δ_e. With A represented by (2.37), the partial derivatives of A at interior points of the triangle element are

$$\frac{\partial A}{\partial x} = \frac{1}{D}\left[q_l A_l + q_m A_m + q_n A_n\right] \tag{2.38}$$

$$\frac{\partial A}{\partial y} = \frac{1}{D}\left[r_l A_l + r_m A_m + r_n A_n\right] \tag{2.39}$$

Similarly, using (I-10), we obtain

$$\frac{\partial L_i}{\partial x} = \frac{1}{D}\, q_i A_i \qquad i \in \Omega \tag{2.40}$$

$$\frac{\partial L_i}{\partial y} = \frac{1}{D}\, r_i A_i \qquad i \in \Omega \tag{2.41}$$

Lets denote the first two terms of (2.23) by I_i, that is

$$I_i = \int_{\Delta e} \left(\nu_e \frac{\partial L_i}{\partial x} \frac{\partial A}{\partial x} + \nu_e \frac{\partial L_i}{\partial y} \frac{\partial A}{\partial y} \right) dxdy \tag{2.42}$$

Using (2.38) through (2.41) to replace the partials and using the transformation formula given in Appendix B, one obtains

$$I_i = \frac{\nu_e}{4\Delta_e}\left[q_i \sum_{j\in\Omega} q_j A_j + r_i \sum_{j\in\Omega} r_j A_j \right] \quad i\in\Omega \tag{2.43}$$

Equation (2.43) gives the contribution of each triangle element to the functional value (2.23). For the elements in the iron region the field density, $\vec{B}$, which is required for updating the reluctivity of the elements in iron at each iteration, can be calculated as follows: From (2.5), $\vec{B}$ can be written as

$$\vec{B} = \frac{\partial A}{\partial y}\vec{a}_x - \frac{\partial A}{\partial x}\vec{a}_y \tag{2.44}$$

Substituting (2.38) and (2.39) in (2.44), the above expression of $\vec{B}$ becomes

$$\vec{B} = \frac{1}{D}\left[r_l A_l + r_m A_m + r_n A_n\right]\vec{a}_x - \left[q_l A_l + q_m A_m + q_n A_n\right]\vec{a}_y \tag{2.45}$$

thus, the value of $|\vec{B}|^2$ is given by

$$|\vec{B}|^2 = \frac{1}{D^2}\left[\left(\sum_{i\in\Omega} r_i A_i\right)^2 + \left(\sum_{i\in\Omega} q_i A_i\right)^2\right] \tag{2.46}$$

Finally, in term of elemental areas, the third term in (2.23) may be written as

$$II_i = \int\int L_i J_s \, dxdy = \frac{J_s \Delta_i}{3} \tag{2.47}$$

Putting (2.43) and (2.47) together for i = l, m, n; the matrix equation for a triangle element can be written as

$$\frac{\nu_e}{4\Delta_e}\begin{bmatrix} q_l^2+r_l^2 & q_l q_m+r_l r_m & q_l q_n+r_l r_n \\ q_l q_m+r_l r_m & q_m^2+r_m^2 & q_m q_n+r_n r_m \\ q_n q_l+r_n r_l & q_m q_n+r_n r_m & q_n^2+r_n^2 \end{bmatrix}\begin{bmatrix} A_l \\ A_m \\ A_n \end{bmatrix} = \begin{bmatrix} \frac{J_s\Delta_e}{3} \\ \frac{J_s\Delta_e}{3} \\ \frac{J_s\Delta_e}{3} \end{bmatrix} \tag{2.48}$$

In matrix notation, (2.48) can be written compactly as

$$S_e A_e = I_e \tag{2.49}$$

Note that the elements of S_e are functions of ν_e which in the case of an iron element is dependent on the field density $\vec{B}$. Since $\vec{B}$ is, in turn, related to the nodal vector potentials, A_i's, (2.49) is nonlinear for elements in the iron.

2.1.3 Matrix Assembly and Global Equations

Once the elemental equations for all the elements in the various regions of R are determined, they can be assembled into a global equation of the form,

$$SA=I \tag{2.50}$$

The coefficient matrix, S, of global equation can be constructed element by element as follows: The diagonal element s_{ii} in matrix S is the sum of the contributions of all elements connected to node i, and the off-diagonal element s_{ij} is the sum of the contributions from the two adjacent elements sharing the common edge ij.

The global matrix equation (2.50) is a set of nonlinear algebraic equations of n^{th} order , where n is the number of nodes in region R. The only practical method of solving these nonlinear equations is by a numerical iterative method. Generalized and modified Newton-Raphson methods are two of the most suitable ways for solving these nonlinear algebraic equations. In this finite element formulation, the vector potential within an element is assumed to be piece-wise linear, as a result the magnetic field $\vec{B}$ and the reluctivity ν are uniform within each element. Hence, it is advantageous to update the Newton-Raphson iteration formula for each of the triangles individually and then use them to update the overall coefficient matrices as follows: First, for each element, we define a mismatch equation,

$$F(A_e) = S_e A_e - I_e = 0 \tag{2.51}$$

In applying the N-R method to the above mismatch equation, at k^{th} iteration, we have

$$F\left(A_e^{k+1}\right) = F\left(A_e^k\right) + \left[J_e^k\right]\left[A_e^{k+1} - A_e^k\right] \tag{2.52}$$

where

$$\left[J_e^k\right] = \frac{\partial F(A_e)}{\partial A_e}\Big|_{A_e = A_e^k} \tag{2.53}$$

Defining the change in A as

$$\Delta A_e^k = A_e^{k+1} - A_e^k \tag{2.54}$$

and setting $F\left(A_e^{k+1}\right) = 0$, we obtain

$$\left[J_e^k\right]\Delta A_e^k = -\left[S_e^k A_e^k - I_e\right] \tag{2.55}$$

$\left[J_e^k\right]$ from (2.53) for the elements in iron are derived in Appendix C as functions of $\dfrac{\partial \nu_e}{\partial |\vec{B}|^2}$, and can be written as

$$\left[S_e^k + \left(\frac{\partial \nu_e}{\partial B^2}\right)^k S_2\right]\left[\Delta A_e^k\right] = -\left[S_e^k A_e^k - I_e\right] \tag{2.56}$$

As in the case of constructing S in (2.50), the linearized element matrices can then be assembled to form the global equation for the entire region.

$$[J]\,[\Delta A] = [b] \tag{2.57}$$

The above set of n linear equations can be solved using either iterative or direct method to obtain $[\Delta A]$ which is then used to update the value of [A] until it converges within some prescribed tolerance.

$$\left[A^{k+1}\right] = \left[A^{k}\right] + \left[\Delta A^{k}\right] \tag{2.58}$$

2.2 Implementation of FE System

Computer solution of electromagnetic field problems by finite element method can be divided in three parts, each involving several steps as shown in Fig. 2.3. Preprocessing is the part dealing with setting up the problem for computer solution and has two steps: generating a finite element mesh consistent with geometry of the device, and representing the material nonlinearity in a form suitable for computer simulation.

The solution part deals with the construction and updating of the elemental and global matrices. The product of the solution process is the vector potential distribution within the machine cross-section. The vector potential distribution is hardly of any use by itself and should be further processed to obtain machine parameters and variables of interest. The task of the postprocessing section is to extract the desired results from field solution.

During the course of this study, a finite element program consisting of all three parts has been developed. The techniques used in the preprocessing and solution parts will be discussed in the rest of this chapter while those of the postprocessing part will be discussed in the next two chapters.

2.2.1 Mesh Generation

The main part of data preparation or preprocessing is to divide the domain of interest into appropriately sized and shaped elements which are called finite elements. The process of discretization is usually referred to as mesh or grid generation. Proper discretization of different regions in a domain can have profound effect on the accuracy of the global and local results obtained from a finite element solution.

The finite elements most commonly used in electromagnetic problems are of triangular shape. The size of the triangular elements in a region depends on the field gradient and the geometry of the material boundaries in that region. Since the formulation of FE method is based on a weighted-integral

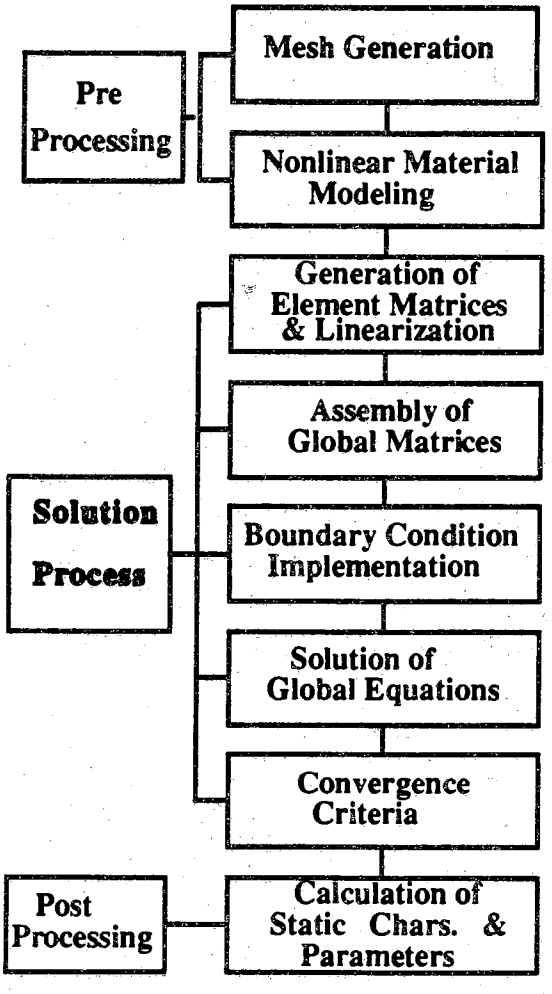

Figure 2.3. Finite element process

minimization of the error in the energy of all the elements in a domain, the accuracy of the FE solution improves when there is a uniform distribution of error over all elements. As the error in field calculations tends to be higher in regions with high field gradient, the size of elements in these regions should be kept small. Thus, a general rule on the sizing of elements is to use larger size elements where the change in the magnitude and direction of flux density is small, and to use smaller size elements where the field gradient is large, or where the flux lines sharply curve. Also, for uniform error distribution, the transition from large elements to small ones should be gradual like the nature of the field itself.

The proportion of triangular elements is the other measure which affects the accuracy of FE results. The optimal proportion for triangular elements is equilateral. However, due to geometrical limitations and computational efficiency, it is not possible to make an entirely equilateral mesh. It has been proved [60] that for mesh integrity no triangular elements should have angles near 180° or, equivalently, no element has too small an angle; that is because the error in approximation within a triangle has been shown to be inversely proportional to $\sin(\alpha)$, where α is the smallest angle [61]. Such conclusion are also consistent with the rule of low aspect ratio [47], which states that the aspect ratio (the ratio of largest edge of one element to the smallest one) of the triangle should be kept as small as possible. The effects of elemental shape on the accuracy of global and local results, especially torque calculation, will be discussed in more detail in the next chapter, but for now we will continue with other aspects of mesh generation.

Symmetry of the mesh along lines of symmetry of the device is also important, as an asymmetric mesh, if not sufficiently fine, can result in unrealistic asymmetry in the FE field solution. For example, the lines of symmetry of an electrical machine are the tooth centerlines (lines of odd symmetry), and slot centerlines(lines of even symmetry).

The mesh generator developed for this study is based on a modular method in which the entire region of the stator and the rotor is divided into basic subregions about selected lines of symmetry. Once a proper mesh for a basic subregion is devised, it can then be transformed to cover the entire cross section of the stator or the rotor. Using such a modular mesh generation approach reduces the effort of meshing to a smaller subregion by exploiting the symmetry of the device; moreover, the resultant mesh for the entire region automatically is symmetric.

An important aspect of mesh generation for machines with moving parts is that the mesh movement, as the rotor rotates, relative to the stator be accomplished efficiently. To facilitate the relative motion, the entire region is divided into three subregions: rotated, distorted, and static as shown in Fig. 2.4. The subregion of the mesh that rotates consists of elements inside the rotor and a cylindrical envelope; nodes in this subregion of the mesh rotate together with a common angle $\Delta\theta$, but the mesh configurations remain unchanged. The subregion that is static begins from the mid airgap layer; it contains all of the stator up to some outer boundary. The distorted subregion consists of the remaining portion of the mesh that is sandwiched between the mid-airgap layer and rotor surface; the finite elements in this subregion will become distorted as the rotor moves, and will need special treatment in order to maintain mesh integrity for satisfying the previously mentioned findings governing the shape of the elements.

To preserve the mesh integrity during rotation, a new indexing scheme is used in which one node on the mid-airgap layer (the node with $\theta = 0$) is chosen as the reference node. After each movement of the rotor, the closest node of the rotor surface to reference node is identified and indexed as number 1. The other nodes on the rotor surface are indexed relative to this node. In this way, the nodes on rotor surface and mid airgap layer are grouped in pairs. Adjacent pairs of nodes are then examined on the basis of the Delaunay criterion [62] as to whether the sides of the triangular elements ought to be redefined to achieve better angle conditions. The Delaunay criterion simply states that for two adjacent triangles, ABC and BCD in Figure 2.5, to be of satisfactory shape, the circumcircle of ABC should not contain D. This is equivalent to keeping all included angles less than 90° for each triangle. If the rotor movement causes D to enter the circumcircle of ABC, then an interchange of edge BC with AD will result in new satisfactory elements. Figures 2.6 to 2.8 show the mesh generated for an SRM using the above mentioned procedures. The iron mesh at aligned and 10° position of the rotor are shown in Figs. 2.6 and 2.7 respectively. Figure 2.8 shows the air mesh in which the outer boundary is chosen outside the stator iron boundary.

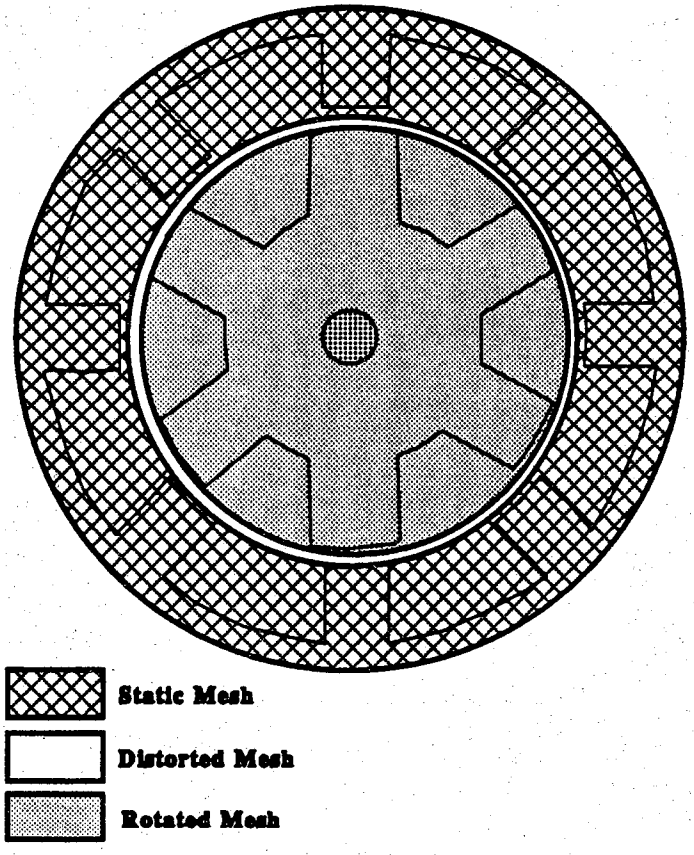

Figure 2.4. Subregions in the mesh of SRM

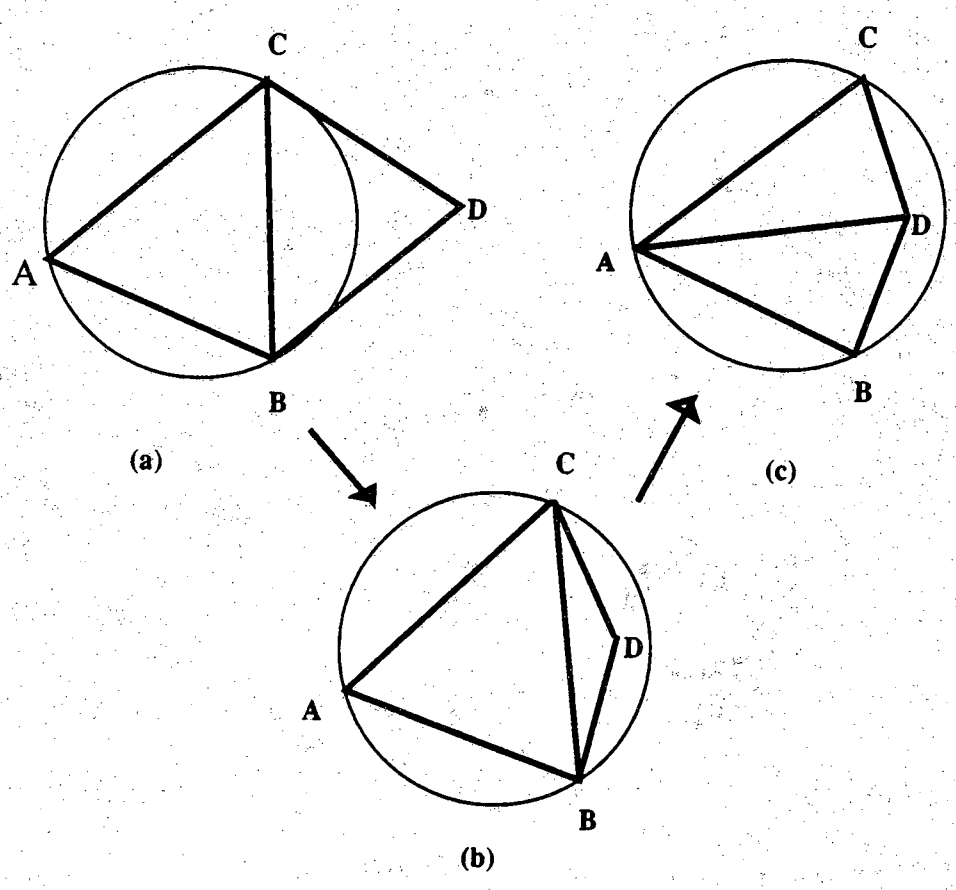

Figure 2.5. Delaunay criterion

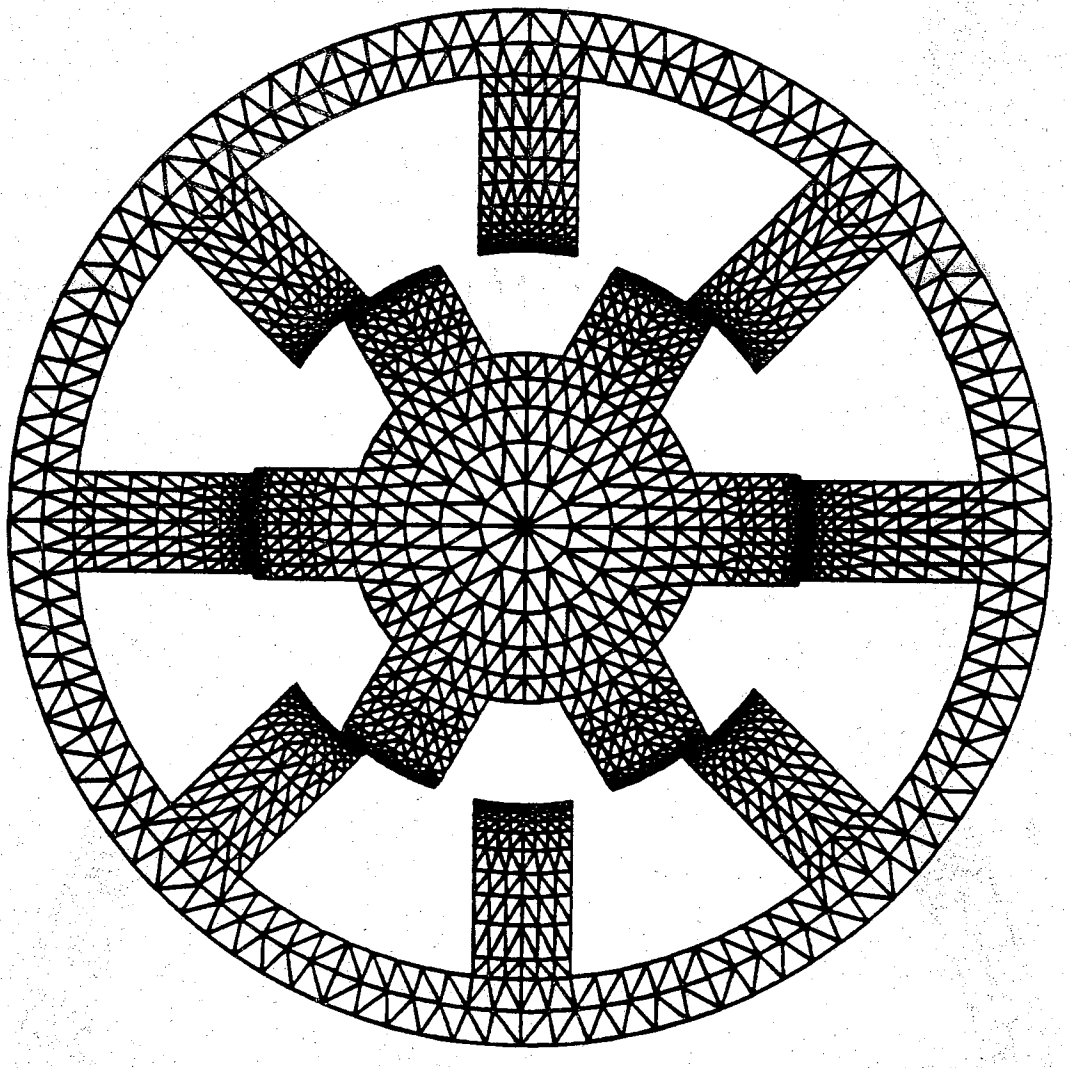

Figure 2.6. Iron mesh at aligned position

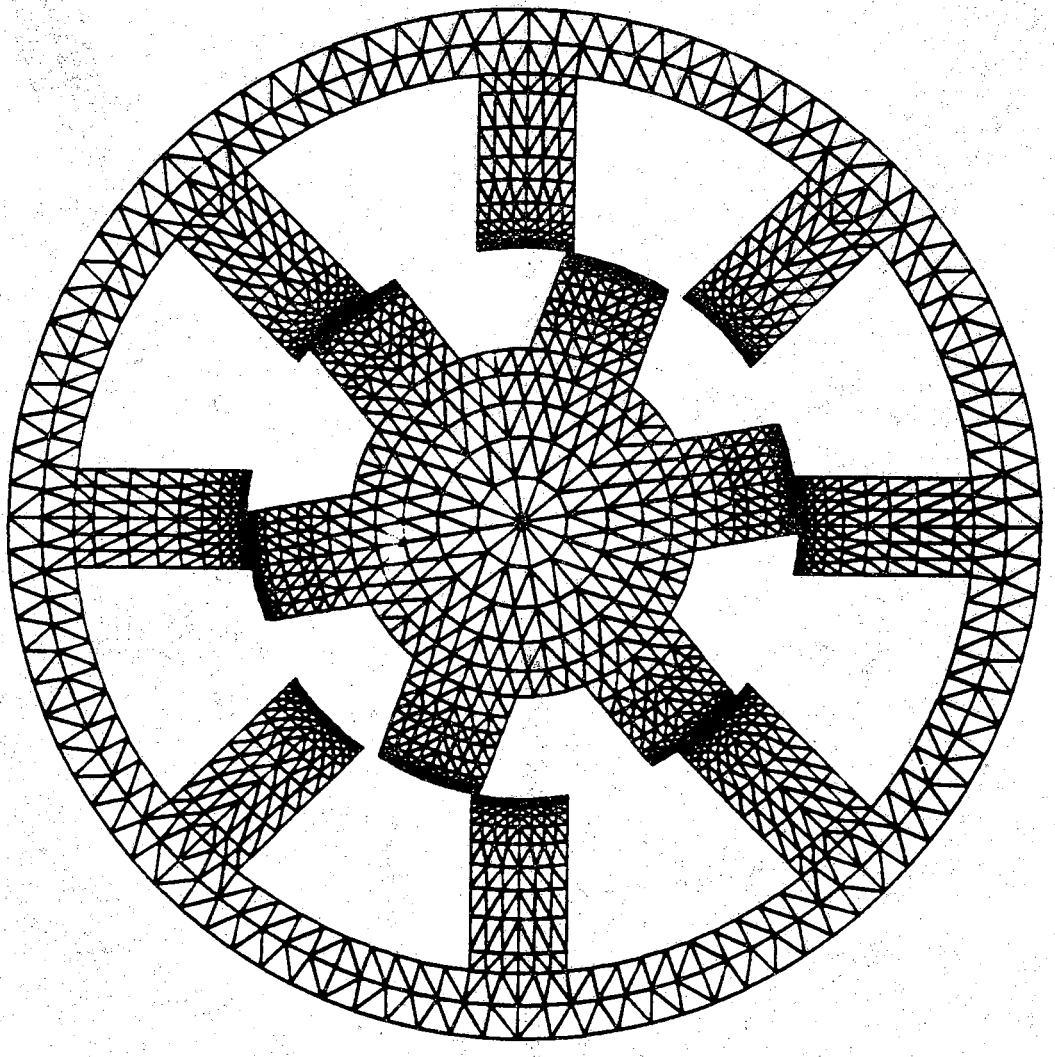

Figure 2.7. Iron mesh at 10 ° position

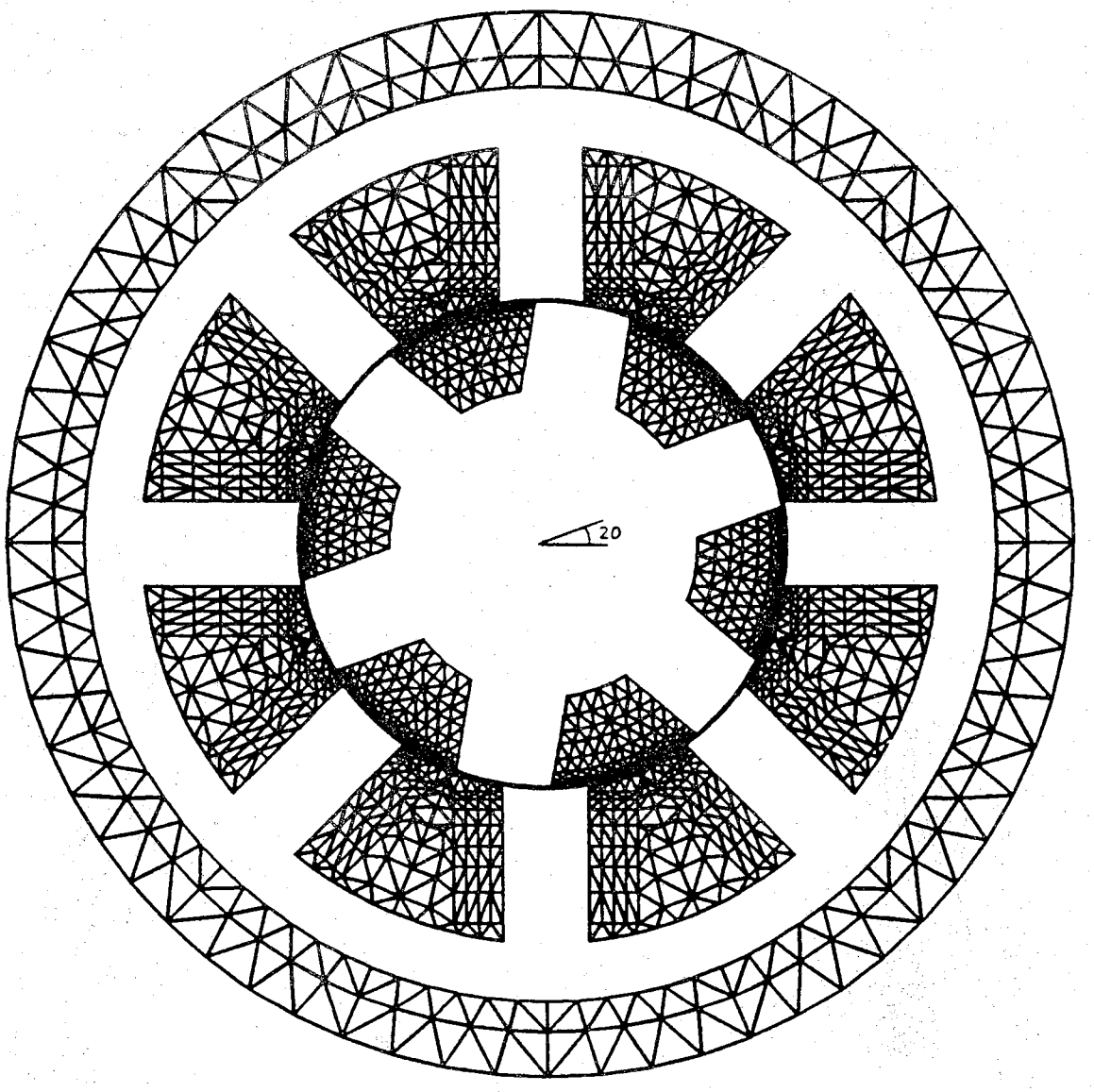

Figure 2.8. Air mesh at 20 ° position

2.2.2 Material Representation

The task of representing the iron magnetic properties is complicated by such phenomena as hysteresis, anisotropy, and a wide range of changes in the slope of the magnetization curve. However, in most of the studies, the effect of hysteresis and anisotropy are ignored, and the concave region near the origin is not modeled. With the above assumptions B-H curve is a single-valued, continuous, and monotonic curve. The nonlinear magnetization characteristic of iron should be represented in a form suitable for computer simulation and it should be an accurate representation because its accuracy directly affects the accuracy of the solution, especially in problems involving highly saturated conditions.

As indicated in (2.56) the value of $(\frac{\partial \nu}{\partial B^2})$, or the slope of $\nu(B^2)$ curve, is required to update the Jacobian matrix in the N-R iteration; therefore, the magnetization curve is modeled to represent reluctivity as a function of the square of the flux density. The data for fully processed, M-19, magnetic steel given in Table E.3 are obtained from the US Steel Handbook. The corresponding B-H curve is shown in Fig. 2.9. In this study a cubic spline interpolation technique is used on the magnetization curve data at uniform stored intervals of flux density of 0.05 Telsa. In the region of high saturation ($B \geq 2.1$) the curve is assumed to be linear with a slope of $\nu = \nu_0$ (reluctivity of the air).

2.2.3 Data Manipulation

The first step of the solution procedure is to derive the element equations, and for the elements in the iron regions the linearized element equations. The derivation of an elemental equation has been described earlier in this chapter and the derivation of the element's Jacobian matrix of (2.56) is discussed in Appendix C.

The second step in the solution procedure is to assemble the global matrix J in (2.57). The size of matrix J is nxn, where n is the total number of nodes in the entire FE domain. As each node of the FE mesh is connected to only a few neighboring nodes, both S and J are very sparse, with the percentage of non-zero usually less than one. Because of the large number of nodes involved in most practical problems, sparsity storage and manipulation techniques are necessary for reasonable computational efficiency. Since the element matrices are symmetric, the global matrix J is also symmetric; storage and computation time can be reduced further using sparsity techniques for

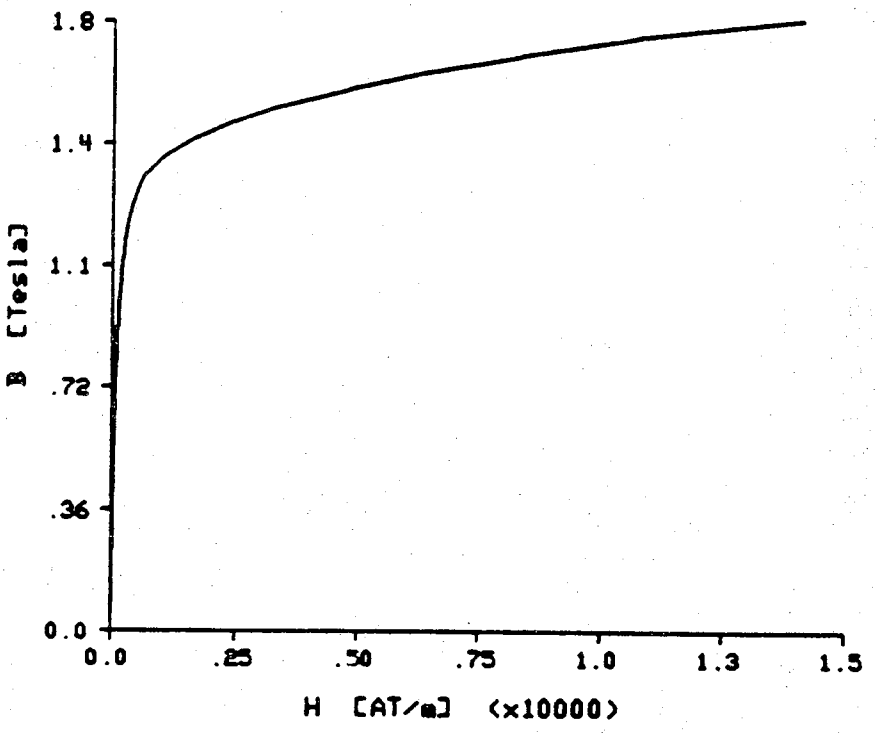

Figure 2.9. B-H curve for M-19 magnetic steel

symmetric matrices. A "row pointer- column index" technique is used in this study for the storage and manipulation of the global matrix which, being symmetric, requires storing of the upper right hand elements.

2.2.4 Boundary Condition Implementation

Maxwell equations describe the magnetic and electric field in a medium and implicitly prescribe their behavior near material interfaces. For practical purposes, the region of interest has to be confined to the local space, for which appropriate boundary conditions have to be specified.

In electromagnetic problems, flux lines are the lines of constant A. Since the flux lines are often conveniently used to give a pictorial view of the field distribution, a closer examination of their relation to potential is necessary. The expression for the flux through a surface S is given by Gauss law as

$$\phi = \int_S \vec{B}\cdot\vec{n}\,da \tag{2.59}$$

Replacing $\vec{B}$ by $\nabla\times\vec{A}$ and using Stokes theorem, (2.59) becomes

$$\phi = \oint_\Gamma \vec{A}\cdot dl \tag{2.60}$$

where Γ is the boundary of the surface S. For two-dimensional field problems where $\vec{A}$ has only the axial component, (2.60) simplifies to

$$\phi = Z(A_R - A_L) \tag{2.61}$$

where Z is the axial length of machine, and A_R and A_L are the vector potential values on the right and left hand side of the contour Γ. Now suppose that the contour is chosen so that $A_R = A_L$; then the contour Γ in (x,y) domain represent a flux line and flux through this contour is zero. With no flux crossing the flux line, adjacent flux lines traced out by following the contour with constant A at two different values contain a certain amount of flux. Thus, the grating density of flux lines in a plot generated with a fixed increment of A indicates the crowding or spreading out of a certain quantity of flux, indirectly showing the flux density distribution.

The flux lines run parallel to a line of odd symmetry, where A is equal in value and opposite in sign on both sides of this line, and along it has a fixed value. For convenience, this value may be taken as zero (A =0 along the line of odd symmetry). Thus, the line of odd symmetry satisfies the Dirichlet homogeneous condition.

On the other hand, along the line of even symmetry the flux lines are orthogonal to the line, that is the homogeneous Neumann condition holds,

$$\frac{\partial A}{\partial n} = 0 \tag{2.62}$$

In a finite element solution, these kinds of boundary conditions are called natural boundary conditions. They are being imposed by the solution procedure without explicit specification.

In rotating machines, the actual exterior surface of stator iron yoke or a remote imaginary cylindrical envelope can be chosen as the outer boundary. Since the flux lines tend to remain within the iron yoke, it can be assumed that little or no flux line leaves the exterior boundary of stator iron, the exterior boundary can be assumed to have constant vector potential, which for convenience is often arbitrarily set at zero. Hence, the outer surface of the stator can be represented as a homogeneous Dirichlet boundary with $A = 0$.

2.2.5 Solution of Global Equations

There has been a lot written on the solution techniques for handling large set of equations like that given by (2.57) [58]. The methods can be categorized as direct or indirect. In direct methods, the set of equations are solved by matrix manipulation based on Gauss elimination and LU decomposition. Indirect methods involve an iterative process which begins with an initial guess refining the estimated solution along a gradient path until it converges. In this study, a direct method using LU decomposition, and an indirect method using conjugate gradient method are applied, finding that the direct method is faster and more reliable.

2.2.6 Convergence Criteria

When using the N-R iterative method, a convergence criterion for stopping the iterative process is required. As error norms can be used to ascertain that the solution has reached some acceptable accuracy, various error norms are used for this purpose. In this study three different error norms are used. The first error norm is on the vector potential at the nodes, given by

$$\frac{\sum_{i=1}^{n} |A_i^{k+1} - A_i^k|}{\sum_{i=1}^{n} |A_i^k|} \leq \epsilon_A \tag{2.63}$$

where k is the number of iteration and ϵ_A is an admissible tolerance, which is set at 0.01 in our study. The second error norm is on the total magnetic energy stored in the field

$$\frac{|W^{k+1} - W^k|}{W^k} \leq \epsilon_W \tag{2.64}$$

where the error tolerance, ϵ_W, has been taken as 0.01 too.

The third error norm used is on the maximum change in the reluctivity of the iron elements, expressed as

$$\frac{\underset{i}{\text{Max}} |\nu_i^{k+1} - \nu_i^k|}{\nu_i^k} \leq \epsilon_\nu \tag{2.65}$$

In this study, ϵ_ν was taken to be 0.1. With the SR machine, it is observed that most of the time the order in which the convergence is obtained is the order that they are presented here; that is, the most severe criterion, especially in problems with highly saturated conditions, is the one concerned with the convergence of reluctivity in iron elements.

2.3 Results and Discussion

Plots of flux lines or equipotential contours can be obtained directly from field solution and can provide valuable information about both the overall accuracy of the data provided by discretization and the saturation level in various parts of the device. Here we present flux distribution plots of SRM at different rotor angles.

Figure 2.10 shows the flux pattern at the aligned position of the stator and the rotor poles. The symmetry and smooth curving of flux lines indicate the sufficient modeling of the field provided by discretization procedure. Also, bulk saturation of stator poles is noticeable. Figures 2.11 and 2.12 show the flux pattern at 10 and 20 degree of rotor rotation respectively. The local saturation at the opposite pole corners and sharply-curved fringing flux lines are noticeable in these figures. Also, small leakages of flux to other poles or stator yoke can be seen here. Finally, the flux pattern at 30 degree rotation

which corresponds to the unaligned position is shown in Fig. 2.13. Symmetry of flux lines is noticeable in this figure.

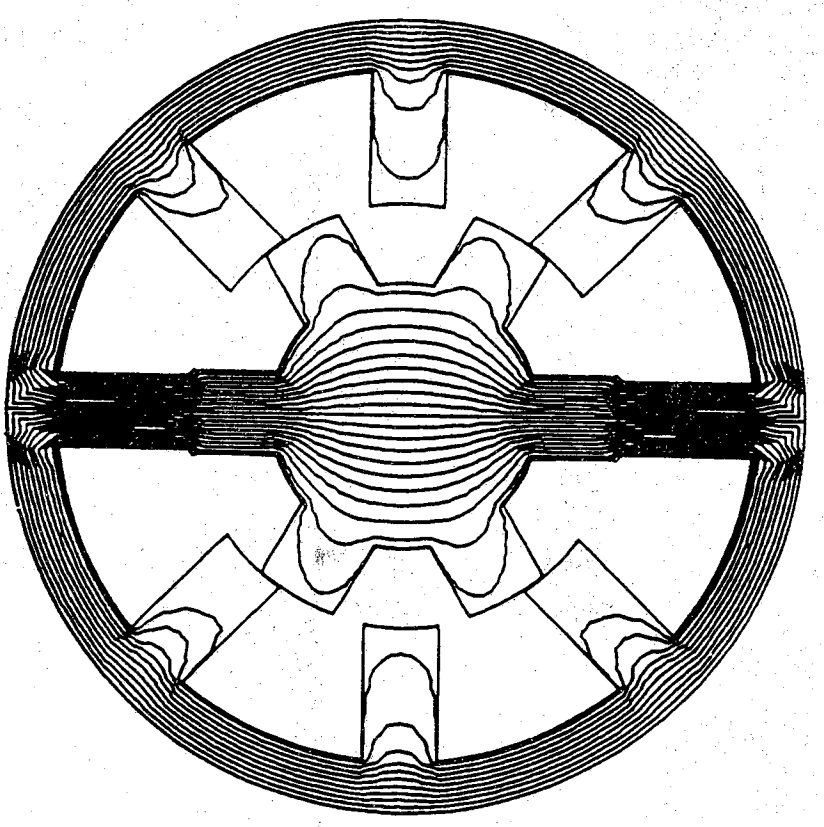

Figure 2.10. Flux lines at aligned position

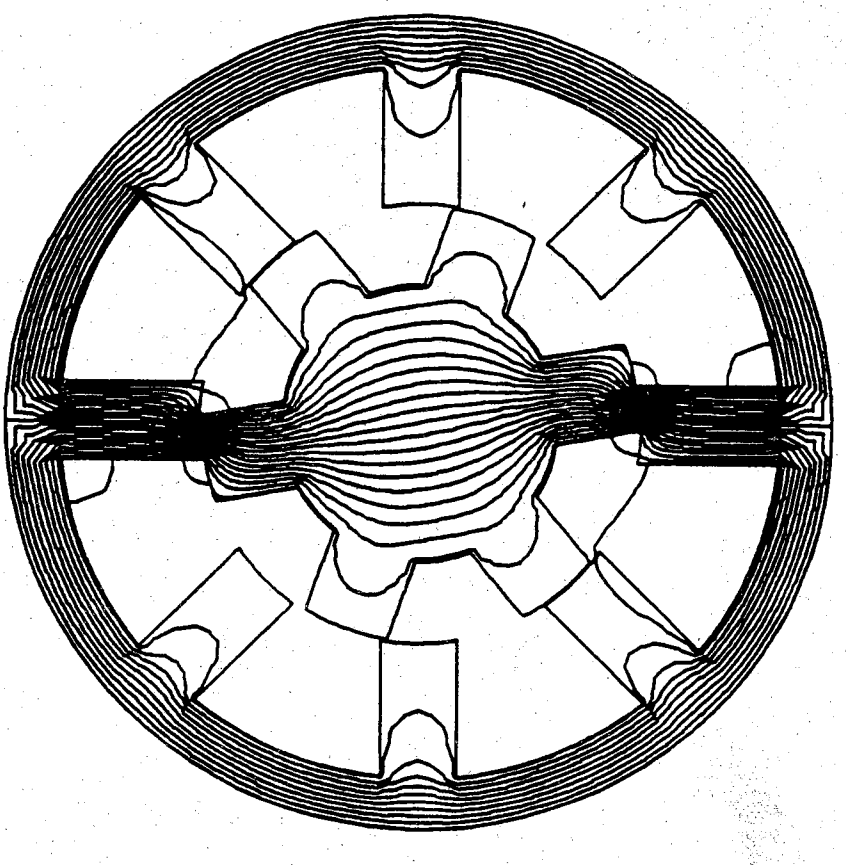

Figure 2.11. Flux lines at 10 ° position

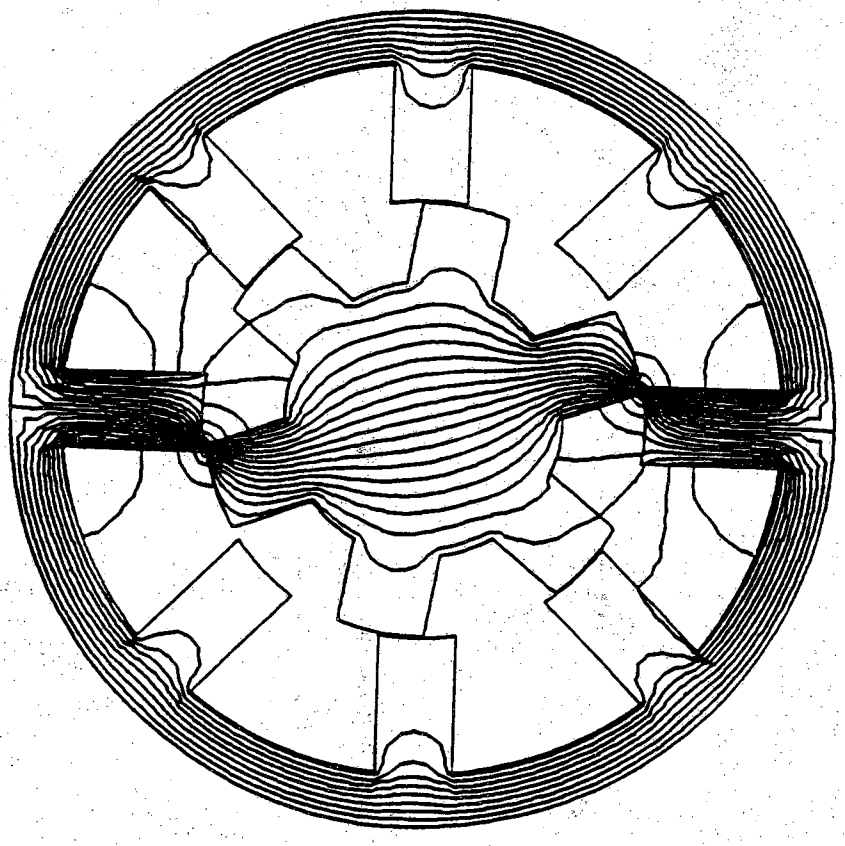

Figure 2.12. Flux lines at 20 ° position

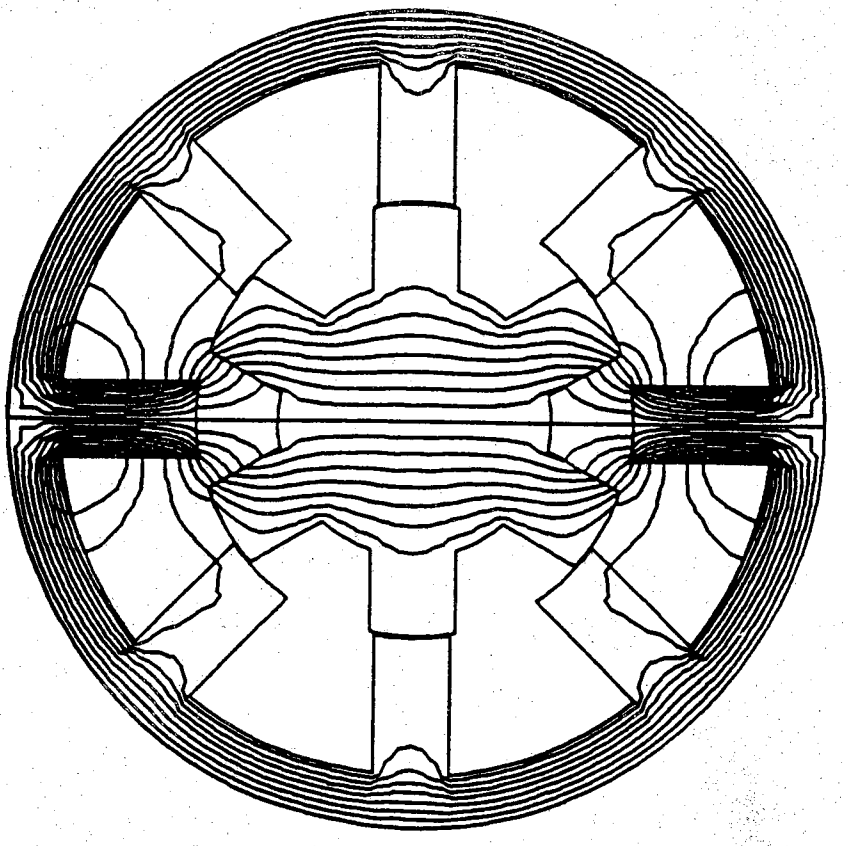

Figure 2.13. Flux lines at unaligned position

CHAPTER 3
METHODS AND ACCURACY OF TORQUE CALCULATION

Predicting the torque of a switched reluctance machine from its finite element field solution is not a straightforward procedure, mainly because the doubly salient iron structure is highly saturated and the airgap is narrow, and also because the accuracy required for getting a reasonable prediction of torque is more stringent than that for a qualitative idea of flux distribution. Nevertheless, an accurate knowledge of the torque forms an essential part of realistic modeling that will be needed to obtain efficient design of the SRM.

The mathematical theory behind the common methods of calculating torque based on a FE field solution are well established [71-77]. The common methods for torque calculation based on FE field solution are: the global virtual work method; the Maxwell stress-tensor method; the Coulomb virtual work method on which the local virtual work method in this study is based; and the Lorentz force formula. Since the Lorentz force formula is limited to force calculation on current-carrying conductors, it will not be considered in this study.

Most of the difficulties in calculating the torque of a switched reluctance machine have to do with the high field gradient in the very narrow airgap near the edges of the excited poles. When the torque is to be calculated by integrating around the airgap, the path crosses pockets of high field gradient where most of the torque is developed, but unfortunately it is in these pockets that the accuracy of the derived field components computed from the local potential distribution is the poorest.

In this chapter, first the basis and formulation of three methods of torque calculation, the global virtual work, the Maxwell-stress tensor, and the local virtual work method are reviewed. This is followed by a discussion on the sources of error in finite element field solution pertaining to requirements for calculating the torque. The previous works on improving the accuracy in the torque calculation are reviewed. Finally, we present our findings that a mesh of uniform, proper shaped and sized elements in the critical region can significantly improve the accuracy of the computed flux density components

and torque. Furthermore, the computed torque/angle characteristic will be smooth and accurate when the proper mesh model is preserved as the rotor is rotated. The computed torque/angle characteristics of test motor from all three different methods using the proposed guidelines in mesh are then checked against the measured torque/angle characteristics.

3.1. Global Virtual Work Method

The method of virtual work is widely used in applied mechanics; it makes use of the fact that the change in the energy of a rotary mechanical system is equal to the product of the torque and incremental displacement, that is

$$T = -\frac{\partial W}{\partial \theta} \tag{3.1}$$

The method of virtual work relies on the fact that torque does not change significantly during small motions and, therefore, is valid for small displacements only. Thus, to evaluate the torque exerted on a rotor body at a position, θ, the field energies for constant flux linkage or, equivalently, the coenergies for constant excitation current, at rotor positions θ and $\theta+\Delta\theta$ are evaluated; the torque then is given by

$$T = \frac{W_2' - W_1'}{\Delta\theta} \tag{3.2}$$

Torque calculation using virtual work method requires two field solutions of the machine at slightly different rotor positions, thus, it has the disadvantage of being prone to errors from the numerical differentiation. In cases where the difference in energy is very small for small displacements, substantial truncation errors in the subtraction may arise. Such errors can be reduced if the precision in the calculation and the representation of field energies can be improved. The accuracy of calculated energy is, in turn, dependent on the mesh configuration and the representation of nonlinear material (magnetization curve).

Proper discretization of the domain and realistic representation of the magnetic material , especially around and in regions of high energy density, can improve the accuracy of torque obtained from global virtual work method. Furthermore, if W_1' and W_2' are computed using similar finite element meshes, errors in W_1' and W_2' are likely to be similar and coenergy difference is more accurate. Further improvements in the smoothness of the torque/angle characteristic can be obtained when the coenergy is evaluated at uniformly spaced rotor positions, and when curve fitting techniques are applied to enable

the differentiation in (5.2) to be performed analytically; the latter approach can only increase the smoothness of the torque/angle characteristic, but does not affect the accuracy of the calculated torque.

3.2. Maxwell-Stress Tensor Method

The Maxwell-stress tensor method is based on the expression for force density, f, which in an electromagnetic system consisting of bodies of iron and current carrying conductors is given by

$$f = J \times B \tag{3.3}$$

where J is the current density and B is the flux density. Equation (3.3) represents only the magnetic portion of the Lorentz force formula. The force density, f, is a vector quantity with components in different directions of coordinate system, and has the dimension of force per unit volume. Thus, the resultant force on a body of iron in each of the directions can be calculated by the volume integration of f over that body in that particular direction.

Using Maxwell equation (2.2) to substitute for J, equation (3.3) becomes

$$f = \nu(\nabla \times B) \times B \tag{3.4}$$

where ν is the reluctivity of the medium. In the xyz-coordinates, the expression for x-component of force density is given as

$$f_x = \nu(B_z \frac{\partial B_x}{\partial z} + B_y \frac{\partial B_x}{\partial y} - B_z \frac{\partial B_z}{\partial x} - B_y \frac{\partial B_y}{\partial x}) \tag{3.5}$$

Using

$$B_i \frac{\partial B_i}{\partial x} = \frac{1}{2} \frac{\partial}{\partial x} (B_i^2) \tag{3.6}$$

in (3.5), after some manipulations, (3.5) can be rewritten as

$$f_x = \nu \frac{\partial}{\partial x} [\frac{1}{2}(B_x^2 - B_y^2 - B_z^2) + \frac{\partial}{\partial y}(B_x B_y) + \frac{\partial}{\partial z}(B_x B_z) - B_x \nabla \cdot B \,] \tag{3.7}$$

Since $\nabla \cdot B = 0$, the last term in (3.7) vanishes; then (3.7) can be written compactly as

$$f_x = \nabla \cdot T_x \tag{3.8}$$

where

$$T_x = \nu \begin{bmatrix} \frac{1}{2}(B_x^2 - B_y^2 - B_z^2) \\ B_x B_y \\ B_x B_z \end{bmatrix} \tag{3.9}$$

The total force in the x-direction is given by the volume integral of f_x over the entire body, that is

$$F_x = \int_\Omega f_x dv = \int_\Omega (\nabla \cdot T_x) dv \tag{3.10}$$

Using the divergence theorem, (3.10) can be reduced to a surface integral.

$$F_x = \oint_S T_x \cdot n \, ds \tag{3.11}$$

where n is the outward normal to the surface S. Likewise, the other components of force in y and z direction can be obtained using the same method. Gathering the x, y, and z components of force together, the force density in all directions is given by

$$F = \oint_S T \cdot n \, ds \tag{3.12}$$

where

$$T = \begin{bmatrix} T_x \\ T_y \\ T_z \end{bmatrix} = \nu \begin{bmatrix} \frac{1}{2}(B_x^2 - B_y^2 - B_z^2) & B_x B_y & B_x B_z \\ B_y B_x & \frac{1}{2}(B_y^2 - B_x^2 - B_z^2) & B_y B_z \\ B_z B_x & B_z B_y & \frac{1}{2}(B_z^2 - B_x^2 - B_y^2) \end{bmatrix} \tag{3.13}$$

Tensor T is known as the Maxwell magnetic stress tensor. Its elements have the dimension of force per unit area, hence they are also referred to as surface stresses. A Maxwell electric stress tensor with the same structure and with B replaced by E and ν by $\frac{1}{\epsilon}$ can be defined for calculating the force in an electrostatic fields. The total force acting on a rigid body can be calculated by integrating the components over a boundary surface enclosing the whole body.

In two-dimensional problems where there is no z-component, T reduces to a 2 x 2 tensor.

$$T = \nu \begin{bmatrix} \frac{1}{2}(B_x^2 - B_y^2) & B_x B_y \\ B_y B_x & \frac{1}{2}(B_y^2 - B_x^2) \end{bmatrix} \tag{3.14}$$

For rotary machines, polar coordinates are better suited to the geometry of the machine, in which case the radial component, τ_r, and the tangential component, τ_θ, are as follows:

$$\begin{aligned} \tau_r &= \frac{1}{2}\,\nu(B_r^2 - B_\theta^2) \\ \tau_\theta &= \nu\, B_r B_\theta \end{aligned} \tag{3.15}$$

τ_r is a tensile stress, which tries to reduce the length of airgap by attracting rotor and stator poles together, and τ_θ is the tangential stress which tries to reduce the airgap separation by increasing the pole overlap area (see Fig. 3.1). When the poles are exactly opposite and the airgap uniform, integration of τ_r and τ_θ over a cylindrical surface enclosing the whole rotor is zero. Moreover, since τ_r is directed along the center, no torque is produced by this component, all the torque is produced by the tangential component of stress. The torque surface density developed by tangential stress is given by

$$t = r \times \tau_\theta = \nu r\, B_r B_\theta \tag{3.16}$$

where t has dimension of torque per unit area. When using two-dimensional FE model, a convenient contour of integration is a cylindrical surface inside the airgap enclosing the whole of the rotor(see Fig. 3.2); in which case the total torque developed is given by

$$T = \nu_0 Z R \oint_\Gamma B_r B_\theta \, d\Gamma \tag{3.17}$$

where Z is the stack length of the motor and R is the radius of the cylindrical surface. Using the discrete solution of the field from the FE method, the integral equation of (3.17) is usually approximated by the summation

$$T = \nu_0\, Z R^2 \sum_{i=1}^{m} B_{ri}\, B_{\theta i}\, \delta\theta_i \tag{3.18}$$

where m is the total number of segments on the circular contour Γ and the summation is over the cylindrical surface generated by Γ (see Fig. 3.3).

Equation (3.18) shows that torque calculation using the Maxwell- stress tensor method depends on the calculated radial and tangential components of

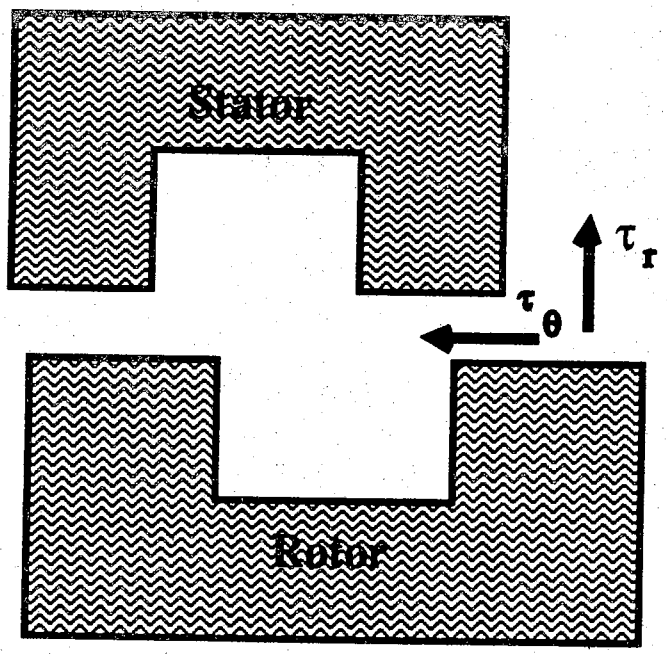

Figure 3.1. Surface stress components

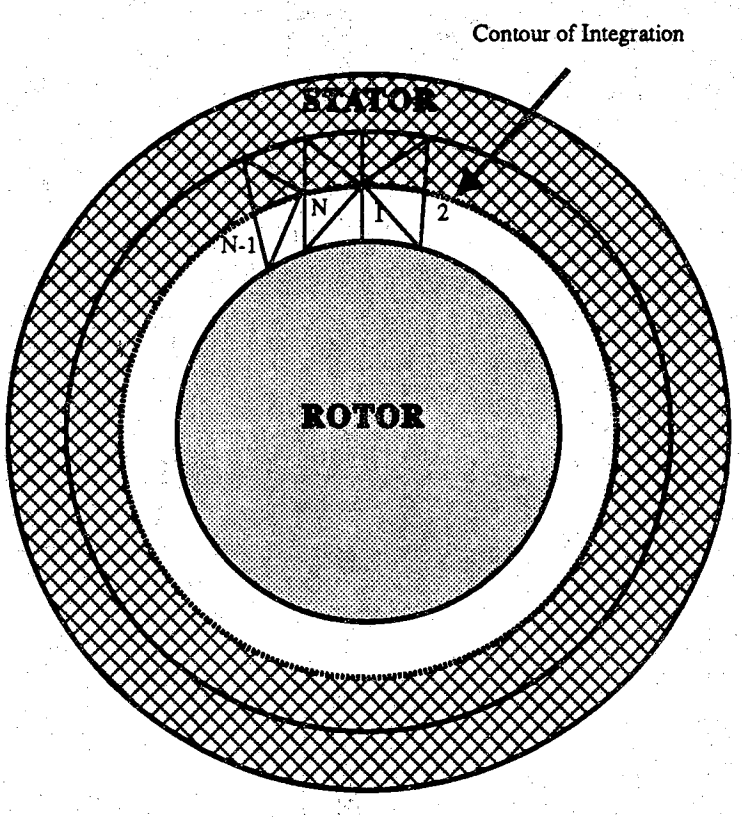

Figure 3.2. Contour of integration for Maxwell-stress tensor method

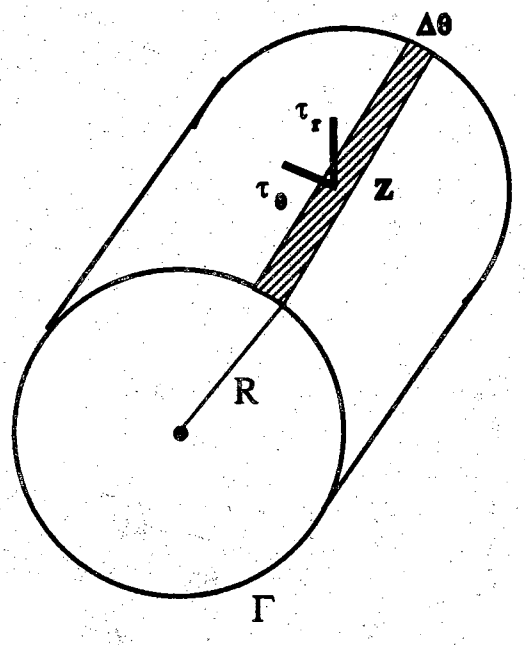

Figure 3.3. Surface of integration for Maxwell-stress tensor method

the flux density on Γ inside the airgap. This kind of calculation which relies on the local information derived from a FE solution is referred to as local calculation. Local calculations are usually more prone to errors than global calculations, since the FE solution is obtained by a weighted- integral minimization of energy. The types of error in FE-based calculations will be discussed in detail later in this chapter.

3.3. Local Virtual Work Method

The local virtual work method referred to in this study is an adaptation of the Coulomb virtual work method or the local Jacobian derivative method. It is also based on the virtual work principle; it differs from the global virtual work method only in the implementation. The electromagnetic coenergy density is given by

$$w' = \int_0^H B\,dH \tag{3.19}$$

Integrating w' over the whole volume gives the total electromagnetic coenergy in the system. Using a FE solution, the electromagnetic coenergy can be obtained by summing up the coenergy in all elemental volumes defined by the triangular element along the machine axis.

$$W' = \sum_e W'_e \tag{3.20}$$

where the summation is over all the elements of FE mesh and W'_e is the coenergy of the e^{th} element, which is given by

$$W'_e = \int_0^{H_e} B_e\,dH_e \cdot V_e \tag{3.21}$$

V_e is the volume of each element along the stack length of motor and can be obtained from

$$V_e = Z\,\Delta_e \tag{3.22}$$

where Z is the stack length of the motor and Δ_e is the area of e^{th} element. Using (3.22), (3.20) can be written as

$$W' = Z \sum_e \Delta_e \int_0^{H_e} B_e\,dH_e \tag{3.23}$$

In the local virtual work method, the torque contribution from an element is calculated analytically using

$$T_e = \frac{\partial W_e'}{\partial \theta} \tag{3.24}$$

Then, adding torque contribution of all elements gives the total torque developed on the rotor. The advantage of this method over the global virtual work method in calculating the elemental torque contribution analytically is that the analytical differentiation introduces fewer errors than the numerical differentiation.

To calculate the torque contribution of each element, it is necessary to derive an expression for T_e. In this study, a new formulation for evaluating T_e is derived that significantly reduces the computational time as compared to that taken by direct implementation of the original formulation by Coulomb [77].

As the area of each element and flux density inside each element are functions of element nodal coordinates, the substitution of (3.21) into (3.24) yields

$$\begin{aligned} T_e &= Z \frac{\partial}{\partial \theta} \left[\int_0^{H_e} B_e dH_e \, \Delta_e \right] \\ &= Z \Delta_e \frac{\partial}{\partial \theta} \int_0^{H_e} B_e dH_e + Z \int_0^{H_e} B_e dH_e \frac{\partial \Delta_e}{\partial \theta} \end{aligned} \tag{3.25}$$

During rotation of the rotor, the mesh consists of three regions: rotated, static, and distorted (see Fig.2.4). The resultant torque contributions from the static and rotated elements are zero, but the resultant torque contribution from the distorted elements in the airgap annulus between rotor surface layer and mid-airgap layer is non-zero. In fact, the change of energy in the distorted element surrounding the rotor body represents the change in energy flow from rotor to stator or vice versa, and with the iron losses neglected this energy flow converts to mechanical energy. Therefore, T_e is only non-zero for distorted elements, which are all located in the airgap region. The elements being in the air, $H_e = \nu_0 B_e$, (3.25) becomes

$$T_e = \nu_0 Z \left[\frac{\Delta_e}{2} \frac{\partial B_e^2}{\partial \theta} + \frac{1}{2} B_e^2 \frac{\partial \Delta_e}{\partial \theta} \right] \tag{3.26}$$

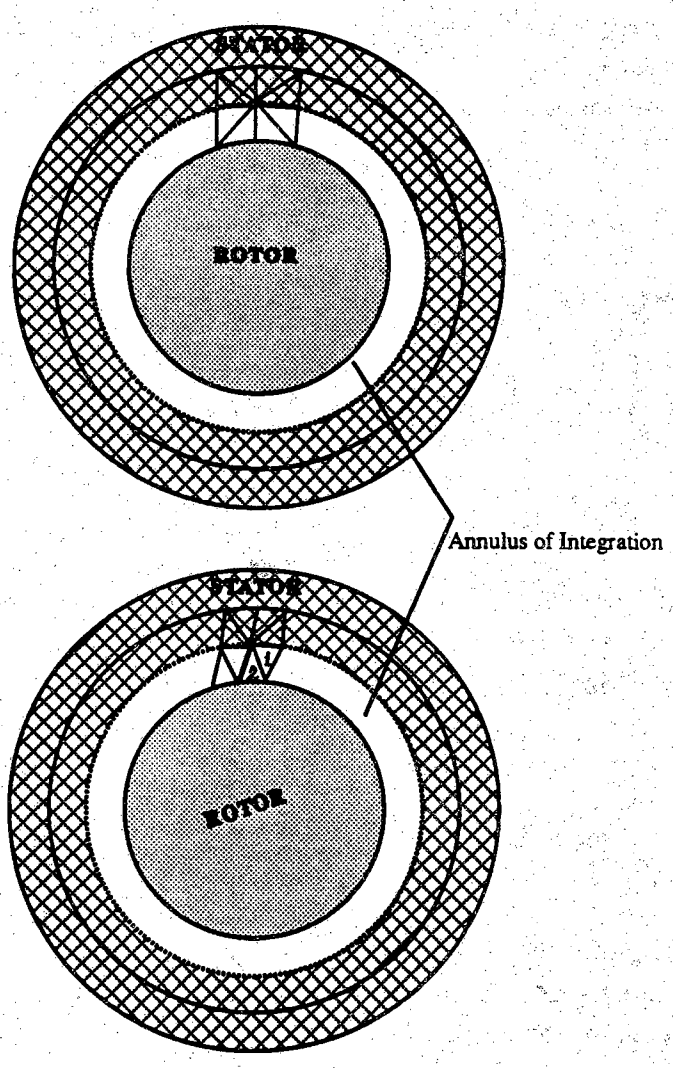

Figure 3.4. Annulus of integration for local virtual work method

Expressions for $\frac{\partial \Delta_e}{\partial \theta}$ and $\frac{\partial B^2}{\partial \theta}$ can be conveniently obtained when Δ_e and B_e are expressed in polar coordinates.

As shown in Fig. 3.4, the elements in the distorted region have either one node or two nodes on the moving surface; however, the radial coordinates of the nodes do not change by rotation of the rotor. To derive an expression for the $\frac{\partial \Delta_e}{\partial \theta}$ term in (3.26), the area of the e^{th} element, Δ_e, is first expressed in term of its nodal coordinates, that is

$$\Delta_e = \frac{1}{2}[r_m r_n \sin(\theta_n - \theta_m) + r_n r_\ell \sin(\theta_\ell - \theta_n) + r_\ell r_m \sin(\theta_m - \theta_\ell)] \tag{3.27}$$

If one of the nodes of the triangle ℓmn, say node ℓ, is perturbed by an angle $\delta\theta$, the change in area with respect to the perturbation is given by partial derivative,

$$\frac{\partial \Delta_e}{\partial \theta_\ell} = r_n r_\ell \cos(\theta_\ell - \theta_n) \tag{3.28}$$

For those elements with two nodes on the moving surface, the change in the area can be calculated by the addition of change caused by movement of the second node. It can be shown that

$$\frac{\partial \Delta_e}{\partial \theta_{mn}} = -\frac{\partial \Delta_e}{\partial \theta_\ell} \tag{3.29}$$

where subscript mn indicates that nodes m and n are perturbed, and that

$$\frac{\partial \Delta_e}{\partial \theta_{\ell mn}} = 0 \tag{3.30}$$

(3.30) shows that there is no change in area of an element where all its nodes are moved by an angle $\delta\theta$.

The term, $\frac{\partial B_e^2}{\partial \theta}$, can be calculated as follows: B_e^2 can be written in terms of its polar components, that is

$$B_e^2 = B_{er}^2 + B_{e\theta}^2 \tag{3.31}$$

Differentiating with respect to θ_i yields

$$\frac{\partial B_e^2}{\partial \theta_i} = 2(B_{er} \frac{\partial B_{er}}{\partial \theta_i} + B_{e\theta} \frac{\partial B_{e\theta}}{\partial \theta_i}) = 2 B_e \cdot \frac{\partial B_e}{\partial \theta_i} \tag{3.32}$$

The algebraic manipulations involved in getting the expressions for the right

hand side of (3.32) and is described in Appendix D; the resulting expression is

$$B_e^T \cdot \frac{\partial B_e}{\partial \theta_\ell} = \frac{r_\ell (A_m - A_n)}{(2\Delta_e)^2} [r_m (A_n - A_\ell) \sin(\theta_m - \theta_\ell)$$

$$+ r_n (A_\ell - A_m) \sin(\theta_n - \theta_\ell)] - \frac{B_e^2}{\Delta_e} \frac{\partial \Delta_e}{\partial \theta_\ell} \tag{3.33}$$

Again, it can be shown that

$$\frac{\partial B_e}{\partial \theta_{mn}} = \frac{\partial B_e}{\partial \theta_m} + \frac{\partial B_e}{\partial \theta_n} \tag{3.34}$$

and that

$$\frac{\partial B_e}{\partial \theta_{\ell mn}} = 0 \tag{3.35}$$

Thus, with the help of expression like those given in (3.26), the torque contribution from the e^{th} element in the distorted region can be calculated; then summing the torque contribution from all the elements in the distorted region yields the total torque developed on the rotor.

The expression in (3.26) shows that torque calculation using the local virtual work method also depends on the locally calculated flux density components; thus it will be subjected to errors in these components as in the case of the Maxwell-stress tensor method.

3.4. Accuracy Consideration

In general, calculations based on a finite element solution of the partial differential equations are subject to several sources of error; the major ones being

- Numerical errors
- Modeling errors
- Approximation errors
- Discretization errors
- Local error

Numerical errors such as round-off and truncation errors have to do with the machine precision and numerical methods used in computational procedures, and have not been found to be of great importance, if higher

precision and methods with higher order truncation are used for the solution.

Modeling errors come from the assumptions made in approximating the real system with a mathematical model that can be handled efficiently. One example of such assumptions in modeling of an SRM is the approximation of the complicated geometry of a three-dimensional device by a two-dimensional discrete model. Another such assumption is the modeling of the nonlinear material as being monotonic, single-valued, isotropic, and homogeneous. The modeling errors can, of course, be reduced by such refinements as three-dimensional FE model and representation of nonlinear material in forms which account for anisotropy and hysteresis phenomena, but the accuracy improvement may not justify the extra efforts required by the computation and modeling.

Approximation errors have to do with insufficient approximation of the field behavior by the choice of basis (or shape) functions. The choice of shape functions is often based on the fact that they should at least satisfy the continuity of the main variable at the boundaries of the elements. However, the choice of the shape function based on the minimum continuity requirement may result in two sources of error: First, if the calculation requires the derivatives of main variable, then the final result may be inaccurate due to the discontinuity of the derivatives not allowed for in the choice of basis functions. Secondly, certain boundary conditions at the element interfaces may be violated because of discontinuity in field derivatives.

First order triangular elements with linear shape functions will be sufficient for the continuity of magnetic vector potential (the main variable) in a two-dimensional finite element model, but at least flux density components, which are spatial derivatives of vector potential, may be discontinuous at the boundary between the elements. Thus, not all boundary conditions mentioned in section 2.1 will be enforced properly (see Fig. 3.3). For example, a formulation based on the vector potential only guarantees the continuity of the normal component of field density, B_n, at the borders of elements, whereas a formulation based on the scalar potential, ϕ (where $H = -\nabla\phi$), enforces the continuity of the tangential component of the field intensity, H_t, at borders of elements in a current-free region. Also, since the solution procedure as outlined in Chapter 2 involves the calculation of flux density for elements in iron to update the elemental reluctivity at each iteration, the accuracy of final solution which depends on the accuracy and continuity of computed flux densities may be at risk.

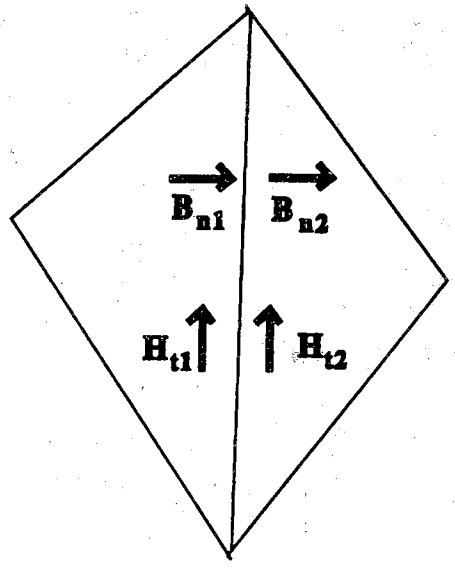

Figure 3.5. Boundary conditions at element interfaces

The approximation errors of the field solution can be reduced if higher order shape functions are chosen. However, the choice of higher order shape functions if applied over the whole domain will require more storage and computation time. For the problem that has only small regions in which the field variation is high, a hybrid method in which higher order shape functions are selectively used for critical regions may be advantageous.

Discretization errors have to do with mesh size and configuration in different regions of the domain. The guidelines for the shape, size, symmetry, and uniformity of the mesh already have been discussed in detail and can be summarized as follows: the triangle elements should not have angles near 180°, should be as close to equilateral proportions as possible; the size of elements should be small where the field gradient is high and large where the changes are small; the symmetry of the field solution should be preserved by symmetry of the mesh; and finally, the grading of the mesh from large elements to small ones should be uniform.

Since the field solution is usually obtained from a direct global extremization of energy, which only requires that the potential distribution over the whole region yields a minimum difference between input and magnetic field energy, the accuracy of the local potential distribution from a finite element field solution is not guaranteed; therefore, secondary results obtained from processing the local potential distribution, such as the flux density and torque, are subject to the same uncertainties.

Once a decision is made about the choice of shape functions, further improvement in accuracy of solution can still be obtained by proper modeling of the mesh. Proper mesh modeling requires a preliminary knowledge of the field distribution patterns based on past experience or previous FE solution. With some ideas, the mesh in different regions can be refined or rearranged to enhance the accuracy of the solution. For example, sharp curving of the flux lines indicating large nonlinearity of the field, should be modeled by elements capable of portraying the field variations in both directions. Since the curvature of flux lines depends on the changes in the flux density components, the rate of change of flux density components is perhaps the best measure for selecting a proper mesh model. For example, in regions where the rate of change of the flux density components is high, the mesh size should be kept small. Also, if field gradient is high in one direction, the size of element edges in that direction should be small, subject to the angle conditions mentioned in Chapter 2. The shape and uniformity of the elements in critical regions can have profound effects on the accuracy of calculation of field components;

properly chosen, these features can enhance the continuity of the flux density components between adjacent elements. We have found that a significant improvement in accuracy of flux density components in an SRM can be obtained with a reasonably fine, but not overly fine, mesh in the airgap simply by selecting properly shaped and uniform triangular elements. Such improvements in accuracy of the computed flux density components are reflected in the results of global solution and also those that rely on local calculations such as the torque. As a result, insufficiency in the choice of shape functions may be somewhat compensated by careful discretization of the domain.

3.5. Previous Work on Torque Calculation

Since the Maxwell-stress tensor and the local virtual work methods rely on the locally calculated flux density components, they are consequently more sensitive to errors in the locally calculated flux density components; when the errors in the flux density components are large, these methods often exhibit discrepancies, sometimes even inconsistencies.

There have been a number of recent papers on techniques to improve the accuracy of the force or the torque computed from a FE field solution [84-88]. In [84], the authors proposed a so-called dual energy method in which they established the lower and upper bounds on the energy of system, claiming that the average of the forces computed at these two bounds would provide a more accurate value of the force.

In [85], the authors investigated the effects of mesh refinement and distance of the remote boundary on the force calculation. Using a two-wire line example, they showed that the local distribution of the flux density could still be not smooth, even after convergence, based on a global measure, has been attained. They concluded that the convergence of the force calculated by the Maxwell-stress tensor method lagged behind that of the potential distribution.

In [86], the authors compared the torque calculated from the global virtual work method with that from the Maxwell stress-tensor method. They suggested using a very fine mesh in the pole overlap region to improve the accuracy of the torque calculated by the Maxwell stress method.

Reference [87] proposed two methods to reduce the mismatch in boundary conditions between adjacent elements: that of extrapolating the flux density from the values at Gauss points inside each element and that of using

non-conforming elements to enforce the continuity conditions on the flux density components. Although the authors could not confirm the improvement from the use of non-conforming elements, they asserted that fulfilling the boundary conditions across the edges of elements could reduce the inaccuracies in the calculated torque.

In [88], the authors examined the accuracy and consistency of the global virtual work method, the Maxwell stress-tensor method, and the local virtual work method. They introduced an error measure, which is based on the Maxwell stress-tensor formulation, to select the contour of integration, and demonstrated its usefulness on a test system consisting of an iron bar placed within two current-carrying conductors.

3.6. Torque Calculation for the SRM

In the case of the SRM, most of the errors in the computed torque from the Maxwell stress-tensor and the local virtual work method are caused by errors in the calculation of the radial and tangential components of the flux density in the critical region of overlapped poles in the airgap. In polar coordinates, the flux density components are given by

$$B_r = \frac{1}{r}\frac{\partial A}{\partial \theta} \quad , \quad B_\theta = -\frac{\partial A}{\partial r} \tag{3.36}$$

To see the significance that accurate prediction of flux density components has on the torque calculation, let's examine the magnified view of flux lines in the overlap region at different rotor angles shown in Figs. 3.6 through 3.9. The sharply curved fringing flux lines in the neighborhood of locally saturated iron are clear in these figures. The accuracy of the field solution is affected by inaccurate modeling or representation of the sharply curved flux lines, and by difficult convergence conditions caused by large changes in reluctivity of highly saturated elements in iron from iteration to iteration. The profile of vector potential in the θ-direction as shown in Fig. 3.10, indicates that the vector potential remains relatively constant at the maximum and minimum level, but changes sharply under the overlap region. The profiles of radial and tangential components of flux density are shown in Figs. 3.11 through 3.14. The profiles of B_r given in these figures are consistent with the profile of A shown in Fig. 3.10. The profiles of the tangential component can also be verified by a close examination of flux lines at the pole tips. The tangential component of flux density is non-zero only at the opposite corners of the overlap region, but zero everywhere else. Both B_r and B_θ have sharp changes

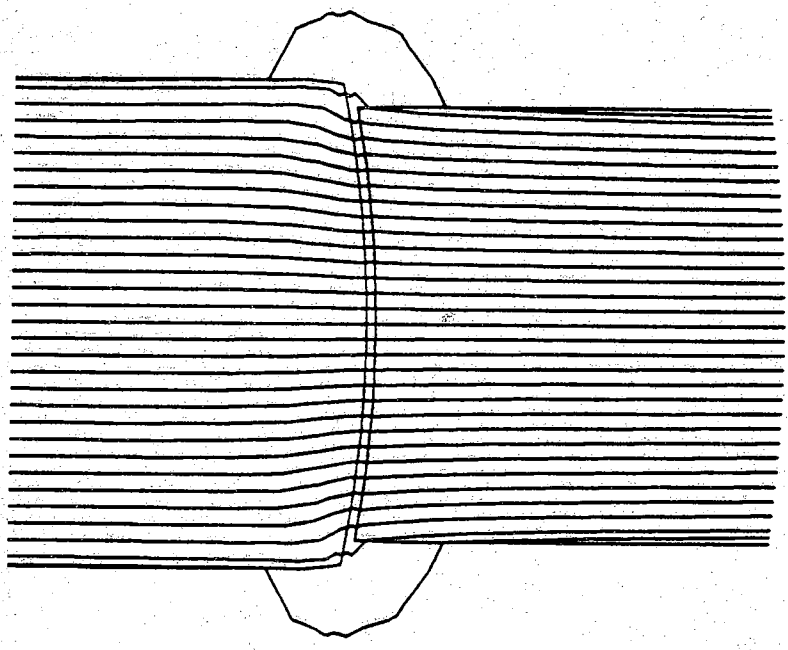

Figure 3.6. Flux lines near pole tips at $\theta = 0°$

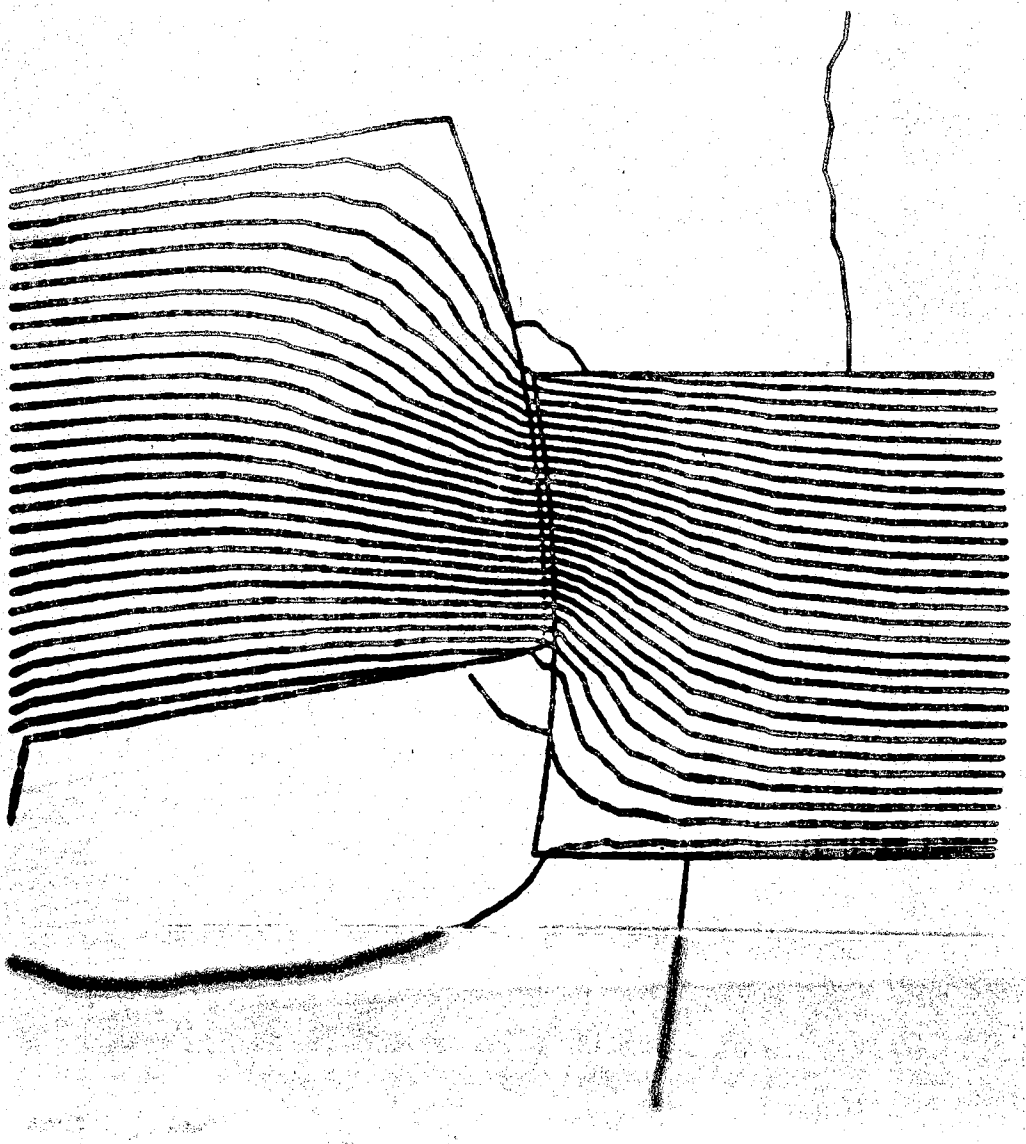

Figure 3.7. Flux lines near pole tips at $\theta = 10°$

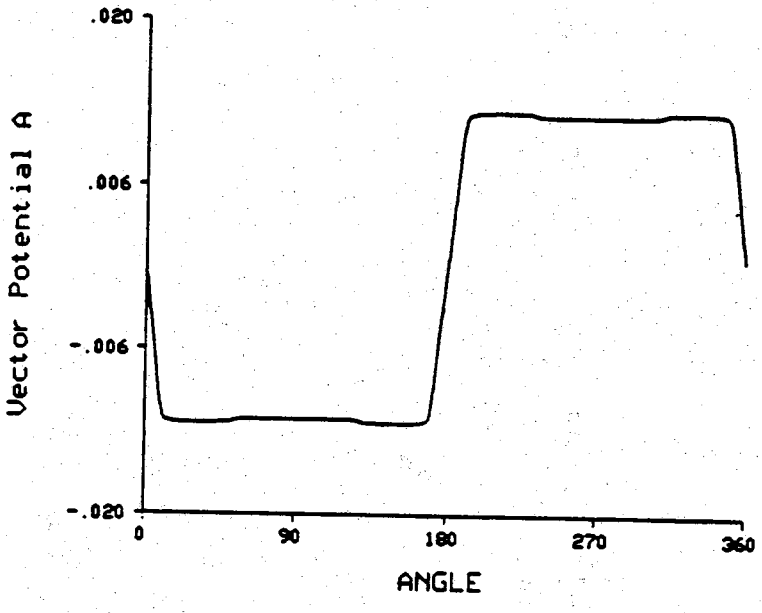

Figure 3.10. Profile of vector potential on the mid-airgap layer

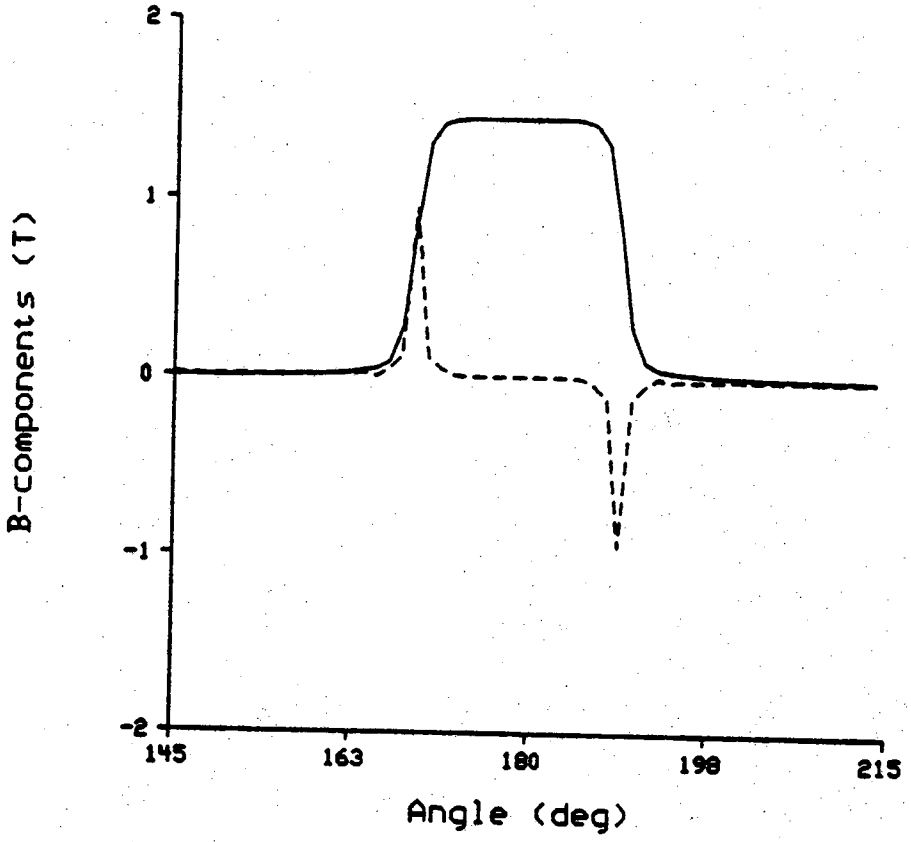

Figure 3.11. Radial and Tangential components of flux density at $\theta = 0^\circ$

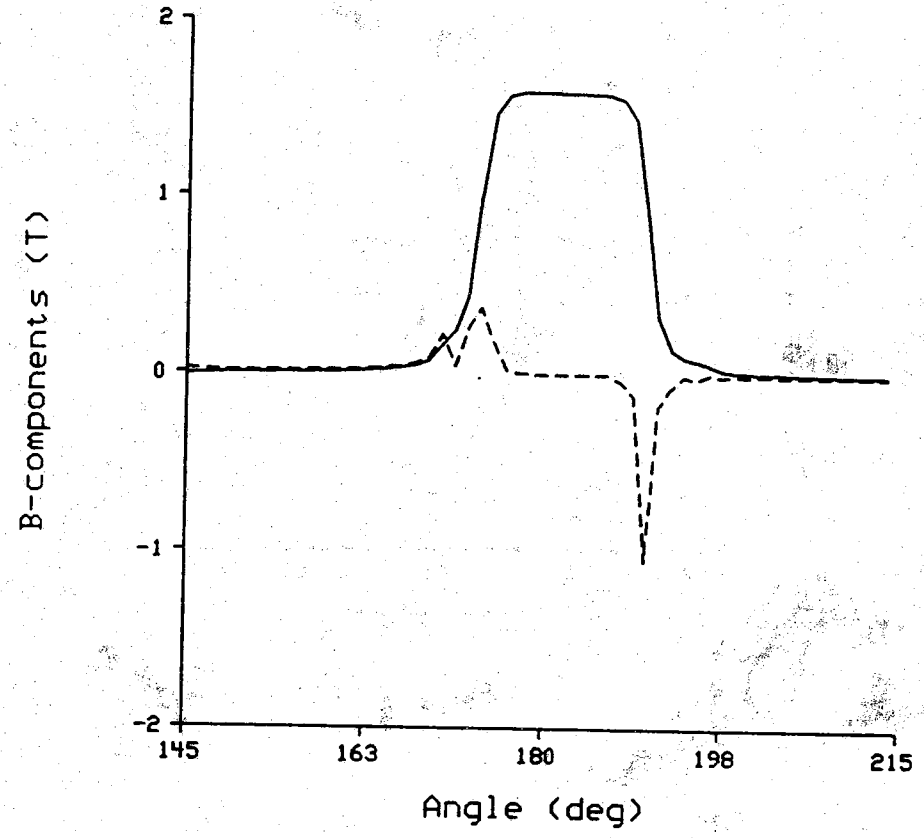

Figure 3.12. Radial and Tangential components of flux density at $\theta = 5^\circ$

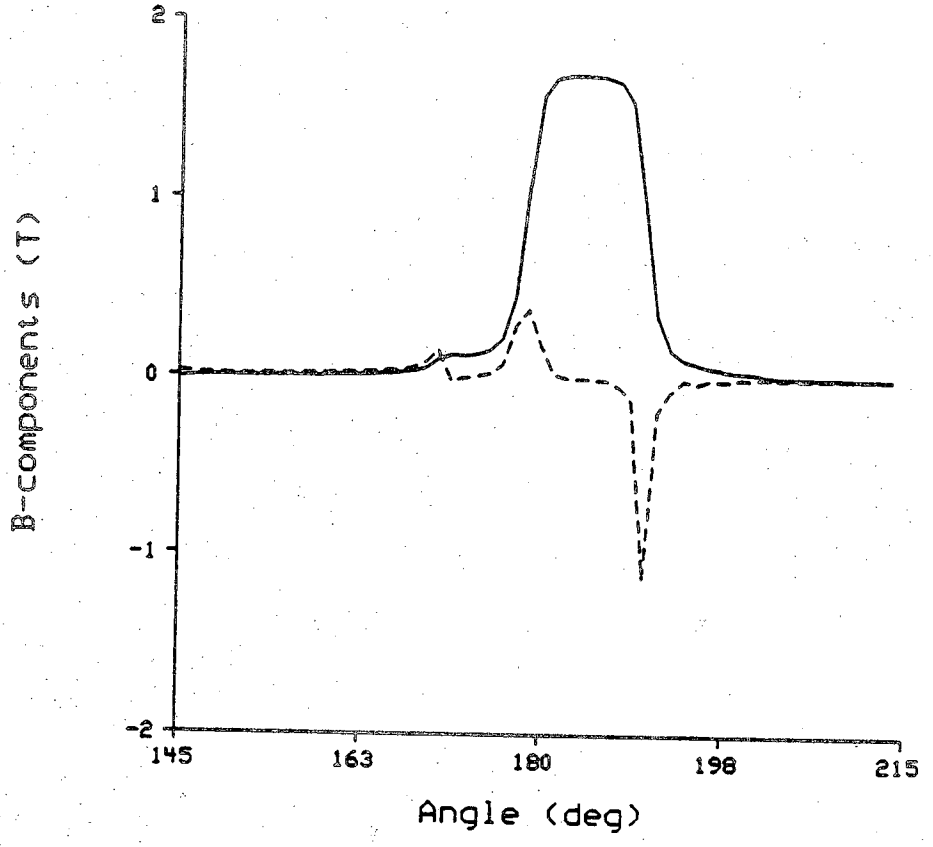

Figure 3.13. Radial and Tangential components of flux density at $\theta = 10^\circ$

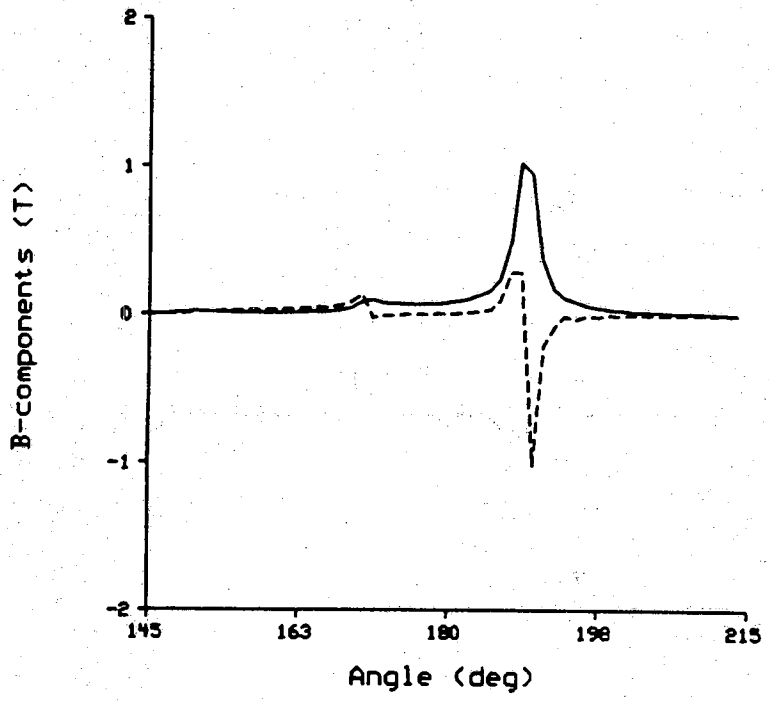

Figure 3.14. Radial and Tangential components of flux density at $\theta = 20^\circ$

at the corners of the opposite poles. Based on the above observation, an accurate modeling of the field at these corners will improve the accuracy of FE solution and, more importantly, will improve significantly the accuracy of the local calculations in these critical regions where the field is intense and the torque contribution is highest.

When using the Maxwell stress-tensor method or the local virtual work method to compute the torque of the SRM, the integration contour invariably has to pass through pockets of high field gradient at the corners of the pole tips, where most of the torque is being developed. The very narrow airgap of the SRM does not allow much room for one to pick an integration contour away from the iron surfaces, as recommended by some workers [88].

The Maxwell tensor method formulation as given by (3.18) is the integral of the product of flux density components around a mid-airgap layer. This product is almost zero everywhere on such a contour except at the pole corners where the tangential component of flux density is non-zero, as shown in Figs. 3.15 through 3.18.

The local virtual work formulation is based on the change of energy in the elements within a circular annulus of the airgap to a small displacement in rotor position. The change of elemental energy is mainly related to change in flux density components. The stored energy in the elements of overlap region is small, because there is no sizable change in the magnitude of flux density in this region, and the energy stored in the airgap elements away from the poles of excited phase is almost zero; therefore, the major contribution in calculated torque using local virtual work also comes from the elements near the pole corners where the change in the flux density and the stored energy are the highest.

One of the ways to improve the accuracy of the computed torque from these two methods is to refine the finite element mesh covering the high field gradient regions at the pole corners. Yet, to keep the computational effort to a reasonable level, the mesh in the airgap should not be too fine. Also, simply adding more layers with no corresponding increase in the number of circumferential elements will result in more elongated triangular elements which are not desirable.

The following simplified analysis, together with the results presented later, will show that indiscriminate addition of elongated elements with large aspect ratio in critical areas is ineffective and counterproductive, because it yields erroneous values for the flux density components. From (IV.7), the

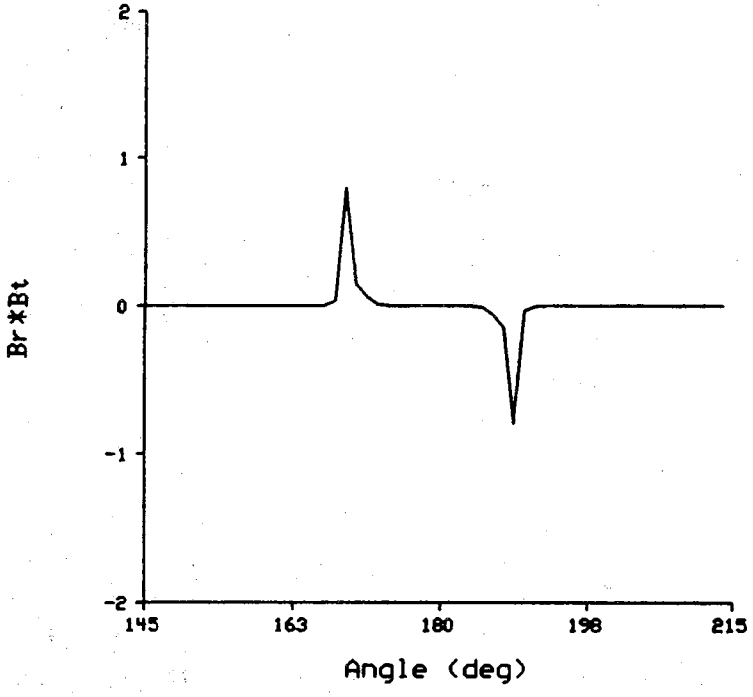

Figure 3.15. Product of flux density components at $\theta = 0$

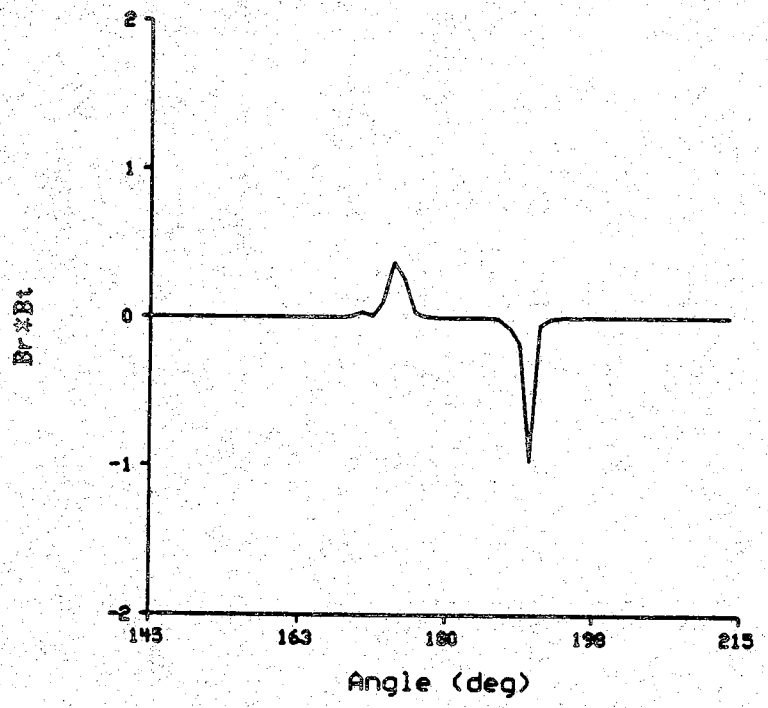

Figure 3.16. Product of flux density components at $\theta = 5$

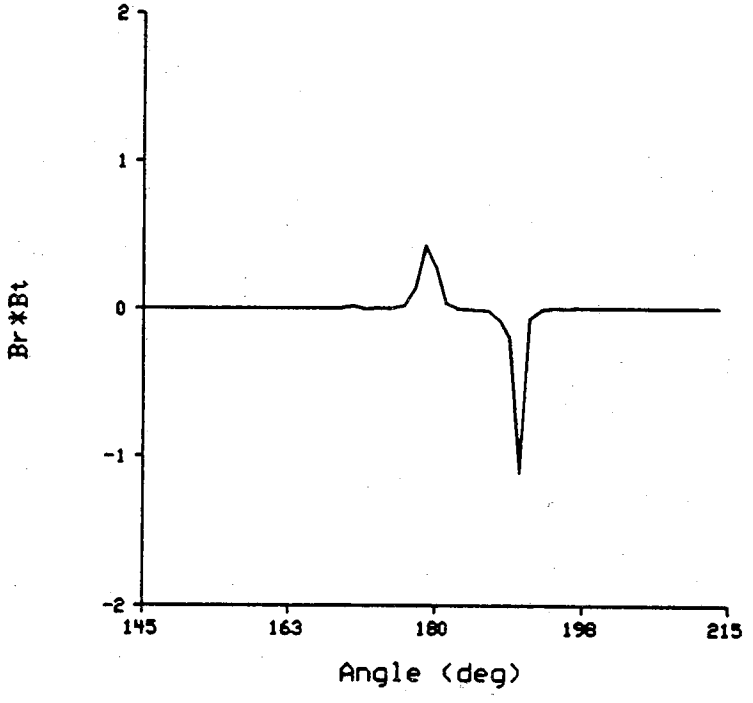

Figure 3.17. Product of flux density components at $\theta = 10$

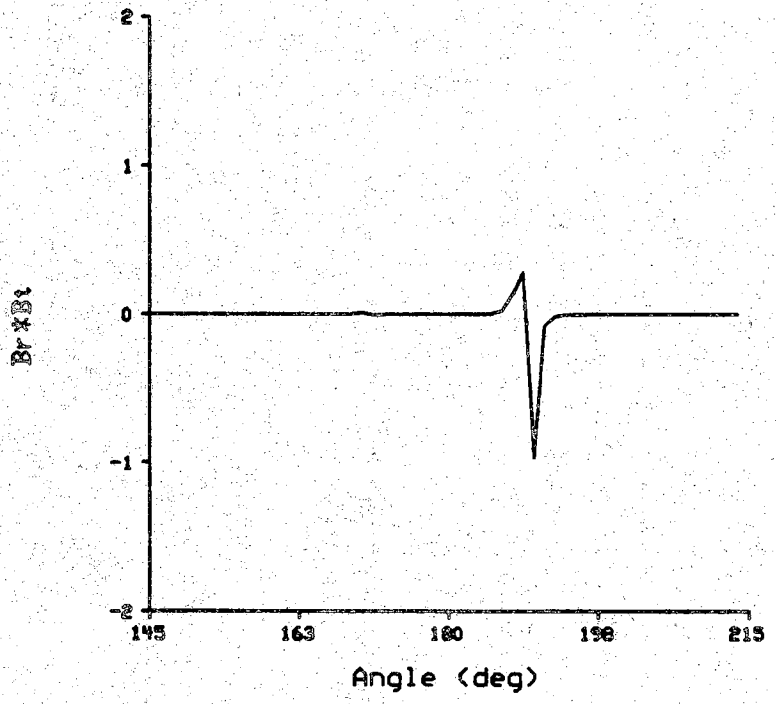

Figure 3.18. Product of flux density components at $\theta = 20$

expression of the tangential component of the flux density is

$$B_\theta = \frac{-1}{2\Delta}\Big[A_l(r_m \sin(\theta_m - \theta) + r_n \sin(\theta - \theta_n)) + A_m(r_n \sin(\theta_n - \theta) + r_l \sin(\theta - \theta_l)) + A_n(r_l \sin(\theta_l - \theta) + r_m \sin(\theta - \theta_m))\Big] \quad (3.37)$$

where l, m, and n are the nodal points, and θ is the angular coordinate of the centroid of the element. For circumferentially elongated elements with high aspect ratio on the annulus, as shown in Fig.3.19(a), (3.37) can be approximated by

$$B_\theta = \frac{(A_m - A_l)}{\delta r} \quad (3.38)$$

where δr is the radial thickness of the annulus. Equation (3.38) shows that the B_θ of such elongated element is mostly dependent on the difference of potentials at the two nodes which are close together and not on that of the remote node. When the nodes l and m are very close together in the same radial direction, the value of A_m could be very close to that of A_l. Moreover, the values of B_θ in the two adjacent elongated triangular elements sharing the short edge lm will be almost equal, indicating that the subdivision of the short edges like lm has brought no significant benefit - as if the functional spaces of the two adjacent triangular elements, lmn and lmo, have degenerated into one representable by a single large triangular element lno. Furthermore, where the variation of potentials from node to node is large, the discontinuity in B_θ between adjacent elements sharing a long edge will be large too. The above illustration expands on what has been mentioned earlier, that of the error in B_θ being an inverse function of the smallest angle in element.

In comparison to the elements of Fig. 3.19(a), those of Fig. 3.19(b) have a lower aspect ratio and a more uniform distribution of the nodal points; both improvements achieved without the added expense of a finer resolution mesh. Another aspect of the improvement becomes evident when the previous expression in (3.38) for B_θ is compared with the following for the new elements shown in Fig. 3.7(b)

$$B_\theta = \frac{(2A_m - A_n - A_l)}{2\,\delta r} \quad (3.39)$$

If (3.38) and (3.39) are compared with standard expression for forward and

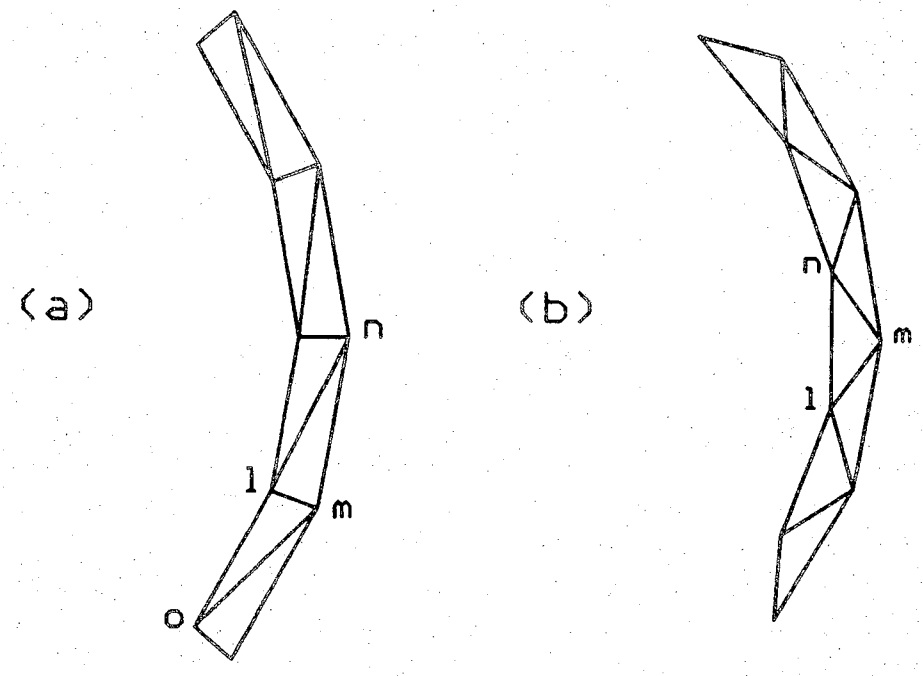

Figure 3.19. Mesh types (a) Elements with large aspect ratio (b) Elements with low aspect ratio

central difference methods of numerical differentiation, the advantage of (3.39) over (3.38) can be appreciated. Thus, the uniform mesh of Fig. 3.19(b) not only provides a more evenly distributed vector potential field solution but also reduces the computational errors and discontinuity in the flux density components. The above analysis indicates that satisfying the maximum angle condition in the critical region is not sufficient by itself; better result can be obtained by minimizing the aspect ratio of the elements and positioning the nodes of the mesh uniformly, especially in the overlapped region under the poles.

3.7. Results and Discussion

Here the computed results of torque/angle characteristics for the test SRM obtained from the global virtual work , the Maxwell-stress tensor, and the local virtual work methods are presented and compared with the experimentally measured static torque at various levels of excitation. At the same time, results are also presented to illustrate the improvements obtainable in the computed torque/angle characteristics when the proposed guidelines for picking the shape of the triangular elements and the stepping of the rotor are followed.

Of particular interest in the torque calculation is the effect of the mesh types on the computed flux density components in the critical regions. Several mesh types for the airgap region were tried out, but for illustration purposes the two shown in Fig.3.20 will suffice: Mesh A in Fig.3.20(a) satisfies the angle conditions, but its elements have aspect ratio higher than five, whereas mesh B, shown in Fig. 3.20(b), is an improved mesh as its elements have aspect ratio less than two.

Figures 3.21 shows the mid-airgap distribution of the tangential and radial components of the flux density in the overlapped region computed from the field solutions with the mesh A and mesh B, respectively, for the case of an angular displacement of 10° and an exciting current of 10A. Since the product of the two components of the flux density is highest at the opposite corners of the overlapped region, most of the torque is developed around these two corners. From both Fig. 3.21, we can see that the distributions of the tangential and radial components of the flux density obtained using mesh B have more uniform steps than those obtained using mesh A. At the pole corners, the tangential component obtained using mesh A not only is lower in magnitude than that obtained using mesh B, but also tended to be oscillatory from element to element in the vicinity of the corner. As we will see later, this

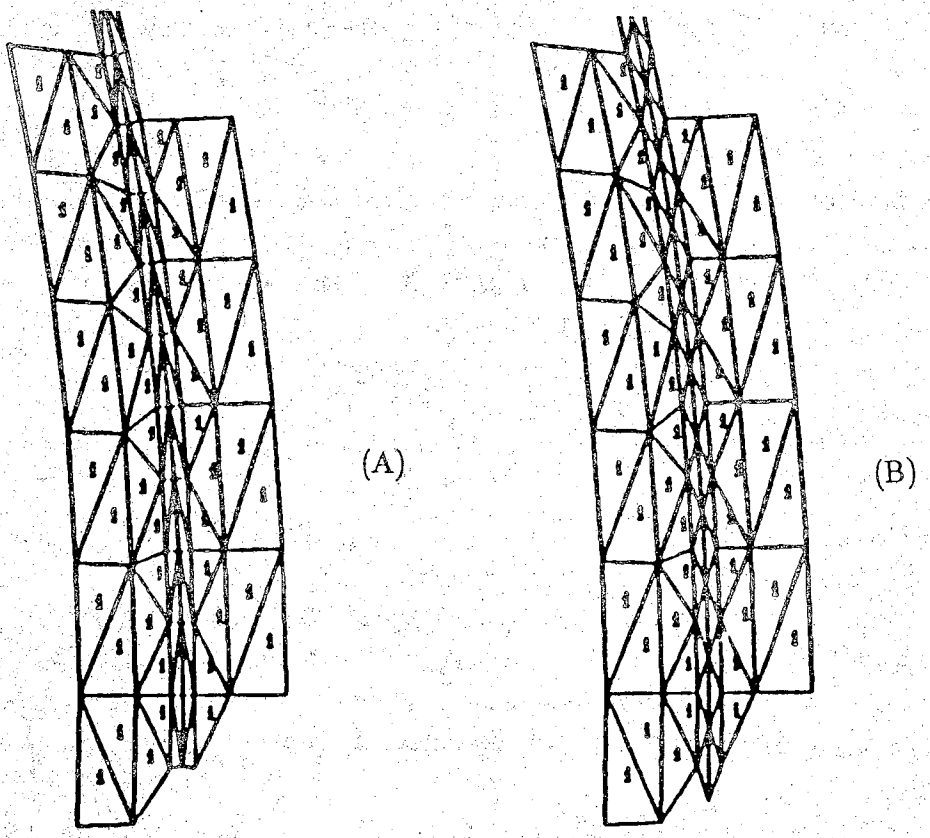

Figure 3.20. Mesh types in the airgap (A) mesh with high aspect ratio (B) mesh with low aspect ratio

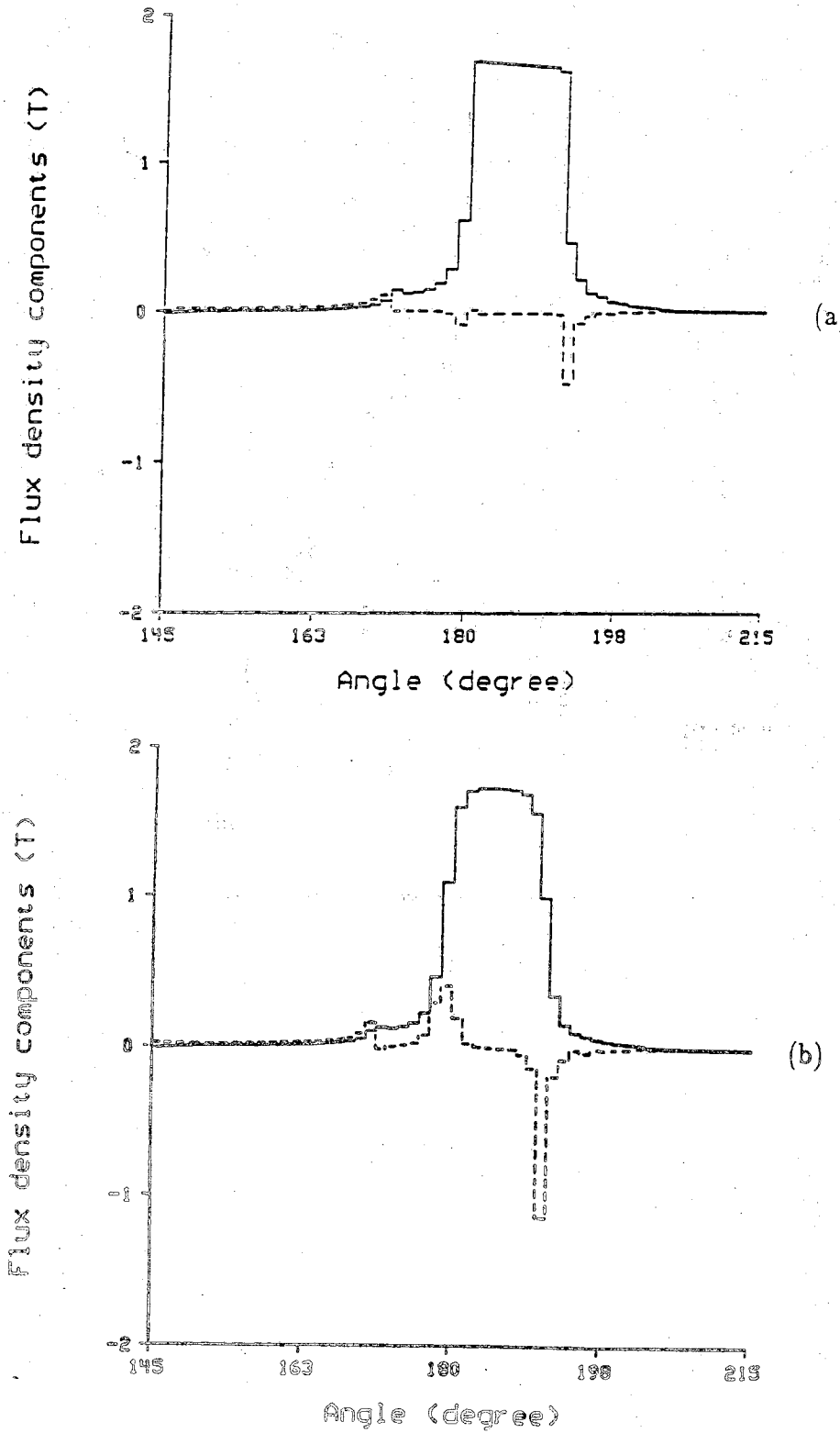

Figure 3.21. Flux density components (a) using mesh A (b) using mesh B

could account for the underestimation of the calculated torque when the mesh used has high aspect ratio elements.

When both the mesh shape and the stepping angle are properly chosen, the computed torque/angle characteristics from the Maxwell stress-tensor and the local virtual methods are smooth and almost indistinguishable. Figure 3.22 shows the measured and the computed torque/angle characteristics for an excitation of 10A. The agreement between the measured and the computed characteristics is good, considering the assumptions we have to made in the computation, especially those on the material model.

To show that the agreement between the computed and measured characteristics is just as good at a different excitation, Figs. 3.23 and 3.24 show similar sets of characteristics for excitation currents of 7.5A and 12.5A. The results in these figures show that when proper care is taken in selecting the shape of the elements and the stepping of the rotor, reasonable accuracy and smoothness of the computed torque/angle characteristic can be obtained with any of the methods.

The following results illustrate what could happen to the computed torque/angle characteristic when the shape of the elements has high aspect ratio and are circumferentially elongated, when the stepping of the rotor angle does not maintain the mesh uniformity, or when the number of layers of the mesh in the airgap is increased from the previous value of two to three and the elements have high aspect ratio. The results shown in Figs. 3.25, 3.26, and 3.27 are obtained from the global virtual work method, the Maxwell stress-tensor method, and the local virtual work method, respectively; all of them are for an excitation current of 10A. The solid curve was obtained with well-shaped triangular elements of the type shown in Fig. 3.19(b) and the uniformity of the mesh at the sliding layers was maintained while the rotor was being rotated through a pole pitch to generate the entire torque/angle characteristic. The dash curve was obtained with the same well-shaped triangular elements for the solid curve but with a rotor step size that did not preserve the uniformity of mesh in the distorted region. The curve with the triangular markers was obtained with not so well-shaped elements that have aspect ratio higher than 5. Merely adding more elements in the critical region without paying attention to their shapes and distribution does not bring about the best result with the Maxwell-stress and local virtual work methods, as illustrated here by the curves with square markers in Figs. 3.26 and 3.27, which were obtained with three instead of two layers of elements and about 50% more nodes in the airgap than those used to obtain the curves with the

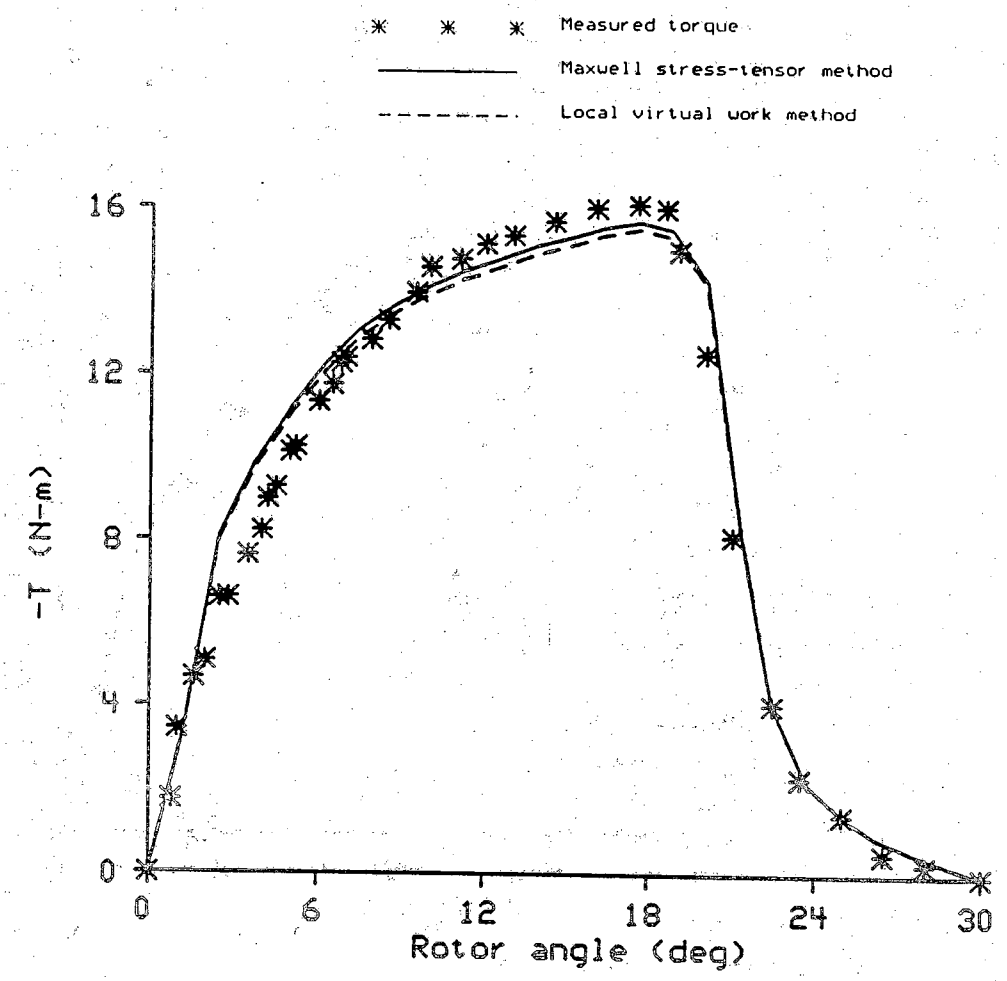

Figure 3.22 - Calculated torque vs. measured at I=10 A

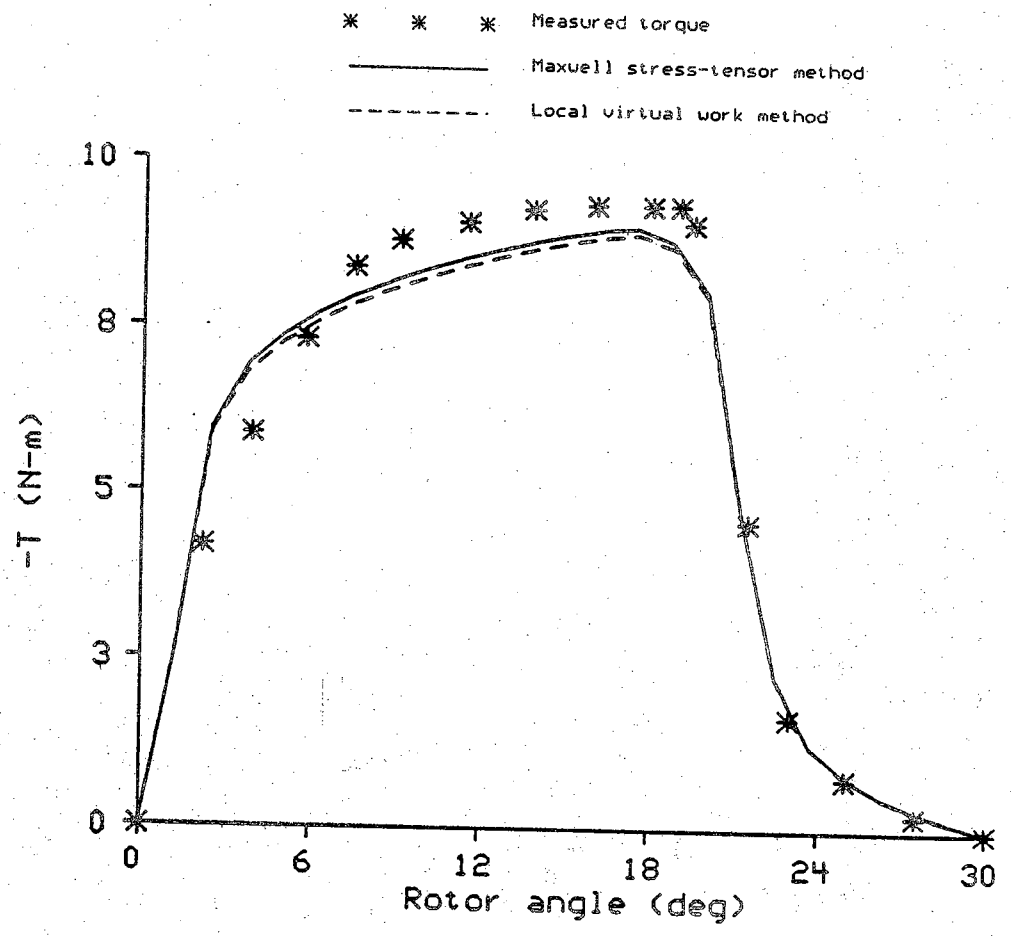

Figure 3.23 Calculated torque vs. measured at I=7.5 A

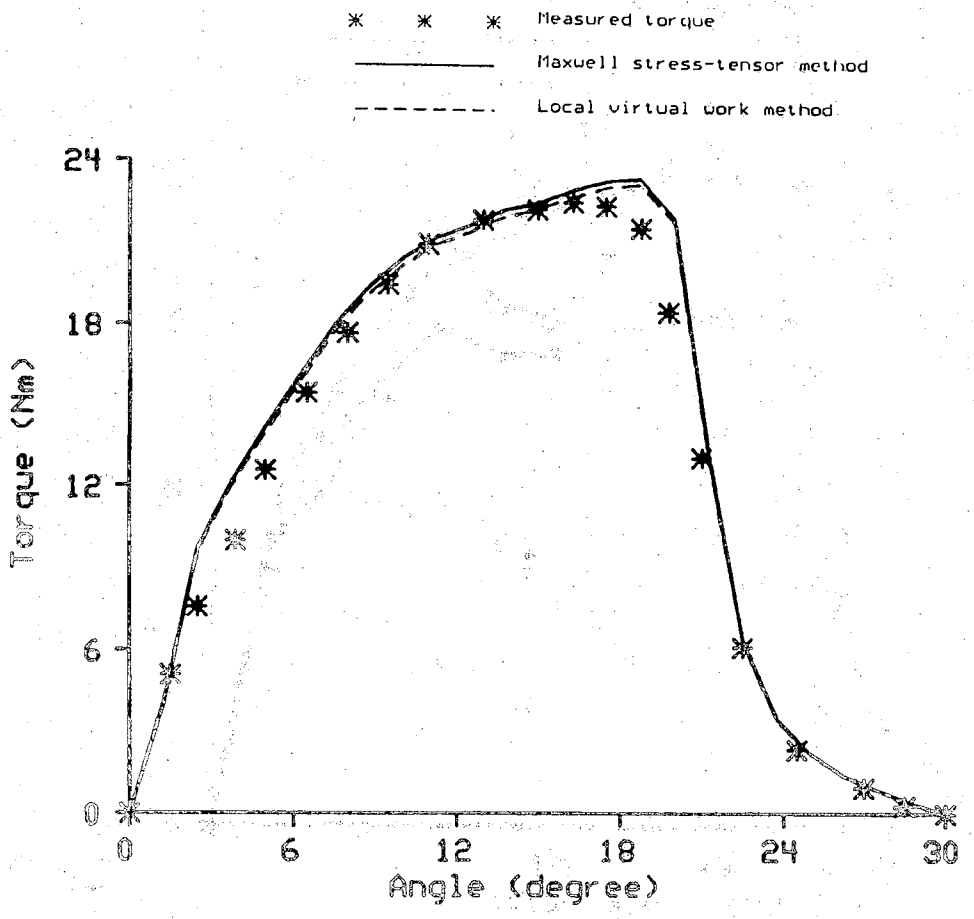

Figure 3.24 Calculated torque vs. measured at I=12.5 A

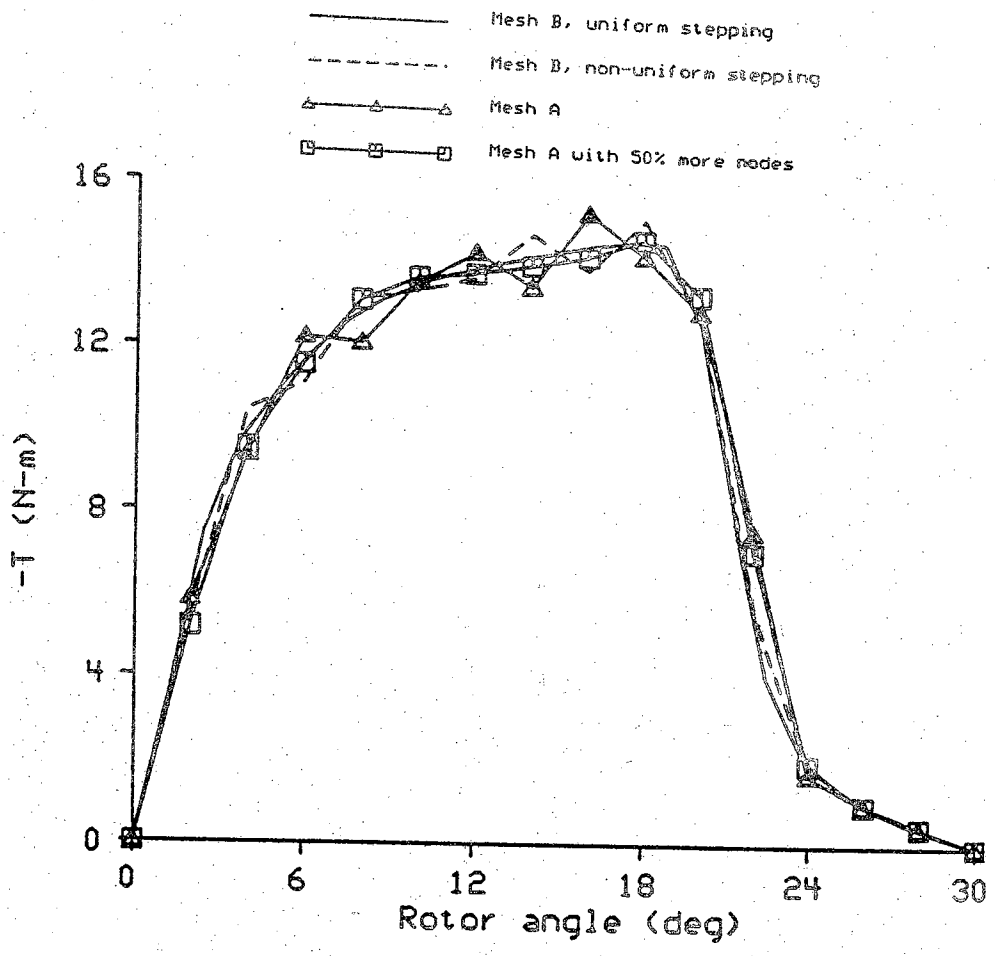

Figure 3.25 Torque/angle characteristics-global virtual work method

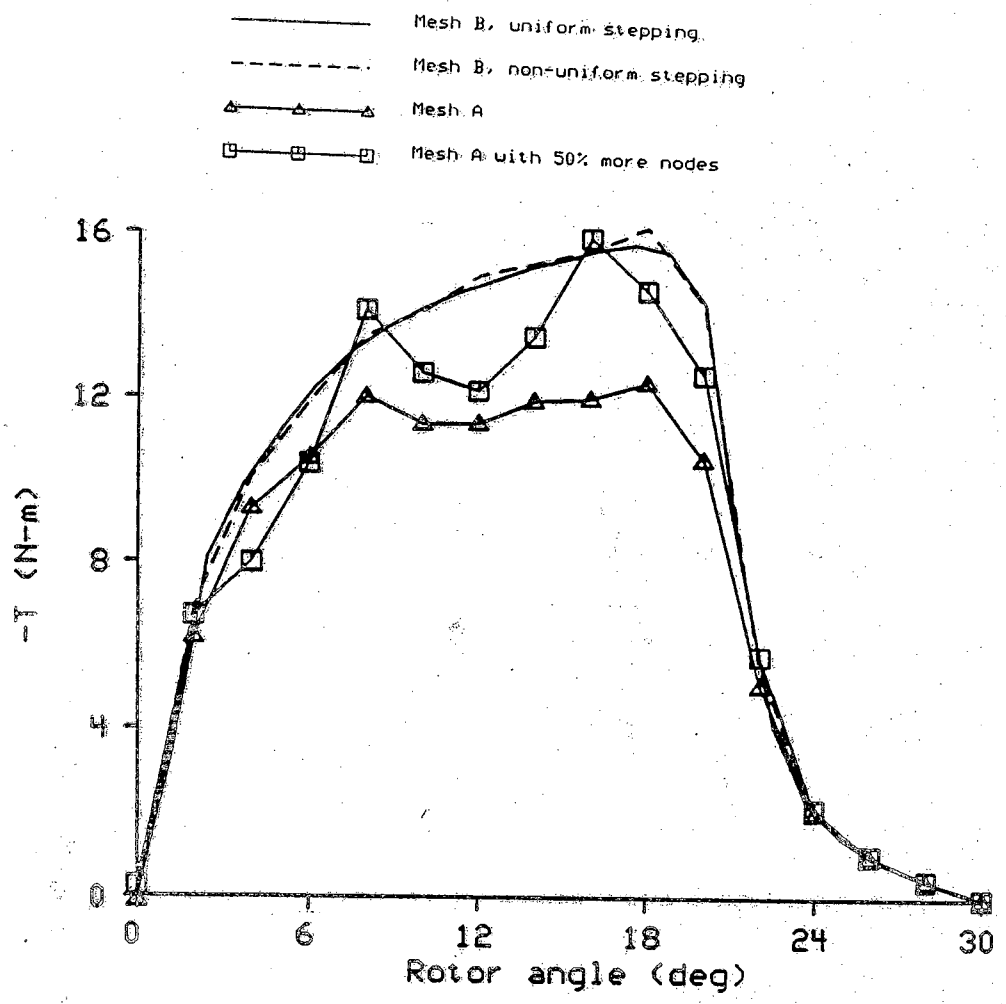

Figure 3.26 Torque/angle characteristics-local virtual work method

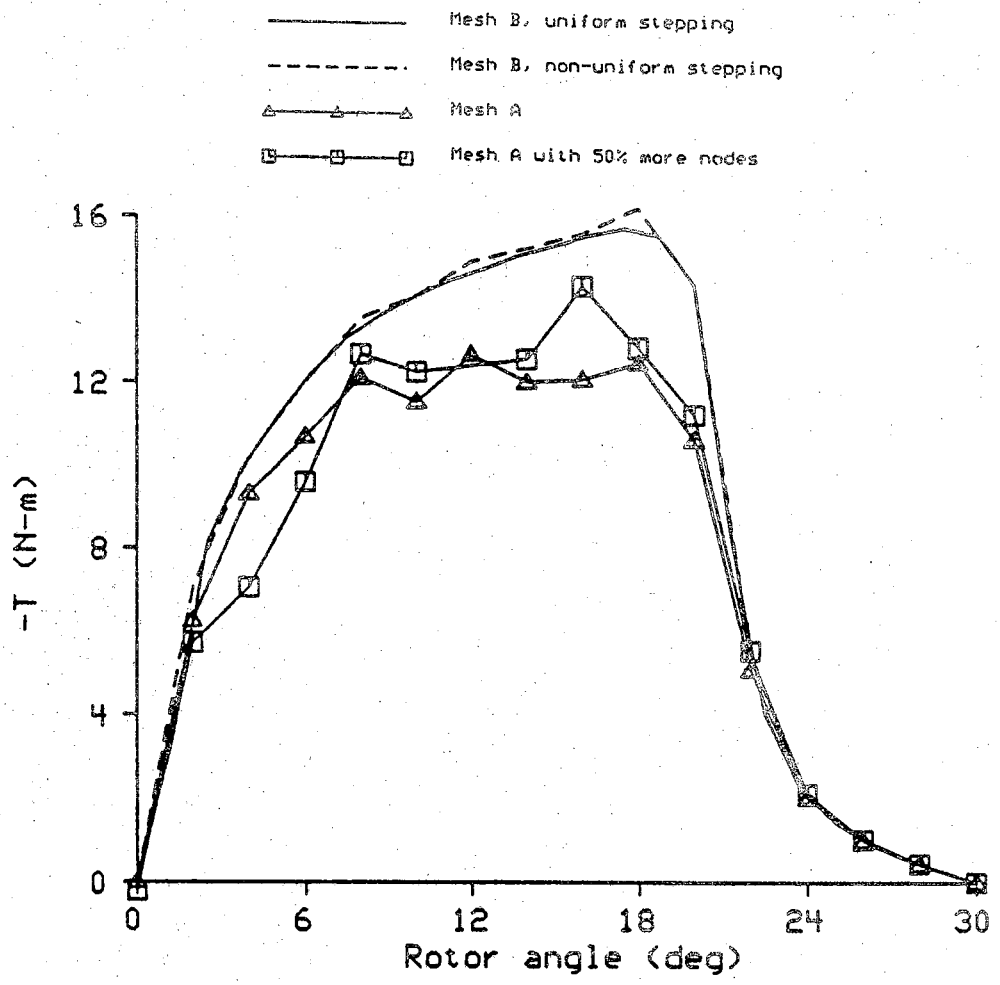

Figure 3.27 Torque/angle characteristics-Maxwell-stress tensor method

triangular markers.

In examining the computed results, we found that the tangential flux density component at a given position and operating condition with elongated elements was usually lower than the corresponding value with properly shaped elements. This may explain why, in the case of the Maxwell stress or local virtual work method, a mesh with poorly shaped elements, even with up to 50% more nodes in the critical areas, yields an erratic torque/angle characteristic that tended to lie below the actual characteristic. The discrepancy is large in the intermediate angles because errors in the computed flux density, especially the tangential component, at the departing pole tips are large, as mentioned earlier using the results presented in Figs. 3.21(a) and 3.21(b).

Thus, we can conclude that for machines like the SRM that have a narrow airgap with very high field gradient, special care must be taken to use elements with low aspect ratio if the errors in the computed torque are to be kept small. The errors will be small when the aspect ratio is small; if possible, the best result is obtained with equilateral triangular elements in the critical field region. The results show that with proper care in selecting the shape and distribution of the elements, all three methods of calculating torque, namely the global virtual work, the Maxwell stress-tensor, and the Coulomb virtual work methods, can provide reasonably accurate torque. Moreover, if the uniformity of the mesh is preserved while stepping through the rotor angles, a smooth and accurate torque/angle characteristic will be generated by any of the three methods used.

CHAPTER 4
STATIC CHARACTERISTICS AND PARAMETERS

This chapter describes the postprocessing procedures which are being used to compute the energy and coenergy, the flux linkage, the inductances, and the terminal speed voltage (emf). The accuracy of these results depend on the accuracy of the FE solution as well as the numerical procedure for the operation involved. Since the mesh arrangement technique described in Chapter 3 improves the local as well as the overall accuracy of the FE solution, it enhances the accuracy of the postprocessing results, too.

The format used is to present the procedure and results obtained for each quantity, one at a time; first the computational procedure that is compatible with the FE solution, and then the results. Results presented are for half of the phase inductance cycle of the test motor, that is 30 °; the results for the other half can be obtained by the rule of symmetry. The angular step size of the rotor rotation is taken to be 1.25 °, which for the mesh used will preserve its uniformity during the rotation. Since the intention is to use the static results later in a steady state simulation of the SRM drive, all the quantities are calculated for a wide range of excitation currents at one ampere intervals. Also a sensitivity analysis is presented, showing the effect on the machine parameters and characteristics due to changes in some of the design parameters.

4.1. Electromagnetic Energy

Both electromagnetic energy and coenergy are calculated during each iteration of FE solution procedure. Since the calculated energy and coenergy can also be used in the computation of other quantities such as the incremental inductances, the torque, and the flux linkage, the calculation of energy and coenergy should be done as accurately as possible.

The energy density in e^{th} element is given by

$$w_e = \int_0^{B_e} H_e dB_e \tag{4.1}$$

For the elements with linear material property (air and current carrying regions), (4.1) also yields the coenergy density of the element, and can be simplified to

$$w_e = w_e' = \frac{1}{2} \nu_0 B_e^2 \tag{4.2}$$

But for an element in the iron region, where the relation between field intensity and flux density is nonlinear, the integration in (4.1) will be carried out numerically.

Since the flux density is constant within each element when MVP is approximated by linear shape functions, the energy of each element can easily be obtained from the product of energy density and the volume of the element, that is

$$W_e = w_e \cdot V_e = w_e \cdot Z \Delta_e \tag{4.3}$$

The total energy of in the SRM is obtained by summing up the W_e over all its elements.

$$W_m = \sum_e W_e \tag{4.4}$$

In our implementation, the magnetic energy density for a range of field intensities on magnetization curve given in Fig. 2.6 is computed at fine intervals using the trapezoidal rule along with the Richardson extrapolation for integration in (4.1) to construct a table of values of energy density versus field intensity. In each iteration of the FE algorithm, the calculation of energy in all elements is done by a table search using the value of field intensity to access the corresponding energy density directly by a simple linear interpolation. In this manner the task of integrating the energy of all elements in iron is reduced to a search and linear interpolation procedure.

Once the energy density of one element is calculated, its coenergy density can be obtained from the relation,

$$w_e' = B_e H_e - w_e = \nu_e B_e^2 - w_e \tag{4.5}$$

Alternatively, the total coenergy of the device can be obtained from the following relationship, once the flux linkage and the total field energy are known.

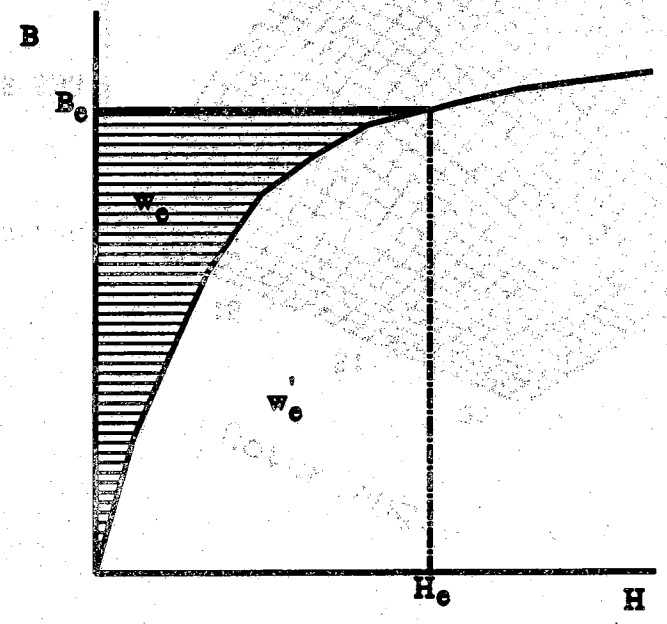

Figure 4.1. Energy and coenergy density in e^{th} element

$$W' = \lambda I - W \tag{4.6}$$

The energy and coenergy profiles of the test SRM calculated for different rotor positions and current levels are given in Fig. 4.2 and Fig. 4.3,respectively.

4.2. Flux Linkage

The total flux linked by each turn of the phase winding is given by the Gauss formula

$$\phi = \int_S B \cdot n \, ds \tag{4.6}$$

where S is the area enclosed by the winding turn. Replacing B by $\nabla \times A$ and using Stokes theorem, (4.6) becomes

$$\phi = \oint_\Gamma A \cdot d\ell \tag{4.7}$$

where the line integration is performed around the closed contour formed by the winding sides. Ignoring the contributions from the end zones, the vector potential is constant along the axial direction of machine, and (4.7) can be simplified to

$$\phi = Z(A_R - A_L) \tag{4.8}$$

where A_L and A_R are the values of the magnetic vector potential at right and left hand sides of the single turn (see Fig. 4.4).

For a thin multi-turn coil, (4.8) can be multiplied by the total number of turns in the coil to obtain the total flux linked by the coil. However, a thick multi-turn coil where the value of vector potential is changing through the winding cross-section should be regarded as a set of hypothetical small coils all having the same turn density. The number of turns in each hypothetical coil can be calculated from the product of turn density and the area of the coil's cross-section:

$$n_k = \frac{N}{S} \cdot S_k \tag{4.9}$$

where S is the cross-sectional area of the whole winding and S_k is the area of coil cross-section. The total flux linked by k^{th} hypothetical coil then can be calculated using

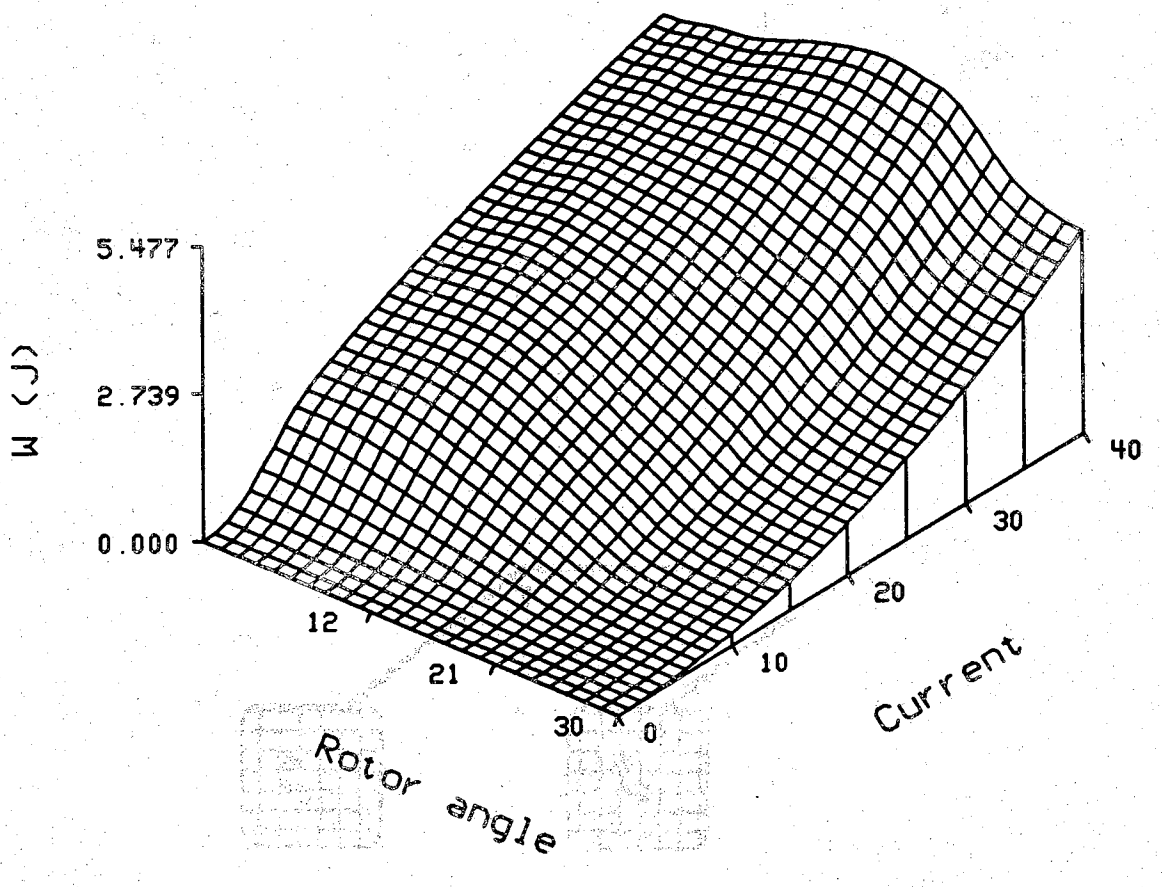

Figure 4.2. Energy profile

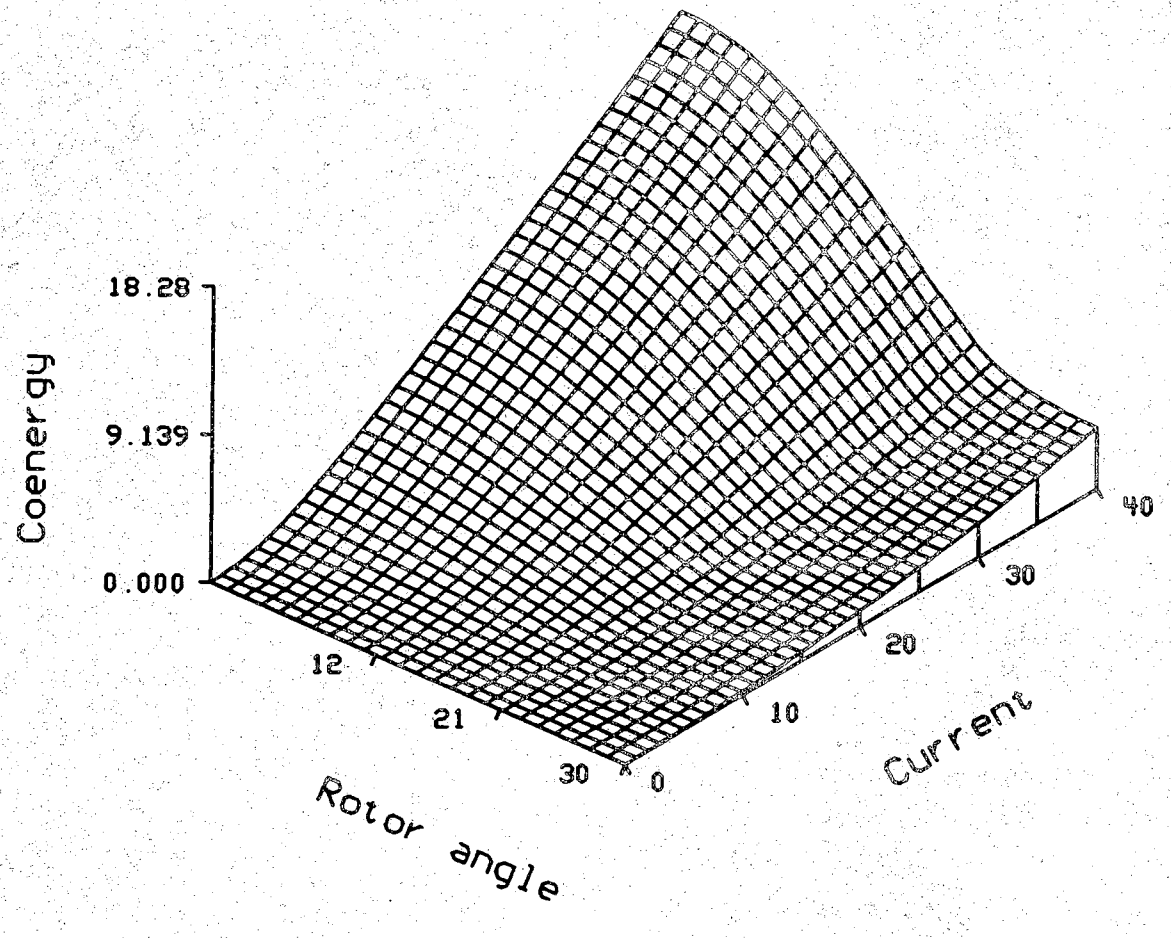

Figure 4.3. Coenergy profile

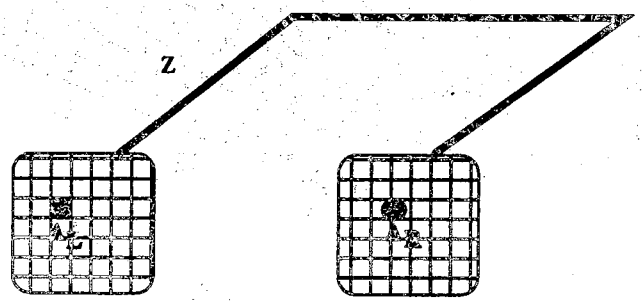

Figure 4.4. Flux linkage of a winding turn

$$\phi_k = n_k(A_{kR} - A_{kL}) \tag{4.10}$$

where A_k is the average value of the vector potential inside the coil's cross-section. The flux linkage of the phase winding is the summation of the flux linked by an entire set of hypothetical coils forming the phase winding,

$$\lambda = \sum_k \phi_k \tag{4.11}$$

The computational procedure for the flux linkage of the phase winding can be based on the discretization of the phase winding's cross-section into finite elements: First the turn-density for each winding cross-section is calculated, then the number of turns in each element inside the winding cross-section is obtained using (4.9). Next, the number of turns of each element is distributed equally to its nodes. Then the turn contribution from various elements sharing the same node will be added to give the number of turns of the hypothetical coil concentrated at each node.

In our implementation, the number of turns of the hypothetical coil at each node is stored in a vector $\overline{N}$, having the same size as the number of nodes in the FE domain. For nodes in the region occupied by a winding, the corresponding entry in $\overline{N}$ shows the turn contribution of that node and a sign to indicate the direction of current flow, The flux linkage of a phase winding is given by the inner product of the vectors $\overline{N}$ and $\overline{A}$, where $\overline{A}$ contains the vector potential at the nodes.

$$\lambda = \overline{N} \cdot \overline{A} \tag{4.12}$$

Computer implementation of expression (4.12) can efficiently calculate the flux linked by each of the stator phase windings. The profile of the flux linkage for one phase of the test SRM for different rotor positions and current levels is shown in Fig. 4.5.

4.3. Inductances

The winding inductance is one of the most important parameters that has considerable impact on the operation and, of course, a key parameter in the simulation of the SRM drive. When dealing with a nonlinear magnetic circuit, the following definitions are common for inductance:

1) Apparent inductance $\quad L \triangleq \frac{\lambda}{i}$ (4.13)

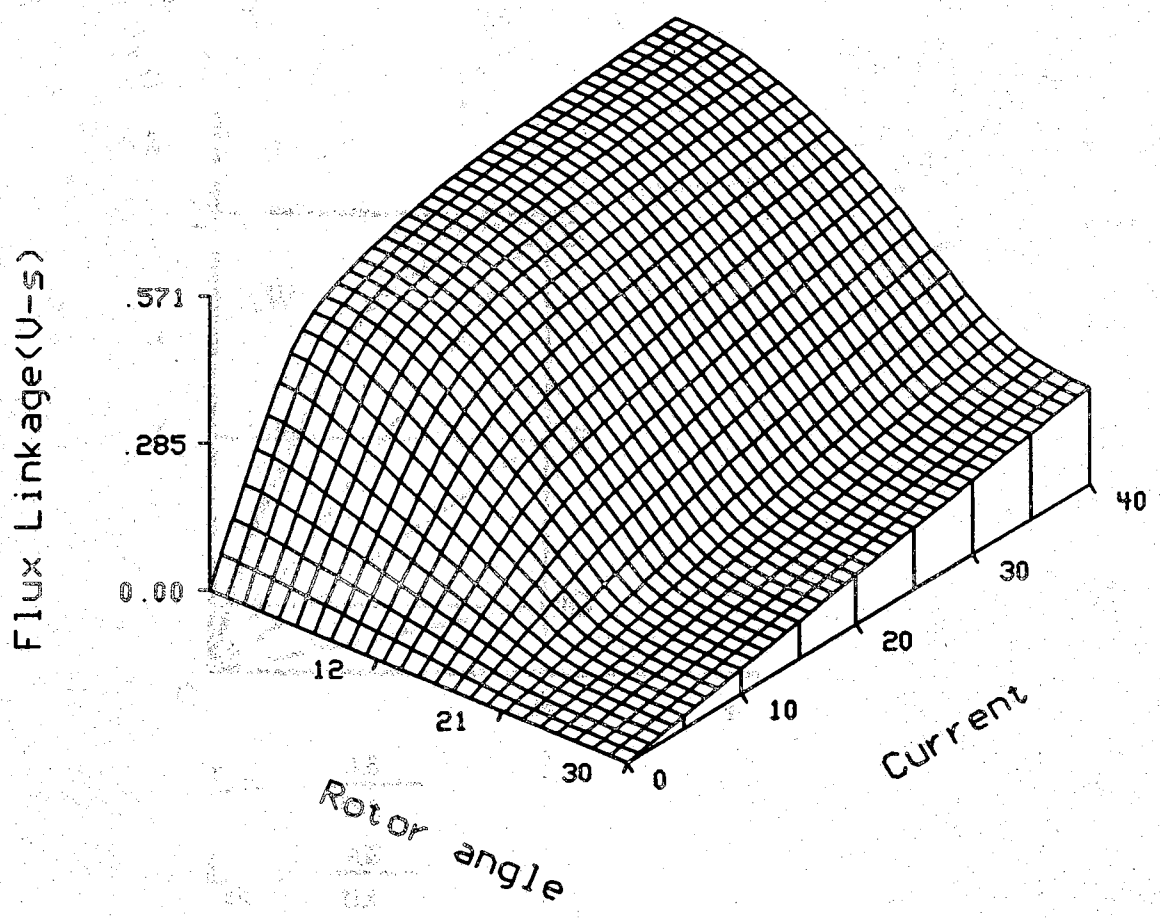

Figure 4.5. Flux linkage profile

2) Incremental inductance $\quad L_{inc} \triangleq \dfrac{\partial \lambda}{\partial i}$ (4.14)

3) Effective inductance $\quad L_{eff} \triangleq \dfrac{2W}{i^2}$ (4.15)

Figure 4.6 shows the graphic interpretation of these three definitions. For the linear magnetic circuits, all three definitions yield the same value for inductance, however, for saturated magnetic circuit the relation between three inductances is given as

$$L > L_{eff} > L_{inc} \tag{4.16}$$

Since the apparent and incremental inductances will be used in the simulation of the SRM drive, only these are calculated. The apparent inductance can be obtained from its definition given by (4.13). The incremental inductance can be calculated using either flux linkage or energy perturbation method. In the flux linkage method, the incremental inductance is computed from the change of flux linkage to a small change in the excitation current at the same rotor position.

$$L_{inc} = \frac{\Delta \lambda}{\Delta i} \tag{4.17}$$

In the energy perturbation method [91], the incremental inductance at a given rotor position is calculated using the following expression:

$$L_{inc} = \frac{[W(i+\Delta i) - 2\,W(i) + W(i-\Delta i)]}{(\Delta i)^2} \tag{4.18}$$

where Δi is a small change in the current. The profiles of the apparent and the incremental inductance of the test SRM are shown in Figs. 4.7 and 4.8, respectively.

4.4. Terminal Speed Voltage(emf)

The speed voltage or voltage induced in the phase winding by the motion of the rotor is another parameter required in the simulation of the SRM drive. For a winding with constant excitation current, the speed voltage can be calculated using Faraday's Law, that is

$$e = \frac{d\lambda}{dt} = \frac{\partial \lambda}{\partial \theta}\,\frac{d\theta}{dt} = \omega\,\frac{\partial \lambda}{\partial \theta} \tag{4.18}$$

To calculate the speed voltage, one needs to calculate $\dfrac{\partial \lambda}{\partial \theta}$, which will be

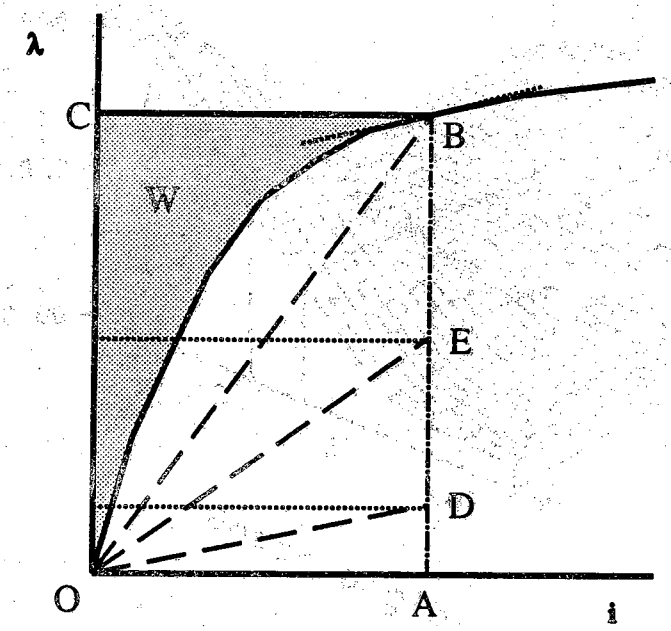

$$L = \frac{AB}{OA}$$

$$L_{eff} = \frac{AE}{OA}$$

$$L_{inc} = \frac{AD}{OA}$$

Figure 4.6. Inductances of a saturated circuits

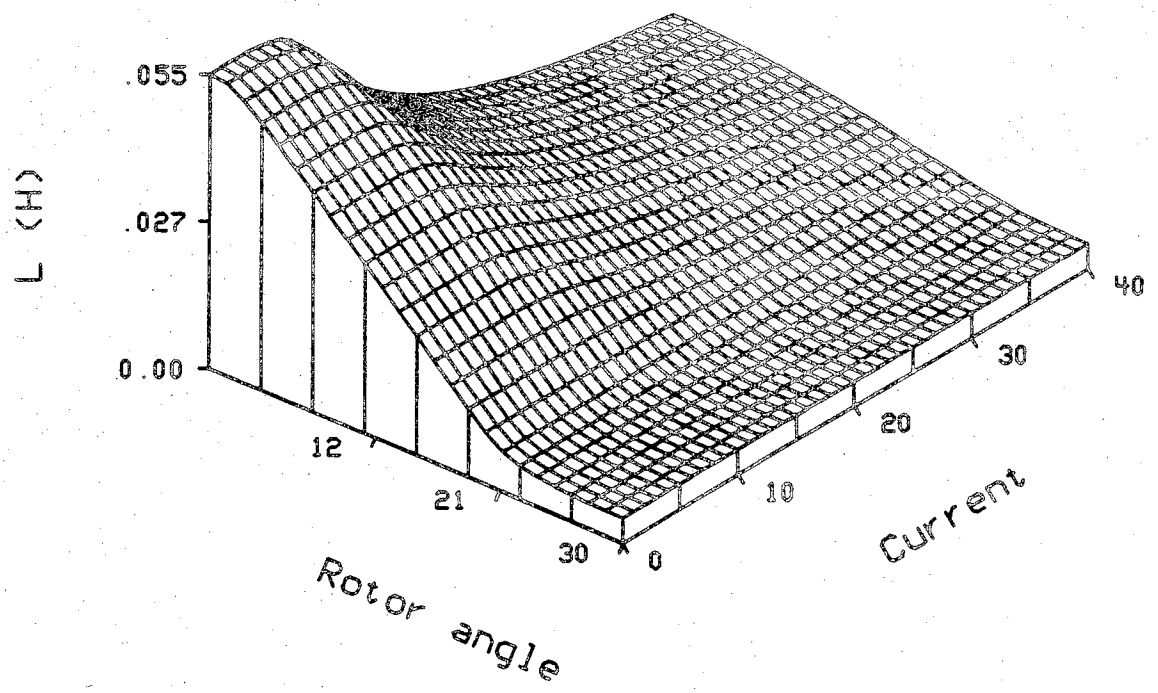

Figure 4.7. Apparent inductance profile

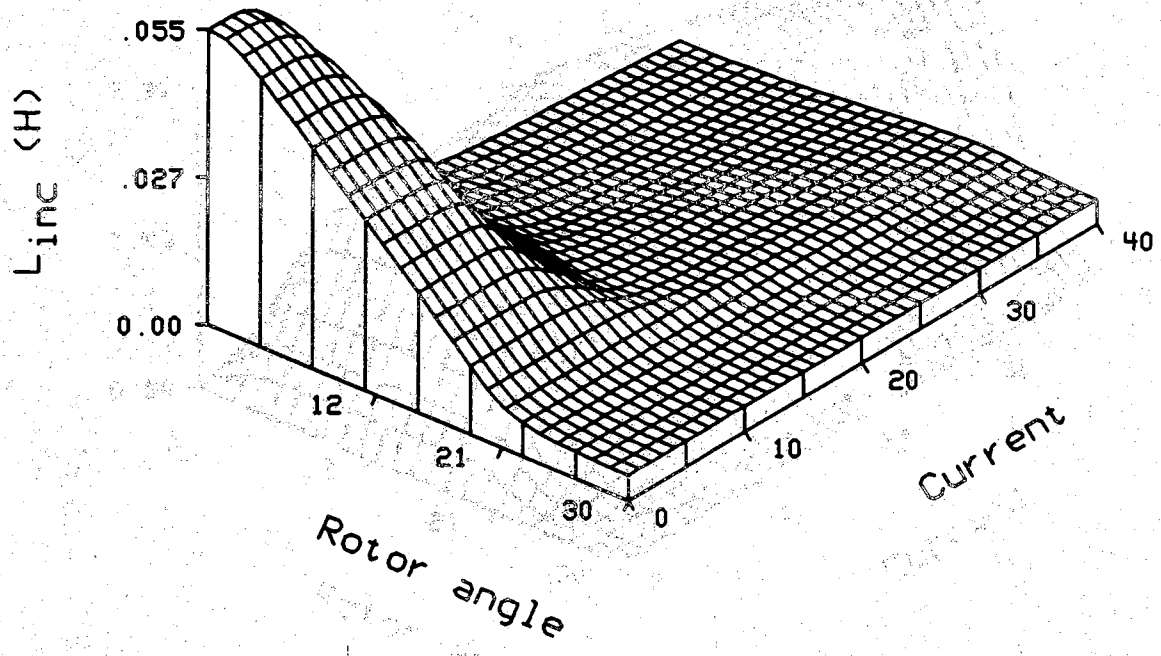

Figure 4.8. Incremental inductance profile

referred to as C_{ω}. We experimented with two methods for calculating C_{ω}. First, a rotor angle perturbation method used the change in flux linkage for small perturbation of rotor position with $C_{\omega} = \frac{\Delta\lambda}{\Delta\theta}$. The second method, which resulted in smoother profiles for C_{ω}, is based on differentiating (4.12), that is

$$C_{\omega} = \frac{\partial\lambda}{\partial\theta} = \bar{N} \cdot \frac{\partial\bar{A}}{\partial\theta} \tag{4.19}$$

The profile of C_{ω} of the test SRM for different rotor angles and current levels is shown in Fig. 4.9.

4.5. Sensitivity Analysis

In this part, a sensitivity analysis showing the effect on the machine parameters and torque characteristic of the test SRM due to the changes in design parameters such as the airgap length, the rotor pole arc, and the magnetization characteristic of the iron is presented. This analysis is not a thorough optimization or refinement study for a special application; it is included here to demonstrate the capability of the developed model for such purposes.

Figure 4.10 shows the effect of a $\pm$ 10% change in the length of airgap of the machine. The dashed curves clearly show the predictable change in torque characteristic of SRM as airgap length changes.

Next, we experimented with two different rotor arcs: one with the rotor pole arc about the same width of the stator pole arc, and the other one with a 10% wider rotor pole than the real one. Figures 4.11 and 4.12 show the changes in inductance and torque characteristics resulting from the perturbations of rotor pole arc. The inductance/angle profile of Fig. 4.11 shows that there is no noticeable change in minimum inductance, but the flat region at the maximum inductance will be wider as the width pole arc increases, which is also predictable. The torque/angle profile of Fig.4.12 shows a shift in the torque characteristics which is proportional to the change in the pole arc, but the higher maximum, which was not predicted before, needs further study.

When the saturation level(B_s) is varied by $\pm$10% about the nominal value (see Fig. 4.13), its effects on the flux/angle and torque/angle characteristics of Figs. 4.14 and 4.15 are not noticeable at small currents. A plausible explanation to this observation is that only a small region of the iron

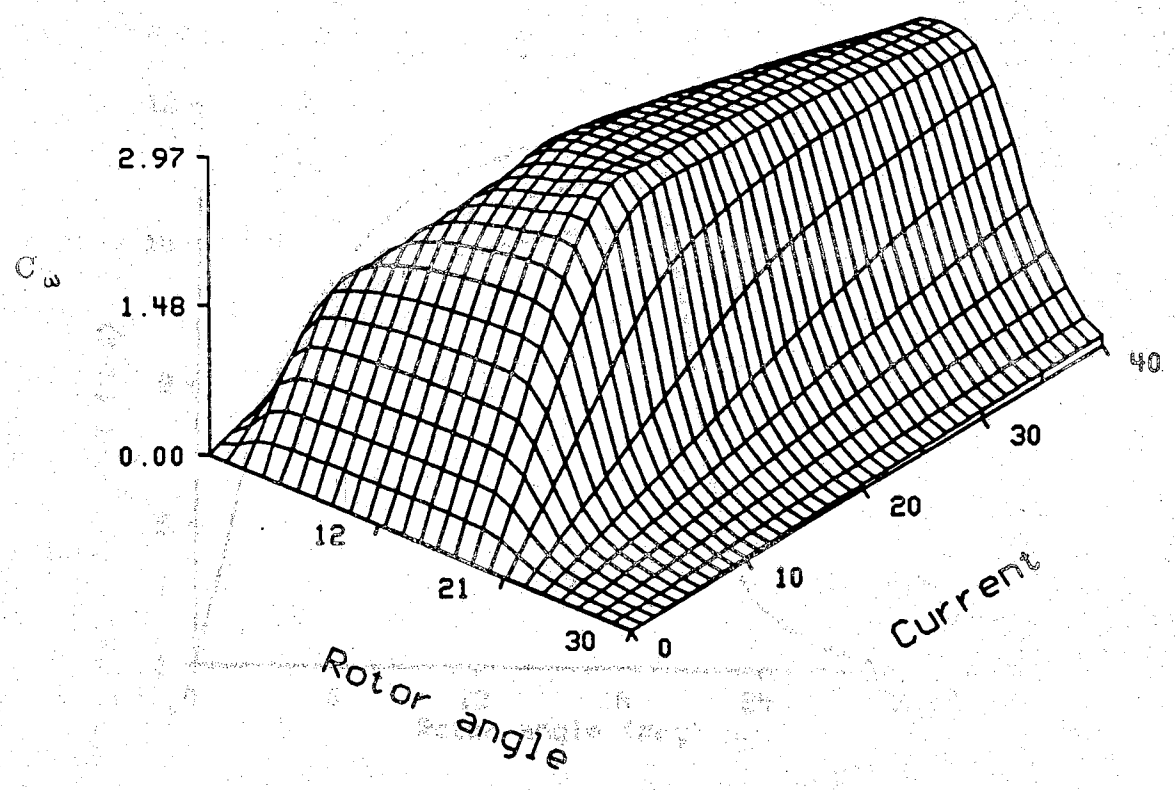

Figure 4.9. C_ω profile

is saturated. Such a change in B_s is academic in nature, in that there is no physical material that will provide such B-H characteristic. But the exercise is useful in that it provides us with an indication of how such a change would affect the performance of SRM.

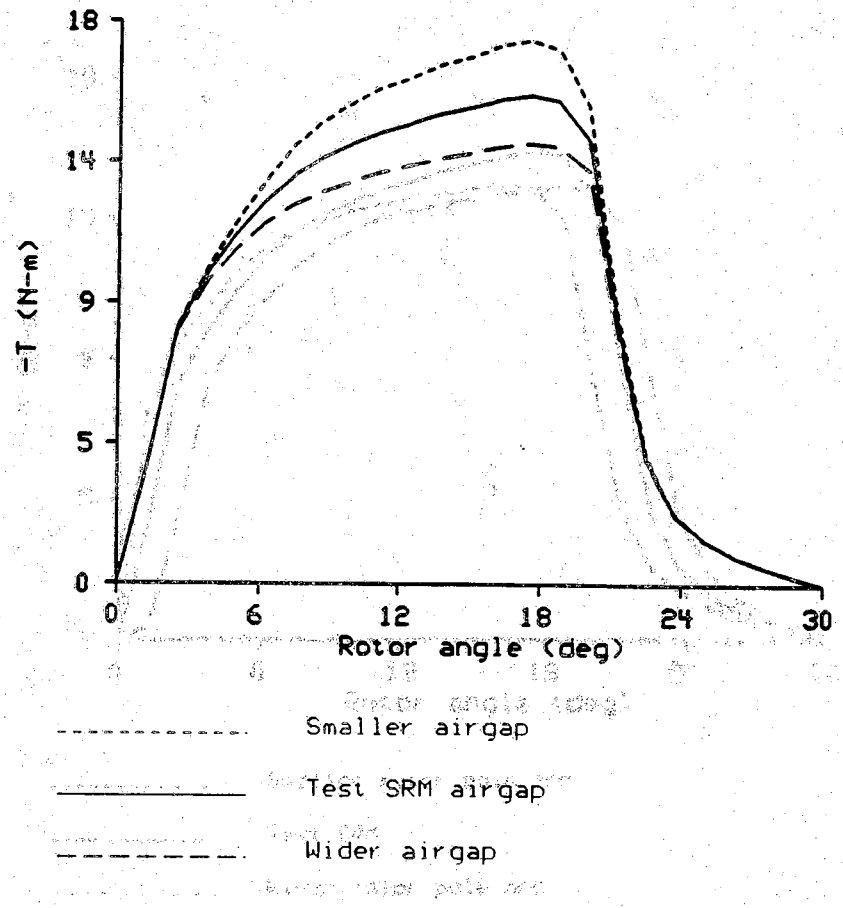

Figure 4.10 Effect of change in airgap length

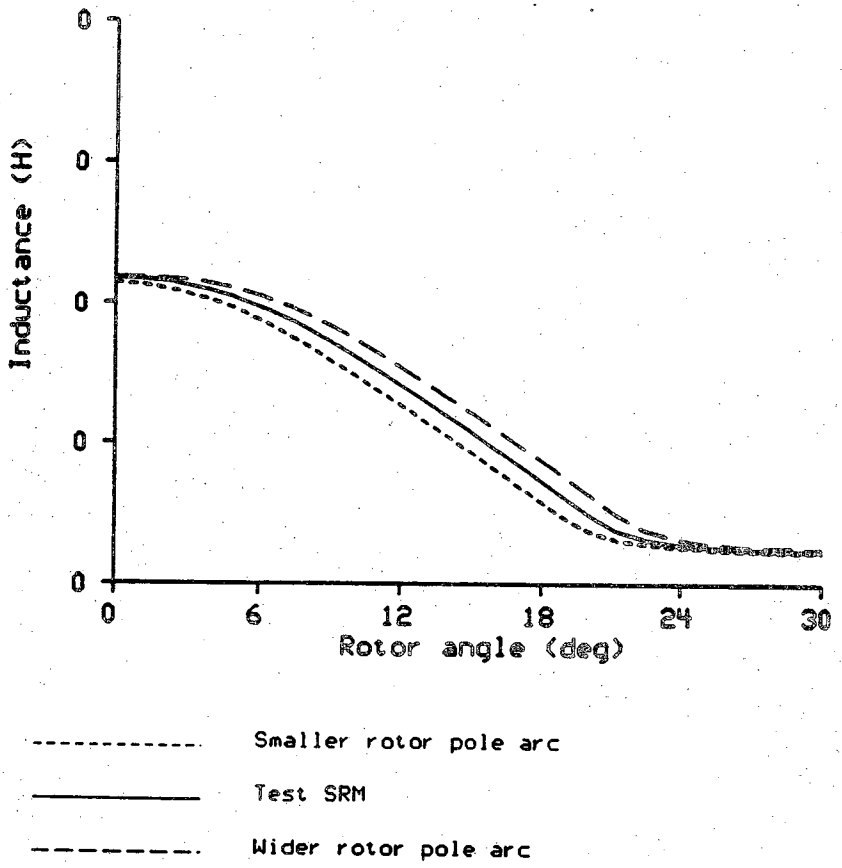

Figure 4.11. Inductance profiles for the change in rotor pole arc

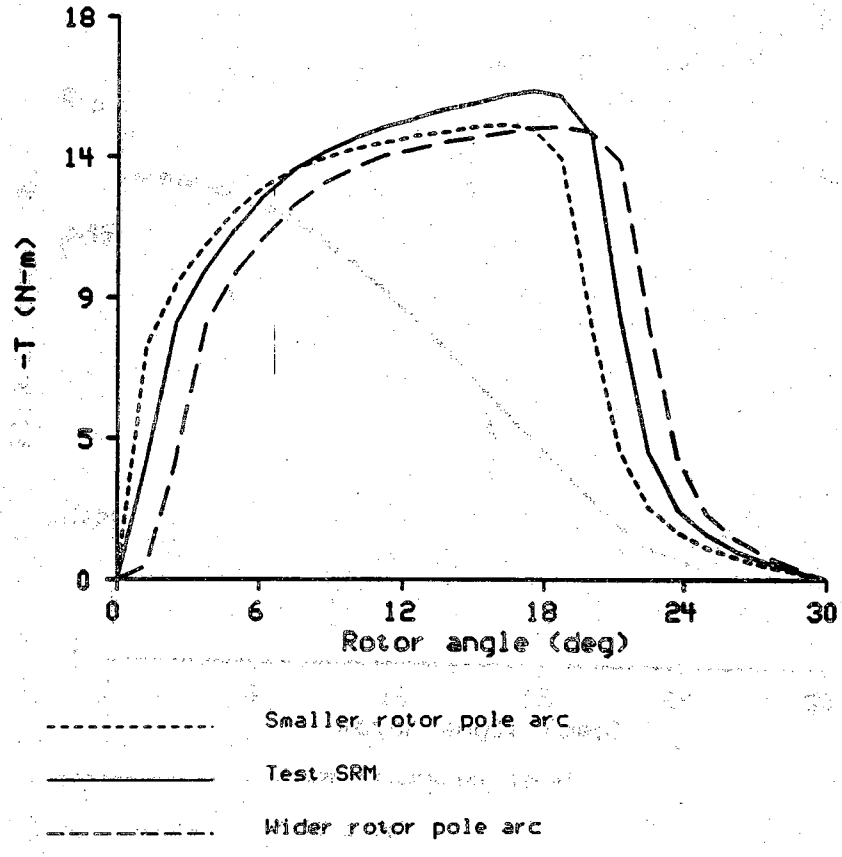

Figure 4.12. Torque/angle characteristics for the change in rotor pole arc

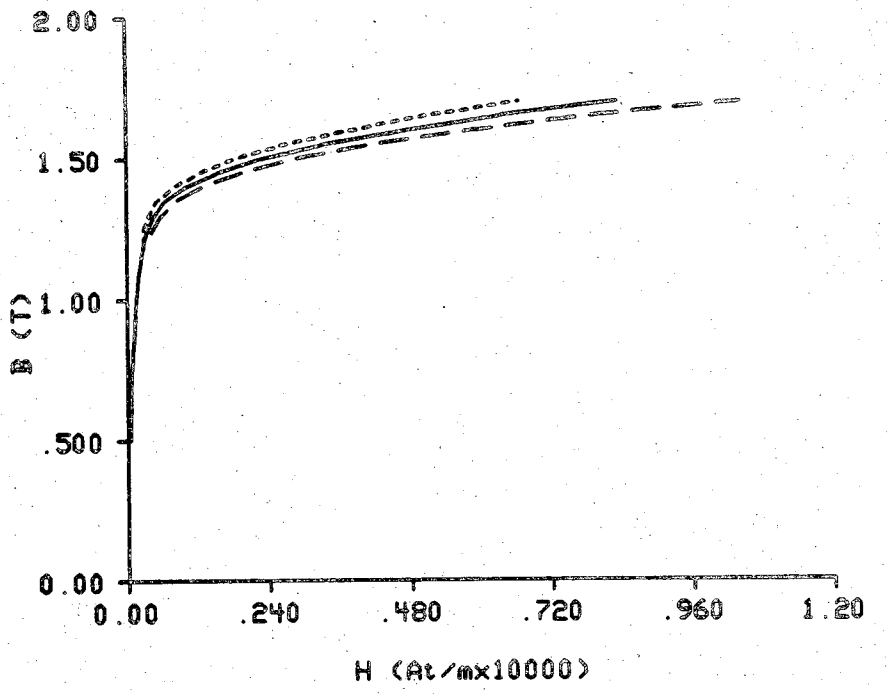

Figure 4.13. Change in B-H curve

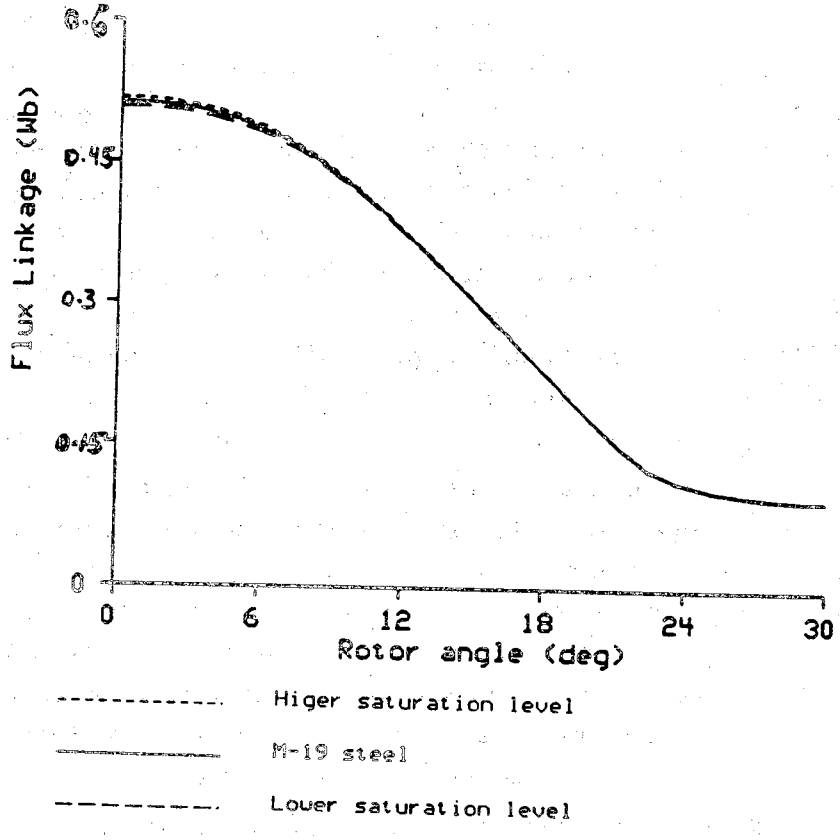

Figure 4.14. Change in flux/angle characteristics for saturation level change

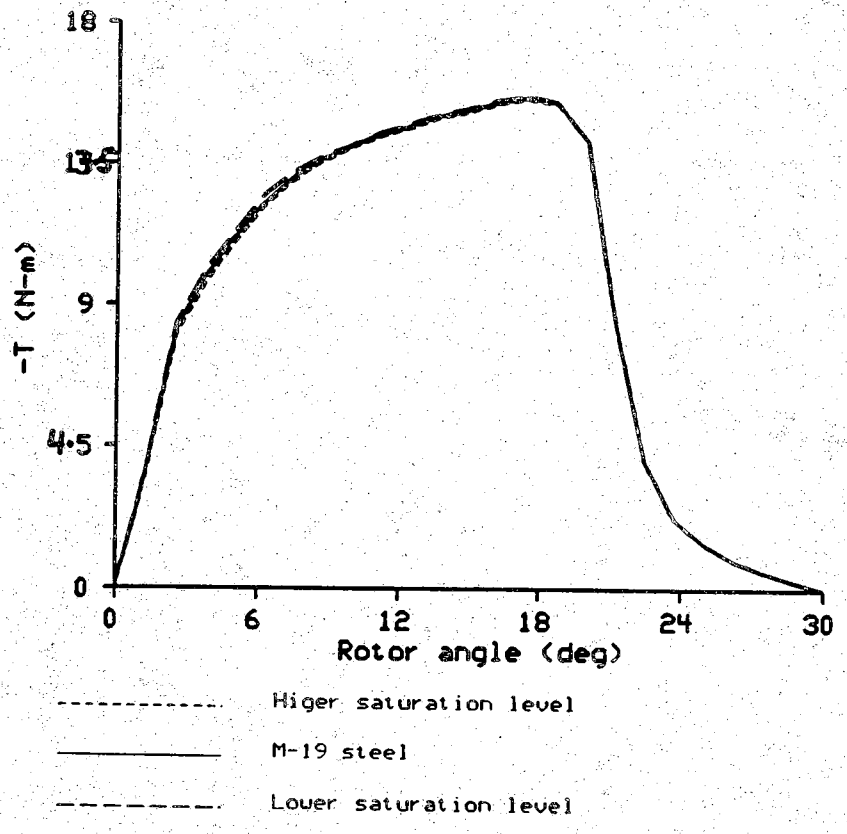

Figure 4.15. Change in torque/angle characteristics for saturation level change

CHAPTER 5
STEADY-STATE PERFORMANCE OF SRM DRIVE

A study of the SRM drive performance is complicated because of the large number of parameters involved. Close relationships between motor design and switching circuit on the one hand and dependency of machine parameters on current and rotor position on the other are the hurdles in any study aimed at the accuratly predicting the SRM drive performance. Evaluation of new designs or improvements from new control strategies requires a realistic model of the system. Such a realistic model should be able to predict drive performance over a wide range of torque/speed variations with sufficient accuracy. Obviously, an understanding of the SRM parameters and their relationships to the control and converter operation is a prerequisite in devising a realistic model.

Simplified models based on linear or idealized nonlinear approximation cannot predict the performance of the SR drive properly because of the high degree of nonlinearity involved. Therefore, a realistic model for the SRM drive should include the nonlinearities. In this chapter, steady-state performance of SRM drive based on parameters and static characteristics obtained from the FE field solution using special postprocessing techniques is simulated. The simulated result shows good agreement with test results, even though the exact data and control strategies of the test drive were not available.

To set the stage for steady-state simulation of the SR drive, it is necessary to examine the relationship between the SRM parameters and control strategies using a simplified model based on idealized magnetic characteristics. First the control strategy for successful operation of SRM in relation to its parameters is discussed. This will be followed by a description of switching strategies for both low speed and high speed modes of operation. The mathematical model and simulation techniques are discussed next, and finally, simulation and experimental results are presented.

5.1 Control strategy

As discussed earlier, both energy conversion and torque production in the SRM rely on the variation of the phase inductance as a pair of rotor poles move in and out of alignment with the stator poles of an excited phase. As the rotor moves, the inductance of each phase undergoes a cyclic variation with a angular period given by

$$\theta_{cy} = \frac{360}{N_r} \tag{5.1}$$

A current pulse is applied to the phase during each cyclic variation of inductance. The shape and timing of the current pulse varies with speed and load torque.

To maximize the energy conversion capability of the SR motor, it is designed to operate under highly saturated conditions. For example, at base speed the energy conversion loops with idealized (piecewise linear) and real (nonlinear) magnetic characteristics for one current pulse are shown in Fig. 5.1. In this figure, the polygon OABC is the ideal energy conversion loop and OMBNO is the real one. For optimal energy conversion, most of the field energy should be converted to mechanical energy, in other words the energy return to the electrical circuit should be minimized (OCD in Fig. 5.1). To achieve a real energy conversion loop close to that of the ideal loop, a control strategy based on the following steps should be adopted: bring the current to its maximum during minimum inductance region (OA), maintain the current constant while flux linkage continues to build up to the saturation value λ_s (AB), commutate the current before the peak region of inductance waveform is reached in order to bring the current down as fast as possible, before the negative torque region where the drop in flux linkage is small (BC). To keep the negative torque component small, minimize the tail current in the CO region where $\frac{\partial L}{\partial \theta} < 0$. Such a flat-topped phase current pulse corresponding to the energy conversion loop of Fig. 5.1 is shown in Fig. 5.2. The points O, A, B, and C correspond to the same points in Fig. 5.1.

The current pulse shown in Fig. 5.2 is obtainable around the base speed of the SRM but not at all rotor speeds and load torques. In practice, with a fixed supply voltage, the shape of the current pulse depends on the speed and load torque. At low speed, the rate of current rise is high because of the small back-emf. Peak current should be limited by chopping. But at high speed, the back-emf becomes dominant; as a result the current peaks before commutation. Usually the base speed is defined as the speed at which the

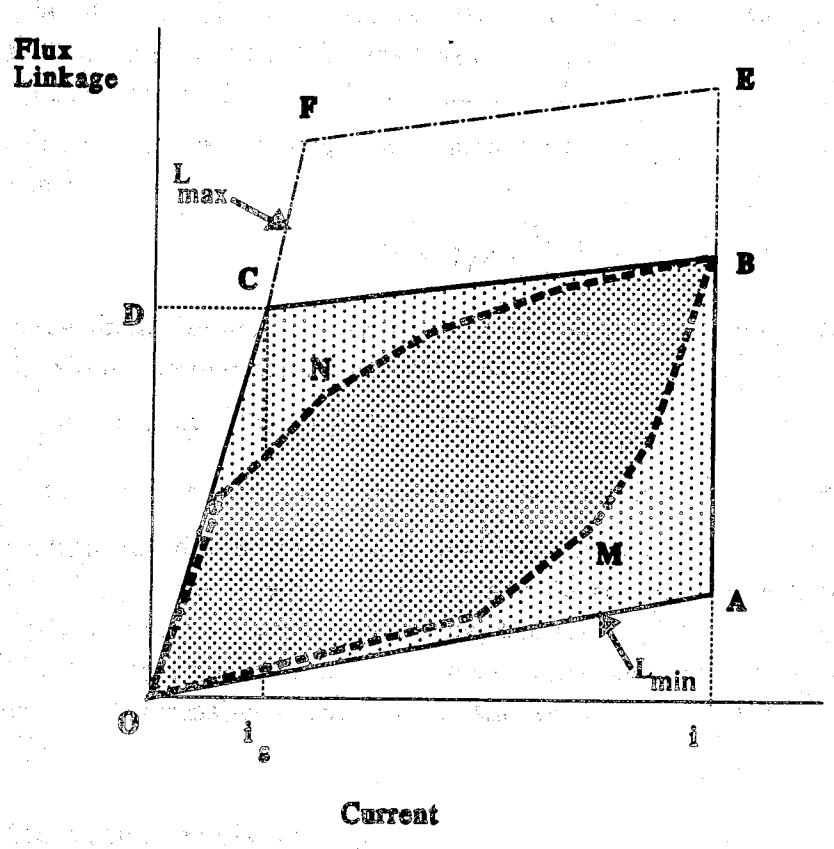

Figure 5.1. Energy conversion loops

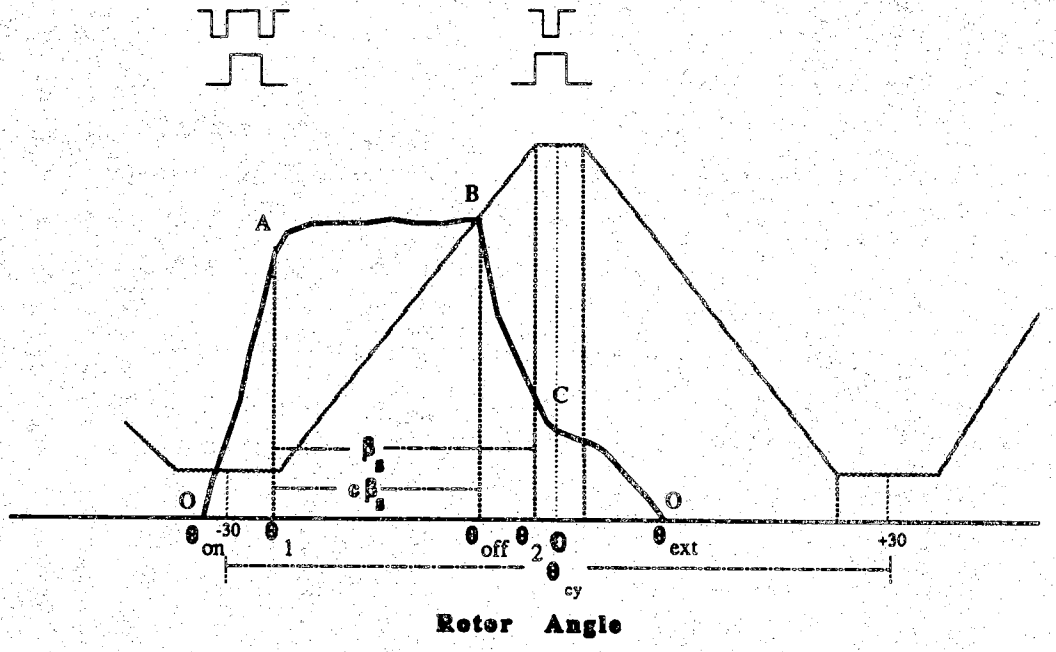

Figure 5.2. Typical flat-top current pulse

back-emf is equal to supply voltage. Typical shapes of the current pulse for an SRM drive at different speeds are shown in Fig. 5.3. When the SRM is to be operated as a variable speed drive, two switching strategies are used: one for low speed operation in which the current level has to be limited by chopping, and the other for high speed operation, in which both the ignition and the conduction angles should be controlled properly in order for the torque to satisfy the load condition and to be as smooth as possible.

The expression for torque at constant current and linear magnetic circuit is given by

$$T = 1/2 \frac{\partial L}{\partial \theta} i^2 \tag{5.2}$$

With the linear inductance waveform given in Fig. 1.2 and constant current, the developed torque has a polarity that changes with the slope of inductance waveform: positive for $\frac{\partial L}{\partial \theta} > 0$, zero when $\frac{\partial L}{\partial \theta} = 0$, and negative when $\frac{\partial L}{\partial \theta} < 0$. However, in a saturated magnetic circuit, torque-current relation is more complicated and the static torque has a rounded shape shown in Fig. 5.4. Nevertheless, in both cases the region with increasing inductance is the active torque- producing region for motoring, the regions near the totally unaligned and the totally aligned position are dead zones for torque production, and the region with decreasing inductance is the active torque- producing region for generation.

5.2 Simplified Analysis

The simplified analysis given here can be used to explain the control strategies adopted and to estimate the voltampere requirement of the drive converter. The assumptions in this analysis are: winding resistances are neglected, the supply voltage is constant, current is flat topped over the region of increasing inductance, and the width of the active torque region is equal to stator pole arc, β_s. This analysis also uses the idealized nonlinear energy conversion loop given in Fig. 5.1 and the corresponding current waveform of Fig. 5.2. The following definitions based on machine parameters are helpful in the algebraic manipulation that follows:

$$\kappa = \frac{L_{max}}{L_{min}} \tag{5.3}$$

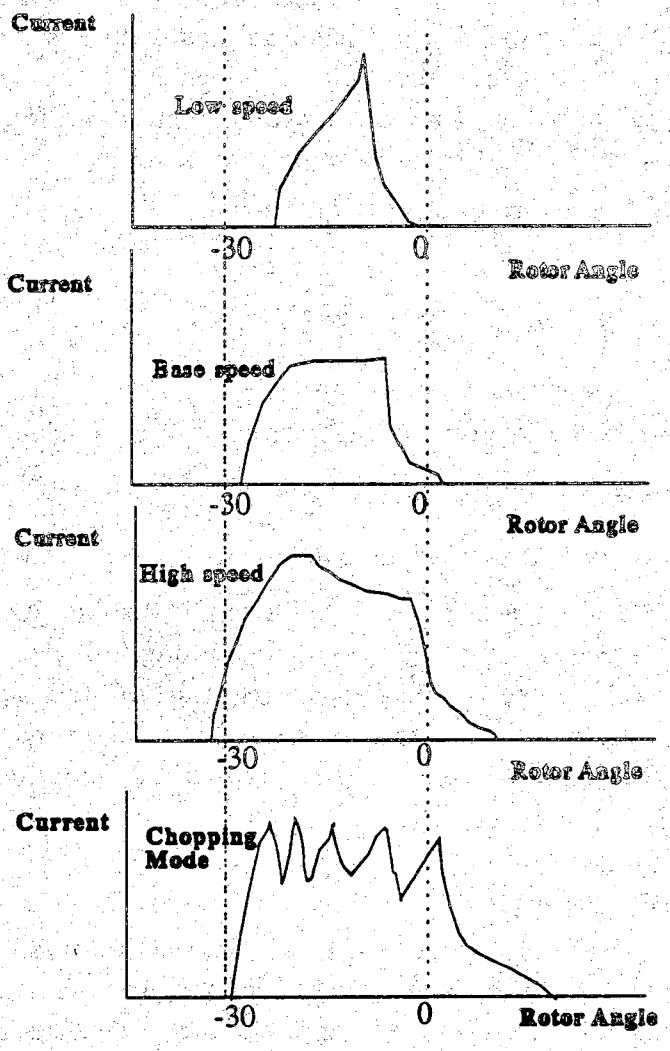

Figure 5.3. Typical current pulse shape at different speeds

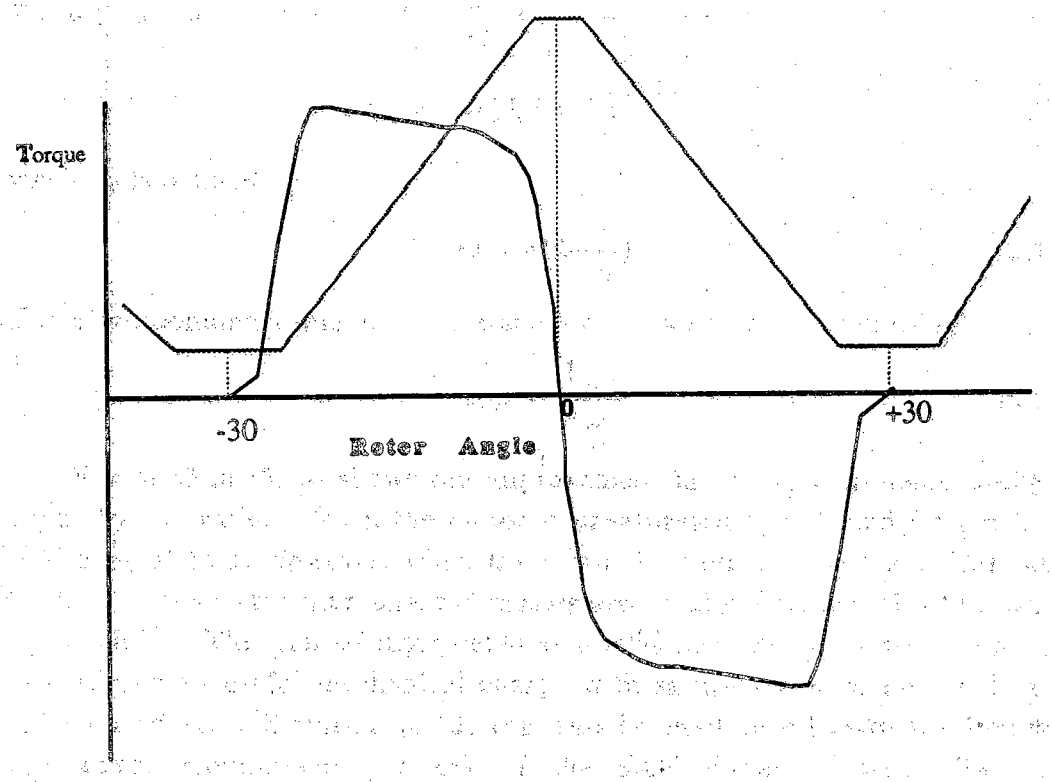

Figure 5.4. Typical static torque/angle characteristic of SRM

$$\eta = \frac{L_a^s}{L_{max}} \tag{5.4}$$

where L_a^s is the saturated inductance of the machine when the rotor and stator poles are aligned; it is a function of excitation current. It is clear that $\kappa > 1$ and $\eta < 1$.

With the voltage drop in the winding resistance neglected and speed assumed to be constant, the phase voltage equation can be written as

$$V = \frac{d\lambda}{dt} = \frac{\omega \Delta\lambda}{\Delta\theta} \tag{5.5}$$

With a conduction angle of, $c\beta_s$, where $c \leq 1$ and λ_s is the flux linkage corresponding to the full conduction angle β_s, the energy converted during each current pulse can be estimated as follows. Substituting for $\Delta\lambda = c\lambda_s$ and $\Delta\theta = c\beta_s$ into (5.5),

$$\lambda_s = \frac{V\beta_s}{\omega} \tag{5.6}$$

Assuming that i_s is the value of the current at which magnetic circuit goes into saturation at the aligned position, then

$$c\lambda_s = (L_{max} - L_{min})\, i_s = L_{min}\, i_s\, (\kappa - 1) \tag{5.7}$$

The expression for λ_s, can be given by

$$\lambda_s = (L_a^s - L_{min})\, i = L_{min}\, i\, (\kappa\eta - 1) \tag{5.8}$$

where i is the peak of the flat-topped current. From (5.7) and (5.8), i_s can be determined, that is

$$i_s = \frac{ic(\kappa\eta - 1)}{(\kappa - 1)} = i\frac{c}{s} \tag{5.9}$$

where s is defined as

$$s = \frac{(\kappa - 1)}{(\kappa\eta - 1)} \tag{5.10}$$

The energy converted is given by the area of the polygon OACDO in Fig. 5.1 and is given by

$$W = OABCO = OACD - OCD = c\lambda_s i - 1/2 c\lambda_s i_s \tag{5.11}$$

substituting i_s from (5.9) and λ_s from (5.6) in (5.11) yields the following expression for energy converted per each current pulse:

$$W = 1/2\,V\,\frac{\beta_s}{\omega}\,ci\,(2-\frac{c}{s}) \tag{5.12}$$

The average power is the sum of all energies converted in one second. Since in each revolution, each phase conducts as many current pulses as the number of rotor poles, N_r, there are qN_r pulses of currents for all phases per revolution. For a frequency of rotation, $f = \frac{\omega}{2\pi}$, the average power is given by

$$P_{ave} = WqN_r f = Vi\frac{\beta_s qN_r}{4\pi}\cdot Q \tag{5.13}$$

where Q is defined by

$$Q = c\,(2-\frac{c}{s}) \tag{5.14}$$

The corresponding value of the average torque can be calculated using

$$T_{ave} = \frac{P_{ave}}{\omega} \tag{5.15}$$

Factor Q in (5.13) shows the improvement in energy conversion brought about by saturation. When the motor is unsaturated, $\eta = 1$, and for $c = 1$, Q is also equal to 1. However, when the motor is saturated, $\eta<1$ and $s>1$, and for $c=1$, Q is greater than one. SR motors are usually designed with Q's about 1.5 or higher. This can be interpreted as a 50% increase in the conversion of field energy to useful mechanical energy with saturation as compared to the unsaturated case. Equation (5.13) can also be used to estimate the inverter voltampere requirement per kW of the SRM power. If the voltampere requirement of each switching device is defined as the product of maximum voltage and the peak current and the maximum voltage on each device, assuming perfect snubbing, is twice the supply voltage, the total voltampere requirement of the inverter, assuming one switching device per phase, is given by

$$S = 2qVi \tag{5.16}$$

The inverter voltampere per kW of motor rating, which is an important measure in the design of the drive system, is obtained from (5.13) and (5.16) as

$$\frac{S}{P} = \frac{8\pi}{\beta_s N_r\,Q} \tag{5.17}$$

Equation (5.17) clearly shows the reduction obtained in converter kVA

requirement to motor rating by a factor Q for a saturated motor. Equation (5.13) also can be used to predict the commutation angle for a given average power, using the relationship between Q and c given in (5.14).

The base speed of the machine as indicated by the flat-top current profile, can be obtained using (5.6) and (5.8) as

$$\omega_b = \frac{V\beta_s}{iL_{min}(\kappa\eta - 1)} \tag{5.18}$$

5.3. Switching Strategies

A realistic control strategy for the SRM drive has to take into consideration the mutual dependence between motor parameters and excitation, and the limitations of the switching circuit. In this section, a brief review of the basic switching strategies used in the SRM drive is made.

At low speed, the rate of increase of the current following the turn-on is high because the back-emf at low speed is small, and peak current has to be limited by chopping. But at high speed, the back-emf becomes dominant. As a result, the current peaks before commutation. In between there is a condition usually referred to as the base speed at which the back-emf is nearly equal to supply voltage and the current has a flat-top profile. When the SRM is to be operated as a variable speed drive, two different switching strategies are used: one for low speed operation in which the current level has to be limited by chopping (current control), and the other for high speed operation, in which both the ignition and the conduction angles should be controlled properly in order for the torque to satisfy the load condition and to be as smooth as possible (angle control).

5.3.1. Switching Signals

Switching of the power switches is synchronized to the rotor position, with the crossing of the rotor poles sweeping past fixed positions being sensed by Hall effect or optical devices. The signal from the position sensor starts a delay counter, and the output of the counter turns on the switching device after the desired delay time has elapsed. The switch is later turned off by a signal coming from another delay counter that is adjusted to give the desired conduction angle. The position sensors should be so placed as to provide sufficient delay in the ignition angle for all operating speeds. For example, the sensor of each stator phase could be placed halfway between the stator poles. Figure 5.5 shows the reference signal, the delay signal for ignition, and the

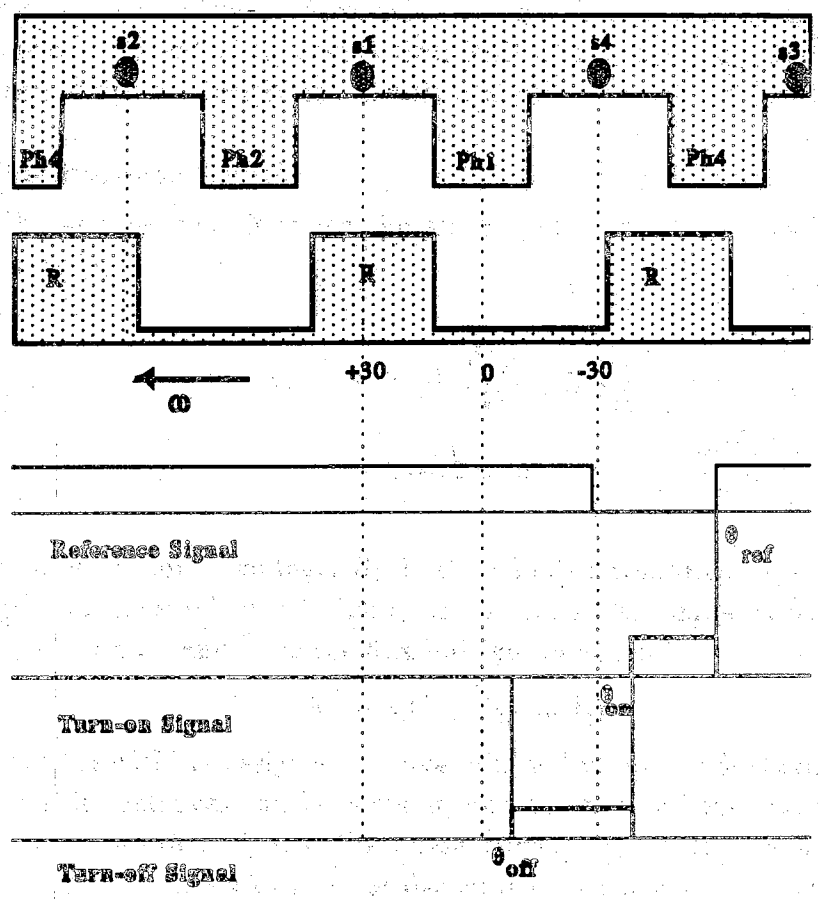

Figure 5.5. Switching signals for phase 1

delay signal for commutating off phase 1, for the case when the sensors are placed midway between the stator poles.

5.3.2. Angle Control

For higher speeds, approaching and above the base speed, the switching of the power devices is controlled by adjusting both the ignition angle, θ_{on}, and the conduction angle, θ_c. Angle control results in a smoother operation than that obtained by chopping control. Thus, for speeds where the current level can be controlled by delaying the ignition, angle control is preferred. Delaying the ignition of the phases at speeds lower than the base speed limits the current peak, so that the current reaches its peak at the commutation point. When the required average torque is low, the ignition angle can be delayed so that the current pulse lies entirely within the active torque region.

At nominal speed and loading, peak current is limited by the back-emf and the current decreases even before the commutation point because the back-emf exceeds the applied voltage ($\frac{di}{dt} < 0$). Thus, to satisfy the increasing power requirement at higher speed, it becomes necessary to turn on the phase earlier, even before the unaligned position, in order for the current to reach a higher level before the active torque region. The conduction angle is adjusted with changes in the load torque. For motoring operation, the excitation voltage should be turned off early enough for the current to drop to as low as possible before the onset of the negative torque region. Current commutated at the flat top region of the inductance waveform has a faster rate of decrease because the value of the incremental inductance near the aligned position is small.

5.3.3. Current Control (Chopping)

At low speeds, both the back-emf and the effective incremental reactance of the motor are reduced proportionately; consequently, with the same applied voltage, the current will rise to a higher level than that at high speed. To prevent the current from exceeding the ratings of the switching devices, it can be controlled simply by turning on and off the switching device. An upper current limit control is used to turn off the switching device whenever the reference current is exceeded. The reference current, subject to an absolute maximum, may be adjusted from an outer speed (or torque) feedback loop to satisfy the load condition. The phase excitation can be turned on as soon as the circuit condition permits, or after some fixed off-time that is longer than

the minimum off-time required by switching devices.

Control in this mode is more complicated due to various limitations associated with the switches and circuit elements, such as the turn-on, turn-off and voltage reversal times of the main and auxiliary switching devices. Moreover, predicting the reference current required to satisfy a certain loading condition is difficult, because the torque-current relation under saturated conditions is complicated. Also, with the small intervals between choppings, random and uncontrolled circuit transients can cause irregular pulsations in the electromagnetic torque and erratic and noisy operation at low speed.

5.4 Steady-State Model

The voltage equations for the stator phase windings of a SRM can be written as

$$v_k = R_k\, i_k + \frac{d\lambda_k}{d\theta} + l_k \frac{di_k}{dt} \qquad (5.19)$$

$$k=1,2,...,q$$

where v_k is the input voltage, R_k is the winding resistance, l_k represents the leakage and external circuit inductances, i_k is the phase current, q is the number of phases, and λ_k is the flux linkage. In general,

$$\lambda_k = \lambda(\theta, i_1, i_2, ..., i_q) \qquad (5.20)$$

But since the SRM is designed to have minimal mutual inductances, the effect of mutual inductances can be ignored, and the flux linkage, λ_k, is a function of the rotor position, θ, and the phase current, i_k. With this simplification, equation (5.19) reduces to a set of decoupled, first order differential equations with state-dependent coefficients. The time derivative of flux linkage can be explicitly written as

$$\frac{d\lambda}{dt} = \frac{\partial \lambda}{\partial \theta}\frac{d\theta}{dt} + \frac{\partial \lambda}{\partial i}\frac{di}{dt} \qquad (5.21)$$

In this equation, $\frac{d\theta}{dt}$ is the rotor angular speed, ω, and $\frac{\partial \lambda}{\partial i}$ is the slope of flux/current curve also known as the incremental inductance, L_{inc}. The first term at the right hand side of (5.21) is usually called the speed voltage or the back-emf, and the second term is called the transformer voltage. For convenience, from here on, the subscript k will be dropped and $\frac{\partial \lambda}{\partial \theta}$ will be

denoted by c_ω. It should be noted that both L_{inc} and c_ω are functions of rotor position and phase current. Substituting for $\frac{d\lambda}{dt}$ from (5.21), (5.19) can be rewritten as

$$v = Ri + c_\omega\, \omega + L_{inc}\, \frac{di}{dt} + l\, \frac{di}{dt} \tag{5.22}$$

For a motor with sizable rotor inertia operating at a steady-state, the speed, ω, can be assumed constant. With $t = \frac{\theta}{\omega}$, (5.22) can be rearranged in a form that can be used to obtain the variation of current with respect to rotor position, that is

$$\frac{di}{d\theta} = \frac{1}{\omega(l + L_{inc})} \left[v_{in} - Ri - c_\omega\, \omega \right] \tag{5.23}$$

Given v_{in} and ω, (5.23) can be solved to obtain the current pulse waveform for different ignition and commutation angles. Knowing the current at each rotor position, it is possible to compute instantaneous torque and flux linkage from static characteristics of the machine, and also the average torque and power, and the average and effective value of the phase current.

5.5 Solution Method and Simulation Techniques

As an illustration of the technique, a simulation study with the following simplifying assumption can be made: iron losses are neglected, voltage drops of the thyristors and the diodes are neglected, the on and off times of the main and auxiliary switching devices are neglected, and the converter is approximated by a controlled, square wave, voltage pulse generator where the duration and number of voltage pulses depend on the control angles, that is

$$v_{in} = \begin{cases} +Vdc & \text{if} \quad \theta_{on} \le \theta \le \theta_{off} \\ -Vdc & \text{if} \quad \theta_{off} < \theta \le \theta_{ext} \\ 0 & \text{if} \quad \theta > \theta_{ext} \end{cases} \tag{5.24}$$

The variable coefficients on the right hand side of (5.23) should be updated at each step of integration using the most recent value of the current and the rotor position. The integration of the differential equations with time-varying coefficients can be carried out using a predictor-corrector method that evaluates the coefficients at each step and iterates until these values converge or using higher order methods with small time steps with intermediate evaluation of state and coefficients. Here the second approach is used, with a

fourth order Runge-Kutta method, and for better accuracy in solution the angle steps are kept very small. The values of incremental inductance and c_ω are obtained at each current and rotor position using B-cubic spline interpolation technique [94].

Simulation of high and low speed modes of operation are performed. The high speed mode of operation is simulated using angle control. The main steps required in the simulation of this mode are shown in Fig. 5.6. The waveforms of the instantaneous current , torque, and flux linkage, and the values of average torque and power are obtained at three different speeds.

The low speed mode of operation is simulated using current control for turning off the switching device whenever the current exceeds the prescribed upper limit and minimum off-time for subsequent turn-on. No angle control or lower limit current control are considered. The switching device of each phase is turned on at the unaligned position of rotor pole and turned off at the aligned position, chopping the current periodically during this interval. The main simulation steps of this mode of operation are shown in Fig. 5.7. The waveform of instantaneous current, torque, and flux linkage, and the values of average torque and power can calculated for several upper current levels at three different rotor speeds.

5.6 Experimental and Simulation Results

The experimental results were obtained using the test set-up shown in Fig. 5.8. Measurement of the flux linkage was obtained from search coils encircling each of the stator poles. The scale factor for the measured current is 11. For the test drive, the control mode changes over from the current limit control to the angle control around 620 rpm. The base speed, as gauged from the current profile, is about 1000 rpm.

Shown in Figs. 5.9 through 5.17 are some of the measured waveforms with the test drive operating under current (chopping) control and under angle control. The corresponding results obtained from the computer program simulating the measured conditions are given in Figs. 5.18 through 5.20 for current control mode and 5.25 through 5.27 for angle control mode. The agreement between measured and computed results for the two modes of control operation is good.

Both experimental and simulation results of the chopping mode of operation, especially at very low speeds, show fluctuations in the upper current limit. The instability of the upper current limit in the experimental

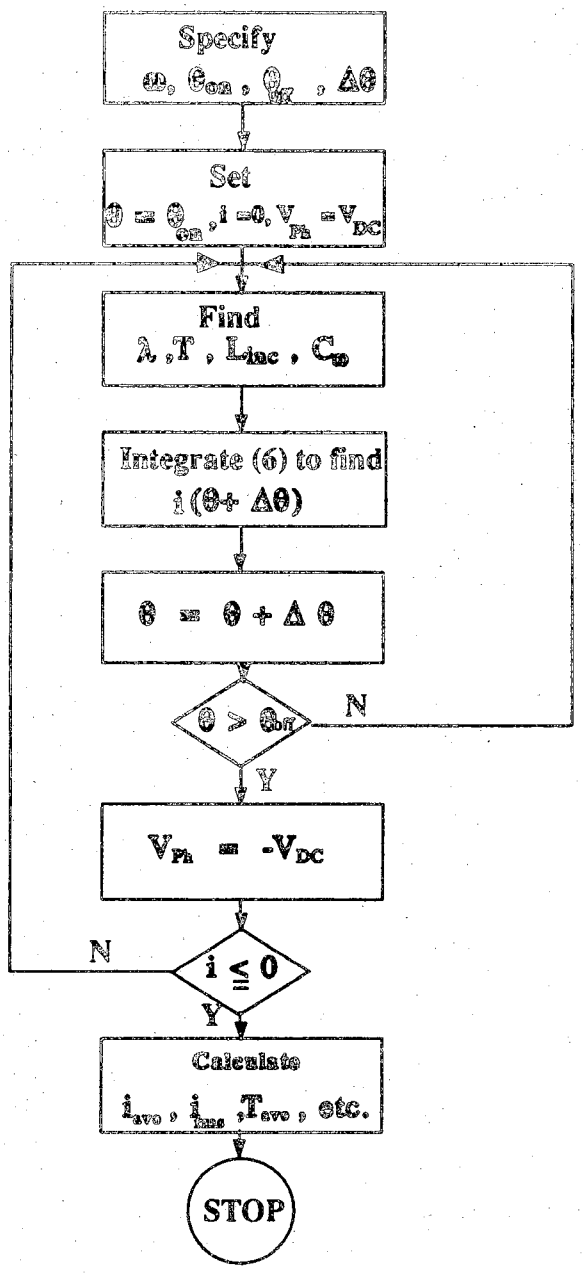

Figure 5.6. Flow diagram for high speed mode

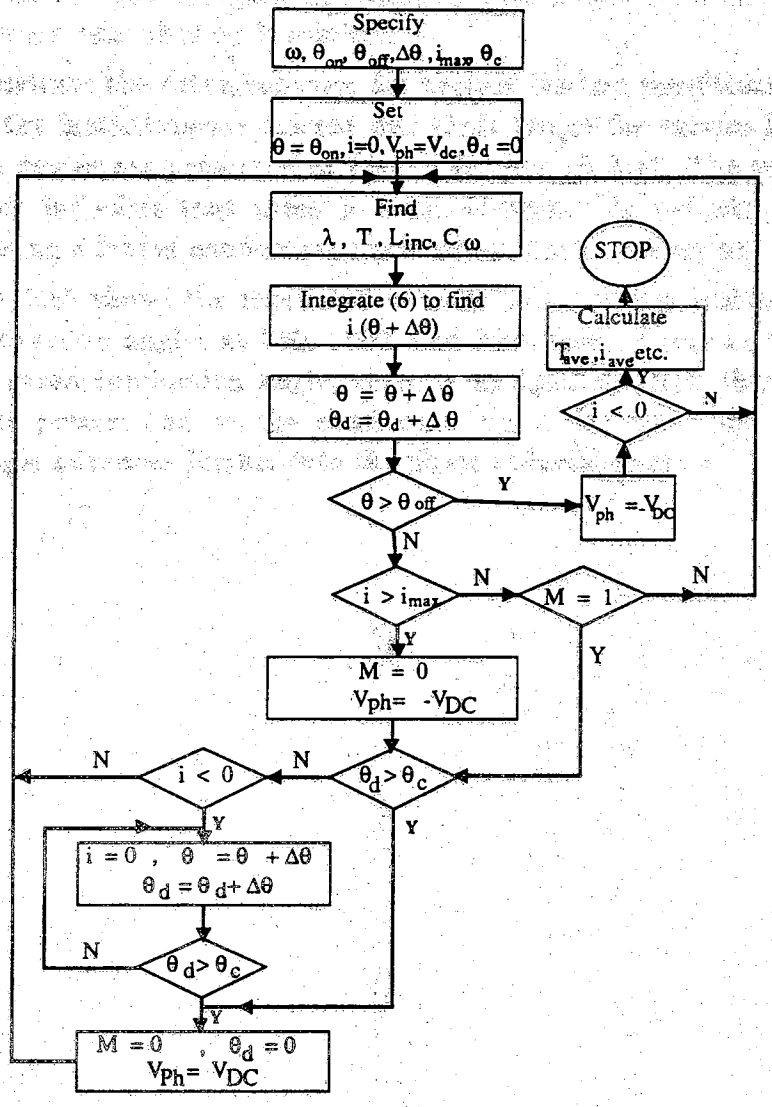

Figure 5.7. Flow diagram for low speed mode

result is due to circuit transients and speed fluctuations, whereas that of the simulation with constant speed may also be attributed to inadequate resolution from the coarse step size of the rotor angle used in the numerical integration when the rate of change of current with respect to angle is high. Such errors can be minimized by using a smaller integration step size for the lower speeds. Lacking the facility to measure the instantaneous torque, there is no basis of comparison for the computed torque waveform. It is, however, apparent from the computed torque waveform that the current pulses in the minimum inductance region do not contribute to any useful torque. Also with long off-time, the ratio of peak to average torque is high, unless a higher current level is permitted at the expense of higher device rating and cost. Figures 5.21 through 5.23 show the current and torque waveforms for a higher current level (24A). A shorter off-time will decrease the peak to average torque ratio, resulting in lower torque ripples as shown in Fig. 5.24; hence less noise and vibration. However, this will require faster and more expensive switching devices.

Figures 5.25 through 5.27 show the results of the drive operating in the angle control mode. While the current waveform at 750 rpm has a peaky profile, that at the nominal speed of 1500 rpm peaks early and decreases in the conduction period because the back-emf at this speed is higher than the applied voltage. Below the base speed (1000 rpm), the peak current can be reduced by delaying the ignition angle further into the phase inductance cycle where the inductance is increasing with angle. Figure 5.26 shows the current profile of the drive at 1000 rpm; the flat-top current is an indication of base speed operation. At speeds higher than base speed, for the current to reach higher levels before the active torque region, the ignition angle should be advanced ahead of the unaligned position (30°).

In these figures are also shown the computed and measured energy conversion loops at nominal speed. The area within the loop represents the converted energy for one current pulse, which when multiplied by the number of pulses per second ($qN_r \times \frac{rpm}{60}$), yields the average power.

The effects of constant on-angle, constant conduction angle, and constant off-angle control strategies on the shaft torque, maximum current, and energy conversion loop are illustrated in Figs. 5.28 through 5.36. The results for three output power levels (4, 3, and 2 kW) are given at three speeds. Comparison of the shaft torque and energy conversion loops will suggest that the constant off-angle control results in less torque pulsation and more efficient energy

conversion. This is due to the fact that all or most of the conduction period lies in the active torque region and also, by early commutation of the phase, negative torque contribution is minimized.

To illustrate the drive behavior for various loading conditions, computed profiles of the instantaneous current and shaft torque for various ignition and conduction angles are presented in Figs. 5.37 through 5.45. The profile of the shaft torque indicates that there is some advantage in reducing the torque ripple by using a longer conduction angle within the active region.

Figure 5.46 shows the computed average power versus ignition angle for several conduction angles at 750, 1000, and 1500 rpm. These curves indicate that for a given conduction angle, there is an ignition angle that maximizes the average power, and as the conduction angle decreases, the maximizing ignition angle advances further into the phase inductance cycle.

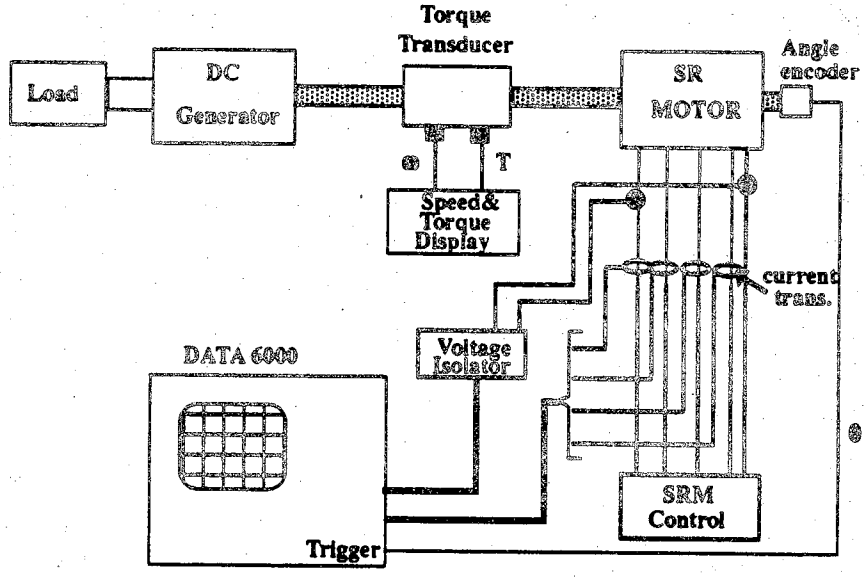

Figure 5.8. Test set-up

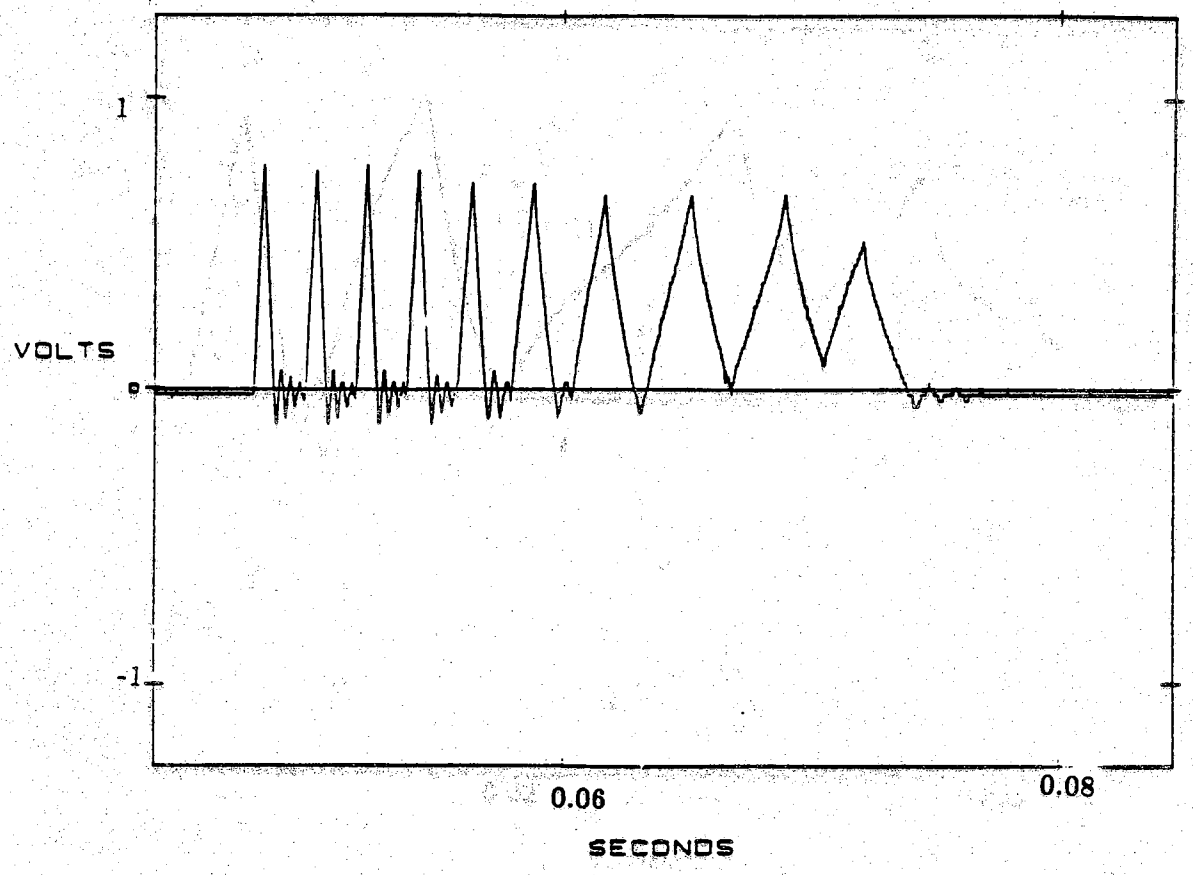

Figure 5.9. Measured phase current at 200 rpm

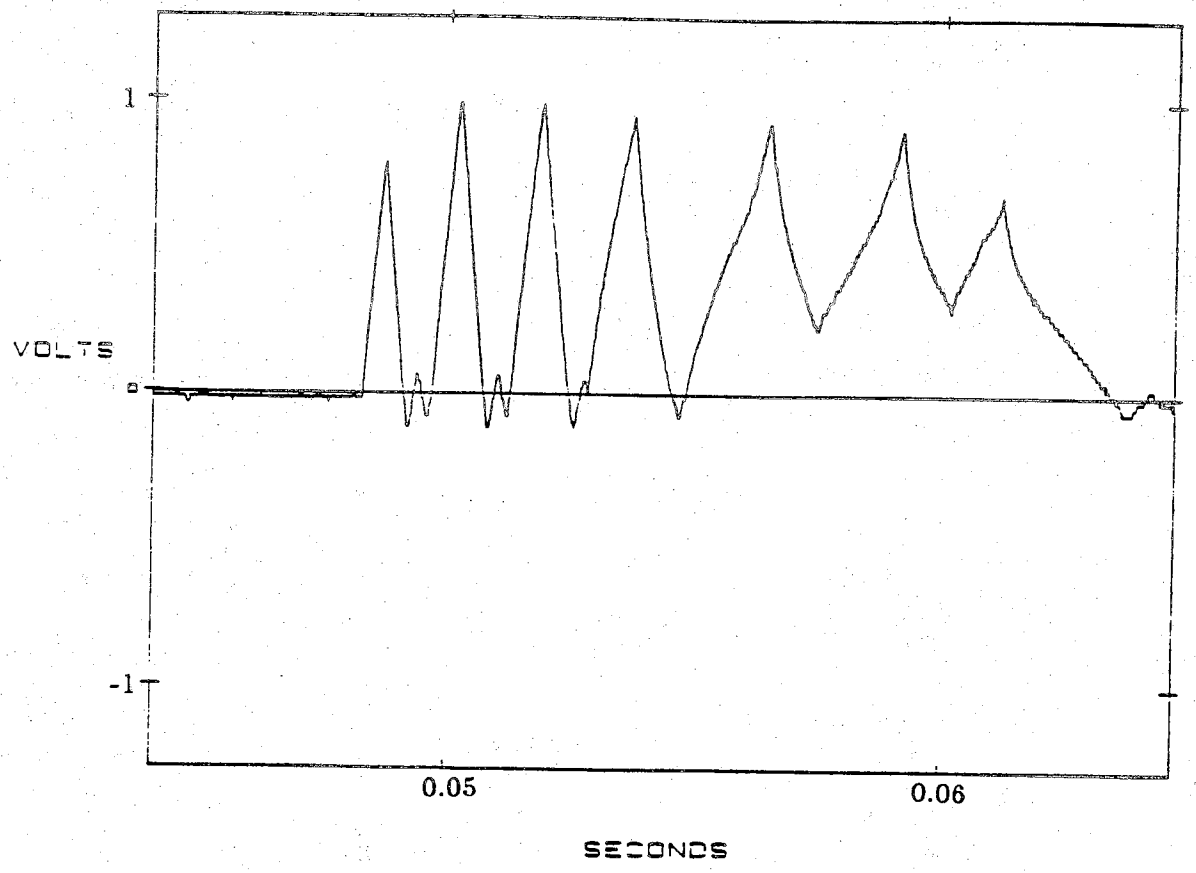

Figure 5.10. Measured phase current at 400 rpm

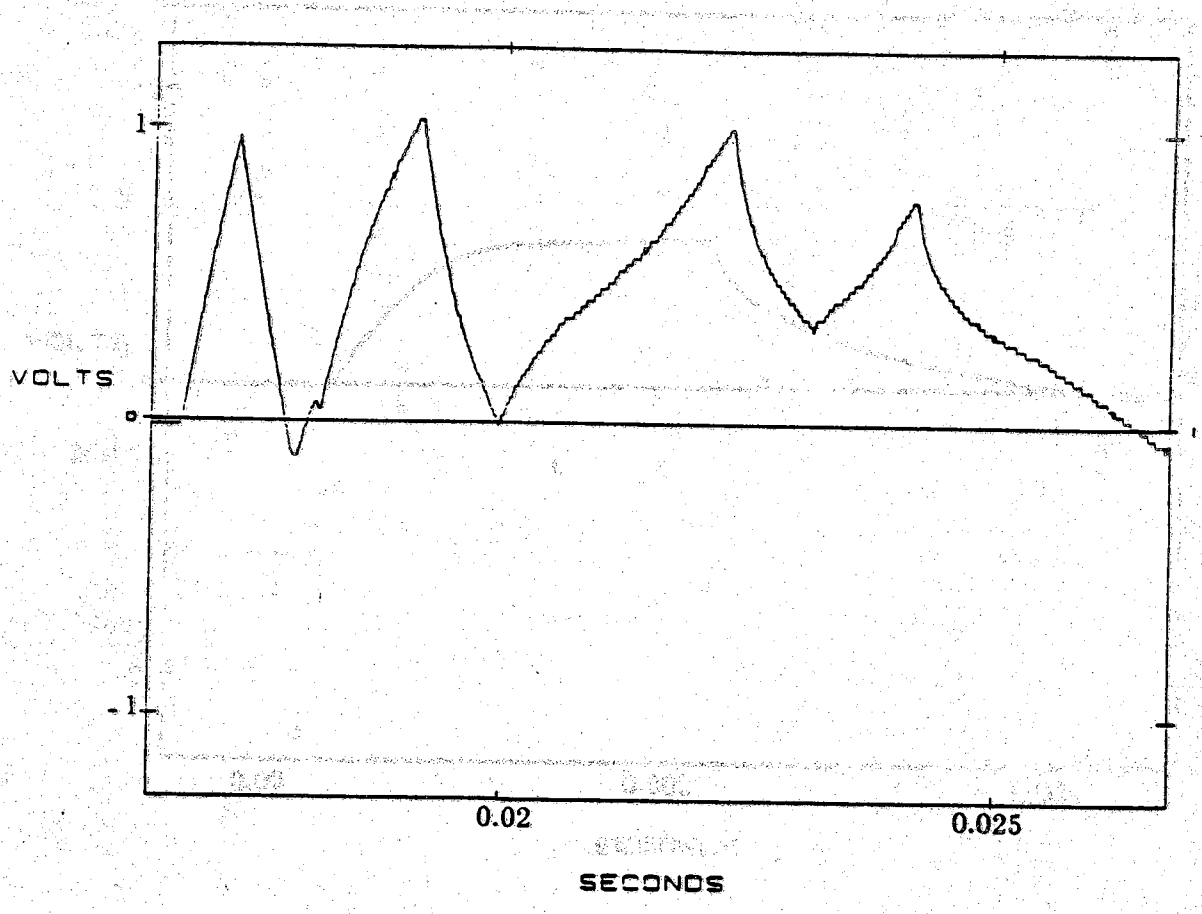

Figure 5.11. Measured phase current at 600 rpm

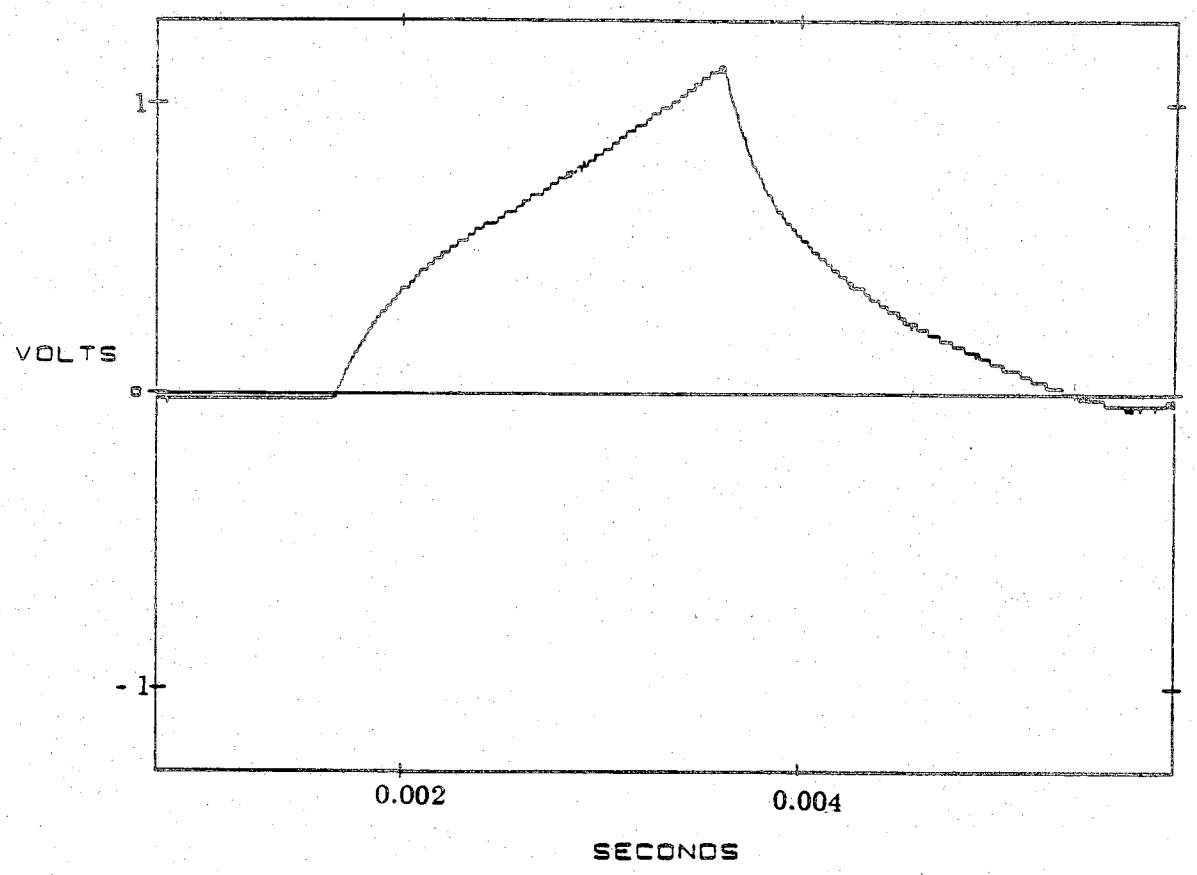

Figure 5.12. Measured phase current at 750 rpm

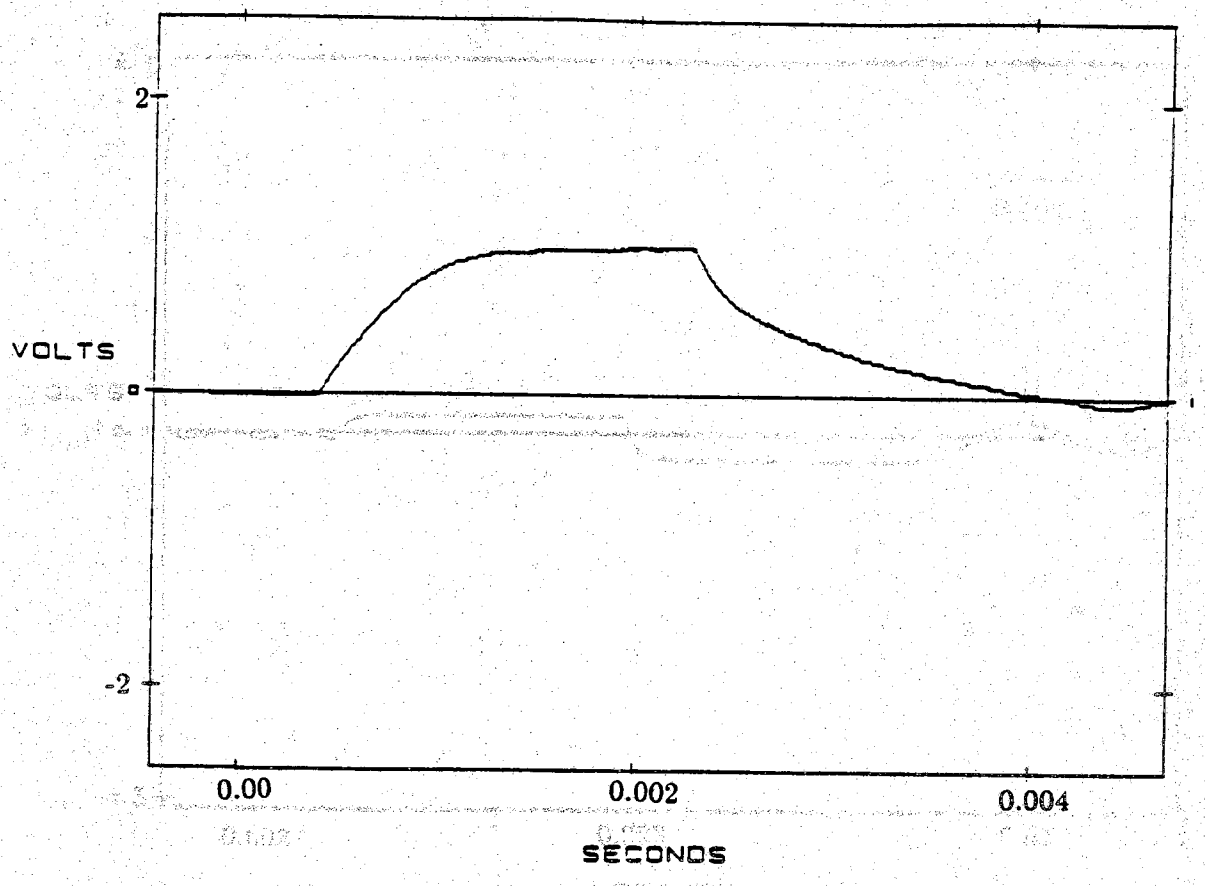

Figure 5.13. Measured phase current at 1000 rpm

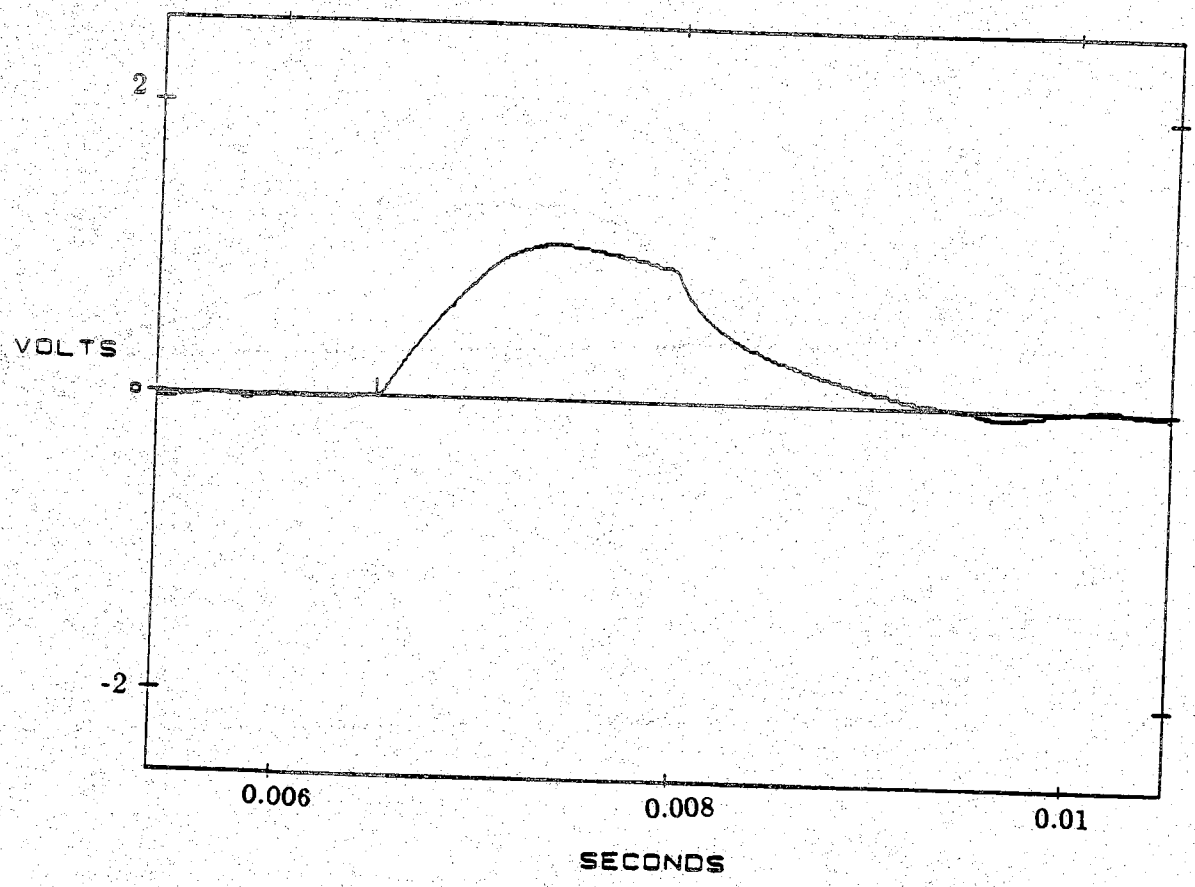

Figure 5.14. Measured phase current at 1500 rpm

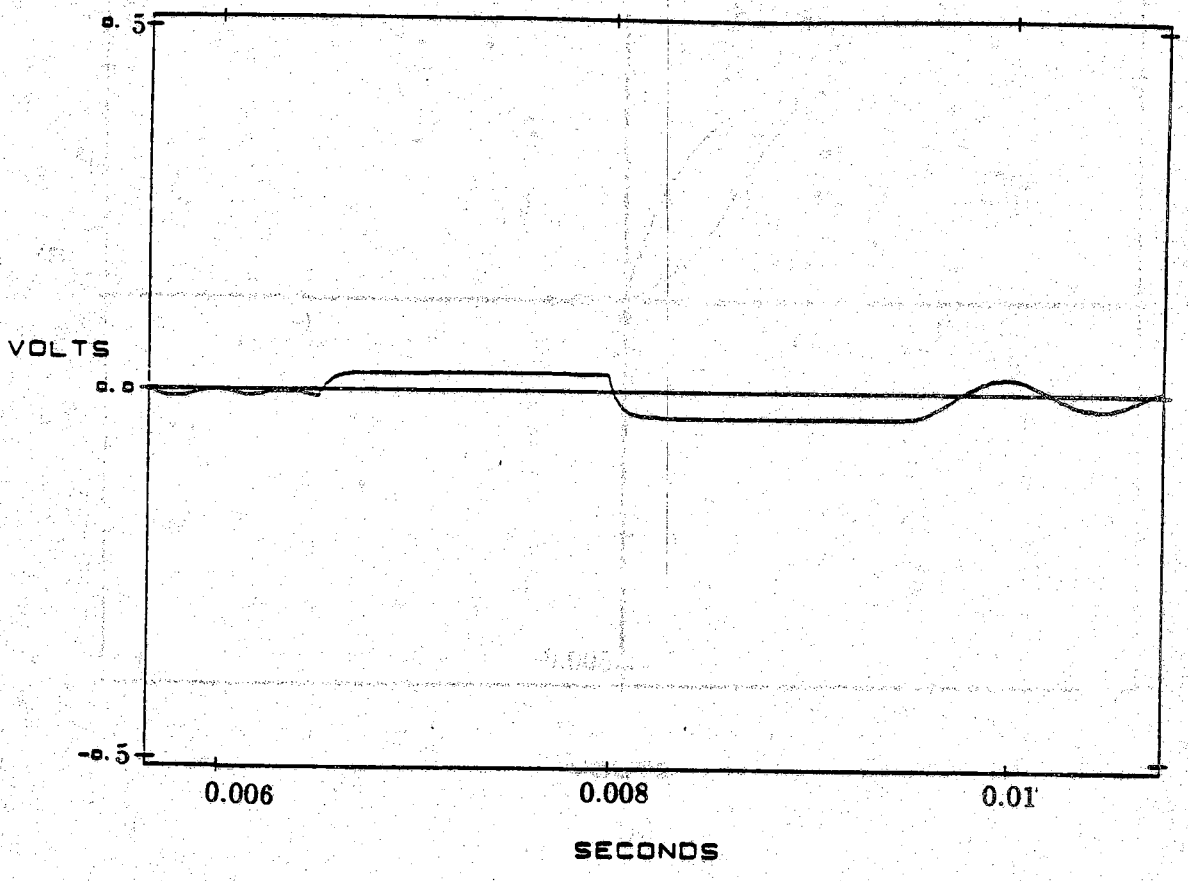

Figure 5.15. Measured terminal voltage at 1500 rpm

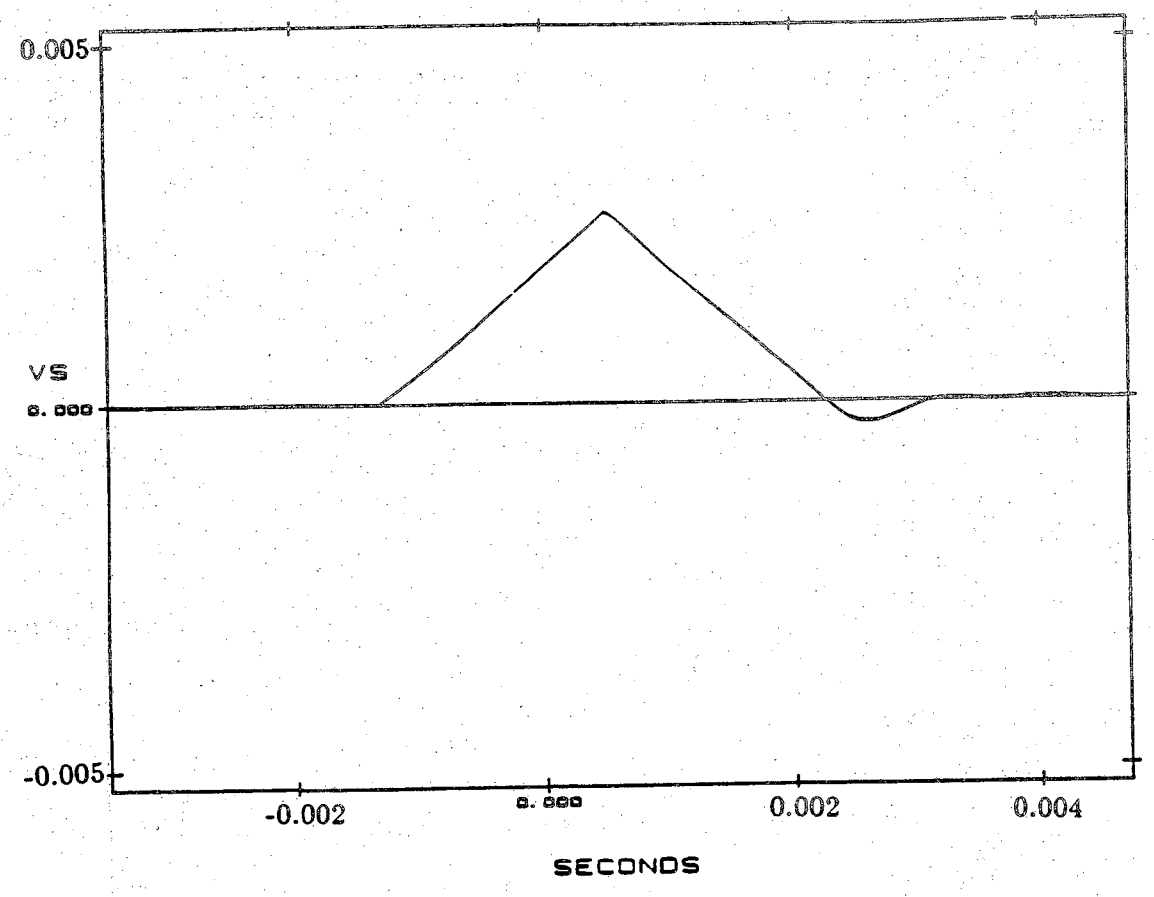

Figure 5.16. Measured flux linkage at 1500 rpm

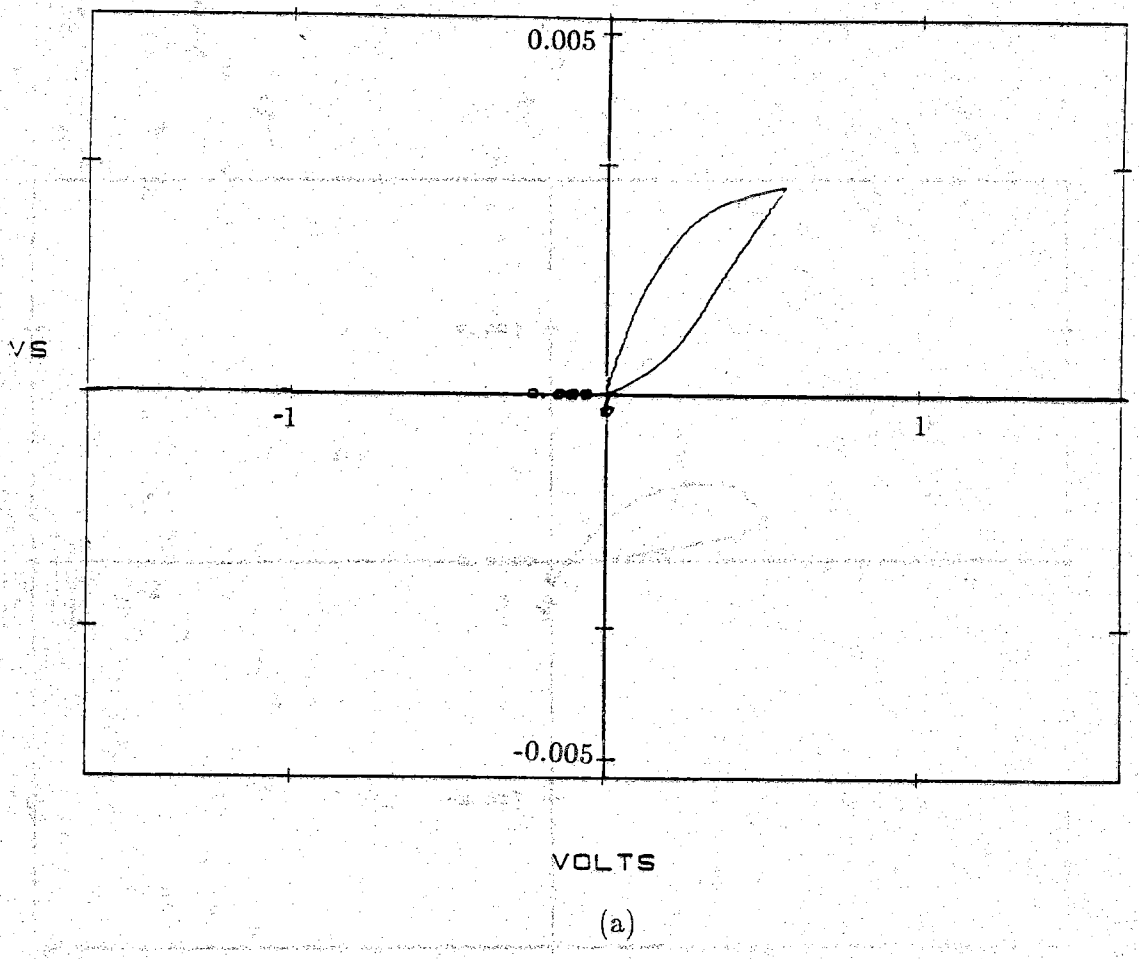

(a)

Figure 5.17. Energy conversion loop
(a) 750 rpm
(b) 1000 rpm
(c) 1500 rpm

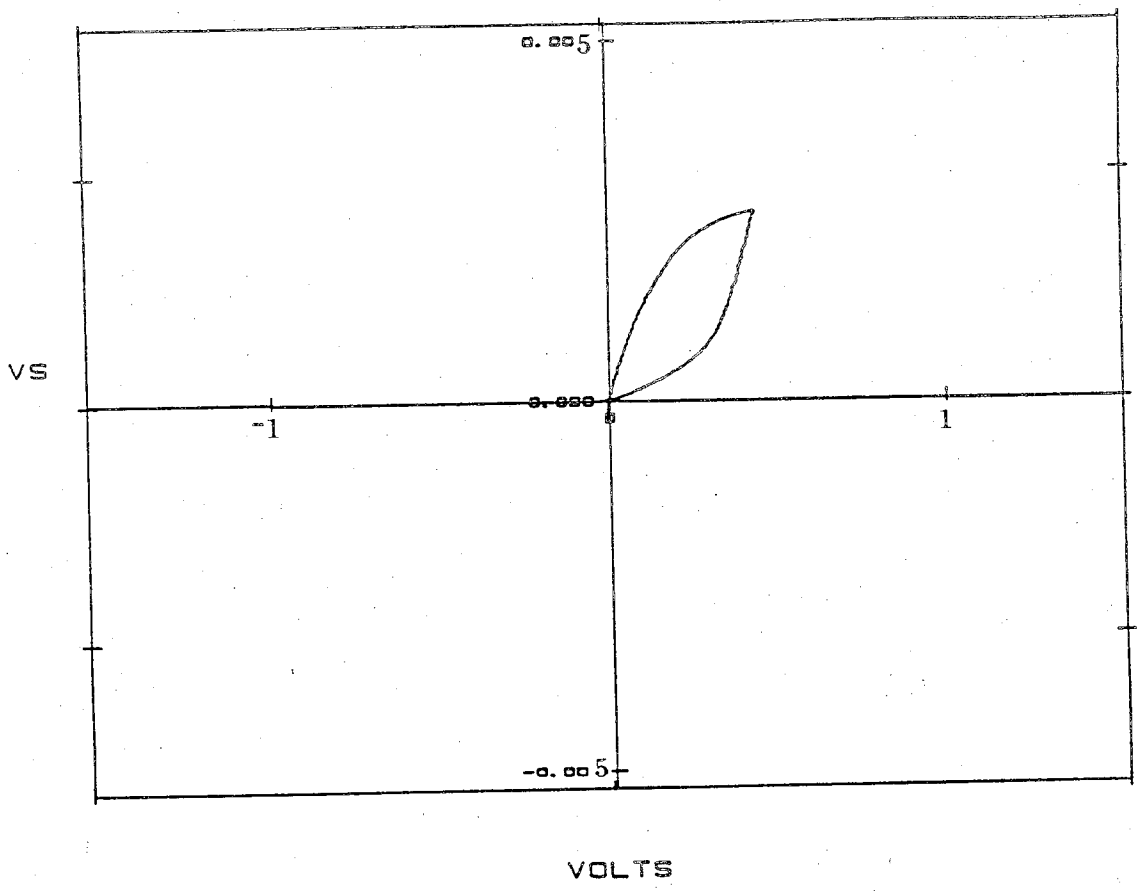

(b)

Figure 5.16. continued.

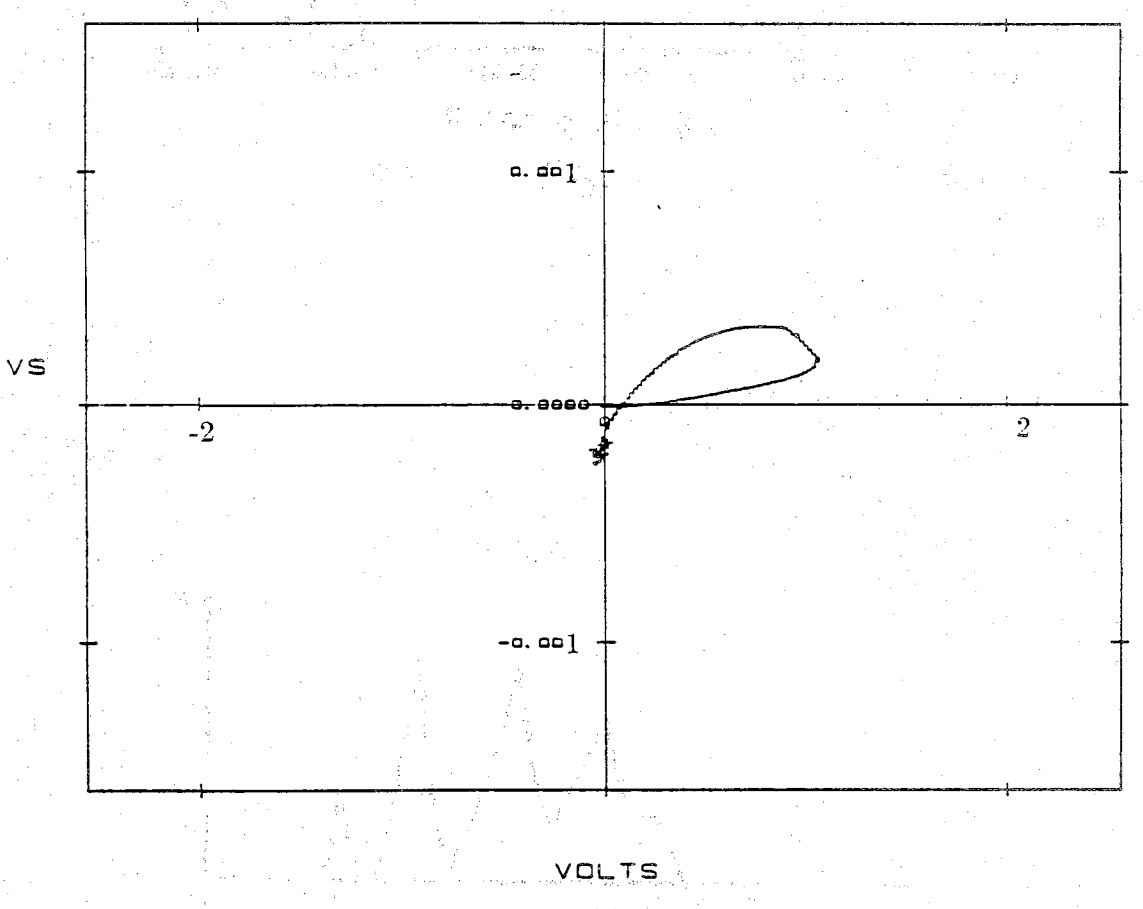

(c)

Figure 5.16. continued.

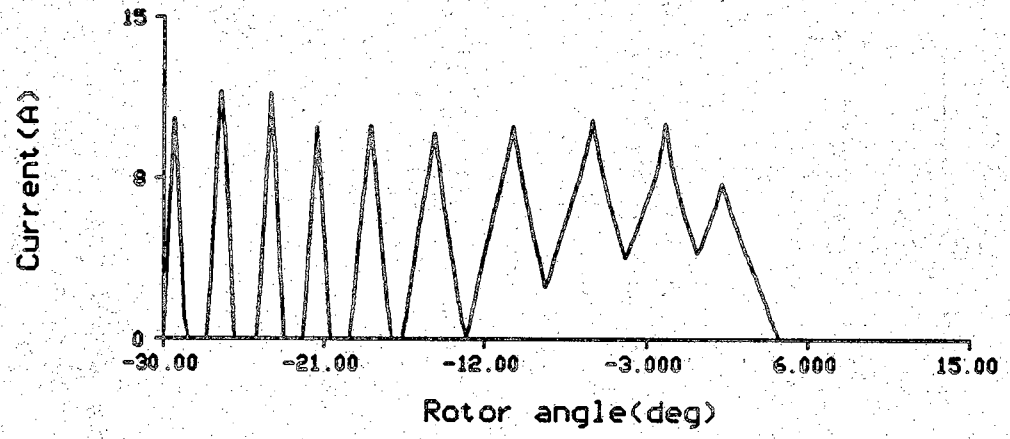

(a)

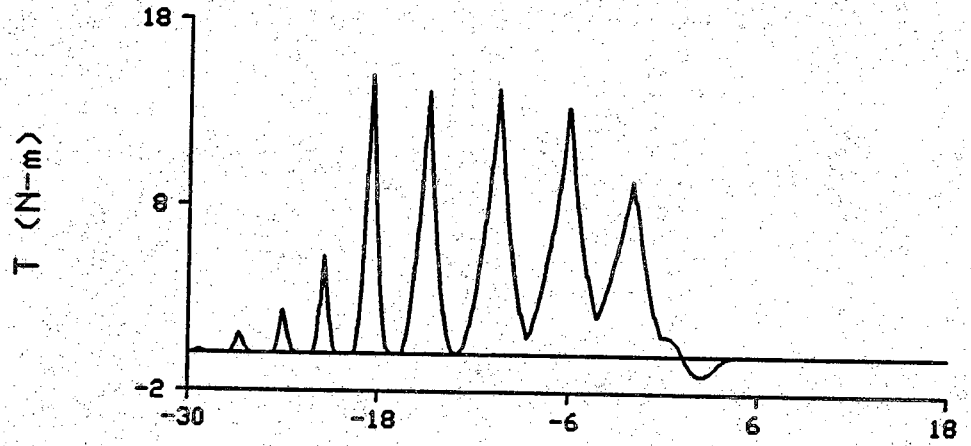

(b)

Figure 5.18. SRM characteristics at 200 rpm, current level 12A
(a) current
(b) torque

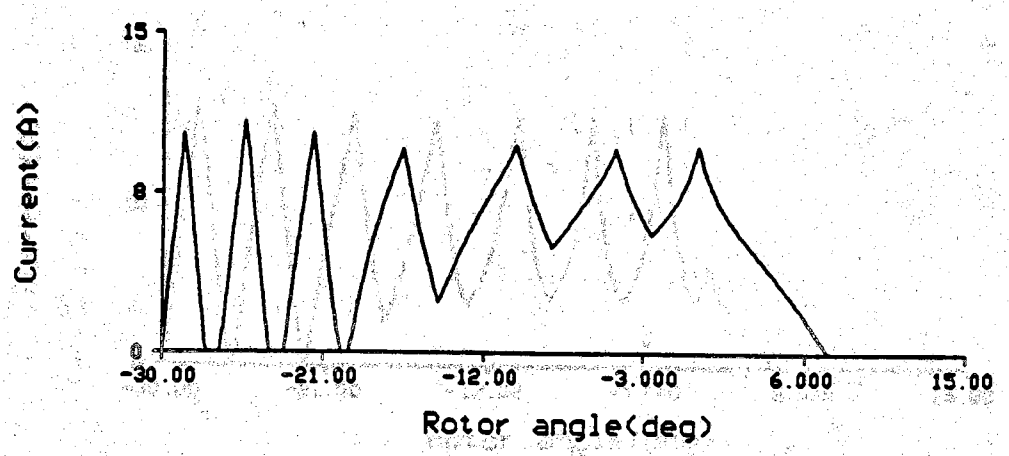

(a)

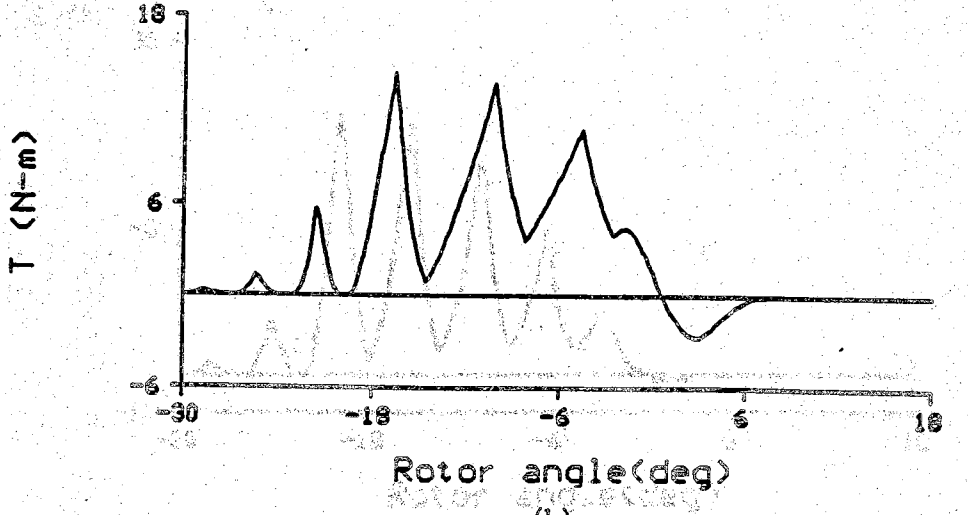

(b)

Figure 5.19. SRM characteristics at 400 rpm, current level 12A
(a) current
(b) torque

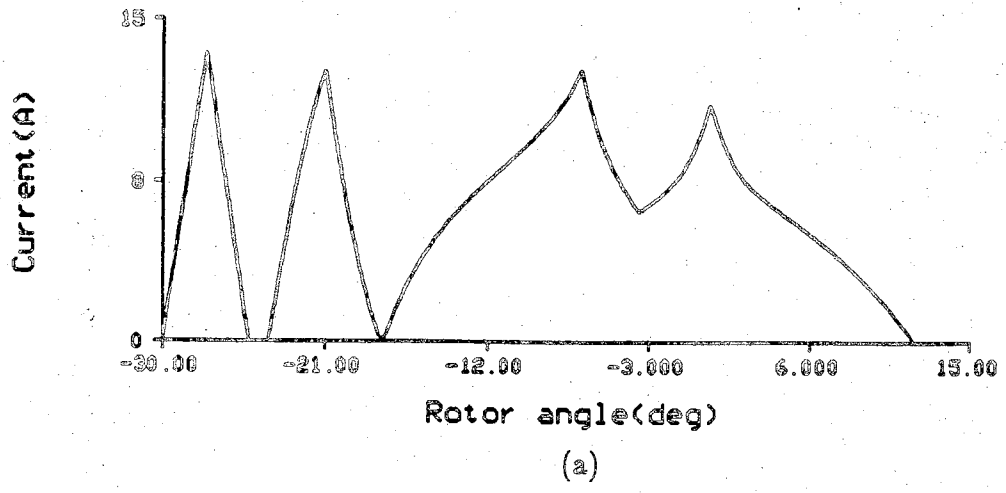

(a)

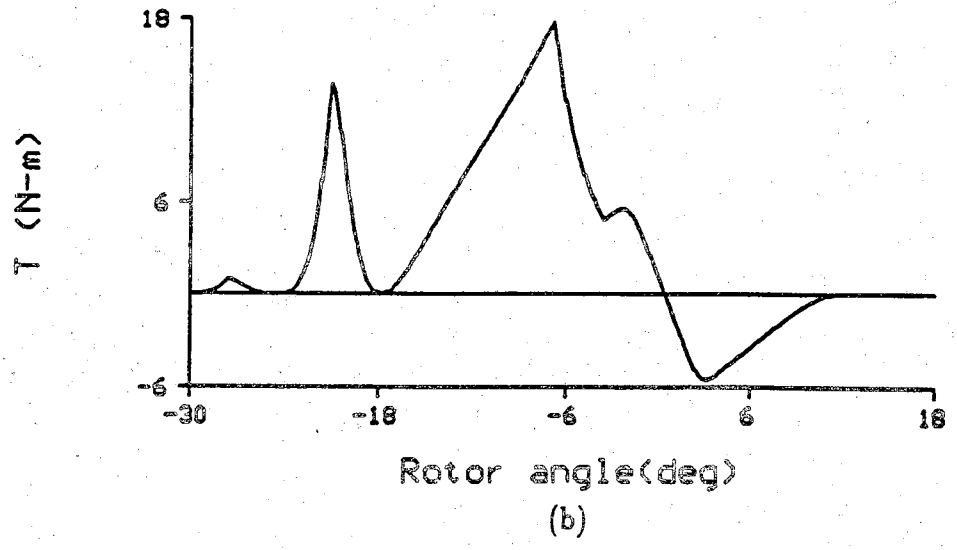

(b)

Figure 5.20. SRM characteristics at 600 rpm, current level 12A
(a) current
(b) torque

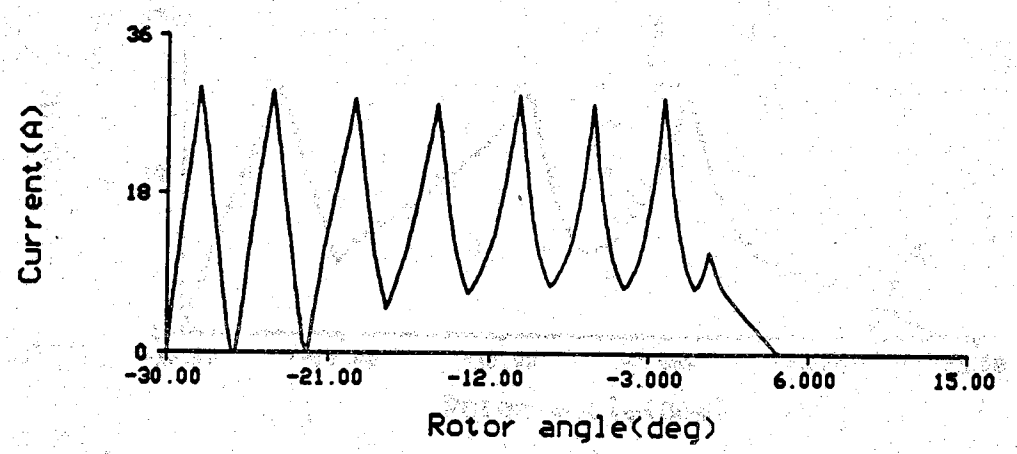

(a)

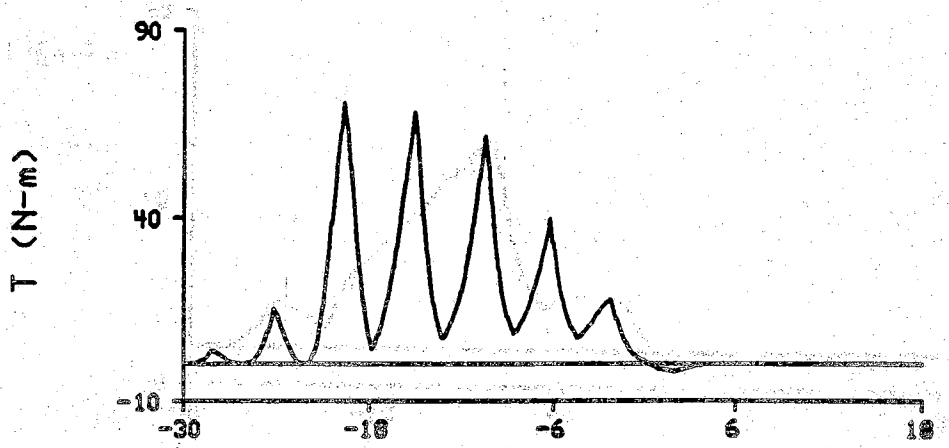

(b)

Figure 5.21. SRM characteristics at 200 rpm, current level 24A
(a) current
(b) torque

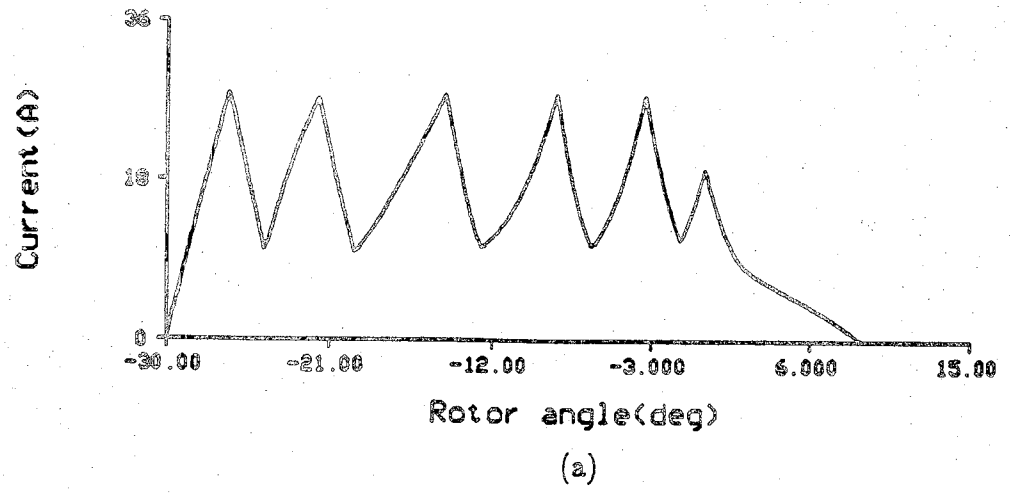

(a)

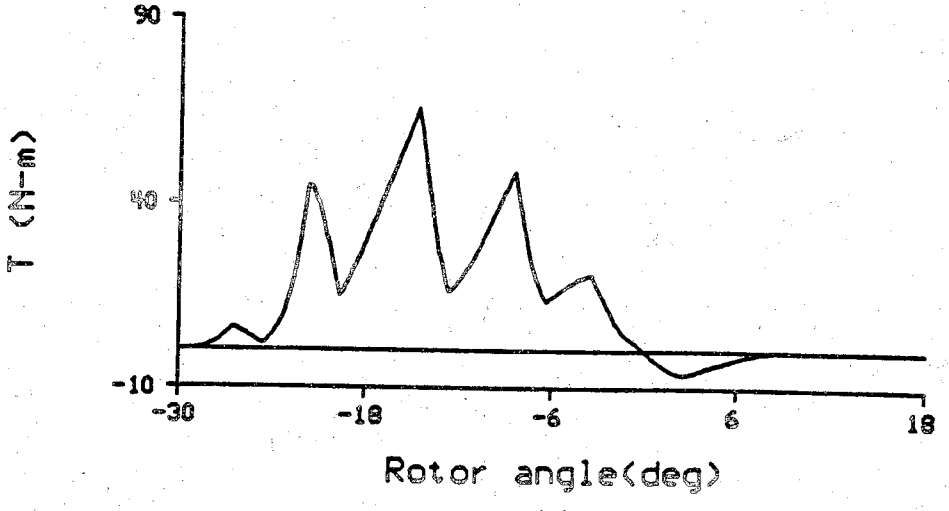

(b)

Figure 5.22. SRM characteristics at 400 rpm, current level 24A
(a) current
(b) torque

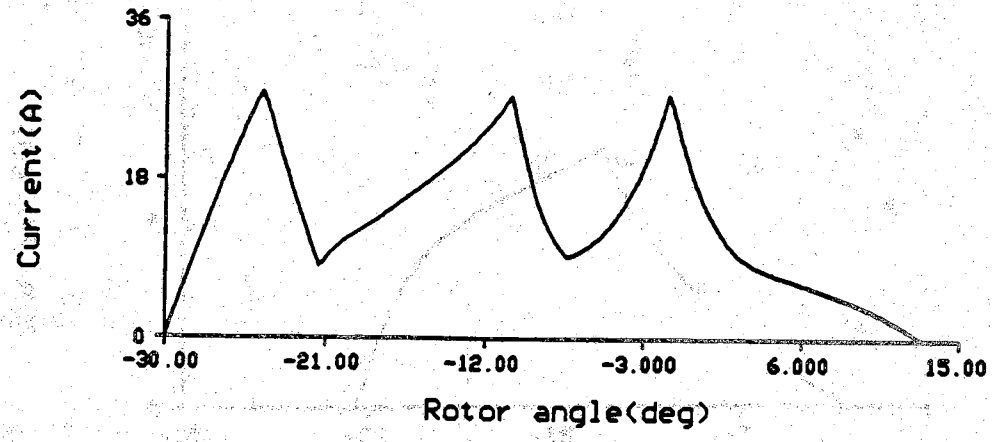

(a)

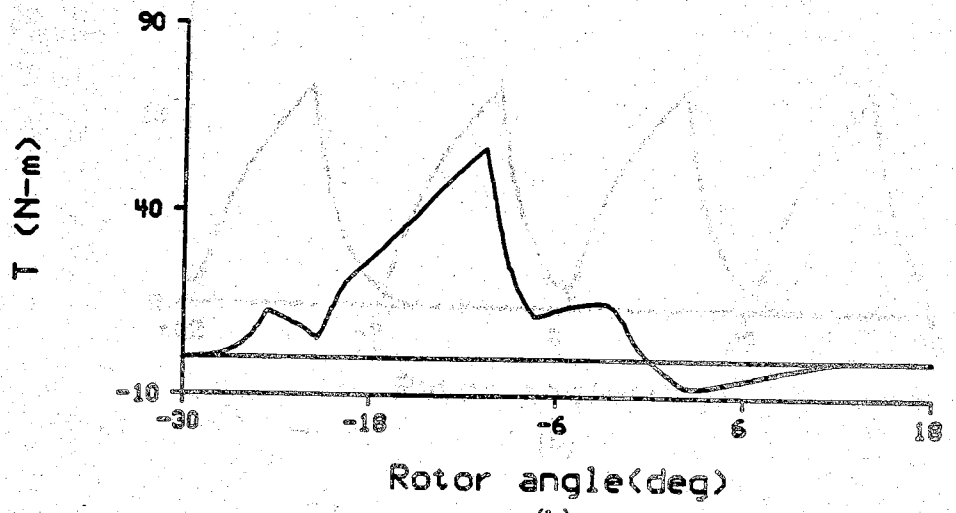

(b)

Figure 5.23. SRM characteristics at 600 rpm, current level 24A
(a) current
(b) torque

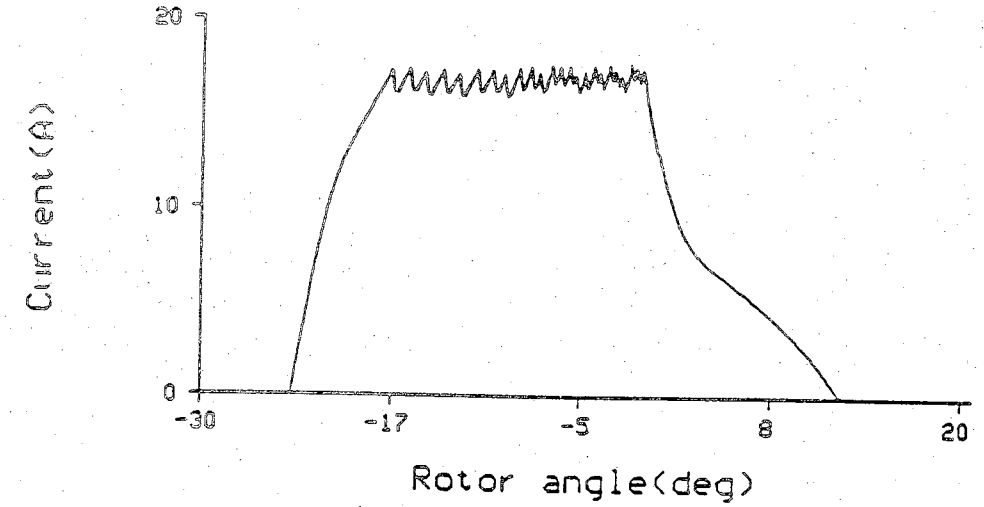

(a)

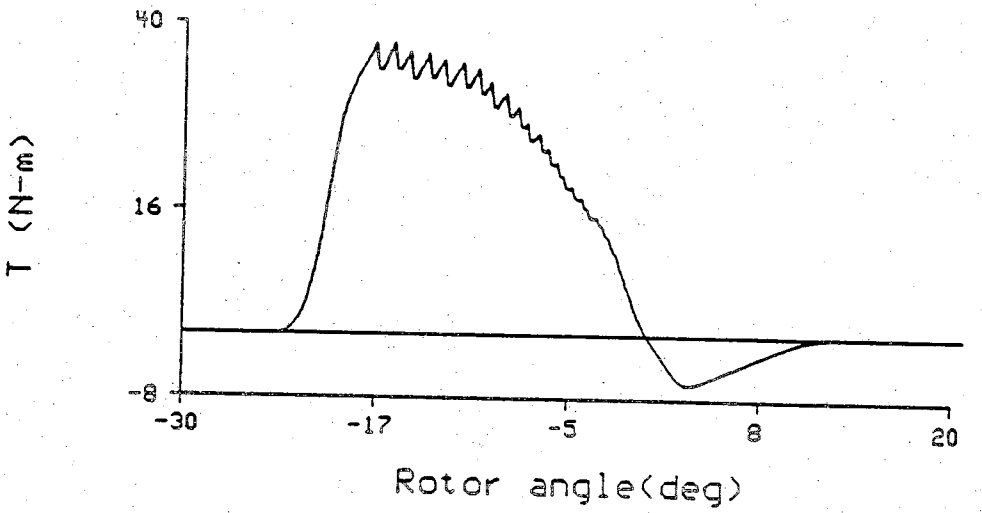

(b)

Figure 5.24. SRM characteristics at 600 rpm, current level 18A, off-time 0.2 degree

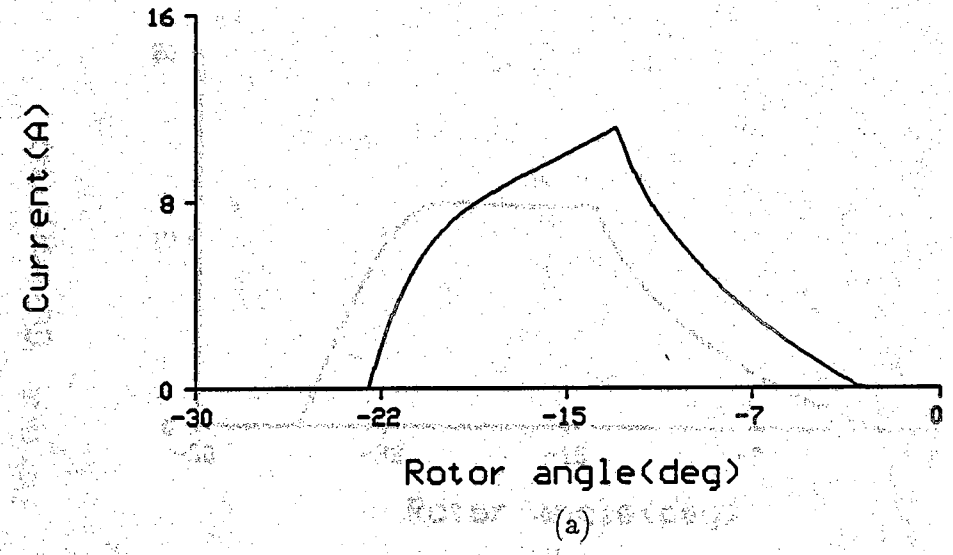

(a)

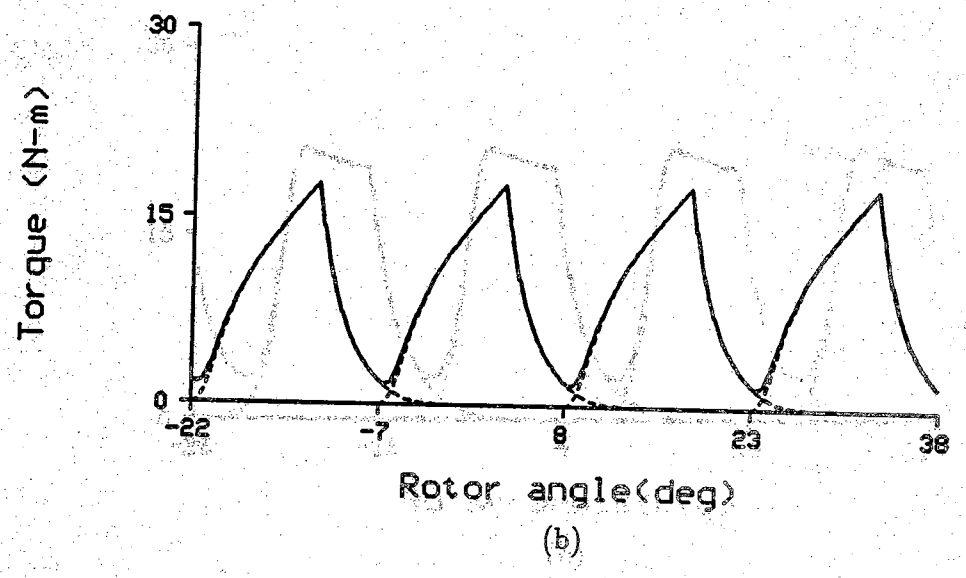

(b)

Figure 5.25. SRM characteristics at 750 rpm
(a) current
(b) torque
(c) flux linkage
(d) energy conversion loop

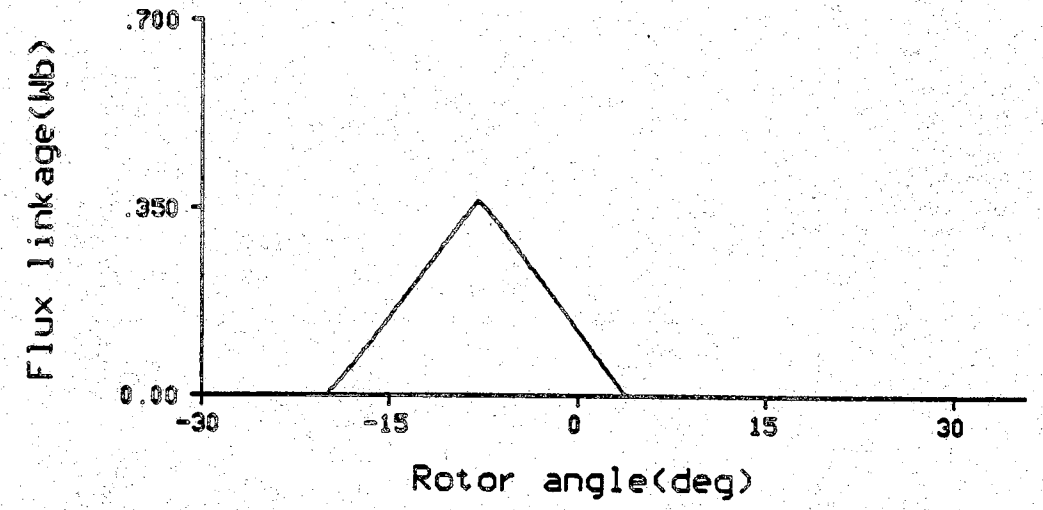

(c)

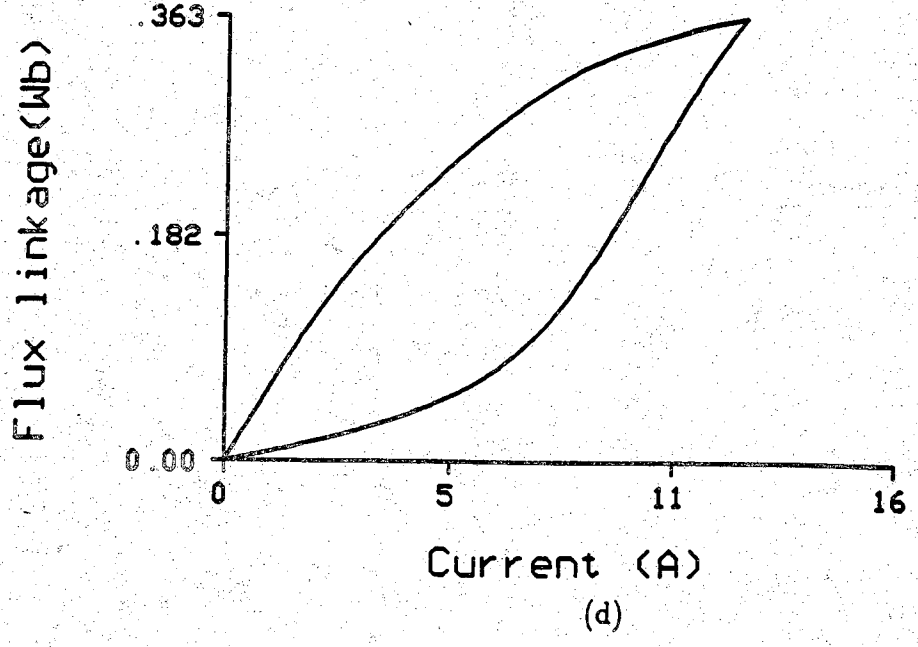

(d)

Figure 5.25. continued.

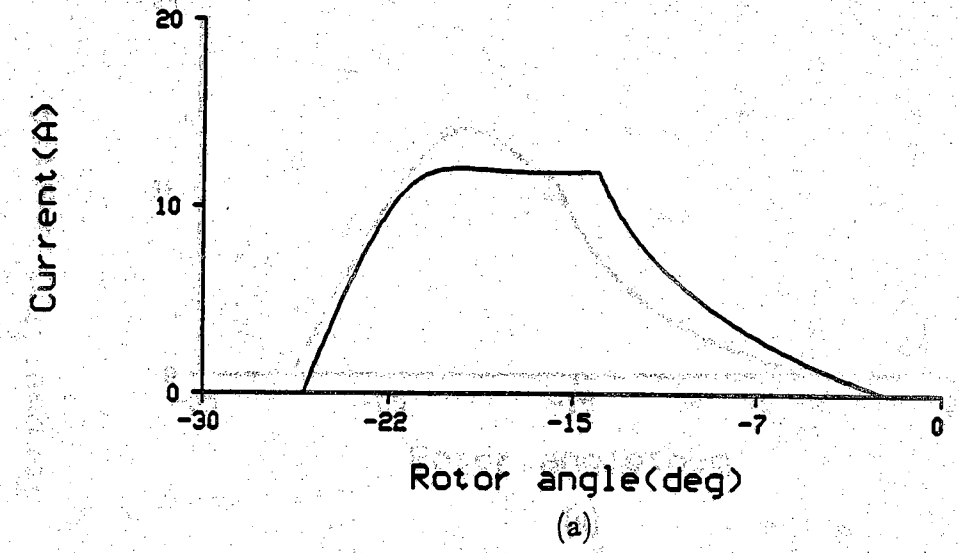

(a)

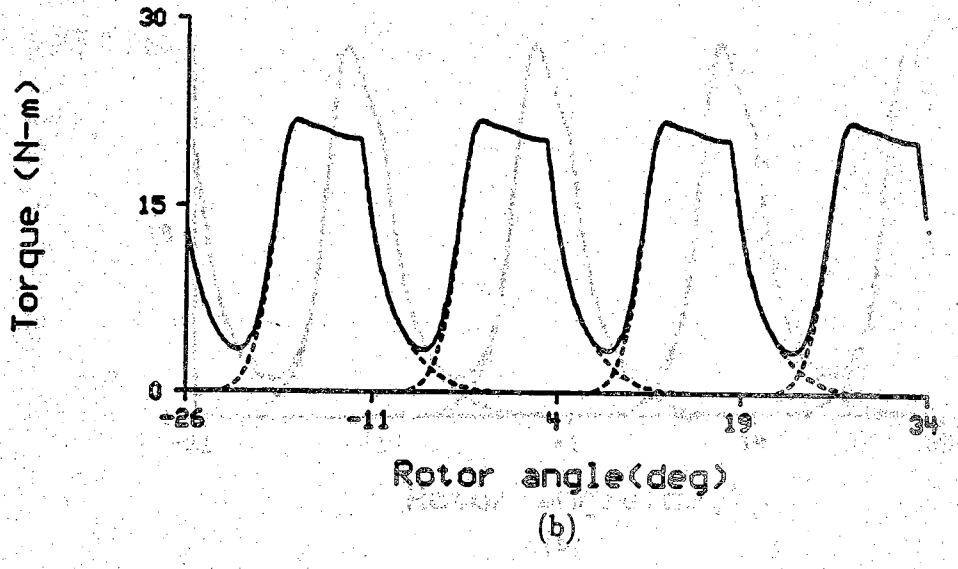

(b)

Figure 5.26. SRM characteristics at 1000 rpm
(a) current
(b) torque
(c) flux linkage
(d) energy conversion loop

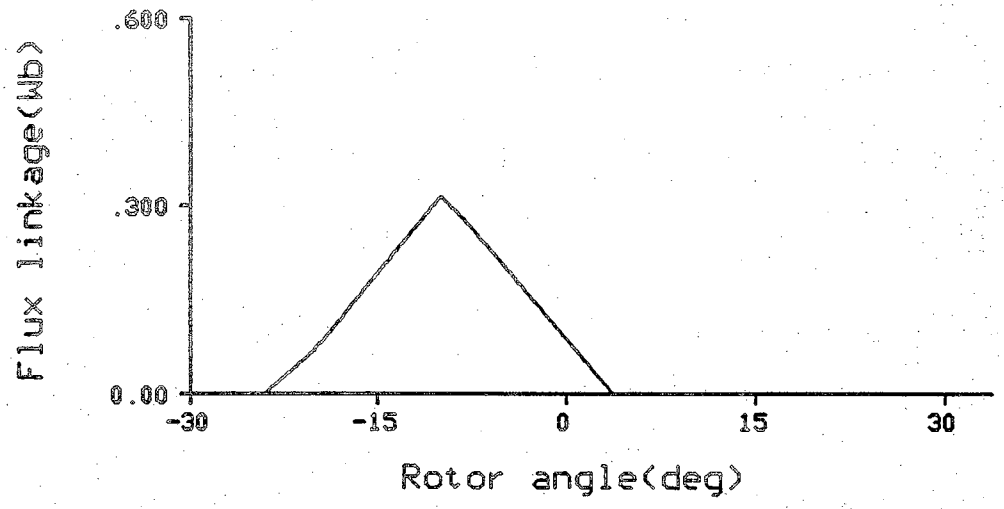

(c)

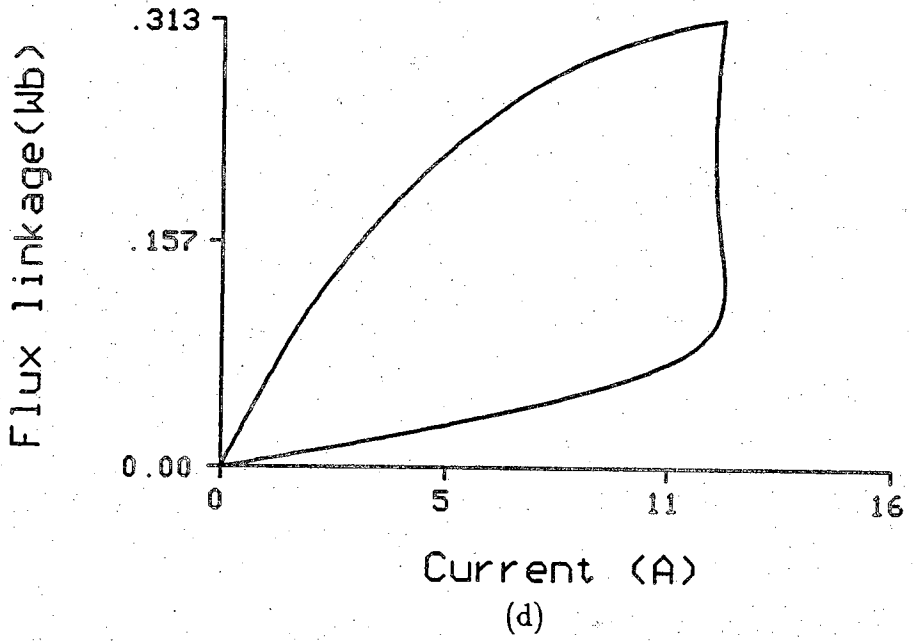

(d)

Figure 5.26. continued.

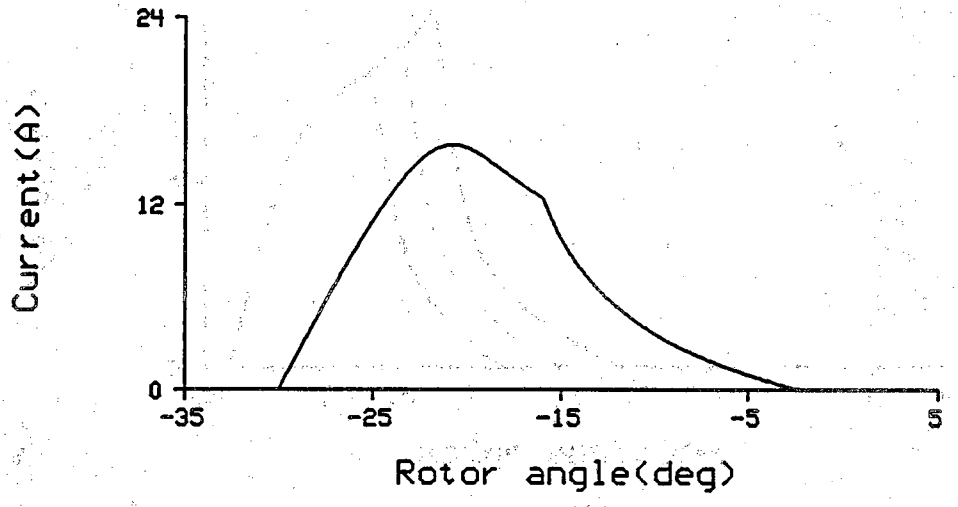

(a)

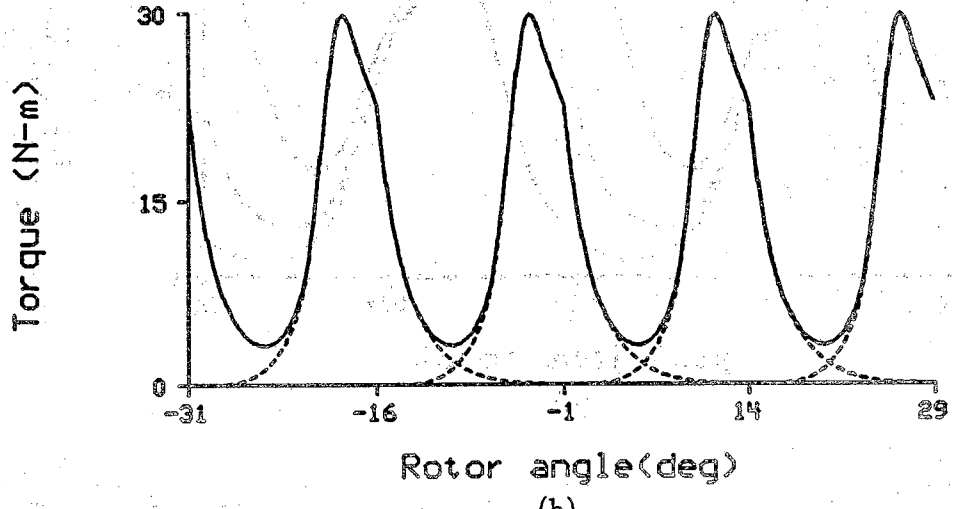

(b)

Figure 5.27. SRM characteristics at 1500 rpm
(a) current
(b) torque
(c) flux linkage
(d) energy conversion loop

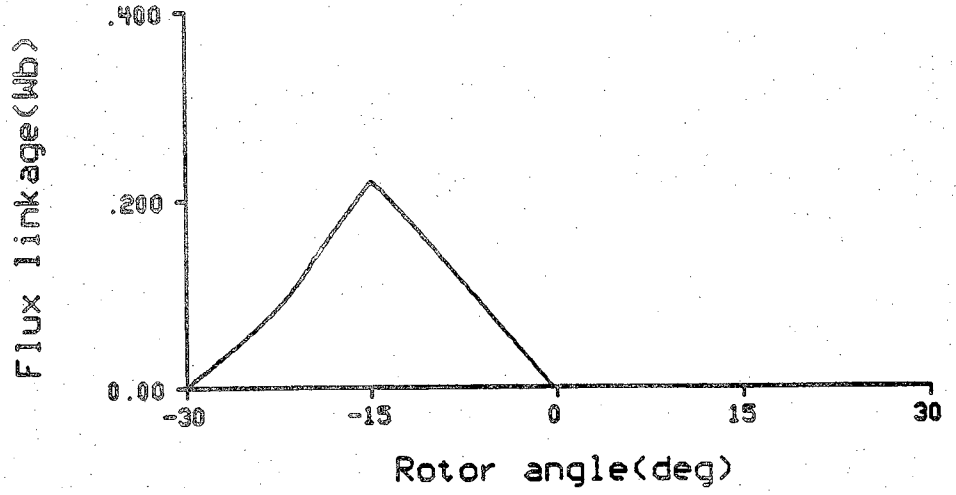

(c)

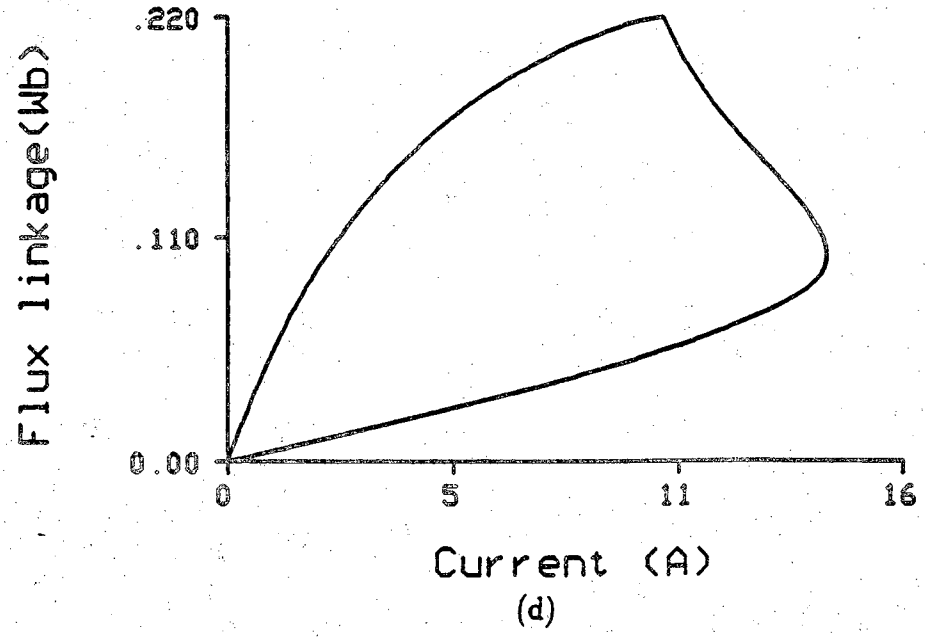

(d)

Figure 5.27. continued.

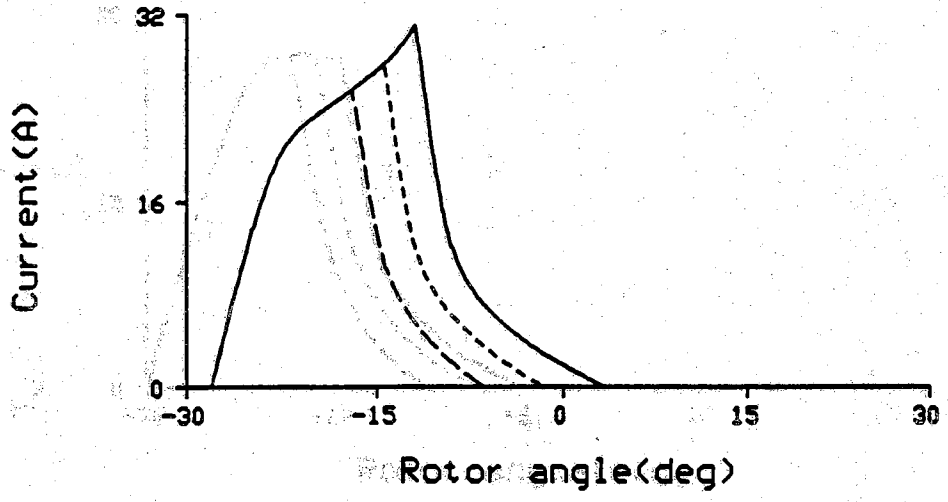

(a)

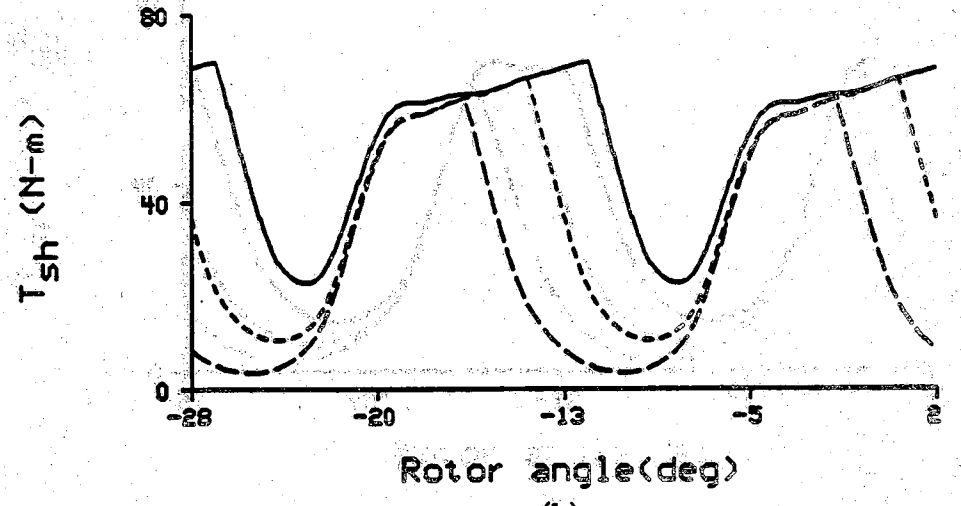

(b)

Figure 5.28. SRM characteristics at 750 rpm, constant on-angle
(a) current
(b) torque
(c) energy conversion loop

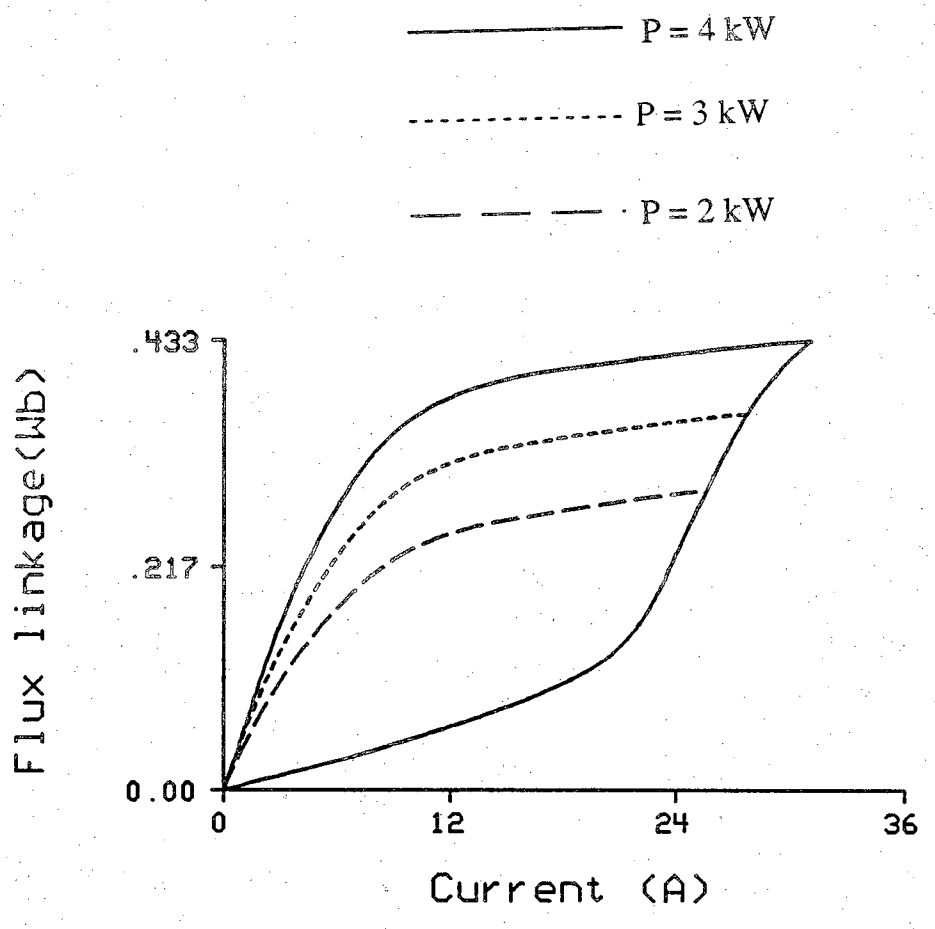

(c)

Figure 5.28. continued.

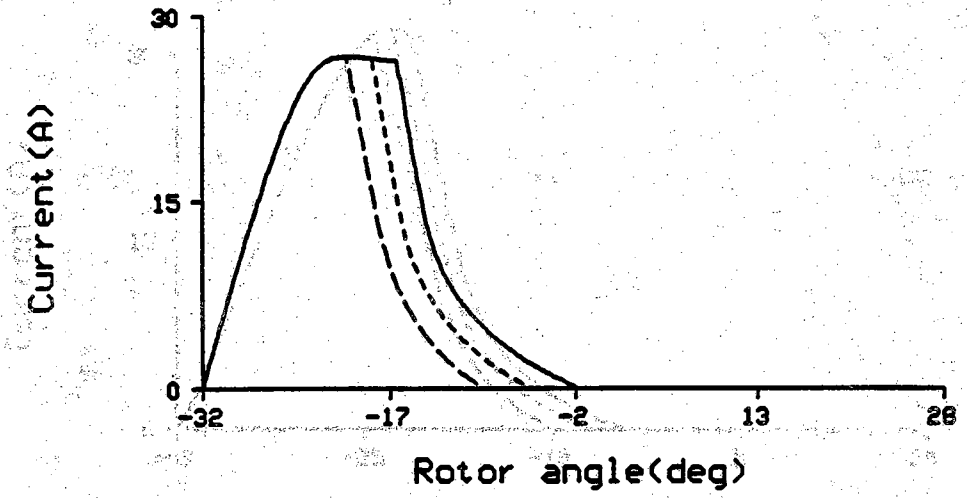

(a)

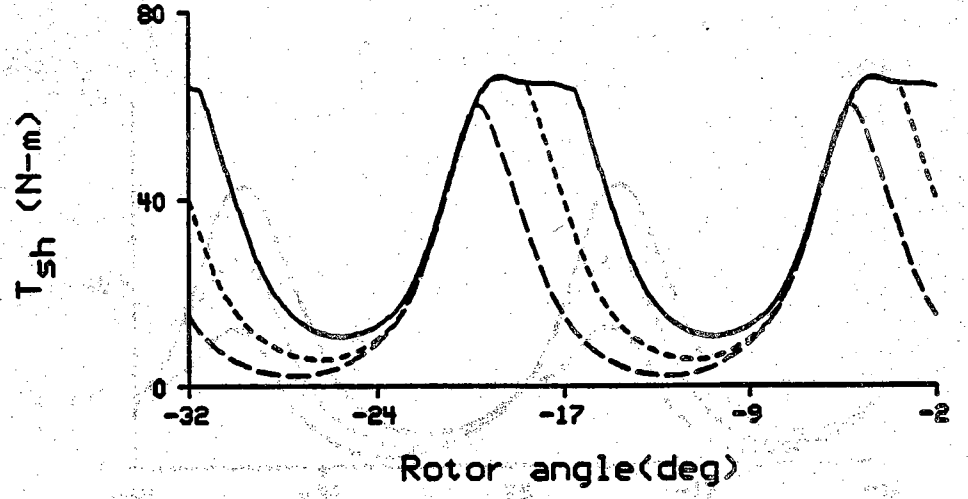

(b)

Figure 5.29. SRM characteristics at 1000 rpm, constant on-angle
(a) current
(b) torque
(c) energy conversion loop

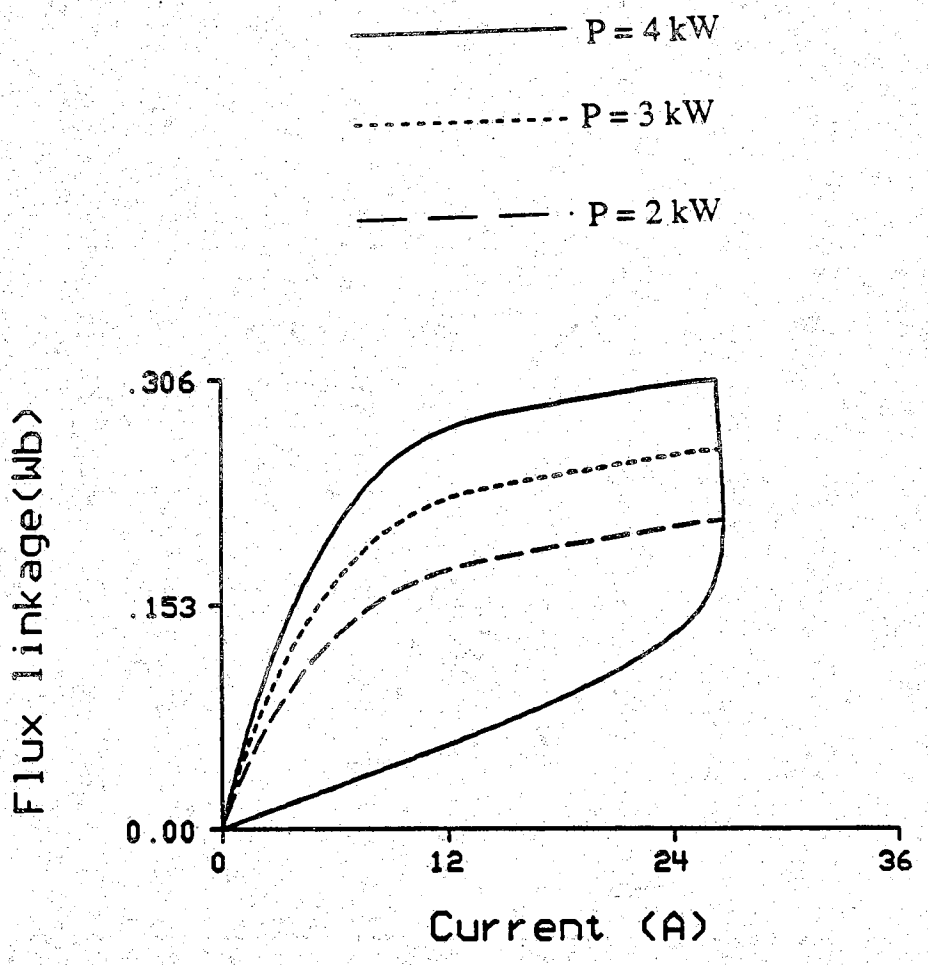

(c)

Figure 5.29. continued.

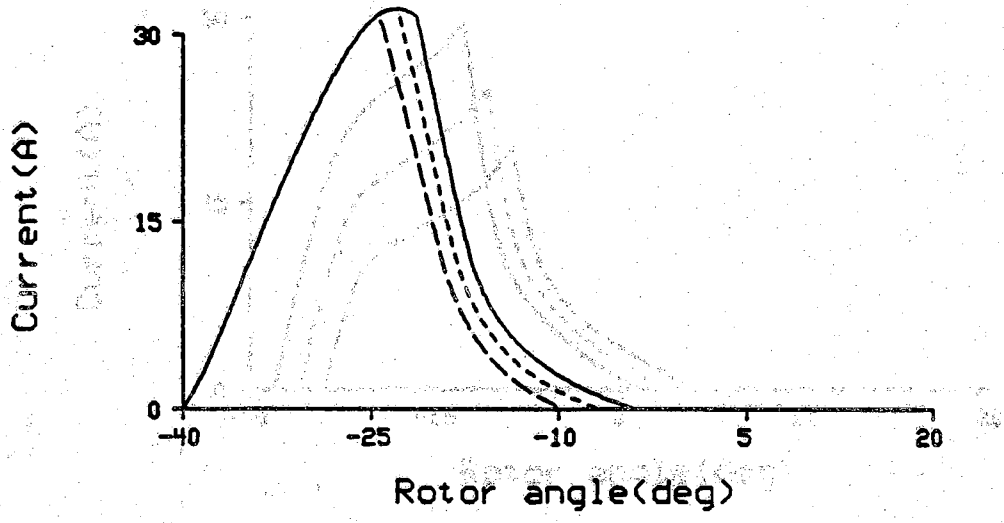

(a)

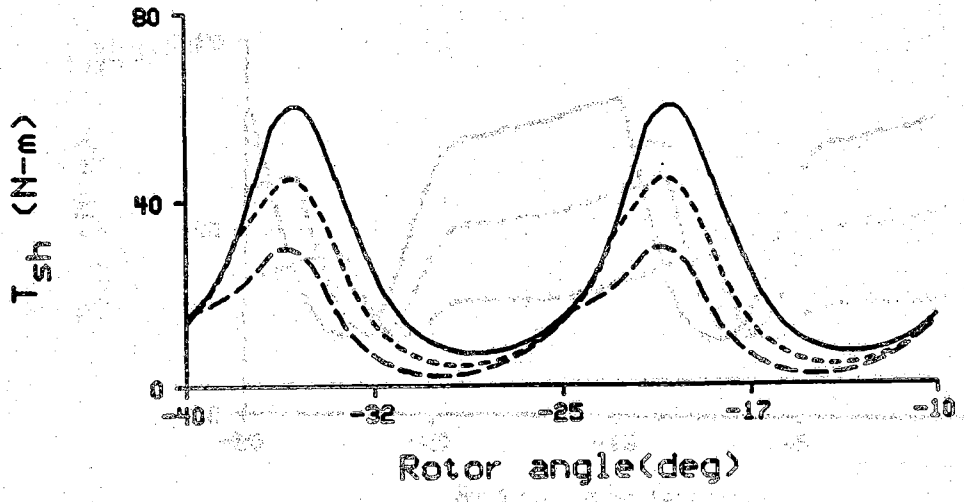

(b)

Figure 5.30. SRM characteristics at 1500 rpm, constant on-angle
(a) current
(b) torque
(c) energy conversion loop

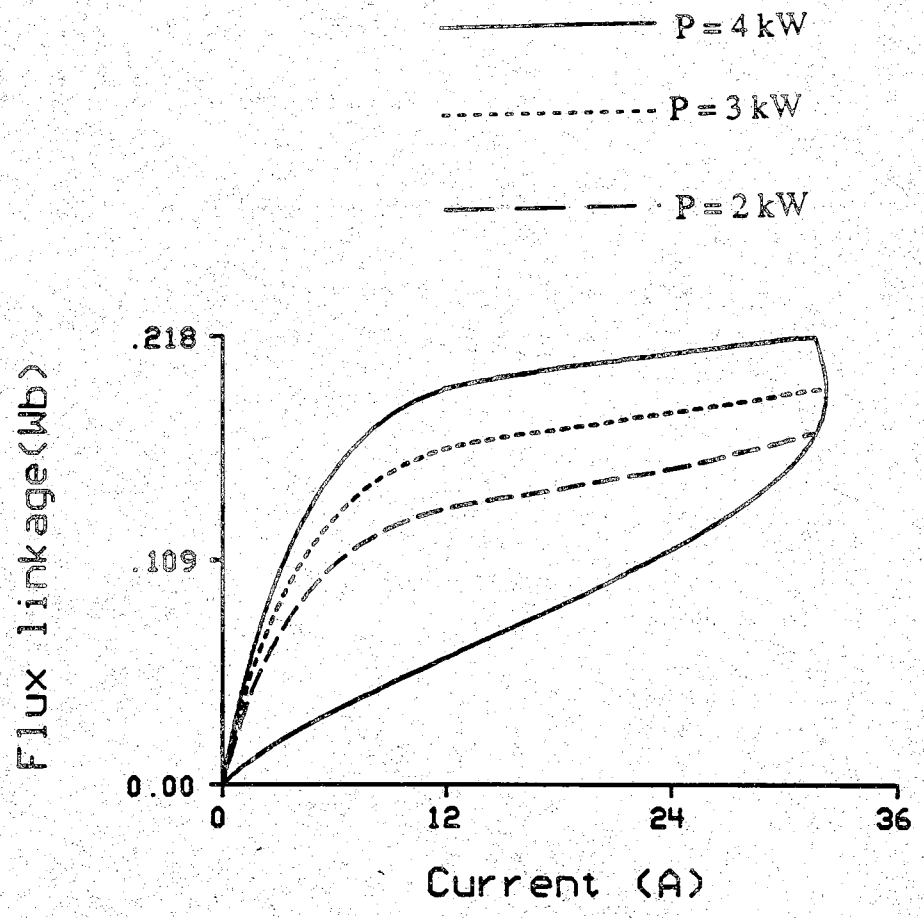

(c)

Figure 5.30. continued.

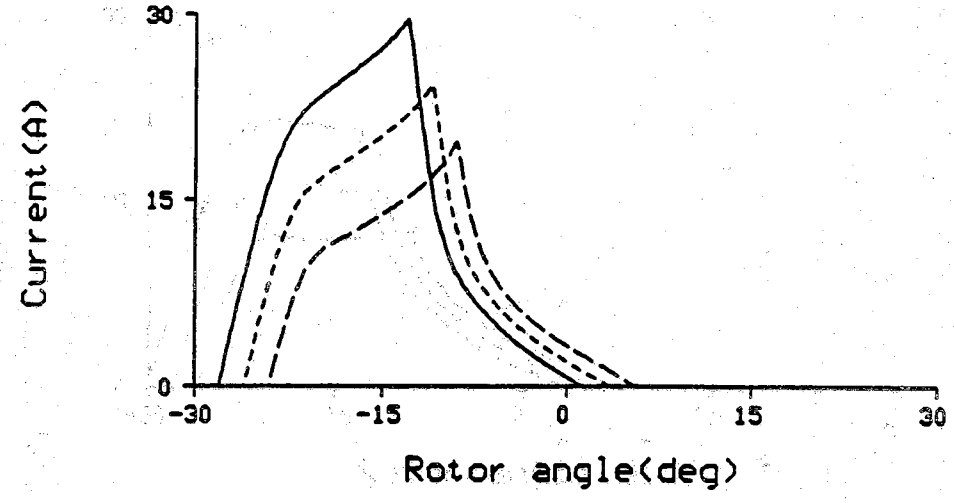

(a)

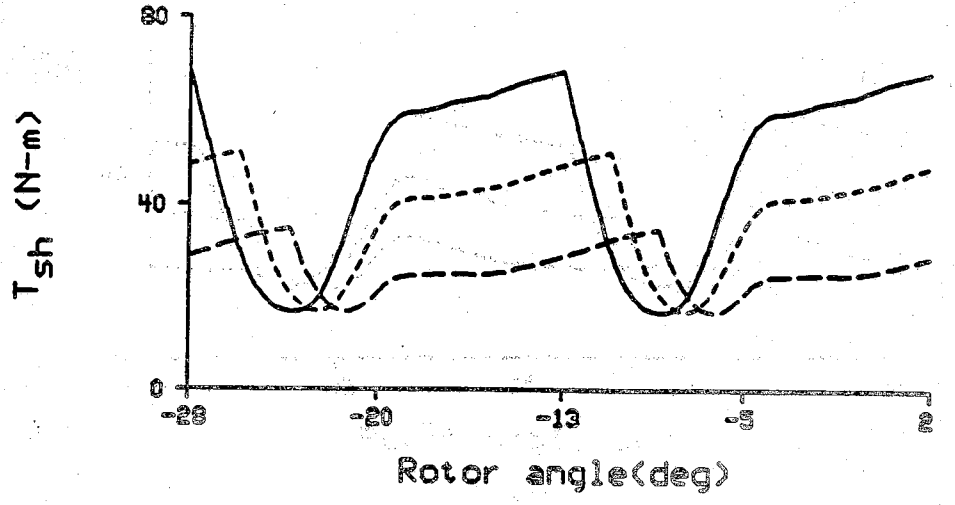

(b)

Figure 5.31. SRM characteristics at 750 rpm, constant conduction-angle
(a) current
(b) torque
(c) energy conversion loop

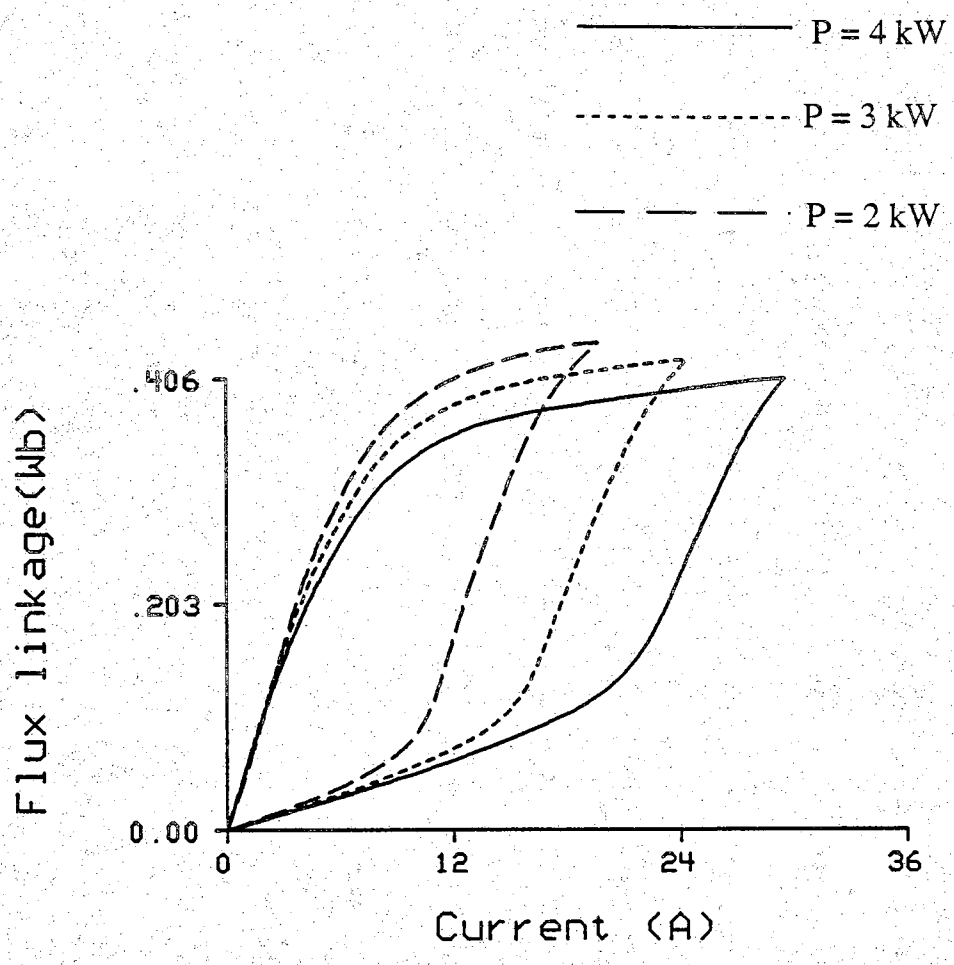

(c)

Figure 5.31. continued.

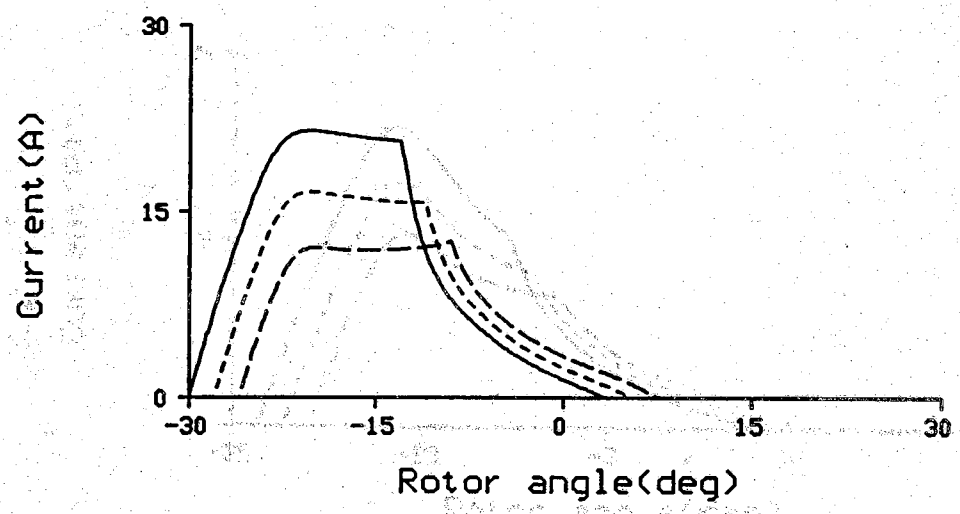

(a)

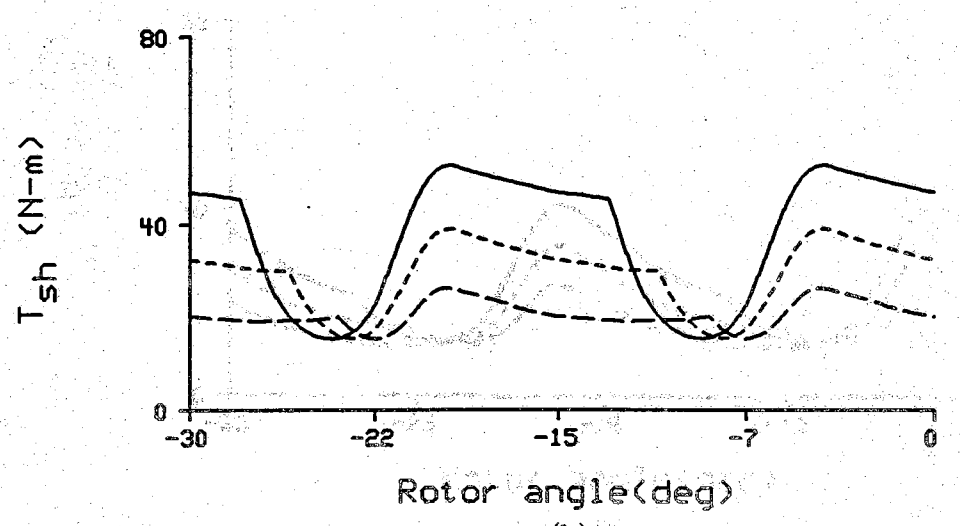

(b)

Figure 5.32. SRM characteristics at 1000 rpm, constant conduction-angle
(a) current
(b) torque
(c) energy conversion loop

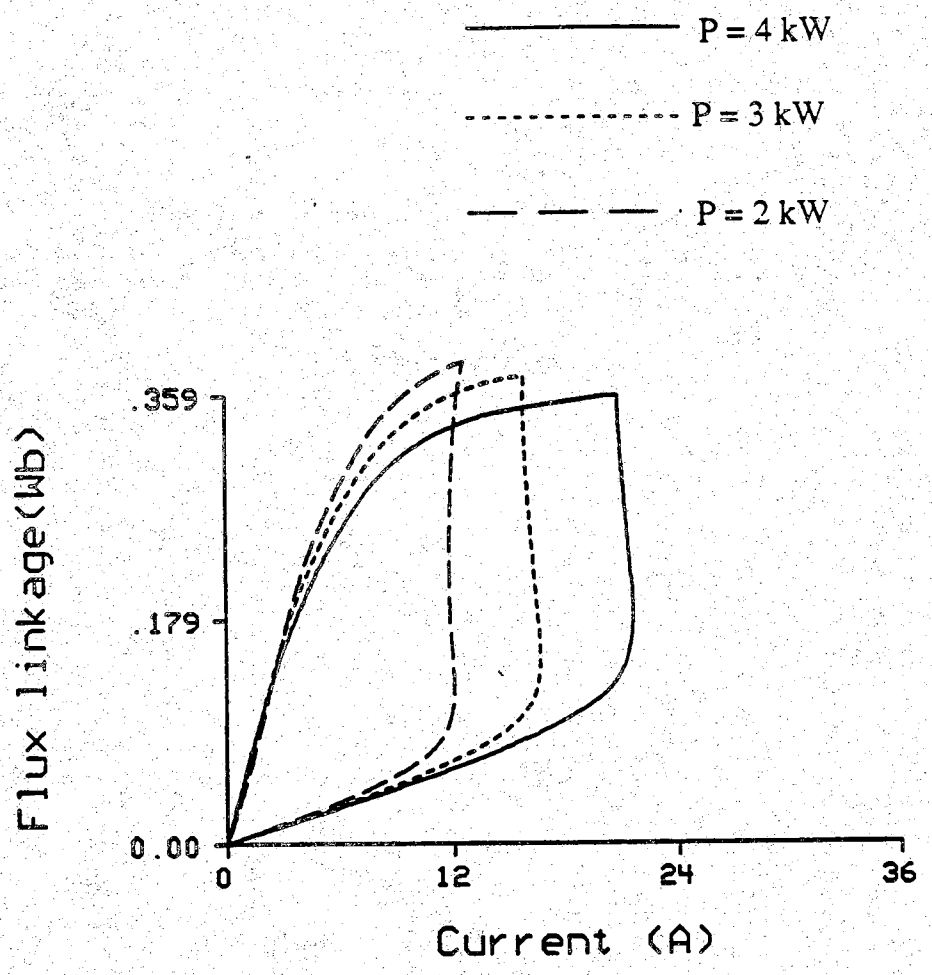

(c)

Figure 5.32. continued.

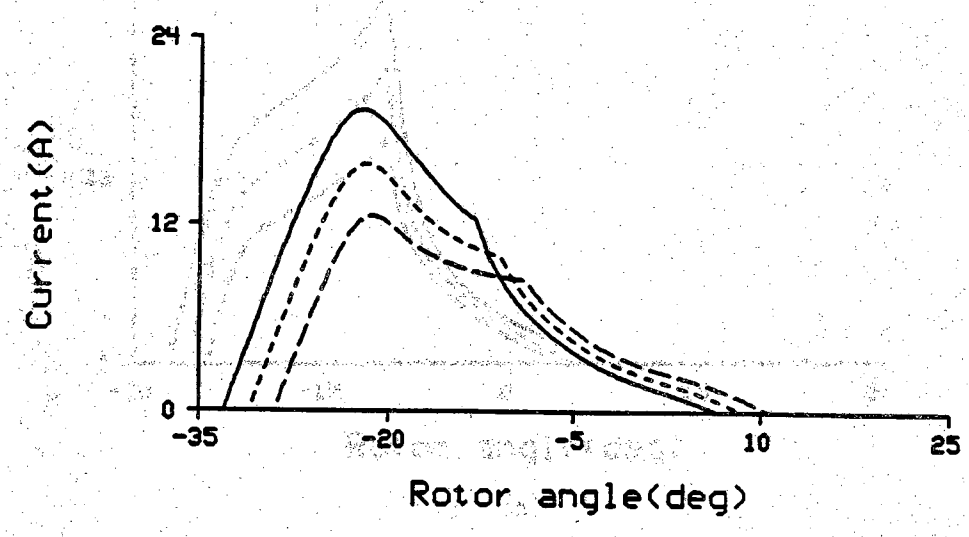

(a)

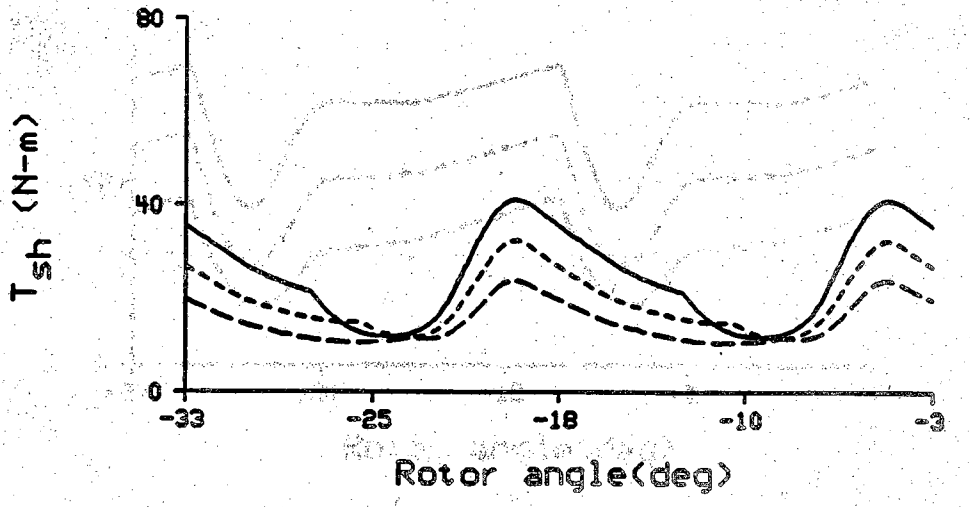

(b)

Figure 5.33. SRM characteristics at 1500 rpm, constant conduction-angle
(a) current
(b) torque
(c) energy conversion loop

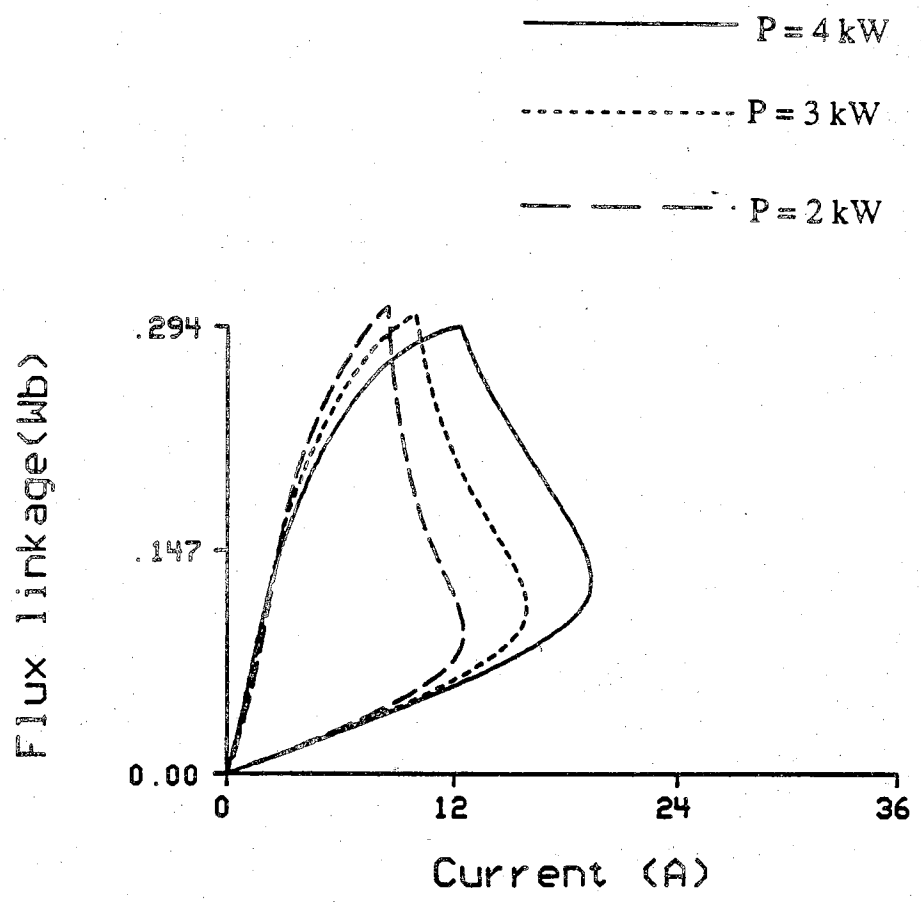

(c)

Figure 5.33. continued.

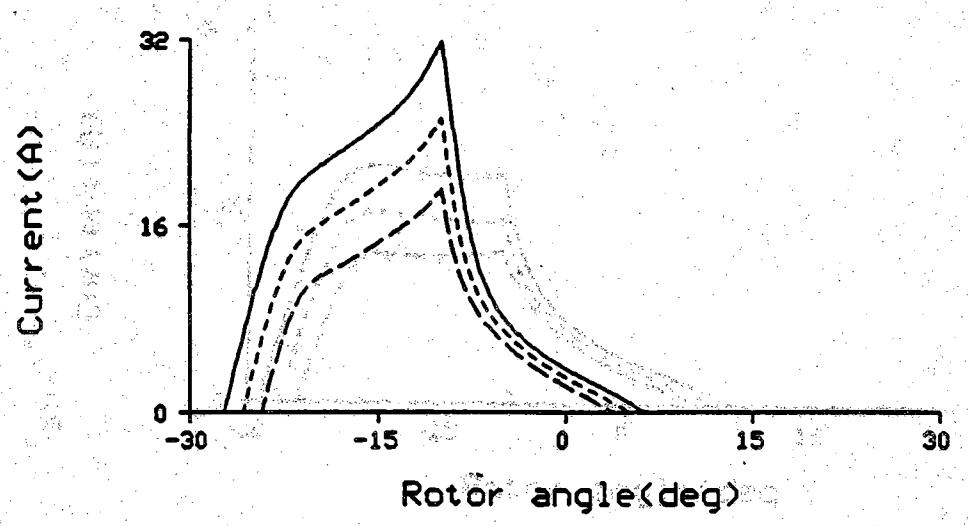

(a)

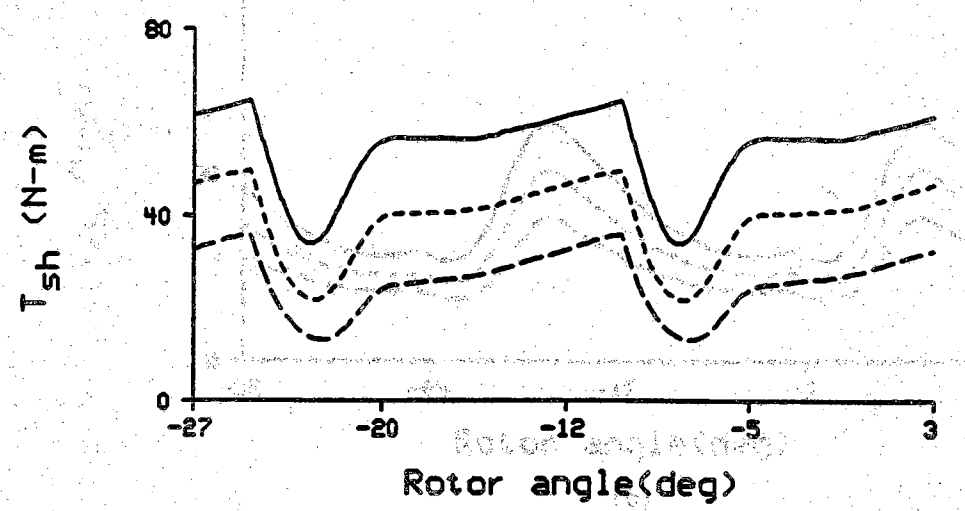

(b)

Figure 5.34. SRM characteristics at 750 rpm, constant off-angle
(a) current
(b) torque
(c) energy conversion loop

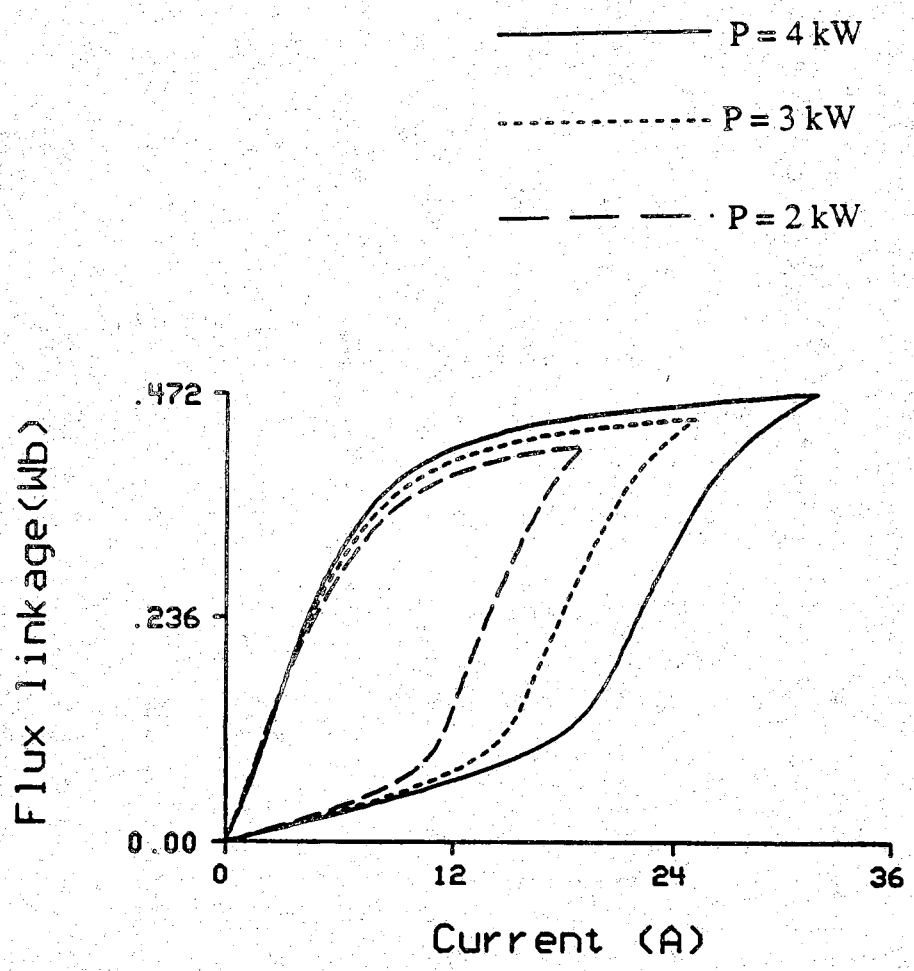

(c)

Figure 5.34. continued.

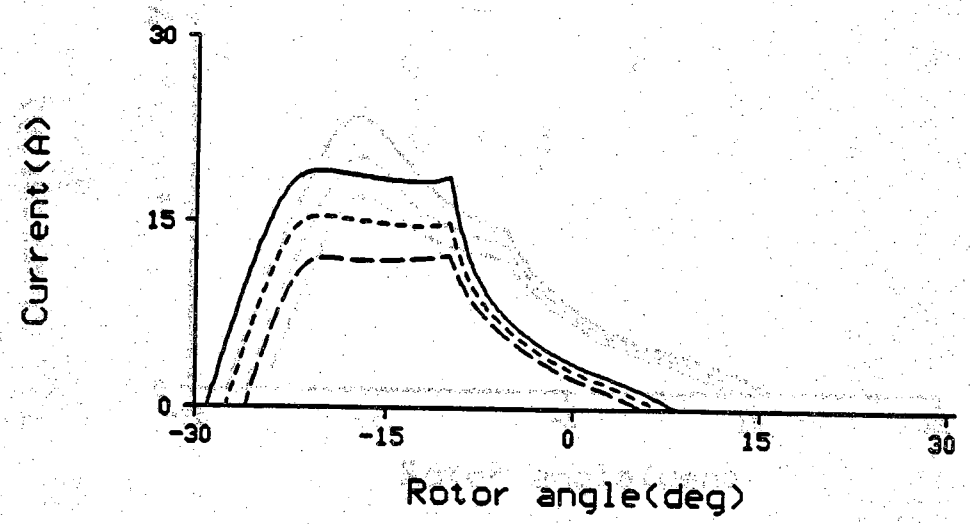

(a)

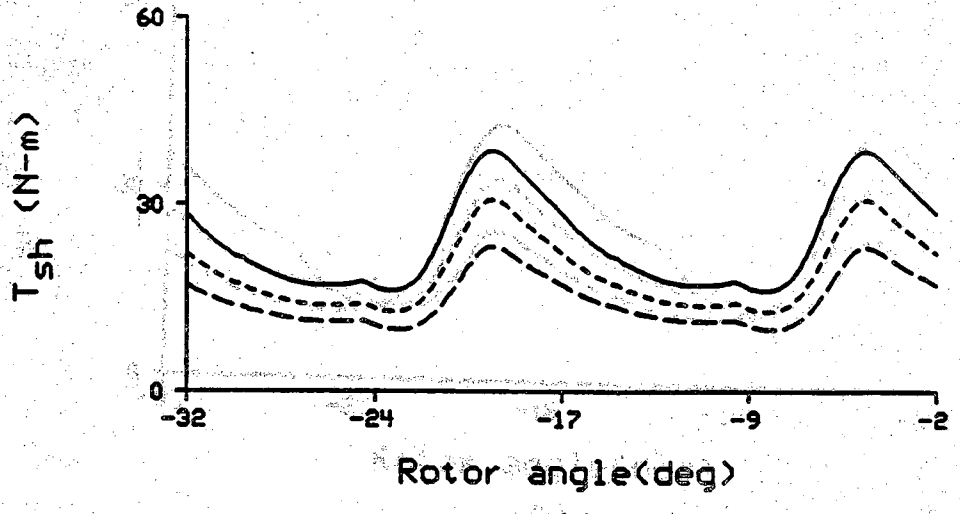

(b)

Figure 5.35. SRM characteristics at 1000 rpm, constant off-angle
(a) current
(b) torque
(c) energy conversion loop

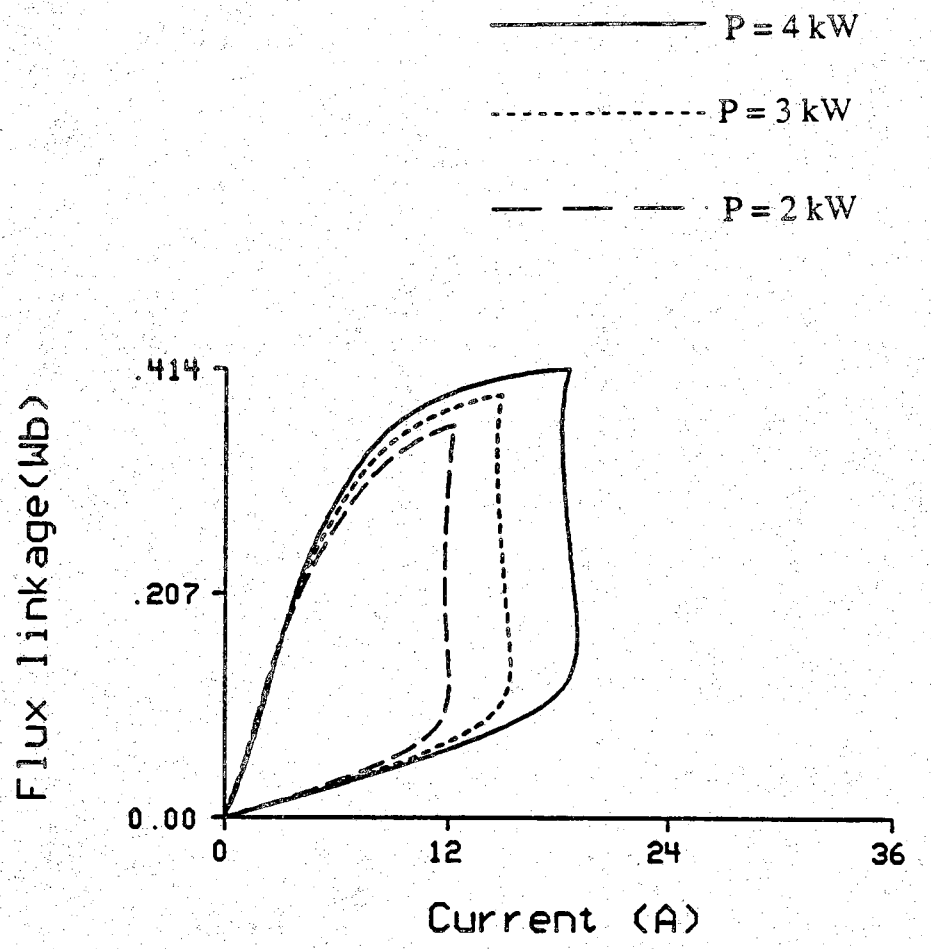

(c)

Figure 5.35. continued.

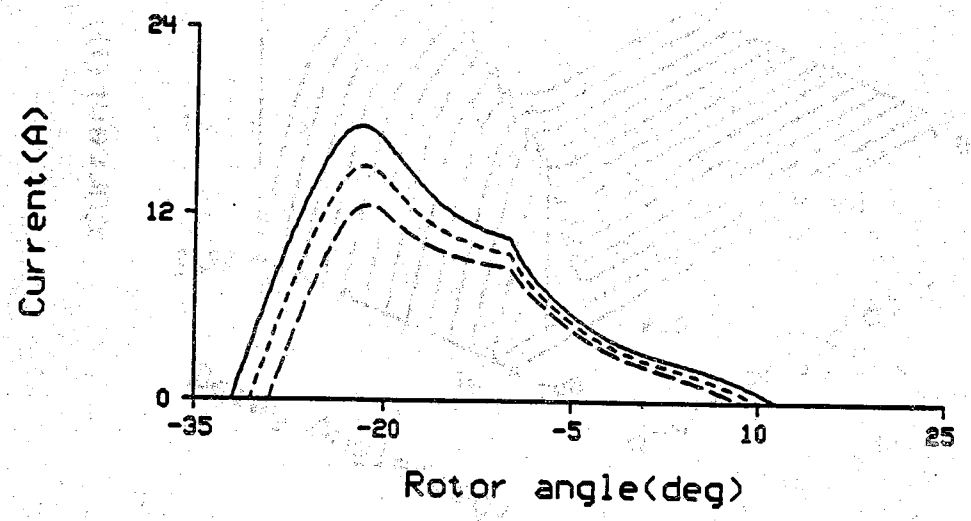

(a)

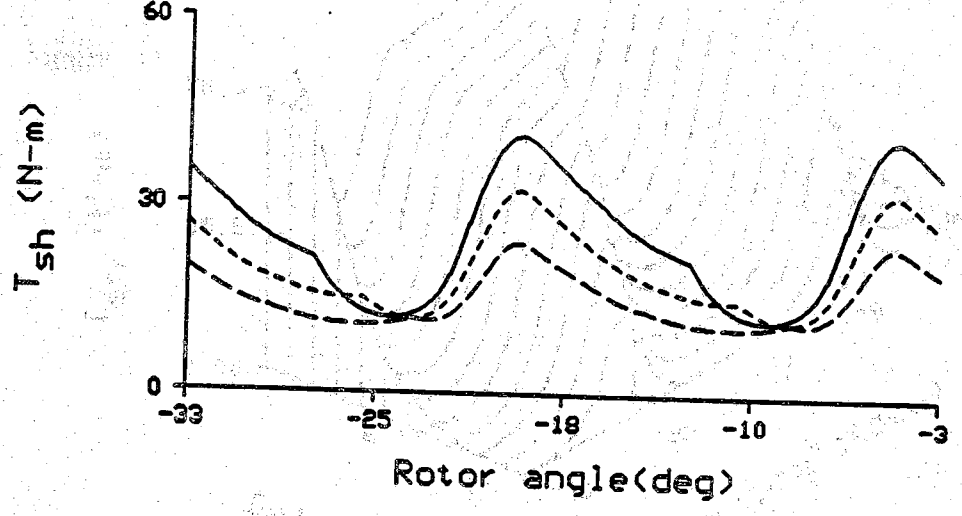

(b)

Figure 5.36. SRM characteristics at 1500 rpm, constant off-angle
(a) current
(b) torque
(c) energy conversion loop

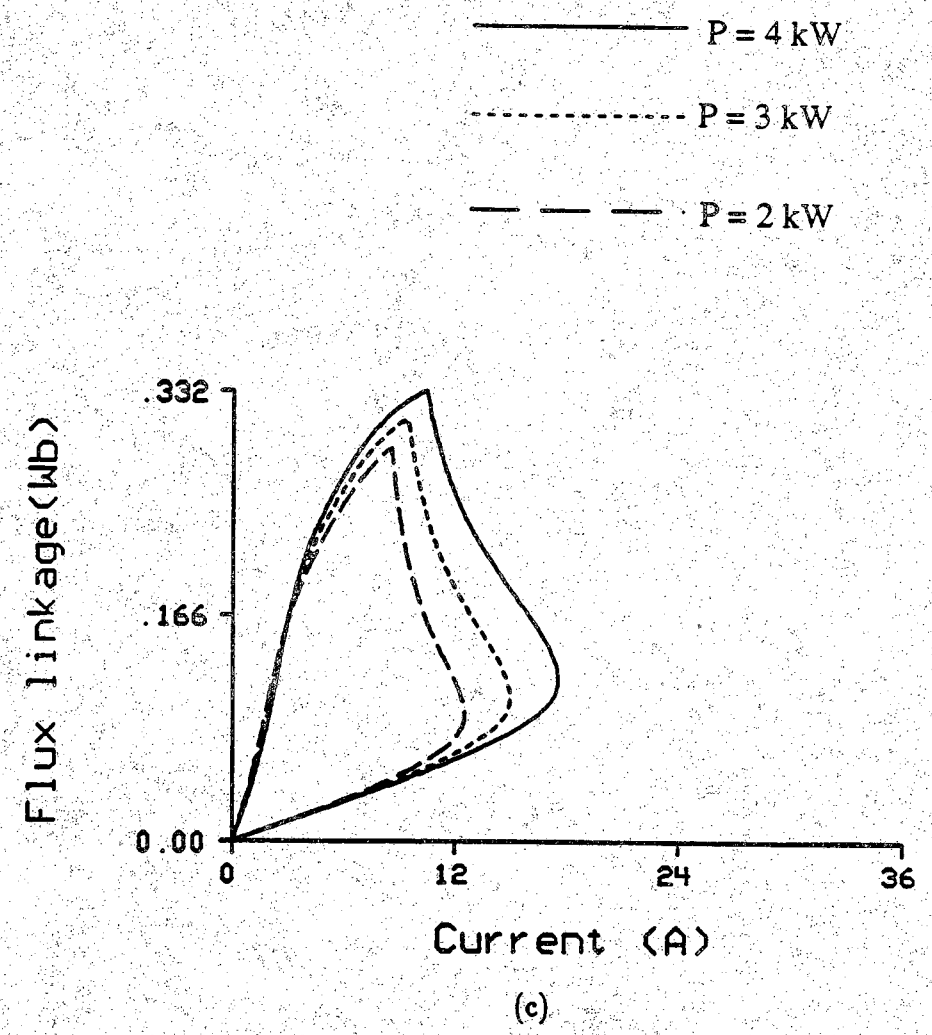

(c)

Figure 5.36. continued.

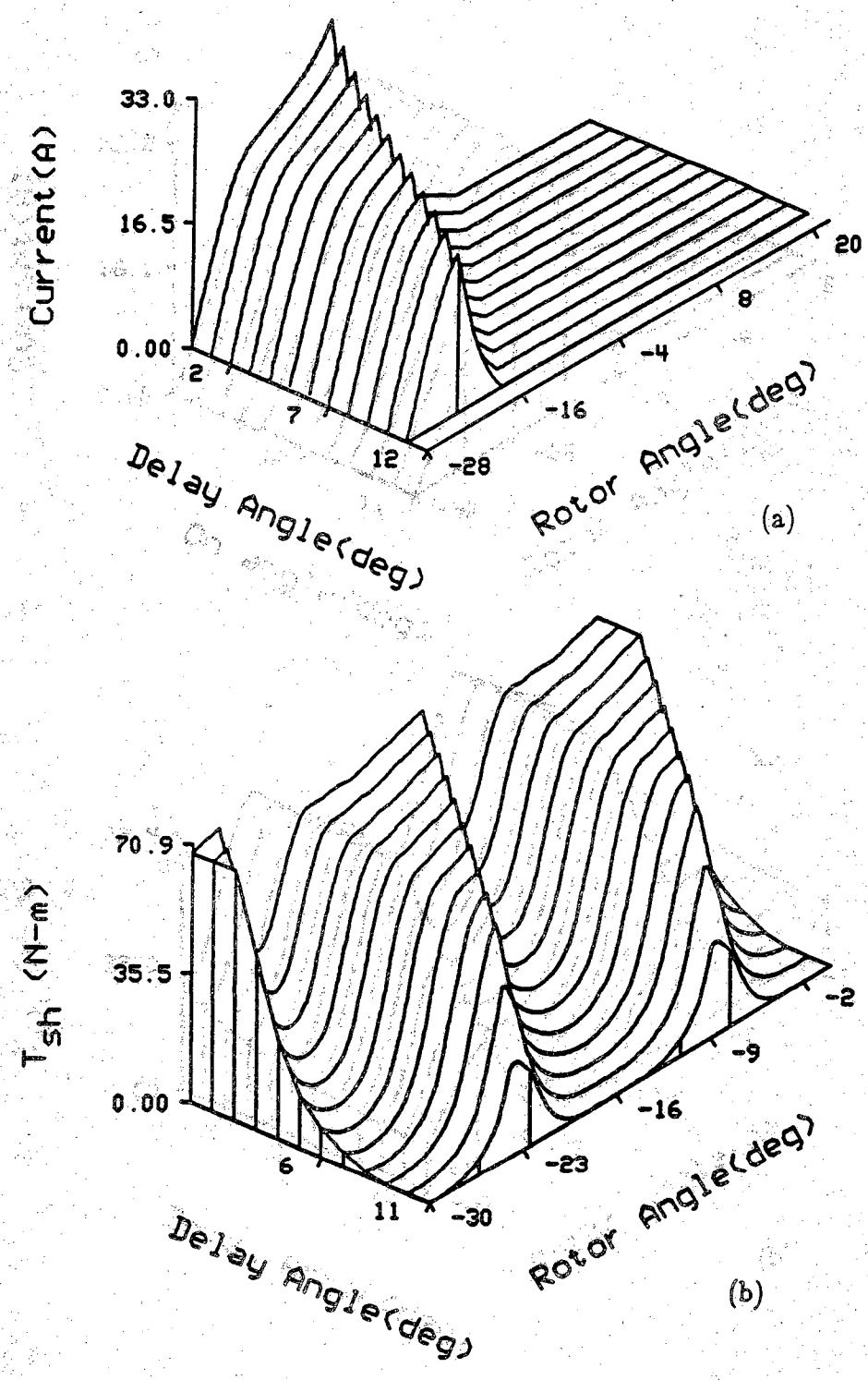

Figure 5.37. SRM profiles at 750 rpm, constant θ_{on}
(a) current
(b) shaft torque

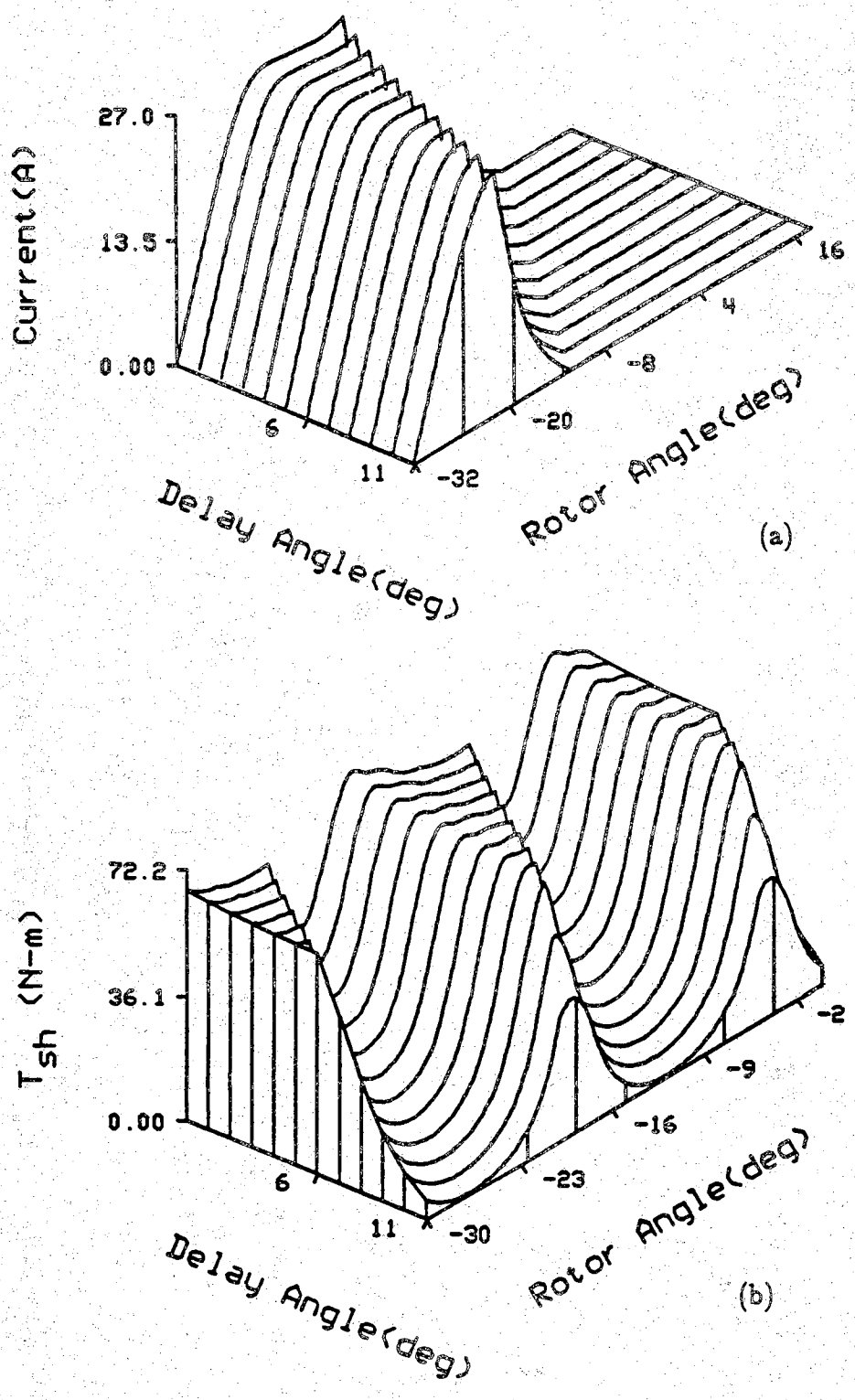

Figure 5.38. SRM profiles at 1000 rpm, constant θ_{on}
(a) current
(b) shaft torque

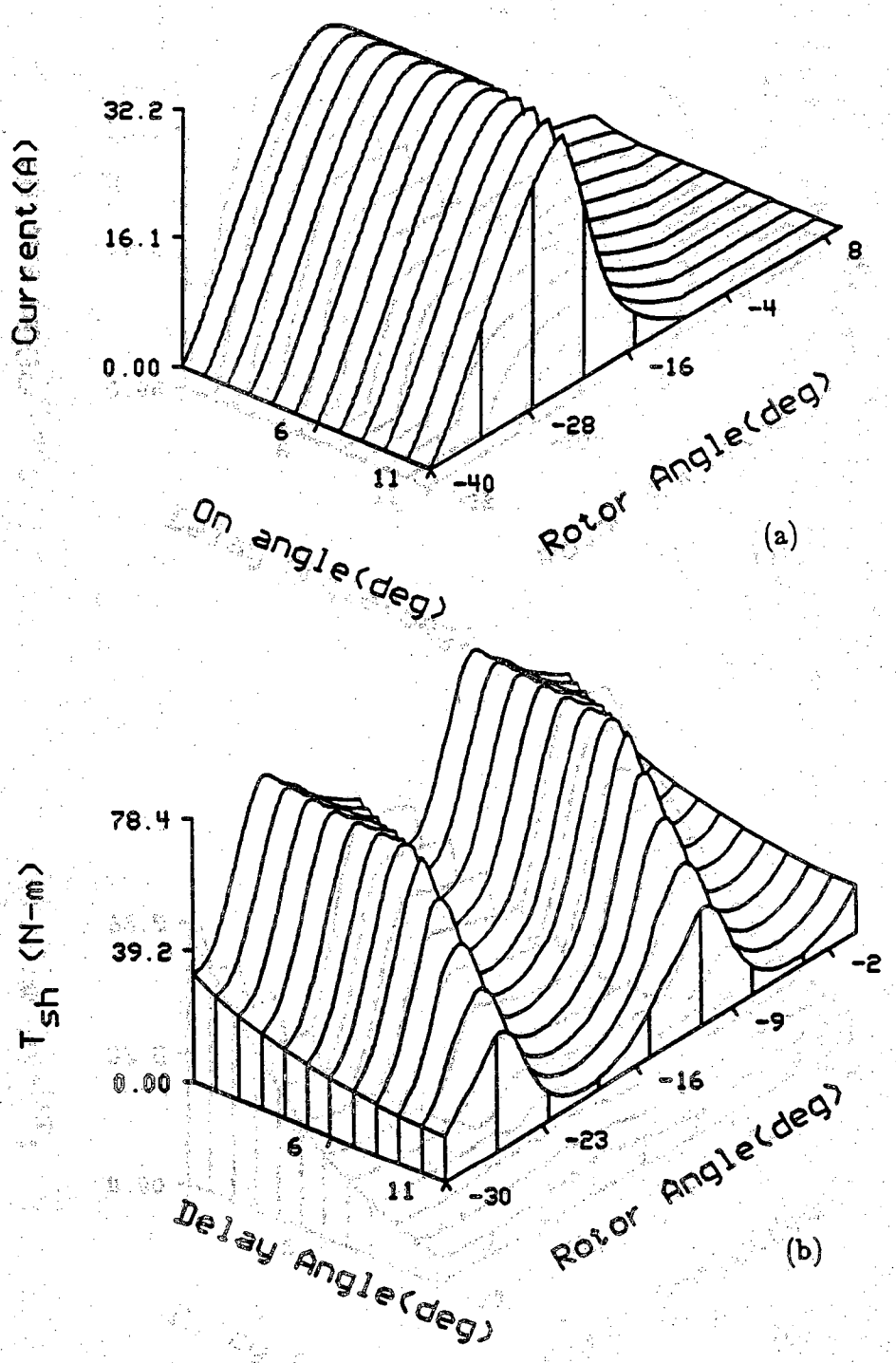

Figure 5.39. SRM profiles at 1500 rpm, constant θ_{on}
(a) current
(b) shaft torque

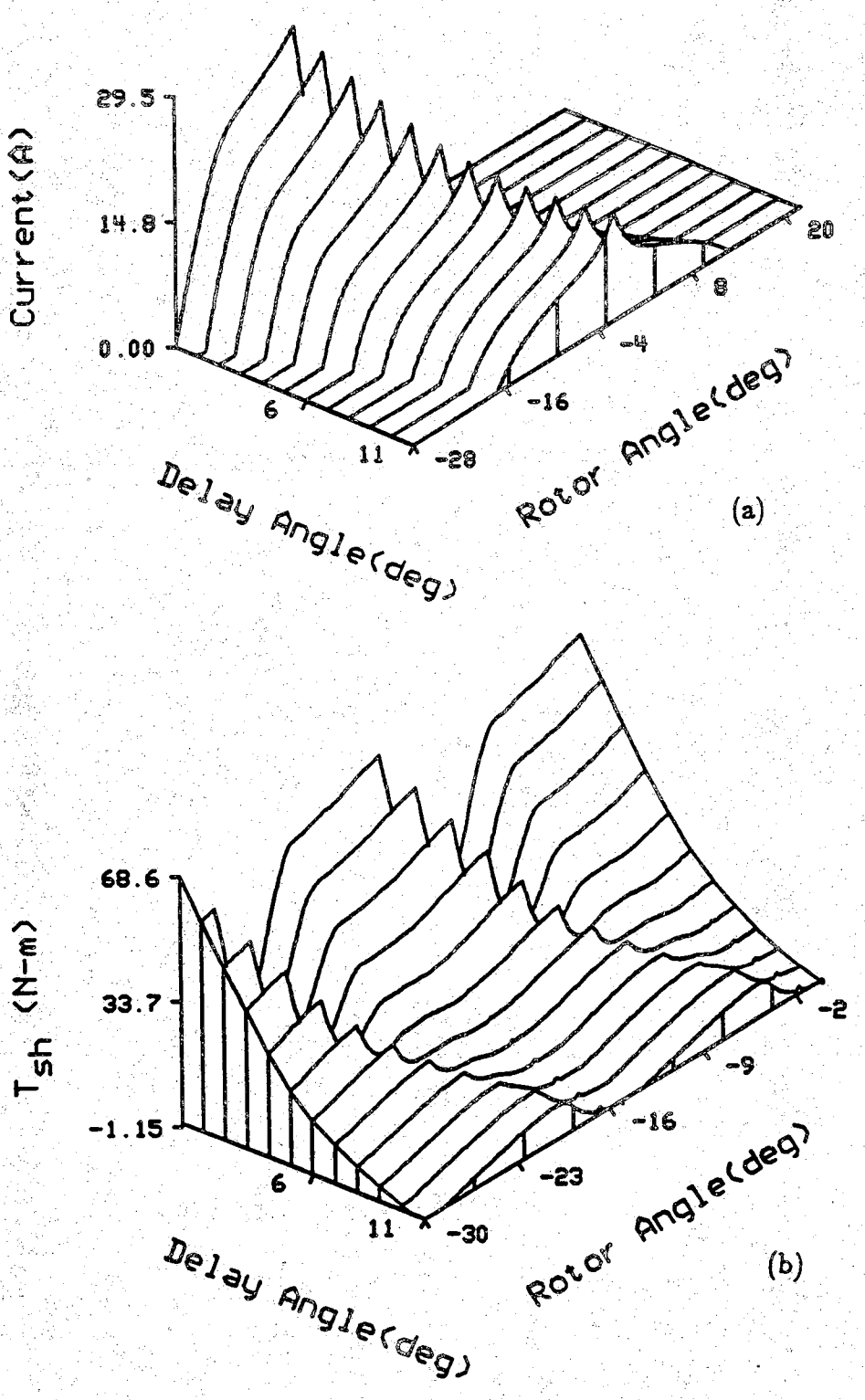

Figure 5.40. SRM profiles at 750 rpm, constant θ_{cond}
(a) current
(b) shaft torque

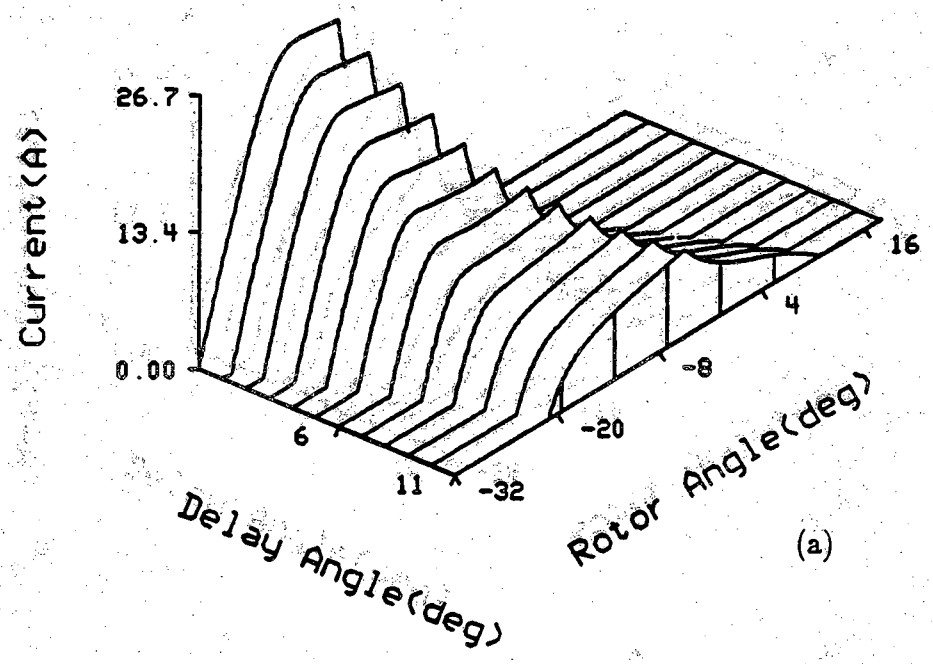

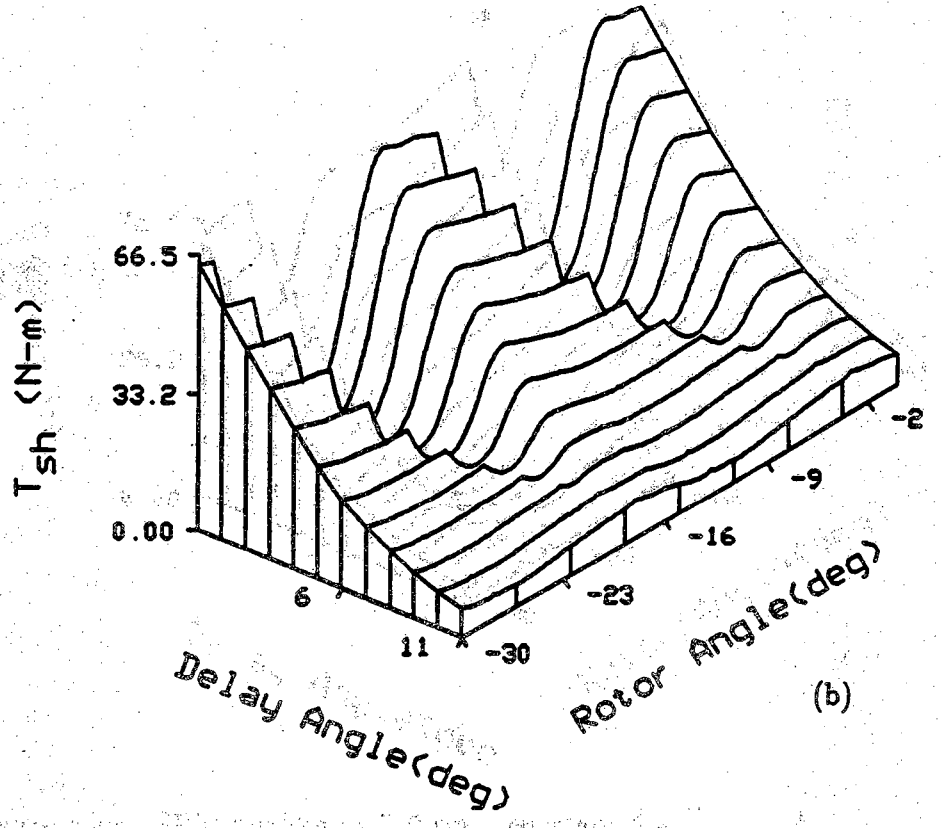

Figure 5.41. SRM profiles at 1000 rpm, constant θ_{cond}

(a) current
(b) shaft torque

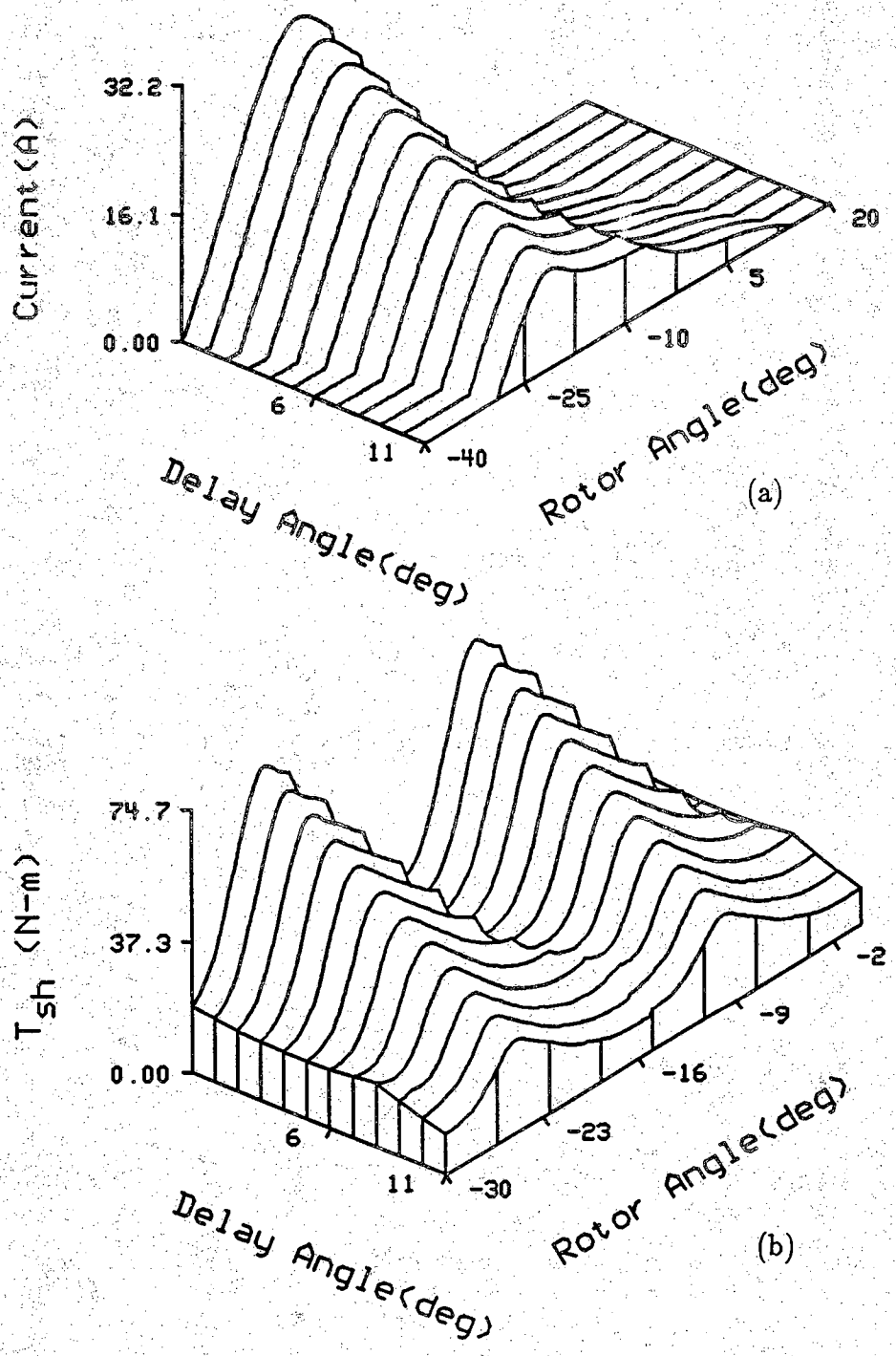

Figure 5.42. SRM profiles at 1500 rpm, constant θ_{cond}
(a) current
(b) shaft torque

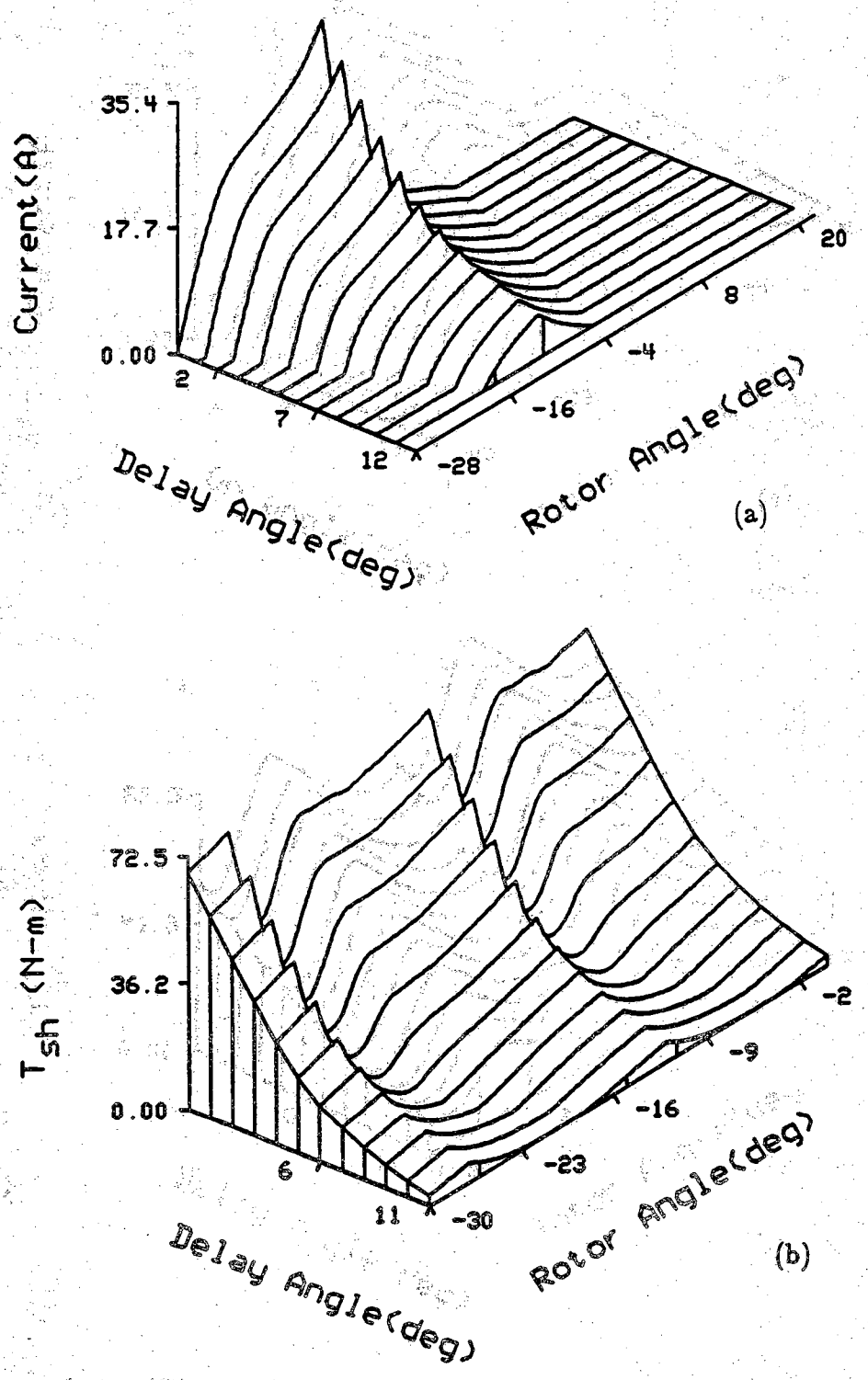

Figure 5.43. SRM profiles at 750 rpm, constant θ_{off}
(a) current
(b) shaft torque

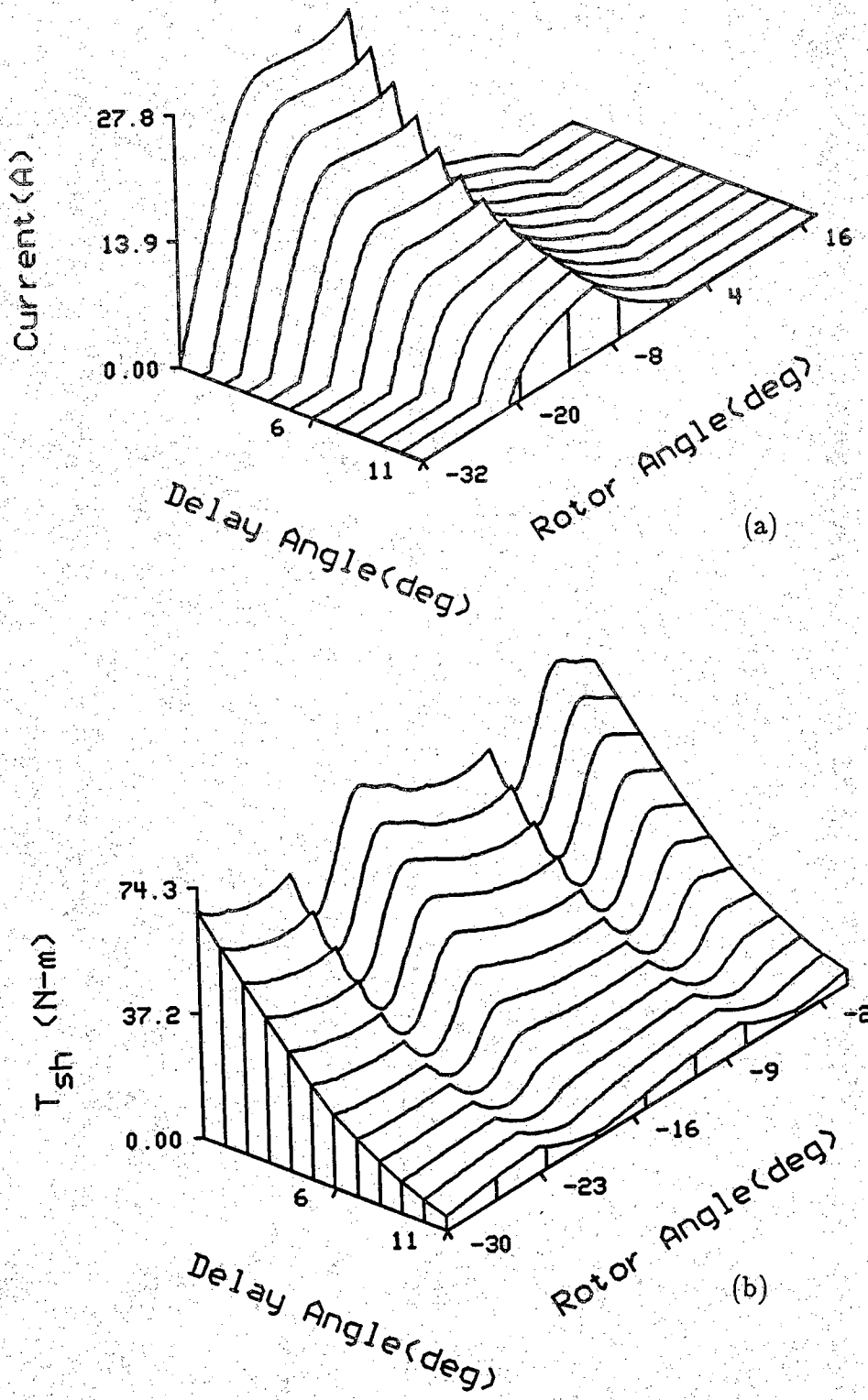

Figure 5.44. SRM profiles at 1000 rpm, constant θ_{off}
(a) current
(b) shaft torque

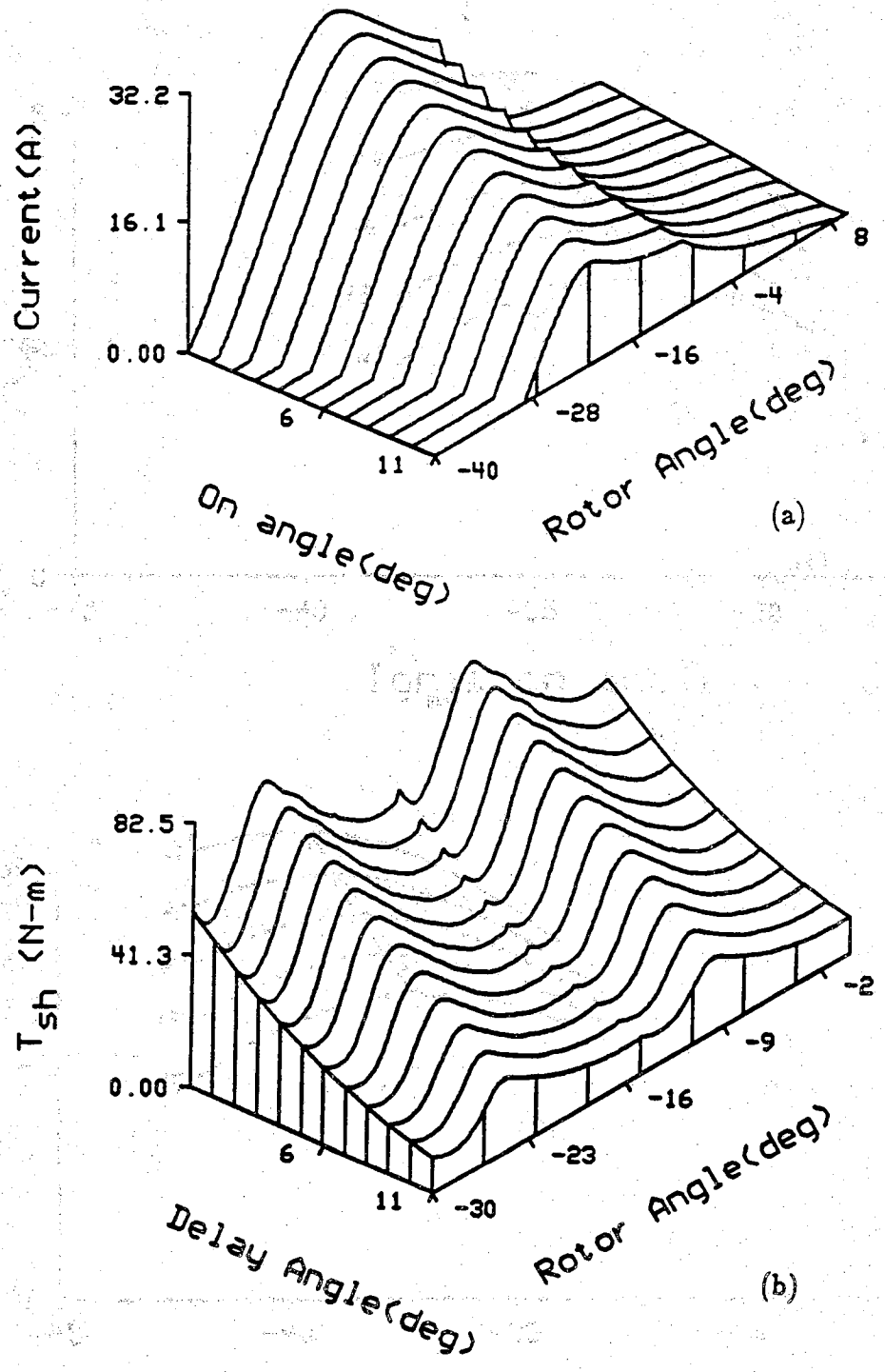

Figure 5.45. SRM profiles at 1500 rpm, constant θ_{off}
(a) current
(b) shaft torque

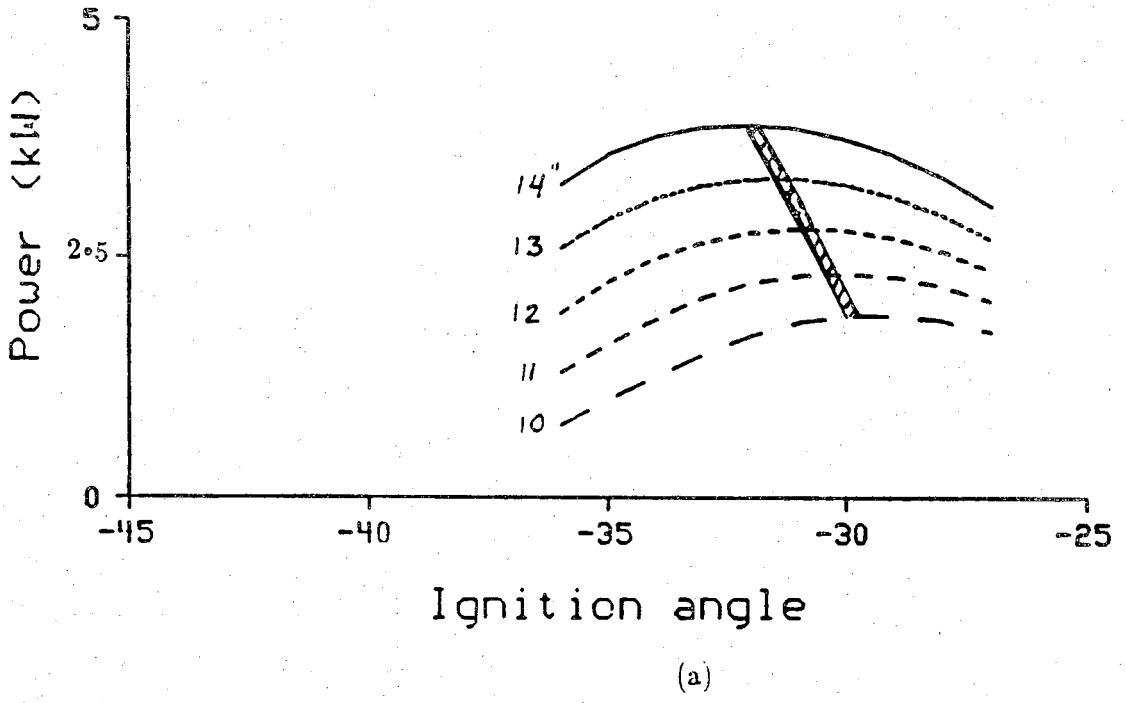

(a)

Figure 5.46 Average power vs. ignition angle at different conduction angles
(a) 750 rpm
(b) 1000 rpm
(c) 1500 rpm

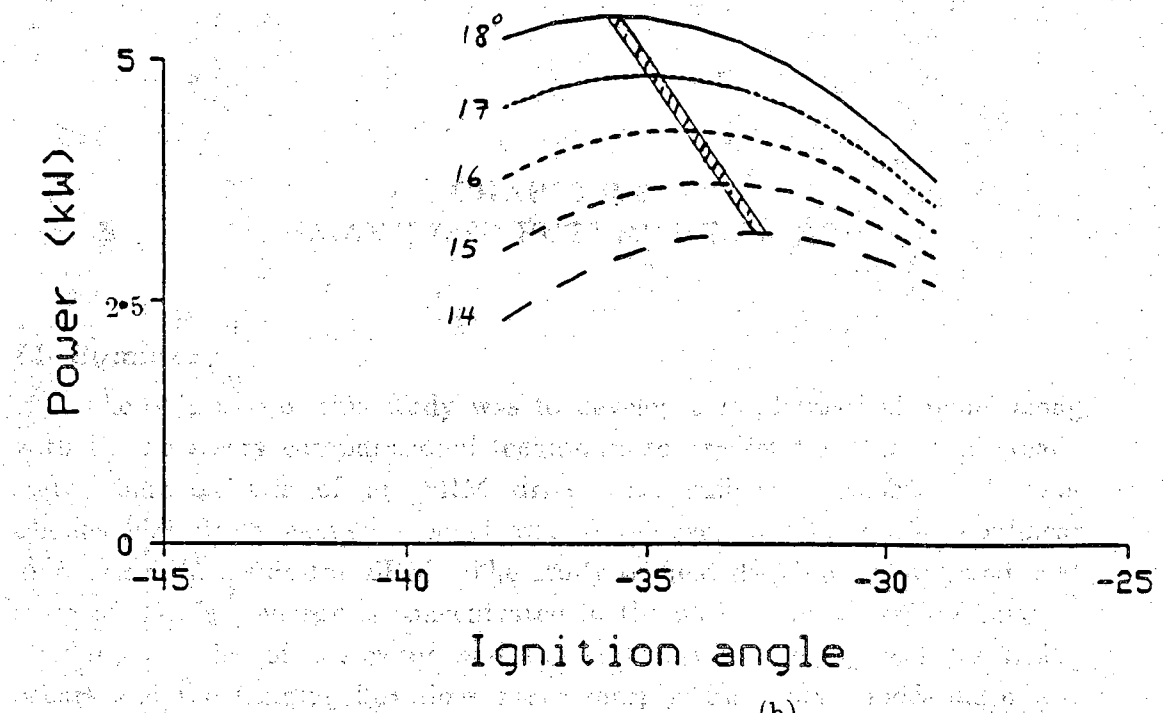

(b)

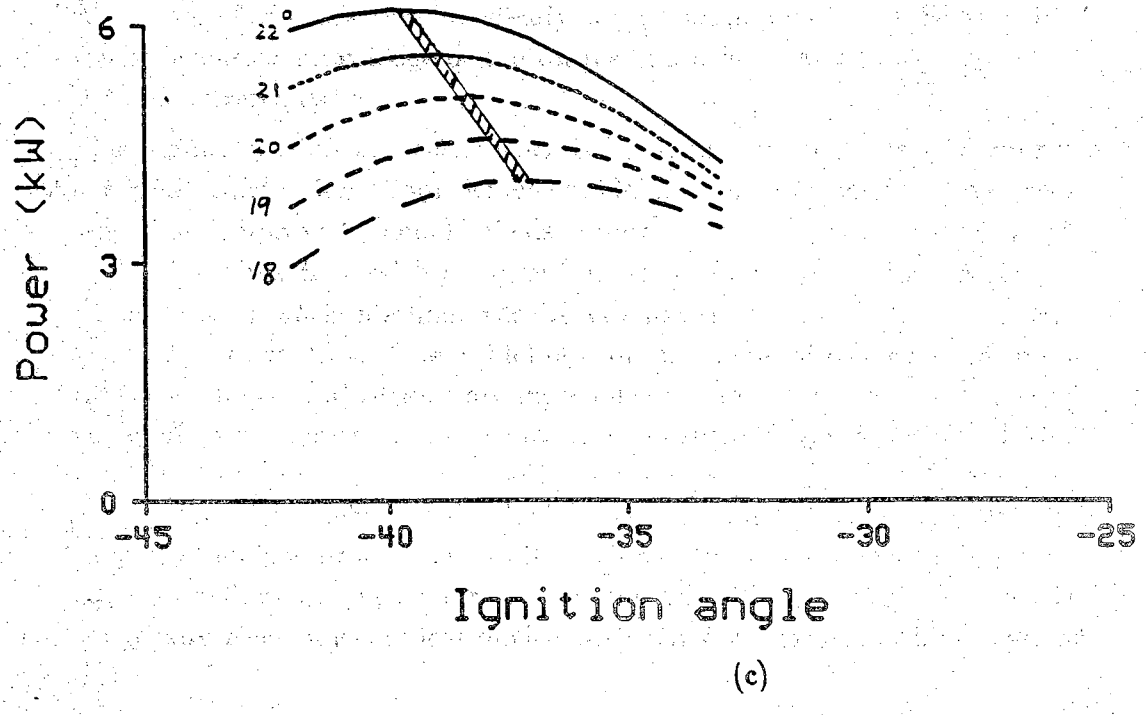

(c)

Figure 5.46. continued.

CHAPTER 6
SUMMARY AND FUTURE RESEARCH

6.1 Summary

The objective of this study was to develop a mathematical model along with the necessary computational techniques to predict the static and steady state characteristics of an SRM drive with sufficient accuracy. A two-dimensional finite element model was developed to handle the nonlinear magnetic field inside the SRM. The study of field distribution revealed that most of the field energy is concentrated in the narrow airgap region between overlapped poles of the rotor and the stator, where high local saturation occurs and the fringing flux lines curve sharply. Inadequate modeling of the field in this region resulted in adverse inaccuracies in the results at the postprocessing stage regardless of the computational method used. However, a realistic model for prediction of steady state characteristics of SRM drives requires an accurate knowledge of the torque and other static characteristics of the SRM as a prerequisite.

The main contribution of this work is the study on the sources of error in SRM torque calculation from which guidelines on the model have been derived. The improved model yields accurate and smooth torque/angle characteristics when used with common methods of torque calculation such as the global virtual work method, the Maxwell-stress tensor method, and the local virtual work method. The guidelines for the shape of elements and mesh uniformity in the critical regions are more effective and efficient than the usual technique of just increasing the elemental density. It has been found that following the proposed guidelines also improves the accuracy of the overall FE solution by proper modeling of the field in critical regions, thus, improving the accuracy of other postprocessing results such as, flux linkage and inductances, too. The guidelines are not restricted to the case of an SRM; they can be applied to any electromechanical device with narrow airgap and high level of saturation.

The spinoffs from the capability to predict the static characteristics with improved accuracy are many: the obvious use of this capability will be in design for optimization or performance studies, as demonstrated by the brief sensitivity study in Chapter 4. A more interesting use of the capability is the transient simulation of the SRM drive. The work on steady state simulation establishes the simulation techniques for the transient simulation. In this case, the steady state simulation also provided us with the opportunity to examine and study the purpose and reasons behind the control strategies that are used in the test motor.

To predict the steady state performance of the SRM drive, the voltage equation of the phase winding was simulated. State-dependent coefficients of the voltage equation were updated using a B-cubic spline interpolation technique on the static characteristics. For this purpose, static characteristics of the SRM over a wide range of excitation currents for a period of phase inductance variation were obtained. The instantaneous torque and flux linkage were calculated for each current and rotor position using the same interpolation technique. Steady state characteristics over a wide range of torque and speed have been calculated using the developed model which compared favorably with the measured. The model can also be used for study of control strategies to obtain better performance in efficiency and smoother operation. The brief sensitivity analysis of Chapter 4 can be extended to other design parameters and material characteristics to study the optimality of design. By including the dynamics of the converter circuit in the present model, the model can be extended for the study of SRM drive transient behavior during load change, start-up, or fault condition.

6.2. Future Research

The work presented in this report can be extended to several areas of research as outlined below.

i) The accuracy of field solution and torque calculation can further be studied using hybrid type FE models. Also, automatic mesh generator programs to modify the mesh in the critical regions according to proposed guidelines will reduce the computational time and modeling effort.

ii) Optimal control of the switching circuit with respect to one or a compromise of performance measures is another extension to this work. Some of the performance measures, which can be

considered are as follows: maximizing specific torque, $(\frac{T_{ave}}{I_{ave}})$, minimizing torque ripple given by $\frac{(T_{max}-T_{min})}{T_{ave}}$, and maximizing kW/kVA rating of the drive.

iii) For specific application such as for low or high speed operation, or for high starting torque, optimization on both motor geometry and switching strategies could be performed with an integrated design approach for lower overall cost.

iv) Analysis of SRM drive transient behavior, especially during speed-up and during low speed mode of operation, is important.

v) Finally, the study of SRM iron losses is of particular importance for the motor designed for high speed operation. A transient FE model should be established to study the iron losses resulting from eddy current flow.

LIST OF REFERENCES

LIST OF REFERENCES

[1] R.H. Park, "*Two-Reaction Theory of Synchronous Machine*", AIEE Trans., Pt.III, Vol.48, 1929, pp.716-727

[2] R.D. Ball, "*Synchronizing Torque of an Unexcited Salient Pole Motor*", Electrical Engineering, Vol.52, Feb.1933, p.136

[3] P.H. Trikey, "*Small Synchronous Motor Without Exciters*", The Electric Journal, Vol.30, No.4, Apr.1933, pp.160-162

[4] P.J. Lawrenson, and S.K. Gupta, "*Developments in the Performance and Theory of Segmented-Rotor Reluctance Machines*", IEE Proc., Vol.111, 1964, pp.1435-40

[5] A. Hughes, and P.J. Lawrenson, "*Electromagnetic Damping in Stepping Motors*", IEE Proc., Vol.122, No.8, Aug.1975, pp.819-826

[6] P.J. Lawrenson and S.R. Vamaraju, "*New 4/6 Pole Reluctance Motor*", Electric Machines and Electromechanics, 1978, pp.311-323

[7] M.R. Harris, A.Hughes, and P.J. Lawrenson, "*Static Torque Production in Saturated Doubly-Salient Machines*", IEE Proc., vol.122, No.10, Oct.1975, pp.1121-26

[8] L.E. Unnewehr and W.H. Koch, "*An Axial Air-Gap Relyctance Motor for Variable Speed Application*", IEEE Trans., PAS-93, 1974, pp.367-376

[9] J.A. Wagner and S.A. Nasar, "*Segmented Secondary Linear Reluctance Motor:A Parametric Study*", Electric Machines and Electromechanics, 1977, pp.1-23

[10] J.A. Wagner and V.D. Zavgorodny, "*Tangential Force Distribution and Force Pulsation in a Linear Reluctance Motor*", Electric Machines and Electromechanics, 1978, pp.341

[11] J.H. Lang and R. D. Thornton, "*Power Optimal Excitation of Reluctance Motor*", Electric Machines and Electromechanics, 1978, pp.123-137

[12] P.J. Lawrenson, J.M. Stephenson, P.T. Blenkinsop, J. Corda, and N.N. Fulton, "*Variable-Speed Switched Reluctance Motors*", IEE Proc., Vol.127, Pt.B, No.4, July 1980, pp.253-265

[13] W.F. Ray, P.J. Lawrenson, R.M. Davis, J.M.Stephenson, N.N. Fulton, and R.J. Blake, "*High Performance Switched Reluctance Brushless Drives*", IEEE Trans., IAS, 1985, pp.1769-1776

[14] M.R. Harris et al, "*Discussion on Variable-Speed Switched Reluctance Motor*", IEE Proc., Vol.128, Pt.B, No.5, Sep.1981, pp.260-268

[15] M.R. Harris, J.W. Finch, J.A. Mallick, and T.J. Miller, "*A Review of the Integral Horsepower Switched Reluctance Drive*", IEEE Trans., IAS, 1985, pp.783-789

[16] N.N. Fulton, P.J. Lawrenson, R.M. Davis, W.F. Ray, and J.M. Stephenson, "*Recent Development in High-Performance Switched Reluctance Drives*", IEE Conf. on Electrical Machines, No.254, 1985, pp.130-133

[17] R.M. Davis, "*The Switched Reluctance Drive*", IEE Conf. on Electrical Machines, No. 254, 1985, pp.188-191

[18] J. Reed, "*Switch Reluctance Drive System*", IEE Conf. on Power electronics & Variable Speed Drives, No. 264, Nov.1986, pp.118-121

[19] J.W. Finch, M.R. Harris, and H.M.B. Metwally, "*Switched Reluctance Motor Excitation Current: Scope for Improvment*", IEE Conf. on Power electronics & Variable Speed Drives, No. 264, Nov.1986, pp.197-202

[20] P.J. Lawrenson, W.F. Ray, R.M. Davis, and J.M. Stephenson, "*Controlled-Speed Switched-Reluctance Motor: Present Status and Future Potential*", First European conference on Electrical Drives/Motors/ Controls, England, 1982, pp.23-31

[21] M.R. Harris, J.W. Finch, and T.J. Miller, "*A Review of the Inegral Horsepower Switched Reluctance Drive*" IEEE Trans., IAS, Vol.22, No.4, July 1986, pp.716-721

[22] R.M. Davis, W.F. Ray, and R.J. Blake, "*Inveter Drive for Switched Reluctance Motor: Circuits and Component Ratings*", IEE Proc., Vol.128, Pt.B, No.2, March 1981, pp.126-136

[23] B.K. Bose, and T.J. Miller, "*Microcomputer Control of Switched Reluctance Motor*", IEEE Trans., Vol.22, No.4, July 1986, pp.708-715

[24] T.J.E. Miller, " *Converter Volt-Ampere Requirements of the Switched Reluctance Motor Drive*", IEEE, IAS,Vol.20, 1984, pp.813-819

[25] R.J. Blake, P.D. Webster, and D.M. Sugden, "*The Application of GTOs to Switched Reluctance Drives*", IEE Conf., Second International Conf. on Power Electronics and Variable Speed Drives, No.264, Nov.1986, pp.24-28

[26] C. Pollock and B.W. Williams, "*A unipolar Converter for a Switched Reluctance Motor*", IEEE Conf., IAS, 1988, pp.44-49

[27] J. W. Finch, and M. R. Harris, "*Switched Reluctance Motors With Multiple Teeth Per Pole: Philosophy of Design*", Proc. Incremental Motion Control, No.13, Illinois 1984, pp.134-141

[28] P.J. Lawrenson, W.F. Ray, R.M. Davis, and J.M. Stephenson, "*Switched Reluctance Motor Drives for Rail Traction*", IEE Proc., Vol.131, Pt.B, No.5, Sep.1984, pp.220-226

[29] J.H. Lang, and F.J. Vallese, "*Variable-Reluctance Motor Drives for Electric Vehicle Propulsion*", Final Report, DOE/CS-54209-26, 1985

[30] R. Arumugam, D.A. Lowther, R. Krisjnan, and J.F. Lindsay, "*Magnetic Field Analysis of a Switched Reluctance Motor Using a Two Dimentional Finit Element Method*", IEEE Trans., MAG-21, No.5, 1985, pp.1883-85

[31] R. Krishnan, R. Arumugam, and J.F. Lindsay, "*Design Procedure for Switched Reluctance Motor*", IEEE Conf., IAS, 1986, pp.858-863

[32] J.F. Lindsay, R. Arumugam, and R. Krishnan, "*Magnetic Field Analysis of a Switched Reluctance Motor with Multitooth per Stator Pole*", IEE Proc., Vol.133, Pt.B, No.6, Nov.1986, pp.347-353

[33] G. E. Dawson, A. R. Eastham, and J. Mizia, "*Switched Reluctance Motor Torque Characteristics*", IEEE Conf., IAS, 1986, pp.864-869

[34] P.H. Chappell, "*Winding Current in a Switched Reluctance Motor*", IEE Proc., Vol.134, Pt.B, No.5, Sep.1987, pp.277-283

[35] P.H. Chappell, "*Current Pulses in Switched Reluctance Motor*", IEE Proc., Vol.135, Pt.B, No.5, Sep.1988, pp.224-230

[36] D.W.J. Pulle, "*Performance of Split-Coil Switched Reluctance Drive*", IEE Proc., Vol.135, Pt.B, No.6, Nov.1988, pp.318-323

[37] R. Arumugan, J.F. Lindsay, and R. Krishnan, "*Sensitivity of Pole Arc/Pole Pitch Ratio on Switched Reluctance Motor Performance*", IEEE Conf. on IAS, 1988, pp.50-54

[38] J.M. Stephenson, and M.A. El-Khazendar, "*Saturation in Doubly Salient Reluctance Motors*", IEE Proc., Vol.136, Pt.B, No.1, Jan.1989, pp.50-58

[39] N.N. Fulton, "*The Application of CAD to Switched Reluctance Drives*", IEE Conf. on Electrical Drives, 1987, pp.275-279

[40] P. Materu, and R. Krishnan, "*Estimation of Switched Reluctance Motor Losses*", IEEE Conf., IAS, 1988, pp.79-90

[41] M.A. Prsa, "*Numerical Prediction of Optimal Switching Angle for VR Step Motors*", IEE Conf. on Electrical Drives, 1987, pp.340-343

[42] J. Corda, and T. Mateljan, "*Optimization of Operation of a Switched Reluctance Motor Using Nonlinear Mathematical Model*", IEE Conf. on Electrical Drives, 1987, pp.352-354

[43] P.D. Webster, "*Isolated Current Measurement for the Switched Reluctance Drive*", IEE Conf. on Power Electronic and Variable Speed Drives, No.264, Nov.1986, pp.177-181

[44] J.P Etter, and J.S. Soffer, " *Current and Voltage LEM Modules*", IEE Conf. on Power Electronics and Variable Speed Drives, No.264, Nov.1986, pp.164-167

[45] P. Sylvester, and M.V.K. Chari, "*Finite Element Solution of Saturable Magnetic Field Problem*", IEEE Trans., PAS-89, No.7, Sep.1970, pp.1642

[46] O.C. Zienkiewicz, *The Finite Element Method,* Third Edition, McGraw Hill, 1985

[47] J. N. Reddy, *An Introduction to the Finite Element Method,* McGraw Hill, 1984

[48] P.P. Sylvester, and D.A. Lowther, *Computer Aided Design in Magnetics,* springer-Verlag, N.Y., 1986

[49] M. Mori, *The Finite Element Method and Its Application,* McMillan, 1983

[50] S.C. Tandon, A.F. Armor, and M.V.K Chari, "*Nonlinear Transient Finite Element Field Computation for Electrical Machines and Devices*", IEEE Trans., PAS-102, No.5, May 1983, pp.1089-1095

[51] M.V.K Chari, S.H. Minnich, and S.C. Tandon, "*Load Characteristics of Synchronous Generator by the Finite Element Method*", IEEE Trans., PAS-100, No.1, Jan.1981, pp.1-13

[52] I.D. Mayergoyz and T. Doong, "*Hybrid Boundary-Volume Galerkin's Method for Nonlinear Magnetostatic Problems*", J. of Appl. Phys., No.57, Apr.1985, pp.3838-3840

[53] P.P. Sylvester, H.S. Cabayan, and B.T. Browne, "*Efficient Techniques for Finite Element Analysis of Electric Motors*", IEEE Conf., PES, N.Y., Jan.1973, pp.1274-83

[54] J.F. Berkery, R.K. Barton, and A. Konrad, "*Automatic Finite Element Grid Generation for Motor Design Analysis*", IEEE Trans., MAG-20, No.5, Sep.1984, pp.1924-26

[55] S.R.H. Hoole, "*Rotor Motion in the Dynamic Finite Element Analysis of Rotating Electrical Machinery*", IEEE Trans., MAG-21, No.6, Nov.1985, pp.2292-95

[56] S.R.H. Hoole, "*Flux Density and Energy Perturbation in Adaptive Finite Element Mesh Generation*", IEEE Trans., MAG-24, No.1, Jan.1988, pp.322-325

[57] D.C. Jiles and D.L. Atherton, "*Theory of Ferromagnetic Hysteresis*", J. of Magnetism and Magnetic Materials, No.61, 1986, pp.48-60

[58] H.G. Jensen, and G.A. Parks, "*Efficient Solution of Linear Matrix Equation*", ASCE, No.96, 1970, pp.49

[59] K.T. Joseph, "*A Note on Integration Over Finite Elements*", Computers and Structures, Vol.9, 1978, pp.523-524

[60] I. Babuska, and A.K. Aziz, "*On the Angle Condition in the Finite Element Method*", SIAM, J. of Num. Analysis,1976, pp.214

[61] J.H. Bramble and M. Zlamal, "*Triangular Elements in Finite Element Method*", Mathematics of Computation, Vol.24, No.112, Oct.1970, pp.809-820

[62] Z.J.Cendes, D. Shenton, and H. Shahnasser, "*Magnetic Field Computation Using Delaunay Triangulation and Complementary Finite Element Methods*", IEEE Trans., MAG-19, No.6, Nov.1983, pp.2551-58

[63] C.M. Ong, C.T. Liu, and C.N. Lu, "*Generation of Connection Matrices For Digital Simulation of Converter Circuits Using Tensor Approach*", IEEE Trans., PAS-107, Nov.1987, pp.906-913

[64] B. Davat, and J. Hector, "*Magnetic Structure and Feeding Circuit Modeling*", IEEE Trans., MAG-19, No.6, Nov.1983, pp.2471-74

[65] T. Nakata, and N. Takahashi, "*Direct Finite Element Analysis of Flux and Circuit Distribution under Spesified Condition*", IEEE Trans., MAG-18, No.2, Mar.1982, pp.325-328

[66] O. Wasynczuk, and M.P. Krefta, "*A Finite Element Based State Model of Solid Rotor Synchronous Machines*", IEEE Trans., Vol.EC-2, No.1, 1987, pp.21-31

[67] T.A. Nyamusa, and N.A. Demerdash, "*Integrated Nonlinear Field-Network Simulation of Permanent Magnet Motor under Normal Condition*", IEEE Conf., PES, N.Y., 1986

[68] M. Riaz, "*The Circuit Field Connection in Two-Dimensional AC Finite Element Analysis of Multiply-Excited Magnetic Structure*", IEEE Trans., PAS-104, No.7, July 1985, pp.1797-1804

[69] J. Finch, "*Magnetic Permeance of Aligned Doubly Salient Structure*", IEE Proc., Vol.133, Pt.B, No.6, Nov.1986, pp.365-366

[70] J. Corda, and J.M. Stephenson, "*Analytical Estimation of the Minimum and Maximum of a Double Salient Motor*", Conf. on Stepping Motors and Systems, England, 1979, pp.50-60

[71] J.G. Lacy, and J.V. Byrne, "*Characteristics of Saturable Stepper and Reluctance Motors*", IEE Conf. on Elec. Machines, No.136, 1976, pp.93-98

[72] V. Karapetoff, "*Mechanical Forces Between Electric Currents*", AIEE Trans., May 1927, pp.563-569

[73] J.A. Stratton, *Electromagnetic Theory,* McGraw Hill, 1941

[74] R.M. Fano, L.J. Chu, and R.B. Adler, *Electromagnetic Fields, Energy, and Forces,* John Wiley&Sons, 1960

[75] C.J. Carpenter, "*Surface Integral Methods of Calculating Forces on Magnetized Iron Parts*", Proc.IEE, Aug.1959, pp.19-28

[76] C.B. Gray, "*Rotor Torque Distribution in Electrical Machines via Maxwell's Stresses*", IEEE Trans., Vol.E-24, No.4, Nov.1981, pp.283-286

[77] J.L. Coulomb, "*A Methodology for Determination of Global Electromechanical Quantities from a Finite Element Analysis and its Application to the Evaluation of Magnetic Forces, Torques, and Stiffness*", IEEE Trans., MAG-19, No.6, November 1983, pp.2514-2519.

[78] J.L. Coulomb, G. Meunier, and J.C. Sabonnadiere, "*Energy Method for the Calculation of Global Quantities and Integral Parameters in a Finite Elements Analysis of Electromagnetic Devices*", IEEE Trans., Mag-21, No.5, 1985, pp.1817-1827

[79] A. Jacobus and W. Muller, "*Numerical Solution of Forces and Torques,*" IEEE Trans., Mag-19, 1983, pp.2589-2592

[80] T. Kaashima, A. Kawahara, and T. Goto, "*Force Calculation Using Magnetizing Currents*", IEEE Trans., Vol.24, No.1, Jan.1988, pp.451-454

[81] J.V. Byrne, "*Tangential Forces in Overlapped Pole Geometries Incorporating Ideally Saturable Material*", IEEE Trans., Mar.72, No.1, March 1972, pp.2-9

[82] J. M. Stephenson and J. Corda, "*Computation of Torque and Current in Doubly Salient Reluctance Motors from Nonlinear Magnetization Data*", IEE Proc., Vol.126, No.5, May 1979, pp.393-396

[83] H.B. Ertan, A. Hughes, and P.J. Lawrenson, "*Efficient Numerical Method for Predicting the Torque/Displacement Curve of Saturated VR Stepping Motors*", IEE Proc., Vol.127, Pt.B., No.4, July 1980, pp.246-252

[84] J. Penman and M.D. Grieve, "*Efficient Calculation of Force in Electromagnetic Devices*", IEE Proc., Vol.133, Pt.B, No.4, July 1986, pp.212-216

[85] S.R.H. Hoole and P.R.P. Hoole, "*On Finite Element Force Computation from Two-and Three-Dimensional Magnetostatic Fields*", J. Appl. Phys., No.57, April 1985, pp.3850-3852

[86] J. Mizia, K. Adamiak, A.R. Eastham, and G.E. Dawson, "*Finite Element Force Calculation: Comparison of Methods for Electric Machines*", IEEE Trans., Vol.24, No.1, Jan.1988, pp.450-457

[87] T. Tarnhuvud and K. Reichert, "*Accuracy Problems of Force and Torque Calculation in FE-Systems*", IEEE Trans., Vol.24, No.1, Jan.1988, pp.443-446

[88] S. McFee and D.A. Lowther, "*Toward Accurate and Consistent Force Calculation in Finite Element Based Computational Magnetostatic*", IEEE Trans., Mag-23, No.5, Sept.1987, pp.3771-73

[89] J.M. Stephenson, and J. Corda, "*Computation of Torque and Current in Doubly Salient Structure Motor from Nonlinear Magnetization Data*", Proc. IEE, Vol.126, No.5, 1979, pp.393-396

[90] F.Piriou, and A.Razek, "*Calculation of Saturated Inductances for Numerical Simulation of Synchronous Machine*", IEEE Trans., MAG-19, No.6, Nov.1983, pp.2628-2631

[91] T.W. Nehl, F.A. Fouad, and N.A. Demerdash, "*Determination of Saturated Values of Rotating Machinery Incremental and Aparent Inductances by an Energy Perturbation Method*", IEEE Trans., PAS-101, No.12, Dec.1982, pp.4441-4451

[92] W. Woodson and J.R. Melcher, *Electromechanical Dynamics,* Vol. I&II, John Wiley & Sons, 1968

[93] W.H. Press, B.P. Flannery, S.A. Teuokolsky, and W.T. Vetterling, *Numerical Recipes,* Cambridge University Press, 1987

[94] D. Quilin and B.J. Davis, *Surface Engineering Geometry for Computer-Aided Design and Manufacturing,* John Wiley&Sons, 1987

[95] M. Moallem and C.M. Ong, "*Predicting the Torque of a Switched Relutance Machine from Its Finite Element Solution*", IEEE-PES Paper No. SM 617-2 EC, PES Summer Meeting, July 1989

[96] M. Moallem and C.M. Ong, "*Predicting the Steady State Characteristics of a Switched Reluctance Motor Drive*", To be presented in IEEE-IAS 1989 Annual Meeting

APPENDICES

Appendix A- Area Coordinates

In this system, the coordinates of an interior point N of the triangle is expressed as

$$N\left(L_l = \frac{\Delta l}{\Delta}\ ,\ L_m = \frac{\Delta m}{\Delta}\ ,\ L_n = \frac{\Delta n}{\Delta}\right)$$

where Δl, Δm, and Δn are the areas of sub n triangles shown in Fig. A-1, and Δ is the area of the original triangle. Defined in this manner, both properties of basis function, (2.3) and (2.4), are satisfied, that is

$$\sum_{i\in\Omega} L_i = \frac{\Delta l + \Delta m + \Delta n}{\Delta} = 1 \tag{A-1}$$

$$L_i(\text{node } j) = \delta_{ij} \tag{A-2}$$

where

$$\delta_{ij} = \begin{cases} 1 \text{ if } i=j \\ 0 \text{ if } i\neq j \end{cases}$$

Note that only two of the three co-ordinates are independent, since (A-1) holds.

If, A, at the point (x,y) inside the triangle is assumed to vary linearly with x and y, then

$$A(x,y) = \alpha_1 + \alpha_2 x + \alpha_3 y \tag{A-3}$$

At the vertices of the triangle,

$$A_l = \alpha_1 + \alpha_2 x_l + \alpha_3 y_l \tag{A-4}$$

$$A_m = \alpha_1 + \alpha_2 x_m + \alpha_3 y_m \tag{A-5}$$

$$A_n = \alpha_1 + \alpha_2 x_n + \alpha_3 y_n \tag{A-6}$$

where the subscripts l, m, and n denote the values at the vertices of the triangle. Taking the inverse of the matrix equation formed by (A-4) through (A-6), the α's can be determined from

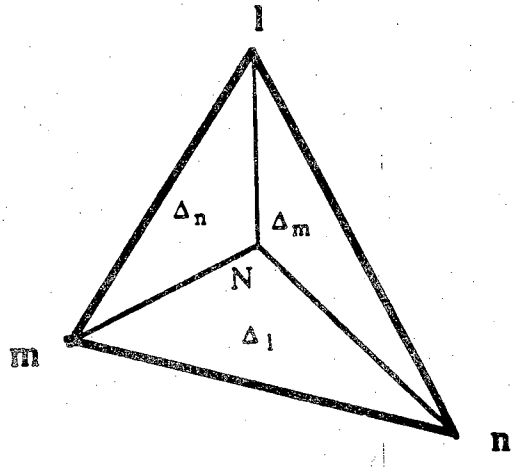

Figure A.1. Area coordinates

$$\begin{bmatrix}\alpha_1\\ \alpha_2\\ \alpha_3\end{bmatrix} = \begin{bmatrix}1 & x_l & y_l\\ 1 & x_m & y_m\\ 1 & x_n & y_n\end{bmatrix}^{-1}\begin{bmatrix}A_l\\ A_m\\ A_n\end{bmatrix} \tag{A-7}$$

Defining a set of new notations for the elements of the adjoint matrix:

$$r_l = x_n - x_m, \quad r_m = x_l - x_n, \quad r_n = x_m - x_l$$
$$q_l = y_m - y_n, \quad q_m = y_n - y_l, \quad q_n = y_l - y_m$$
$$p_l = x_m y_n - x_n y_m, \quad p_m = x_n y_l - x_l y_n, \quad p_n = x_l y_m - x_m y_l$$

and

$$D = 2\Delta = p_l + p_m + p_n$$

(A-7) can be rewritten as

$$\begin{bmatrix}\alpha_1\\ \alpha_2\\ \alpha_3\end{bmatrix} = \frac{1}{D}\begin{bmatrix}p_l & p_m & p_n\\ q_l & q_m & q_n\\ r_l & r_m & r_n\end{bmatrix}\begin{bmatrix}A_l\\ A_m\\ A_n\end{bmatrix} \tag{A-8}$$

Back substituting the expressions for α_1, α_2, and α_3 into (A-3), the vector potential at the interior point (x,y), is given by

$$A(x,y) = \frac{1}{D}\left\{[p_l\ p_m\ p_n] + x[q_l\ q_m\ q_n] + y[r_l\ r_m\ r_n]\right\} \times \begin{bmatrix}A_l\\ A_m\\ A_n\end{bmatrix} \tag{A-9}$$

Appendix B- Integration and Differentiation in Area Coordinates

To facilitate integration and differentiation in an element with irregular sides, a mapping of domain to a right-angled triangle as shown in Fig. B-1 is used

$$(x,y) \xrightarrow{T} (u,v) \tag{B-1}$$

where T is the transformation operator from (x,y) domain to (u, v) domain. For mapping of triangles, mapping of three vertices are needed. Lets define a set of 3 basis functions,

$$x = \sum_{i=}^{\Omega} f_i(u,v)\, x_i \tag{B-2}$$

$$y = \sum_{i=}^{\Omega} f_i(u,v)\, y_i \tag{B-3}$$

The basis function should have the properties:

$$f_i(u_j,v_j) = \partial_{ij} \tag{B-4}$$

$$\sum_{i=1}^{N} f_i(u,v) = 1 \tag{B-5}$$

An obvious choice is the set

$$f_1 = 1-u-v \ , \ f_m = u \ , \ f_n = v$$

that has above properties. Substituting for f_i in (B-2) and (B-3), we have,

$$\begin{bmatrix} x \\ y \end{bmatrix} \begin{bmatrix} x_m-x_1 & x_n-x_1 \\ y_m-y_1 & y_n-y_1 \end{bmatrix} \begin{bmatrix} u \\ v \end{bmatrix} + \begin{bmatrix} x_1 \\ y_1 \end{bmatrix} \tag{B-6}$$

>From Appendix A, we have

$$x_m-x_1 = r_n$$

$$y_m-y_1 = -q_n$$

$$x_n-x_1 = -r_m$$

$$y_n-y_1 = q_m$$

and inverse transformation matrix is

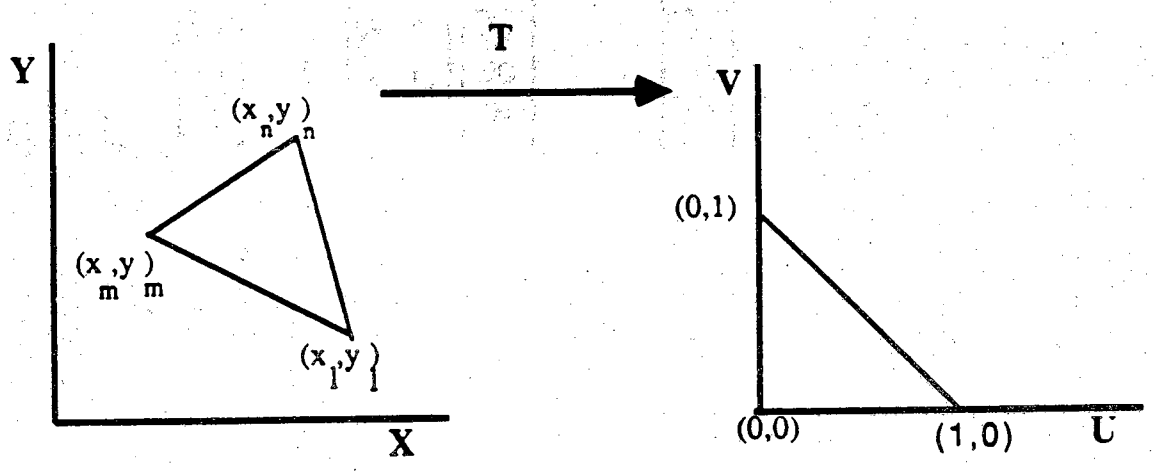

Figure B.1. Transformation of coordinates

$$T^{-1} = \begin{bmatrix} r_n & -r_m \\ -q_n & q_m \end{bmatrix} \tag{B-7}$$

Then the transformation matrix T is

$$T = \frac{1}{r_n q_m - r_m q_n} \begin{bmatrix} q_m & r_m \\ q_n & r_n \end{bmatrix} \tag{B-8}$$

By inspection

$$r_n q_m - r_m q_n = D = 2\Delta_e$$

Thus

$$\begin{bmatrix} u \\ v \end{bmatrix} = \frac{1}{D} \begin{bmatrix} q_m & r_m \\ q_n & r_n \end{bmatrix} \begin{bmatrix} x - x_1 \\ y - y_1 \end{bmatrix} \tag{B-9}$$

The vector potential in the new domain is given by:

$$A = (1-u-v)A_1 + uA_m + vA_n \tag{B-10}$$

To the evaluate a double integral in new domain, one needs to transform both the function and differential area to the new domain

$$I = \int\int g(x,y)\, dxdy \tag{B-11}$$

$$g(x,y) \xrightarrow{T} G(u,v)$$

$$dxdy = |J|\, dudv$$

where J is the Jacobian matrix given by

$$J = \begin{bmatrix} \frac{\partial x}{\partial u} & \frac{\partial y}{\partial u} \\ \frac{\partial x}{\partial \nu} & \frac{\partial y}{\partial \nu} \end{bmatrix} = \begin{bmatrix} r_n & -q_n \\ -r_m & q_m \end{bmatrix} = [T^{-1}]^t \tag{B-12}$$

and

$$|J| = r_n q_m - r_m q_n = 2\Delta = D \tag{B-13}$$

Then I can be evaluated as

$$I = D \int_0^1 dV \int_0^{1-u} G(u,v)\, dudv \tag{B-14}$$

Similarly, for differentiating of a function g(x,y) in new domain, we have

$$\frac{\partial g}{\partial x} = \frac{\partial G}{\partial u}\frac{\partial u}{\partial x} + \frac{\partial G}{\partial v}\frac{\partial v}{\partial x}$$

$$\frac{\partial g}{\partial y} = \frac{\partial G}{\partial u}\frac{\partial u}{\partial y} + \frac{\partial G}{\partial v}\frac{\partial v}{\partial y}$$

or in matrix form

$$\begin{bmatrix} \frac{\partial g}{\partial x} \\ \frac{\partial g}{\partial y} \end{bmatrix} = \begin{bmatrix} \frac{\partial u}{\partial x} & \frac{\partial v}{\partial x} \\ \frac{\partial u}{\partial y} & \frac{\partial v}{\partial y} \end{bmatrix} \begin{bmatrix} \frac{\partial G}{\partial u} \\ \frac{\partial G}{\partial v} \end{bmatrix} \tag{B-15}$$

Using (B-9), (B-15) can be rewritten as

$$\begin{bmatrix} \frac{\partial g}{\partial x} \\ \frac{\partial g}{\partial y} \end{bmatrix} = \frac{1}{D} \begin{bmatrix} q_m & q_n \\ r_m & r_n \end{bmatrix} \begin{bmatrix} \frac{\partial G}{\partial u} \\ \frac{\partial G}{\partial v} \end{bmatrix} = [J]^{-1} \begin{bmatrix} \frac{\partial G}{\partial u} \\ \frac{\partial G}{\partial v} \end{bmatrix} \tag{B-16}$$

Appendix C- Elemental Jacobian Matrix

Within each finite element, the Jacobian matrix is

$$[J_e] = \frac{\partial[S_e A_e - I]}{\partial A_e} = \frac{\partial[S_e A_e]}{\partial A_e} \tag{C-1}$$

or in more expanded form

$$[J_e] = \left[\partial[S_e A_e]/\partial A_l \mid \partial[S_e A_e]/\partial A_m \mid \partial[S_e A_e]/\partial A_n\right]$$

$$= \left[\frac{\partial[S_e]}{\partial A_l}[A_e] + [S_e]\frac{\partial[A_e]}{\partial A_l} \mid \cdots \mid \cdots\right] \tag{C-2}$$

Each element of $[J_e]$ has two parts, the first part is given by

$$\left(S_{ij}\right)_1 = \frac{\partial \nu_e}{\partial A_i} S_e' A_e = \frac{\partial \nu_e}{\partial A_i} U_i \tag{C-3}$$

where S_e' is S_e/ν_e and its (ij)th elements is $S_{ij}' = q_i q_j + r_i r_j$ and

$$U_i = S_{il}' A_l + S_{im}' A_m + S_{in}' A_n \tag{C-4}$$

To evaluate $\dfrac{\partial \nu_e}{\partial A_i}$, express

$$\frac{\partial \nu_e}{\partial A_i} = \frac{\partial \nu_e}{\partial B^2} \cdot \frac{\partial \vec{B}^2}{\partial A_i} \tag{C-5}$$

The second term on right hand side of (C-5) can be evaluated from (2.45) as

$$\frac{\partial \vec{B}^2}{\partial A_i} = \frac{2}{D^2}\left(r_i \sum_{j=1}^{n} r_j A_j + q_i \sum_{j=1}^{n} q_j A_j\right) \tag{C-6}$$

Now using (2.41), one obtains

$$\frac{\partial \vec{B}^2}{\partial A_i} = \frac{2}{\Delta} U_j \tag{C-7}$$

The first term on the right hand side of (C-5) is the slope of ν—$\vec{B}^2$ curve which is obtained from the B-H curve. It can be shown that

$$\left(S_{ij}\right)_1 = \frac{2}{\Delta} \times \frac{\partial \nu_e}{\partial \vec{B}_e^2}\left(U_i \cdot U_j\right) \tag{C-8}$$

Now, matrix S may be defined as

$$\left[S_{ij}\right] = \left(u_i \cdot u_j\right) \tag{C-9}$$

The second part of the (ij)th element of $[J_3]$ can be shown to be given by

$$\left(S_{ij}\right)_2 = \left(S_e ij\right) \tag{C-10}$$

Thus, the Jacobian $[J_e]$ can be expressed as the sum of the two matrices

$$\left[J_e\right] = \left[S_e\right] + \left[\frac{\partial \nu_e}{\partial \vec{B}_e^2} S\right] \tag{C-11}$$

with its elements as

$$\left(J_e\right)_{ij} = \left(S_e\right)_{ij} + \left(\frac{\partial \nu_e}{\partial \vec{B}_e^2}\right)\left(S\right)_{ij} \tag{C-12}$$

Appendix D- Field Variables and Partial of Flux Density in Polar Coordinates

The magnetic vector potential,A, inside an element is expressed as a function of the MVP's at the nodes of that element, that is by

$$A = \sum_{i \in \Omega} L_i A_i \tag{D-1}$$

where Ω is the set of elements node, {l, m, n}. The area coordinates,L_i, as defined in Appendix A are given as

$$L_i = \frac{\Delta i}{\Delta} = \frac{1}{\Delta}(P_i + q_i x + r_i y) \tag{D-2}$$

To obtain A in polar form, we make the following substitution for cartesian coordinates x and y:

$$\begin{aligned} x &= r\cos\theta \\ y &= r\sin\theta \end{aligned} \tag{D-3}$$

In polar coordinates, the expression for the area of a triangle,Δ_e, is

$$\Delta_e = \frac{1}{2}[r_m r_n \sin(\theta_n - \theta_m) + r_n r_\ell \sin(\theta_\ell - \theta_n) + r_\ell r_m \sin(\theta_m - \theta_\ell)] \tag{D-4}$$

and that for area coordinate of node ℓ is

$$L_\ell = \frac{1}{2\Delta}[r\, r_m \sin(\theta_m - \theta) + r\, r_n \sin(\theta - \theta_n) + r_m r_n \sin(\theta_n - \theta_m)] \tag{D-5}$$

The above expression for area coordinates can be substituted in (D-1) to obtain MVP in polar coordinates.

The components of the flux density,B, in polar coordinates can be obtained from

$$B_r = \frac{1}{r}\frac{\partial A}{\partial \theta}, \quad B_\theta = -\frac{\partial A}{\partial r} \tag{D-6}$$

Differentiating A with respect to θ and r, respectively, we obtain

$$\begin{aligned} B_r = \frac{1}{2\Delta} \{ & A_\ell[-r_m \cos(\theta_m - \theta) + r_n \cos(\theta_n - \theta)] \\ & + A_m[-r_n \cos(\theta_n - \theta) + r_\ell \cos(\theta_\ell - \theta)] \end{aligned}$$

$$+ A_n[-r_\ell \cos(\theta_\ell - \theta) + r_m \cos(\theta_m - \theta)]\} \tag{D-7}$$

$$B_\theta = \frac{1}{2\Delta}\{A_\ell[-r_m \sin(\theta_m - \theta) + r_n \sin(\theta_n - \theta)]$$

$$+ A_m(-r_n \sin(\theta_n - \theta) + r_\ell \sin(\theta_\ell - \theta)]$$

$$+ A_n(-r_\ell \sin(\theta_\ell - \theta) + r_m \sin(\theta_m - \theta)\} \tag{D-8}$$

To find the partial derivatives of B_r and B_θ due to small rotation of rotor, $\delta\theta_i$, let (D-7) be written as:

$$B_r = \frac{b_r(\theta_i)}{2\Delta(\theta_i)}, \quad B_\theta = \frac{b_\theta(\theta_i)}{2\Delta(\theta_i)} \tag{D-9}$$

Now differentiation B_r and B_θ with respect to θ_i yields

$$\frac{\partial B_r}{\partial \theta_i} = \frac{1}{2\Delta}\frac{\partial b_r}{\partial \theta_i} - \frac{b_r}{2\Delta^2}\frac{\partial \Delta}{\partial \theta_i} \tag{D-10a}$$

$$\frac{\partial B_\theta}{\partial \theta_i} = \frac{1}{2\Delta}\frac{\partial b_\theta}{\partial \theta_i} - \frac{b_\theta}{2\Delta^2}\frac{\partial \Delta}{\partial \theta_i} \tag{D-10b}$$

where the partial derivatives $\frac{\partial b_r}{\partial \theta_i}$, $\frac{\partial b_\theta}{\partial \theta_i}$, and $\frac{\partial \Delta}{\partial \theta_i}$ can be calculated as follows:

$$\frac{\partial b_r}{\partial \theta_\ell} = (A_m - A_n) r_\ell \sin(\theta - \theta_\ell) \tag{D-11a}$$

$$\frac{\partial b_\theta}{\partial \theta_\ell} = (A_m - A_n) r_\ell \cos(\theta - \theta_\ell) \tag{D-11b}$$

$$\frac{\partial \Delta}{\partial \theta_\ell} = \frac{1}{2}[r_n r_\ell \cos(\theta_\ell - \theta_n) - r_\ell r_m \cos(\theta_m - \theta_n)] \tag{D-12}$$

The dot product, $B \cdot \frac{\partial B}{\partial \theta_\ell}$, in (3.32) can be evaluated with the help of expression given in (D-10).

$$B \cdot \frac{\partial B}{\partial \theta_\ell} = B_r \frac{\partial B_r}{\partial \theta_\ell} + B_\theta \frac{\partial B_\theta}{\partial \theta_\ell}$$

$$= \frac{1}{2\Delta}[B_r \frac{\partial b_r}{\partial \theta_\ell} + B_\theta \frac{\partial b_\theta}{\partial \theta_\ell}] - \frac{B^2}{2\Delta} \frac{\partial \Delta}{\partial \theta_\ell} \quad \text{(D-13)}$$

Term in brackets on the right hand side of (D-13) using expressions from (D-7), (D-8), and (D-12) after some trigonometric manipulations, can be written as

$$B_r \frac{\partial b_r}{\partial \theta_\ell} + B_\theta \frac{\partial b_\theta}{\partial \theta_\ell} = \frac{r_\ell(A_m - A_n)}{2\Delta}[r_m(A_n - A_\ell)\sin(\theta_m - \theta_\ell)$$

$$+ r_n(A_\ell - A_m)\sin(\theta_n - \theta_\ell)] \quad \text{(D-14)}$$

Now substituting for the term in brackets and for $\frac{\partial \Delta}{\partial \theta_\ell}$ from (D-14) and (D-11), $B \cdot \frac{\partial B}{\partial \theta_\ell}$ is as follows:

$$B_e \cdot \frac{\partial B_e}{\partial \theta_\ell} = \frac{r_\ell(A_m - A_n)}{2\Delta^2}[r_m(A_n - A_\ell)\sin(\theta_m - \theta_\ell) + r_n(A_\ell - A_m)\sin(\theta_n - \theta_\ell)]$$

$$- \frac{B^2}{2\Delta}[r_n r_\ell \cos(\theta_\ell - \theta_n) - r_\ell r_m \cos(\theta_m - \theta_n)] \quad \text{(D-15)}$$

Appendix E- Parameters and Material Characteristics of Test SR Motor

The test motor is a 4 kW , 6/8, 4-phase switched reluctance motor from TASK Drive of UK and the control is OULTON 112. The nameplate data for the SR motor is given in Table E.1.

Table E.1. Nameplate data for SR test motor

phases:	4
Rated hp:	5.5
Rated Voltage:	380/415 volts
Nominal Current:	9 Amps
Supply Frequency:	50/60 Hz
Nominal Speed:	1500 rpm

E.1. Motor Geometry

As the exact dimensions of the test motor were not available, the values given are our best estimate based on direct measurement. A cross-section of the test motor is shown in Fig. E.1. These data is given in Table E.2.

E.2. Material Characteristics

The FE program requires the material characteristics for all regions in the motor cross-section. The regions occupied by air and the winding were assigned a permeability of the value equal to that of the free space(ν_0). Rotor and stator, and rotor shaft are assumed to have the magnetic characteristics of M-19 steel given in Table E.3.

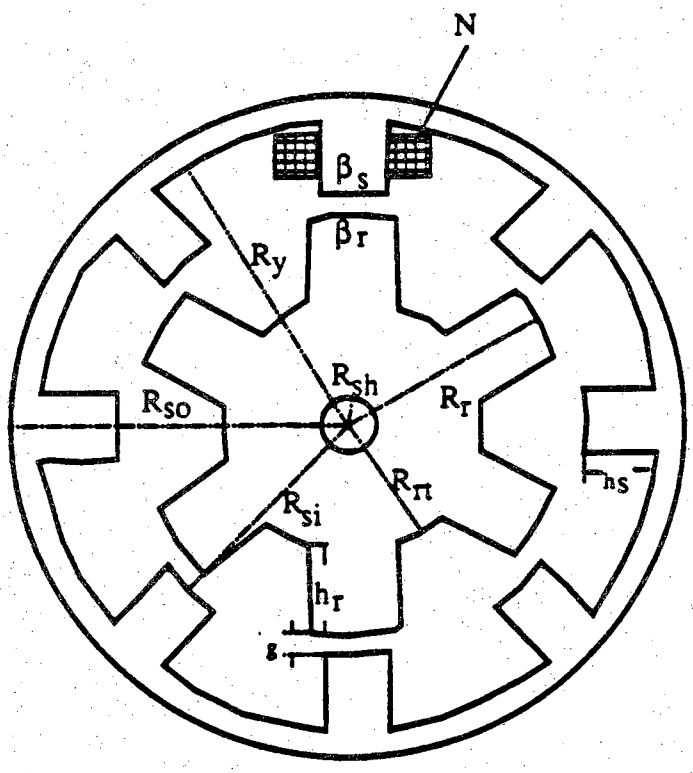

Figure E.1. Dimensions of the test SR motor

Table E.2. Geometric data of the SR motor

(All dimensions in milimeters)

R_{sh}:	15.0
R_{rt}:	30.3
R_r:	47.82
R_{si}:	48.18
R_y:	78.4
R_{so}:	89.8
g :	0.36
h_r:	17.52
h_s:	30.22
Z :	151
β_r:	22.5°
β_s:	20.2°
N :	56 turns
N_s:	8
N_r:	6

Table E.3. Motor lamination B-H data

B (Tesla)	H (At/m)
0.0	0.0
0.5	54.
0.55	60.5
0.6	67.6
0.65	74.8
0.7	83.5
0.75	93.5
0.8	104.4
0.85	116.9
0.9	131.3
0.95	148.2
1.0	167.1
1.05	187.8
1.1	214.9
1.15	250.7
1.2	298.4
1.25	374.
1.3	485.5
1.35	652.6
1.4	1010.6
1.45	1551.8
1.5	2308.
1.55	3342.
1.6	4775.
1.65	6366.
1.7	8356.
1.75	10743.
1.8	14165.
1.85	18303.
1.9	23874.
1.95	30240.
2.0	44565.
2.05	79580.
2.06	87537.7